Dissertation

Control of Laser Plasma Based Accelerators up to 1 GeV

GeV

Kei Nakamura

The University of Tokyo, Japan

and

Lawrence Berkeley National Laboratory, USA

December 2007

Control of Laser Plasma Based Accelerators up to 1 GeV

GeV

Copyright © 2007

by

Kei Nakamura

Abstract

Analysis and Control of
Laser Plasma Based Accelerators up to 1 GeV

by

Kei Nakamura

Doctor of Philosophy in Engineering

The University of Tokyo, Japan

Professor Mitsuru Uesaka, Chair

Lawrence Berkeley National Laboratory

Dr. Wim Leemans, Dissertation supervisor

This dissertation documents the development of a broadband electron spectrometer (ESM) for GeV class Laser Wakefield Accelerators (LWFA), the production of high quality GeV electron beams (e-beams) for the first time in a LWFA by using a capillary discharge guide (CDG), and a statistical analysis of CDG-LWFAs.

An ESM specialized for CDG-LWFAs with an unprecedentedly wide momentum acceptance, from 0.01 to 1.1 GeV in a single shot, has been developed. Simultaneous measurement of e-beam spectra and output laser properties as well as a large angular acceptance ($> \pm 10$ mrad) were realized by employing a slitless scheme. A scintillating screen (LANEX Fast back ,LANEX-FB) - camera system allowed faster than 1 Hz operation and evaluation of the spatial properties of e-beams. The design provided sufficient resolution for the whole range of the ESM (below 5% for beams with 2 mrad divergence). The calibration between light yield from LANEX-FB and total charge, and a study on the electron energy dependence (0.071 to 1.23 GeV) of LANEX-FB were performed at the Advanced light source (ALS), Lawrence Berkeley National Laboratory (LBNL). Using this calibration data, the developed ESM provided a charge measurement as well.

The production of high quality electron beams up to 1 GeV from a centimeter-scale

accelerator was demonstrated. The experiment used a 310 μm diameter gas-filled capillary discharge waveguide that channeled relativistically-intense laser pulses (42 TW, 4.5×10^{18} W/cm^2) over 3.3 centimeters of sufficiently low density ($\simeq 4.3 \times 10^{18}$/cm^3) plasma. Also demonstrated was stable self-injection and acceleration at a beam energy of $\simeq 0.5$ GeV by using a 225 μm diameter capillary. Relativistically-intense laser pulses (12 TW, 1.3×10^{18}W/cm^2) were guided over 3.3 centimeters of low density ($\simeq 3.5 \times 10^{18}$/cm^3) plasma in this experiment.

A statistical analysis of the CDG-LWFAs' performance was carried out. By taking advantage of the high repetition rate experimental system, several thousands of shots were taken in a broad range of the laser and plasma parameters. An analysis program was developed to sort and select the data by specified parameters, and then to evaluate performance statistically.

The analysis suggested that the generation of GeV-level beams comes from a highly unstable and regime. By having the plasma density slightly above the threshold density for self injection, 1) the longest dephasing length possible was provided, which led to the generation of high energy e-beams, and 2) the number of electrons injected into the wakefield was kept small, which led to the generation of high quality (low energy spread) e-beams by minimizing the beam loading effect on the wake. The analysis of the stable half-GeV beam regime showed the requirements for stable self injection and acceleration. A small change of discharge delay t_{dsc}, and input energy E_{in}, significantly affected performance.

The statistical analysis provided information for future optimization, and suggested possible schemes for improvment of the stability and higher quality beam generation. A CDG-LWFA is envisioned as a construction block for the next generation accelerator, enabling significant cost and size reductions.

To my wife, Heather Zhao,
my parents, Akira and Toshiko Nakamura,
my brothers, Tetsu and Yu.

Contents

List of Figures

Acknowledgements

Throughout my graduate career, 4 years in Japan and 4 years in USA, I have been supported by many colleagues, friends, and family. Without them, this work would not have been possible.

I would like to express my gratitude to Wim Leemans, my dissertation supervisor. I can not list my thanks to Wim because they are actually uncountable. He has kept on encouraging me with his warm and energetic support. The time I spent with him and his group is the most exciting and precious experience in my career. He is truly one of the greatest scientists, leaders, and supervisors I've ever met.

My great thanks go to Mitsuru Uesaka, who has taught, supported, and guided me for over 8 years. He kindly accepted my extraordinary request to conduct doctoral research in the USA. Without his support, nothing would have even been started.

I would like to show great appreciation to Yosuke Katsumura, Zensho Yoshida, Shuichi Hasegawa, Shin-ichiro Kado, and Kazuyuki Demachi for being on my committee, taking time to read my thesis, and providing many valued comments.

I have been a bike commuter, and never failed to ride with my iPod. That red Italian bike brought from Japan has been definitely a part of my life, and a song "float on" from Modest Mouse has been frequently played for almost 4 years.

I wish to thank my family in Japan. Even that far away from home, they have always supported and taken care of me and Heather as if we have been in Japan.

I wish to express my gratitude to my wife, Heather Zhao for her warmest encouragement all thourgh the time.

KEI NAKAMURA

Lawrence Berkeley National Laboratory
Berkeley, December 2007

Chapter 1

Introduction

Charged particle accelerators have contributed to a broad range of scientific fields, serving high energy and elementary particle physics through particle colliders, and providing radiation ranging from THz to x-rays for various applications in material science, chemistry, biology, or medicine. The accelerating structure of those conventional accelerators is based on radio frequency (RF) cavities, where the field gradient is limited at the $\simeq 100$ MV/m level due to material breakdown. Demands for higher energy particles from future facilities have led to the construction of large scale facilities, and even larger machines are planned.

A plasma-based accelerator is a promising candidate for a next generation accelerator. By using a plasma as a media for an accelerating structure, more than a thousand times higher field gradient than what current RF-based technology can provide has become possible. Recently, a generation of GeV-class high quality (a few percent energy spread) electron beams (e-beams) has been demonstrated with a centimeter scale laser wakefield acceleration (LWFA) [1–3]. This dissertation consists of contributions to the development of the GeV class LWFA. Such an LWFA is envisioned as a construction block for the next generation accelerator, enabling significant cost and size reductions.

In this Chapter, a brief history of plasma-based accelerator experiments is presented, followed by an overview of LWFA development in the LOASIS Program at Lawrence Berkeley National Laboratory (LBNL). The mechanism for generation of high energy and quality e-beams from an LWFA is briefly discussed as well. This Chapter will provide the motivation and background for the work presented in this dissertation.

1.1   Plasma Based Accelerator Experiments

A charged particle accelerator based on a plasma wave (wakefield) excited by an intense laser pulse was proposed by Tajima and Dawson in 1979 [4], followed by the concept of particle beam driven plasma wave (plasma wakefield acceleration, PWFA) in 1986 [5]. When an intense laser propagates through a plasma, the electromagnetic field gradient (ponderomotive force) of the laser pushes plasma electrons outward, while ions remains stationary. The resulting space-charge field subsequently causes a density oscillation behind the drive laser. This density oscillation (plasma wave) is called wakefield, and is illustrated in Fig. 1.1. For the linear regime (small electric field), the corresponding temporal frequency of the wakefield (plasma frequency) is given by:

$$\omega_p = \sqrt{\frac{4\pi e^2 n_e}{m_e}} \; , \tag{1.1}$$

where c is the speed of light in vacuum, m_e the rest mass of the electron, n_e the plasma electron density, and e the charge of an electron. The phase velocity of a plasma wave v_{pp} is given approximately by the group velocity of the laser beam in the plasma $v_{pp} \simeq v_g = c\sqrt{1 - (\omega_p^2/\omega_0^2)}$, where ω_0 is the central angular frequency of the laser pulse. For a sufficiently low density plasma, a characteristic wavelength of the plasma wave becomes:

$$\lambda_p = \frac{2\pi v_g}{\omega_p} \simeq \frac{2\pi c}{\omega_p} \; . \tag{1.2}$$
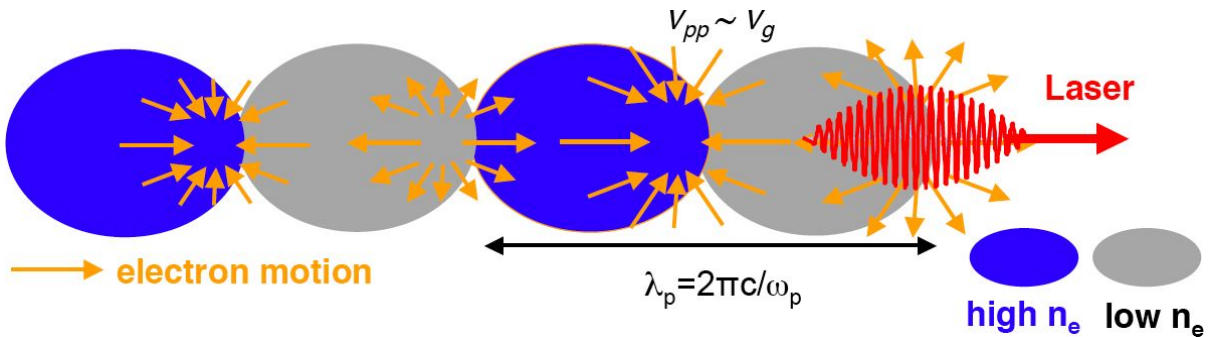
Figure 1.1: Illustration of a laser-driven plasma wakefield.

In the case of a PWFA, the space charge force of a particle beam drives the wakefield instead of a laser beam, and the phase velocity of the plasma wave is given approximately by the beam velocity $v_{pp} \simeq v_{beam}$. For a sufficiently high energy driving e-beam, a characteristic wavelength of the plasma wave becomes $\lambda_p = 2\pi v_{beam}/\omega_p \simeq 2\pi c/\omega_p$. These wake field acceleration (WFA) concepts allow realization of an accelerating structure with exceptionally high field gradient. For example, from Gauss's law, the Electric field E_0 can be estimated as:

$$E_0 = \frac{m_e \omega_p c}{e} \,, \tag{1.3}$$

or $E_0 \simeq 100$ GV/m for $n_e \simeq 10^{18}$ cm^{-3}. This electric field is thousands of times higher than what conventional accelerators can achieve in RF cavities.

The LWFA concept immediately drew the attention of many plasma scientists from around the world, and has been intensely studied for more than 25 years (for a review, see Ref. [6] for a theoretical overview, and Ref. [7] for recent experimental results). Note that this introduction does not cover plasma-based electron acceleration via laser-solid interactions [8–12].

Although there was some early work done by Joshi et al. in 1981 on Raman scattering [13], the first experimental proof of plasma-based acceleration of electrons was achieved via plasma beat wave acceleration (PBWA), where two long laser pulses with slightly different frequencies were used to resonantly excite a plasma wave (see Ref. [6], and references therein). The method was proposed by Tajima and Dawson [4] as an alternative to the LWFA due to the unavailability of short (≤ 1 ps), intense ($> 10^{17}$ W/cm^2) lasers at that time. In 1992, Kitagawa and coworkers [14] observed the acceleration of background electrons via PBWA employing two lines of a CO_2 laser. The total electron energy gain was 10 MeV and a 1.5 GV/m accelerating gradient was measured. External injection of e-beams into the plasma-based accelerating structure was first demonstrated via PBWA by Clayton et al., reported in 1993 [15, 16]. Electrons with an energy of 2.1 MeV were accelerated to 9.1 MeV by the resonantly excited wakefield with an accelerating gradient of 0.7 GV/m. The PBWA concept has been experimentally studied by several other groups as well [17–20], but interest has waned due to the availability of short pulse and high power lasers based on the technique called Chirped Pulse Amplification (CPA). In 1988, a compact terawatt laser system based on the CPA was first

demonstrated by Mourou and coworkers [21]. After this invention, laser plasma-based accelerators have evolved with the growth of CPA technology.

The acceleration of electrons using a single CPA-based laser was first demonstrated in 1995 with electrons injected from a laser-solid interaction by Nakajima and coworkers [22]. Up to 18 MeV electrons were observed using injected electrons of 1 MeV energy. The concept of LWFA with injected beams was also experimentally studied by Amiranoff et al. [23, 24] using an RF accelerator coupled to the LWFA. Although it successfully proved the concept experimentally, this scheme was not practical due to the low coupling efficiency between the RF-accelerated electrons and the plasma-based accelerating structures. The characteristic structure scale lengths were orders of magnitude different between the structures, and the required precision for RF-laser timing synchronization far exceeded what could be achieved at that time. Also reported in 1995, using a single CPA based laser, was acceleration of background electrons [25, 26]. Total energy gain up to 40 MeV with 100 GV/m accelerating gradient was achieved. Those experiments utilized Nd:glass based laser systems with pulse lengths τ_L which were more than a few hundred fs. Plasma densities were somewhat high (typically $\lesssim 10^{20}/\text{cm}^3$) to introduce strong self modulation of the laser pulses. The self modulation is the longitudinal and transverse modulations of the laser pulse due to the interaction with the plasma wakefield leading to laser pulse steepening and radial focusing/defocusing, which occur in the time scale of the plasma oscillation $\tau_p \sim 1/\omega_p$. A laser pulse longer than τ_p undergoes the self modulation, and eventually leads to the generation of large amplitude wakefields and self trapping of electrons into plasma accelerating structures via wave breaking. This operational regime is called the self modulated laser wakefield acceleration (SM-LWFA). Although experiments with such high energy, high power, sub-picosecond Nd:glass based lasers (for example, $\simeq 250$ TW in 650 fs [27], $\tau_L \gg \tau_p$) are still actively being pursued [27–39], the majority of research has shifted to experiments with shorter pulse duration ($\tau_P \lesssim \tau_L \lesssim 100$ fs), higher repetition rate Ti:Sapphire based CPA laser systems [40–55]. Experimental setups for SM-LWFA experiments were simple and similar everywhere. As an example, a typical setup for LBNL LWFA experiments is shown in Fig. 1.2. A laser beam was focused by an off-axis parabola (OAP) onto a gas jet target, typically Hydrogen, Helium or Nitrogen. The interaction lengths for the SM-LWFA were on the order of the Rayleigh range (self channeling could increase the interaction length somewhat), typically less than a millime-
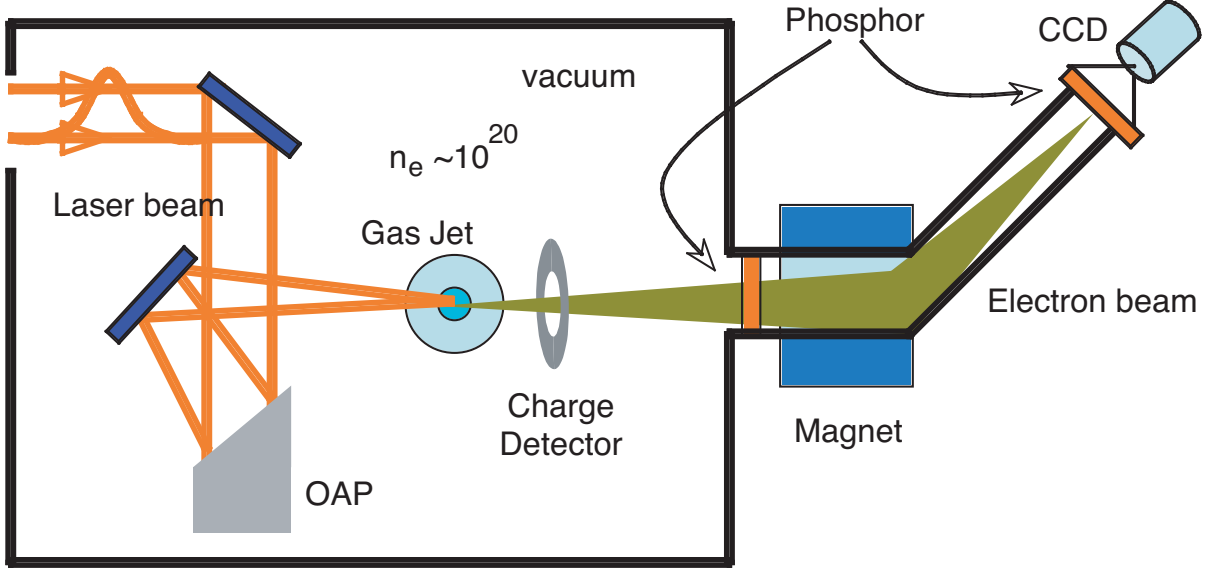
Figure 1.2: Schematic of the SM-LWFA experiment at LBNL. A laser pulse was focused by an off-axis parabola (OAP) onto a gas jet target. The total charge was measured by a charge detector ICT (Integrating Current Transformer) and Phosphor screens. An electron magnetic spectrometer was used to measure the energy spectrum of e-beams.

ter. For those SM-LWFA experiments, resultant e-beam energy spectra were broadband, usually characterized by an exponential or Boltzmann-like distribution with characteristic temperatures as shown in Fig. 1.3. This was probably due to high plasma density giving short dephasing length and heavy beam loading, and enhanced multi-bucket injection from long laser pulse length $\tau_L \gtrsim \tau_p$ (discussed later in this Section and in Chapter 2). The total accelerated charge was high (up to several nano-Coulombs), but the number of electrons at high energy (> 10 MeV) were a small fraction of the total charge ($\lesssim 10$ pC [42]).

The maximum energy observed from SM-LWFA experiments as a function of the input laser power (TW) is shown in Fig. 1.4. E-beams with up to 300 MeV have been observed from SM-LWFA experiments. The observed maximum energy depends on many laser-plasma parameters, such as laser energy, pulse length, power, and contrast, as well as plasma density, temperature, and profile. Furthermore, it may depend on the detection efficiency of electron diagnostics. Nevertheless, Fig. 1.4 shows the simple tendency of higher power leading to higher energy, and that the resultant maximum energies are comparable between the long and short-pulse laser system at similar input laser power. A
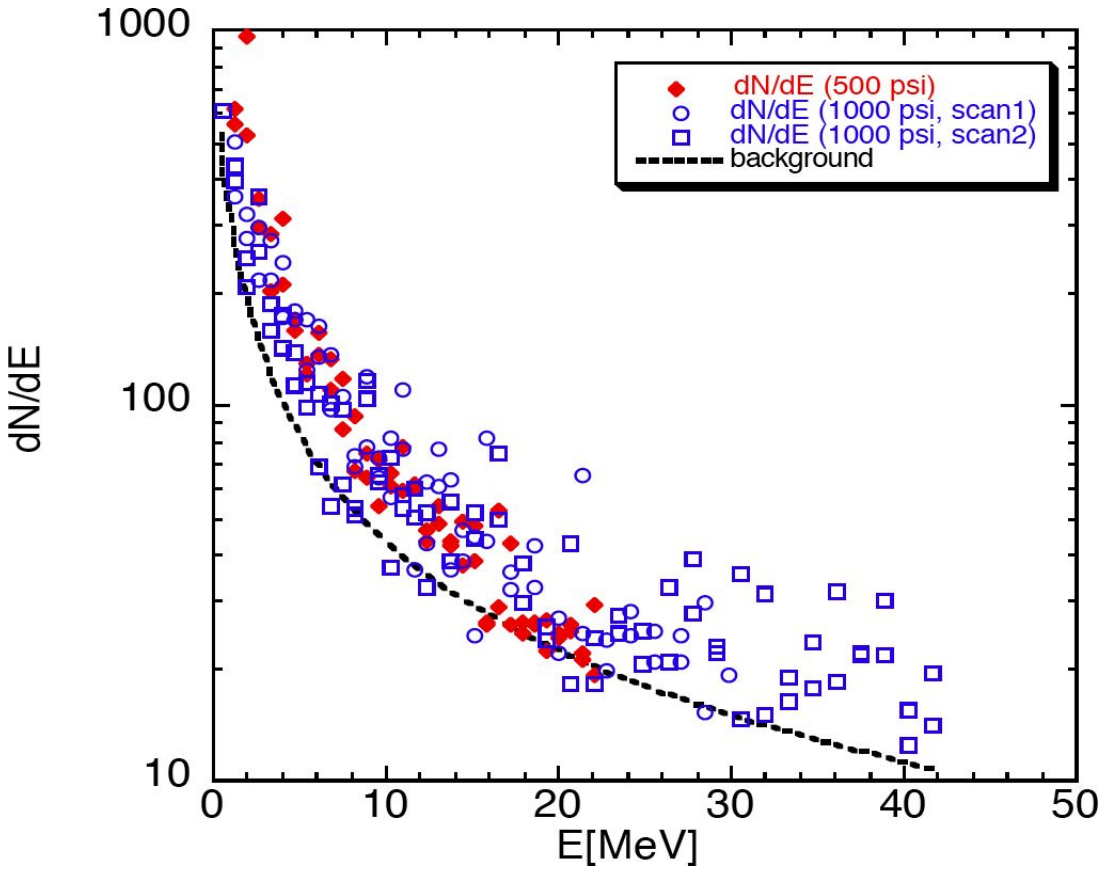
Figure 1.3: Example of e-beam energy spectrum from SM-LWFA experiments at LBNL.

typical pulse length from a Nd:glass laser is 10 times longer than that from a Ti:Sapphire laser, which means it requires 10 times more energy to achieve an equivalent power. Thus, Ti:Sapphire based systems have provided higher laser-energy to electron-energy efficiency than Nd:glass based systems. Note that laser energy to whole e-beam energy efficiency was not considered here. As the pulse length of the laser approached the plasma wavelength, the experimental regime shifted from heavily self modulated LWFA $\tau_L \gg \tau_p$ to slightly self modulated LWFA $\tau_L \gtrsim \tau_p$. Together with this shift, the capability to perform a large field of systematic parameter scans, benefitting from efficient and high repetition rate Ti:Sapphire laser systems, has contributed to many findings, enabled experiments with error-bars, and has led to a new generation of plasma-based accelerators.

Reported in 2004 from three different groups, LBNL, Laboratoire d'Optique Appliquée (LOA), and a collaboration of the Imperial College and Rutherford Appleton Laboratory (RAL), were the generation of quasi-monoenergetic e-beams (QME) [56–58]. This break-
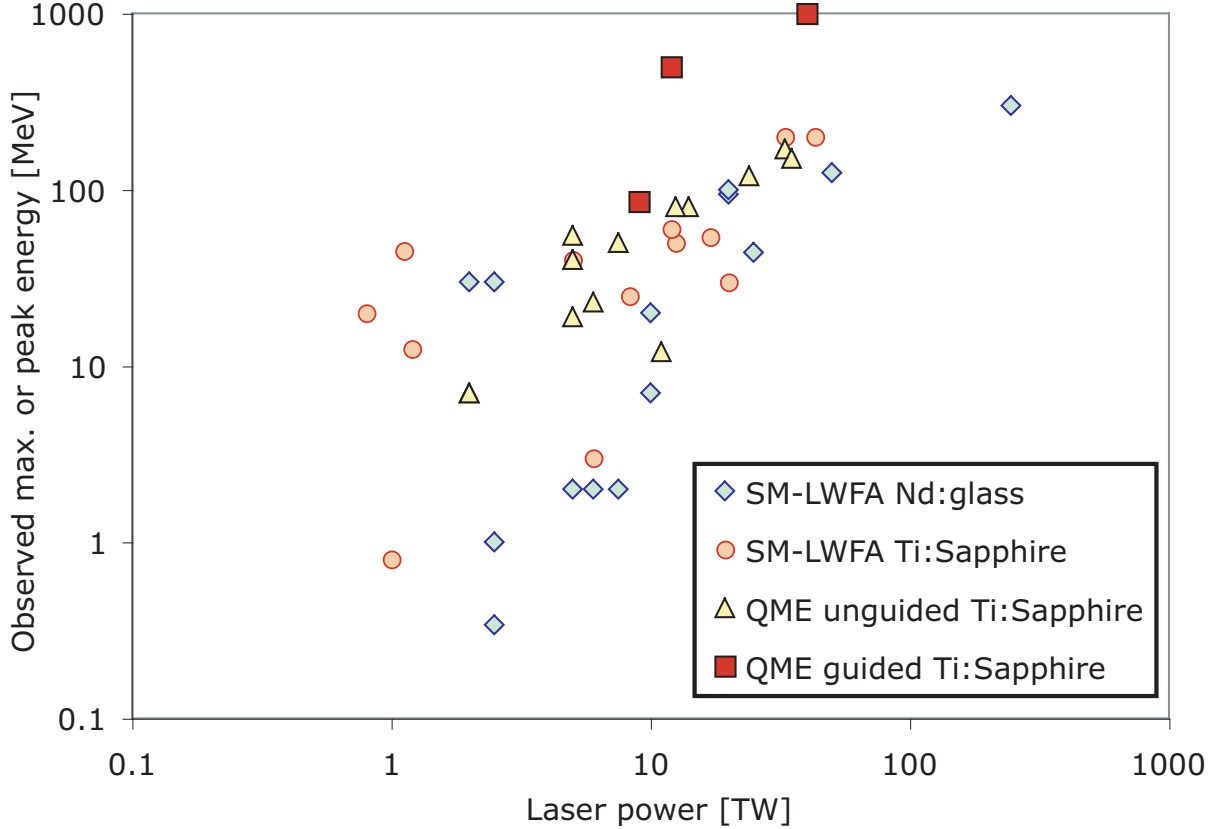
Figure 1.4:   Observed maximum energy from SM-LWFA experiments, and peak energy from quasi-monoenergetic e-beams (QME) as a function of input laser power [TW]. Blue diamond: experiments using Nd:glass based systems, orange circle: experiments using Ti:Sapphire based systems, yellow triangle: quasi-monoenergetic e-beams without guiding (Ti:Sapphire), red rectangle: quasi-monoenergetic e-beams with guiding (Ti:Sapphire).

through was achieved by matching the interaction length with the dephasing length (the length in which accelerated particles outrun the wakefield). The nature of this slippage comes from the fact that the velocity of a relativistic electron ($v_e \simeq c$) is faster than the phase velocity of the plasma wave v_{pp}. An analytical approximation for the depasing length L_{dph} in the 1D regime can be expressed as [59]:

$$L_{dph} \simeq \lambda_p \left(\frac{\omega_0}{\omega_p} \right)^2 \times \begin{cases} 1 & \text{for} \quad a_0^2 \ll 1, \\ 2a_0^2/\pi & \text{for} \quad a_0^2 \gg 1. \end{cases} \qquad (1.4)$$

Here a_0 is laser strength parameter, or normalized vector potential for the laser pulse. This is a key parameter for the discussion of laser driven wakefield acceleration, as detailed in

Chapter 2. From Eqs. 1.2 and 1.4:

$$L_{dph} \propto n_e^{-3/2} \; . \tag{1.5}$$

In the 2004 experiments, the dephasing length was controlled via the plasma density, which was typically in low $10^{19}/\text{cm}^3$ (somewhat lower than those used in the SM-LWFA experiments). Interaction lengths were extended by focusing the laser beam with a larger F number [57, 58], or by providing a pre-formed plasma channel [56] whose axial plasma profile was arranged such that the plasma channel guided the intense laser beam like an optical fiber. The first scheme, namely the large spot scheme, required higher power laser systems to compensate the reduced focus intensity. The second scheme, namely the guided scheme, required additional lasers to provide a preformed channel. For both schemes, advanced Ti:Sapphire laser systems played a critical role in the experiments.

The maximum energy gain was limited by two elements, plasma density and interaction length. With a given laser intensity, plasma density had to be high enough to realize self-trapping of electrons. Higher plasma density provides shorter dephasing length, consequently leading to smaller energy gain. In the case dephasing length is longer than interaction length, interaction length limits total energy gain. For self-trapping based LWFAs, the higher laser power to allow self-trapping with lower density plasma, and sufficiently longer interaction length to accommodate dephasing length are required to produce higher energy electron beams.

The generation of QMEs has now been reported from many groups around the world, and its optimization, scaling, beam quality, and stability has been studied [60–73]. Reported e-beam energies of the QMEs versus input laser power (TW) are shown in Fig. 1.4. One can see that the peak energy is comparable to the observed maximum energy from SM-LWFAs.

After the demonstration of high quality (quasi mono-energetic) e-beam generation from the LWFA, the improvement of beam quality, stability, and reproducibility have become the focus of research. Reported from LOA in 2006 was a demonstration of controlled injection of electrons onto a wakefield by using a counter propagating laser beam [74]. The concept was originally proposed by Esarey et al., [75–79], and has been pursued experimentally at LBNL as well [80, 81]. In previous experiments, electron injection has relied

on self-trapping, via wave breaking or high temperature plasma, which were not readily controlled. This LOA result showed that via laser-triggered injection, tunability of the e-beam energy and high stability (100% injection with a few percent fluctuation of peak e-beam energy) were achieved [74].

Also in 2006, the University of Tokyo (U-Tokyo) reported e-beam generation improved by an external magnetic field [82]. In the U-Tokyo experiments, the external magnetic field was used to condition the pre-formed plasma generated by a laser pre-pulse. Their early work was focused on how the laser pre-pulse affected the injection and acceleration processes [46, 47, 63]. By having an active control of the pre-pulse induced pre-formed plasma such that the plasma profile had a channel-like property, the resultant e-beams were improved to have smaller beam divergence, higher total charge, and higher stability (100% injection) [82].

Recently, the PWFA concept has been studied, mostly by a University of California Los Angels (UCLA) - Stanford Linear Accelerator Center (SLAC) - University of Southern California (USC) collaboration [83–88] using electron and positron beams at SLAC. SLAC was the only user facility in the world that could provide high energy (up to 50 GeV) electron and positron beams. Reported in 2007 was the use of 50 fs, 42 GeV e-beams as a wakefield driver, and measurements of the tail of the drive beam gaining energy of up to 43 GeV [88]. High reproducibility and stability was reported at many conferences. Although generation of e-beams with single energy peak structure has not been demonstrated yet, this was the highest net energy gain yet achieved by plasma-based accelerators. If a witness beam can be arranged at the right location (phase of the wakefield), a high quality and high energy PWFA becomes possible, as opposed to simply accelerating the tail of a long drive beam.

Reported by LBNL in 2006 was the generation of a 1 GeV, quasi mono-energetic e-beam by using a capillary discharge waveguide and a $\simeq 37$ fs, $\simeq 42$ TW Ti:sapphire laser [1, 2]. The capillary discharge waveguide was capable of guiding intense lasers ($\simeq 4 \times 10^{18}$ W/cm^2) for more than 30 mm with low plasma density (down to $\sim 10^{18}$/cm^3), which gave a long dephasing length leading to high net energy gain. This was the highest energy obtained from an LWFA, and its laser power - e-beam energy efficiency was excellent (see Fig. 1.4). Also reported was the stable generation of high quality 0.5 GeV e-beams ($\sim 80\%$ injection with $\sim 6\%$ fluctuation of peak e-beam energy, detailed in Chapter 4). It was first

shown that self-trapping and acceleration can be stabilized to produce QMEs with such high energy. These results lead to increased interest and discussion of practical LWFA e-beam applications.

As has been discussed in this Chapter, plasma-based accelerators now provide high quality beams and hence their practical applications can be discussed. Applications of LWFA e-beams have been explored such as radio-isotope production [32, 42, 89, 90], THz radiation generation [44, 91], x-ray generation [92–95], and pump-probe experiments [96]. For radio-isotope production, a LWFA could be a compact apparatus. As a THz radiation source, a LWFA may provide not only a compact apparatus compared to conventional accelerator facilities, but also e-beams with much shorter bunch duration, and hence higher THz frequencies [97–100]. Furthermore, the vacuum-plasma boundary of the SM-LWFA can be a high field THz source because the e-beam can contain more than a nano-Coulomb in a very short time duration ($\simeq$ plasma period ~ 10 fs). Short pulse, high field THz radiation may benefit a broad range of ultrafast sciences. Synchrotron radiation from an LWFA was demonstrated experimentally and has been intensely studied by Rousse and co-workers [95, 101–104]. The time duration of LWFA synchrotron x-rays was found to be as short as 100 fs. Although conventional synchrotron light sources can generate far higher energy photons using > 1 GeV e-beams [105–107], this few keV ultrafast x-ray radiation could provide a powerful tool for femtosocond x-ray diffraction or absorption spectroscopy. By using an undulator, an LWFA driven XUV FEL could be designed using GeV-class LWFA electron beams [108]. Combining ability to generate a broad spectral range of radiation with e-beams and the intrinsically synchronized laser beam, a LWFA could provide an ideal apparatus for an ultrafast pump-probe experiments. A pulse radiolysis experiment was carried out by using e-beams from SM-LWFA in ref. [96]. Although it was demonstrated that a SM-LWFA could provide sufficient charge to perform chemical studies, a femtosecond pump probe experiment was not realized, probably due to the broadband property and space charge effect in high charge e-beams [109]. E-beams from SM-LWFA contained a total charge of nC, and such a high charge e-beam would be stretched out longitudinally during propagation in addition to the velocity difference between low and high energy electrons. Although it has been demonstrated that the SM-LWFA e-beam can have short pulse duration ($\simeq 50$ fs) at the exit of the plasma [98], femtosecond pump probe experiments hence also require that the e-beams have to be of

high quality (low energy spread). Ultrafast pulse radiolysis [110, 111] using high quality e-beams from LWFA has been pursued at U-Tokyo [112]. The pulse duration of quasi-monoenergetic e-beam (peak energy of 20 MeV with 20% energy spread, $\simeq$ 30 pC) was measured to be $\simeq$ 130 fs after the propagation of 180 mm [113]. For femtosecond pump probe experiments, higher quality e-beams may be required. For all kind of applications, stability remains a key issue, and there still are many things to be addressed for the applications. Plasma based accelerator experiments, however, have shifted from high power plasma experiments to accelerator experiments. Applications can be discussed with practically achievable parameters, and may be realized in near future.

This dissertation consists of contributions to the development of the capillary discharge guided (CDG-) LWFA at the LOASIS Facility, and details are discussed in following Sections and Chapters.

1.2 LOASIS Laser Plasma Based Accelerators

The LOASIS group (Lasers, Optical Accelerator Systems Integrated Studies) was started in 1993 by Wim Leemans, then opened LOASIS Facility in 1995 (the l'OASIS group in the Center of Beam Physics (CBP), became LOASIS Program in 2005). First developed at the LOASIS Facility was a laser-driven hydrodynamic expansion waveguide [114] using the ignitor heater method [115] to allow operation in Hydrogen gas. A multi-output high-power Ti:Sapphire amplifier named Chihuahua was built (see Fig. 1.5), which provided two fs laser pulses (75 fs, 30 mJ each), and an energetic long pulse (160 ps, 280 mJ) for these experiments. One of the short laser pulses (ignitor) was used to initially ionize the gas from a gas jet via tunnel ionization, then the long laser pulse (heater) was introduced to heat the plasma through collisions. The heated cylinder of gas expanded, creating a radial plasma density distribution with a minimum on axis, which was used to guide the 2nd short laser pulse at intensity $\simeq 5 \times 10^{17}$ W/cm^2 over $\simeq$ 10 Rayleigh lengths.

The first report of the generation of energetic e-beams from the LOASIS LWFA was in 2001, using a newly developed high power Ti:Sapphire amplifier, named Godzilla [42]. The Godzilla amplifier provided $\simeq$ 500 mJ in $\simeq$ 50 fs ($\simeq$ 10 TW), and it was focused by a F/4, 30 cm focal length OAP providing a spot size of approximately $w_0 = 6$ μm, or Rayleigh length $z_R = \pi w_0^2 / \lambda = 141$ μm with λ the laser wavelength. The generation of

high energy electrons (> 25 MeV) was verified via gamma-neutron activation experiments and a magnetic spectrometer [42].

By combining the two experiments and lasers, a channel guided LWFA and, as shown in Sec. 1.1, generation of quasi-monoenergetic e-beams from a LWFA, were first achieved and reported in 2004 [56, 68, 116]. In this experiment a laser beam intensity up to a few 10^{18} W/cm^2 was guided over $\simeq 10$ Rayleigh lengths, with only small distortions in a laser mode profile. The laser lost up to 90% of its energy due to energy deposition into the plasma (wake generation) and leakage from the guiding structure. By using a 9 TW laser, a 86 $\pm$1.8 MeV e-beam with 3 mrad divergence in full-width half maximum (FWHM) was obtained. This laser-driven hydrodynamic expansion waveguide was shown to be efficient with higher density plasma (> 10^{19} cm^{-3}) due to the fact that the heating relies on inverse-Bremsstrahlung but harder to generate channels for lower plasma density. The required laser energy for channel generation scales linearly with its length.

For applications such as synchrotron light sources [105–107, 117] or as modules in particle colliders [118], GeV or even higher energy would be desirable. In order to obtain a higher energy e-beam, an LWFA with longer accelerating structure becomes essential, because a net energy gain ΔW may be given by a product of an accelerating field strength E_z and accelerating length L_{acc}:

$$\Delta W = E_z L_{acc}. \tag{1.6}$$

As discussed in the previous Section, the acceleration length has to be matched to the dephasing length, which can be extended by using lower density plasma (see Eq. 1.5). Key technologies for a higher energy LWFA would be a lower density plasma, longer accelerating length, and higher power laser.

The acceleration length can be extended by either using large laser spot (large Z_R) scheme or using a plasma channel for guiding. The required laser-plasma parameters to obtain GeV e-beams with a channel-guided LWFA were studied via scaling laws [119–121], which can be summarized as follows. If the acceleration length is limited by the dephasing

length, $L_{acc} \simeq L_{dph}$, the dephasing limited energy gain ΔW_{dph}, in practical units, is:

$$\Delta W_{dph}(\text{MeV}) \simeq \frac{630 I(\text{W cm}^{-2})}{n_e(\text{cm}^{-3})} \times \begin{cases} 1, & \text{for} \quad a_0^2 \ll 1, \\ (2/\pi)/N, & \text{for} \quad a_0^2 \gg 1, \end{cases} \qquad (1.7)$$

where I is the laser intensity, and N is the number of plasma periods that the bunch is located behind the laser pulse. If the acceleration length is limited by the pump depletion length L_{pd}, in which laser deposit all the energy onto plasma, the pump depletion limited energy gain ΔW_{pd} in practical unit is:

$$\Delta W_{pd}(\text{MeV}) \simeq \begin{cases} 3.4 \times 10^{21}/(\lambda^2(\mu\text{m})n(\text{cm}^{-3})), & \text{for} \quad a_0^2 \ll 1, \\ 400 I(\text{W cm}^{-2})/n(\text{cm}^{-3}), & \text{for} \quad a_0^2 \gg 1. \end{cases} \qquad (1.8)$$

As an example, assume a $P = 50$ TW, 40 fs (2 J) Ti:Sapphire laser ($\lambda = 0.8$ μm) focused to a spot size of $w_0 \simeq 25$ μm, which gives calculated peak intensity $I = 2P/\pi w_0^2 \simeq 5 \times 10^{18}$ W/cm^{-2} and $a_0 \simeq 8.6 \times 10^{-10}\lambda$ $(\mu\text{m})I^{1/2}$ (W/cm^2) $\simeq 1.5$. Considering the nonlinear regime, one obtains $\Delta W_{dph} \simeq \Delta W_{pd} = 1000$ MeV and $L_{dph} \simeq 2.95$ cm with a plasma density of $n_e = 2 \times 10^{18}$ cm^{-3}. From the scaling law, 1 GeV e-beams can be obtained by a 3 cm guided 50 TW laser and a plasma density of 2×10^{18} cm^{-3}. Without guiding, which has an advantage in simplicity of the setup, a simulation suggested that 1 PW laser system may be able to provide high quality GeV e-beams [122]. In the guiding case, interaction length can be extended without making spot size larger. Experimental results [56–58] also suggested higher efficiency using the guided approach.

Although guiding of an intense laser by a laser-driven hydrodynamic expansion waveguide over several mm was demonstrated [56, 68, 116], guiding over cm scale distances with lower density plasma was a significant challenge. As discussed, the lower plasma densities for a centimeter scale laser-driven hydrodynamic expansion waveguide made that approach unpractical because low efficiency heating needs high energy heater. The Ignitor - heater concept [114, 115, 123] was not the only way to achieve a guiding of an intense laser, and however, other guiding concepts relying on the use of preformed plasma channels have been pursued by several groups around the world [124–128]. An alternative plasma channel technology, based on capillary discharge guides (CDG), was developed at
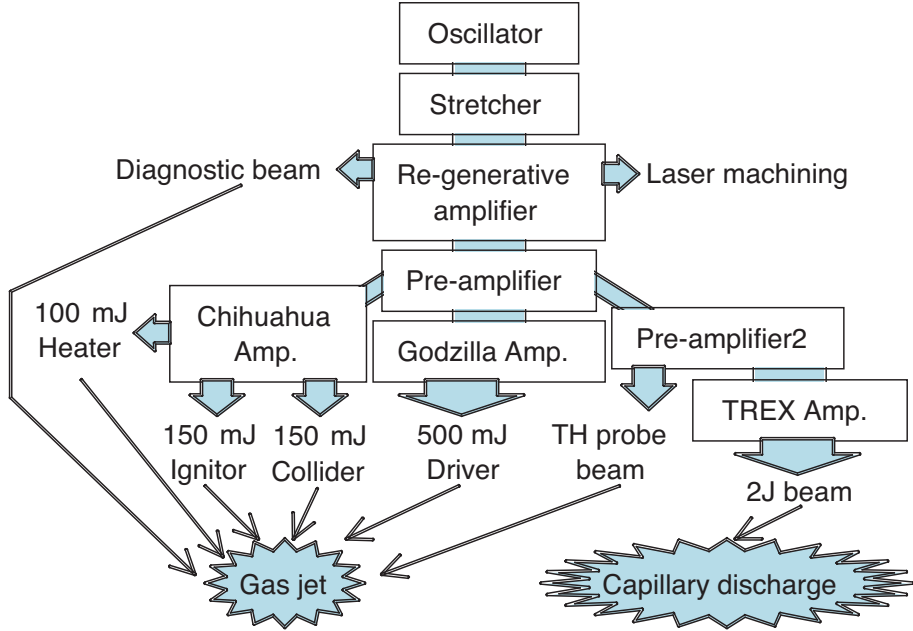
Figure 1.5: Schematic of laser system of LOASIS Facility.

Oxford University [129–131]. A moderate intensity laser ($\simeq 10^{17}$ W/cm^{-2}) was guided over 5 cm without significant distortion or loss [131], but no high intensity laser was available to produce relativistic e-beams at Oxford University.

With the goal of GeV-class e-beam generation from a LWFA, a CDG-LWFA has been developed at the LOASIS Facility, collaborating with Oxford University. Construction of a 100 TW-class Ti:Sapphire amplifier had already started in 2002, aimed at higher energy e-beam generation. It employed cryogenic cooling of a Ti:Sapphire crystal using compressed helium gas to cancel the heavy thermal loading induced by the high power pump lasers. Amplification up to 4 J/pulse (before compression) with 10 Hz operation has been achieved. Shown in Fig. 1.5 is a schematic of the LOASIS Laser Facility. As of October 2007, a total of eight beams are available for a variety of experiments from three high-power and three mid.-power Ti:Sapphire amplifiers.

Critical to the GeV-class CDG-LWFA was the development of a diagnostic for the e-beam, namely an electron spectrometer (ESM). As discussed throughout this Chapter, LWFA can provide a variety of e-beams, such as high-charge broadband beams (down to $\simeq 0$ MeV) and high quality and energy beams (up to GeV energy), and there is often significant shot-to-shot variability. To measure all these beams, and to allow a wide range

of parameter scans, a broadband, high resolution, high repetition rate ESM was essential. One of the objectives of this dissertation was to develop, implement, and operate such an electron spectrometer. A broadband single shot ESM was designed and developed for a GeV-class CDG-LWFA. It has served as the main diagnostics for the development of the LOASIS GeV LWFA, and has successfully measured GeV class e-beams.

The other objective of this dissertation was to understand how to control a GeV-class LWFA. Thousands of shots with a broad range of laser and plasma parameters were statistically analyzed to elucidate the complicated physics in the laser-plasma interactions. The analysis showed the requirements for stable operation, and provided information for future optimization.

1.3 Summary and Outline

As presented in this Chapter, since their invention, laser plasma-based accelerators have progressed rapidly along with advancing laser technologies. By using channel guiding, high quality, 100 MeV e-beams can be provided in a mm scale LWFA. A centimeter scale LWFA has been developed at the LOASIS Facility by using a capillary discharge waveguide. A broadband single shot ESM for GeV class LWFA was developed, and through statistical analysis of the measurements, the control of the GeV class CDG-LWFA was discussed.

Chapter 2 describes the theoretical foundations for LWFA. Physics of laser-plasma interactions relevant to wakefield acceleration is described, providing insight on LWFA operation, and the foundations for analysis and discussion presented in Chapter 4.

Chapter 3 details the design and development of a broadband ESM for GeV class LWFA [3]. This diagnostic efficiently covers a wide range of energy in a single shot with sufficient resolution. As the main diagnostic for the GeV-class LWFA at LBNL, it was essential to the achievement of high quality GeV e-beam generation from a CDG-LWFA. Along with its development, the e-beam energy dependence of the scintillating screen was studied at the Advanced Light Source (ALS), LBNL. The developed ESM successfully provided a charge monitor as well.

Chapter 4 describes the development of the GeV-class LWFA. Taking advantage of the high repetition rate system, thousands of shots have been taken with a broad range of laser plasma parameters. A statistical analysis of the CDG-LWFA operation is pre-

sented. Complicated inter-dependence of laser-plasma parameters are presented, and the key technology for controlling a GeV-class LWFA are discussed.

Lastly, conclusions and prospects for future LWFAs are discussed in Chapter 5.

Chapter 2

Theoretical Foundations for LWFA

2.1   Introduction

In this Chapter, a brief summary of the equations describing laser-plasma interactions relevant to electron acceleration is presented. This Chapter together with Chapter 1 provides a foundation for the discussion and analysis presented in Chapter 4. Section 2.2 describes generation of the wakefield, and Section 2.3 discusses particle trapping and acceleration. For a comprehensive review, see Ref. [6] and references therein.

2.2   Wakefield Generation

Plasma wakefields generated by non-evolving drive laser pulses can be described analytically in the three-dimensional (3D) linear regime, and 1D (plane wave) non-linear regime [6]. Calculation of the wakefield in the 3D nonlinear regime or calculation including the self-consistent evolution of the drive laser pulse is sufficiently complicated to require numerical calculation. Here, we consider a cold fluid, where collisions and thermal effects are negleceted. The collision time is typically much greater than the driver laser pulse duration, and the thermal velocity is typically much less than the quiver velocity of

an electron in the laser radiation fields. Starting from the fluid-Maxwell equations:

$$\nabla \cdot \boldsymbol{E} = 4\pi e(Zn_i - n_e) , \tag{2.1}$$

$$\nabla \cdot \boldsymbol{B} = 0 , \tag{2.2}$$

$$\nabla \times \boldsymbol{E} = -\frac{\partial \boldsymbol{B}}{c\partial t} , \tag{2.3}$$

$$\nabla \times \boldsymbol{B} = \frac{\partial \boldsymbol{E}}{c\partial t} + \frac{4\pi e(Zn_i\boldsymbol{v}_i - n_e\boldsymbol{v}_e)}{c} , \tag{2.4}$$

where $\boldsymbol{v_i}$ and $\boldsymbol{v_e}$ are the fluid velocities for the ions and electrons, respectively, and n_i and n_e are the ion and electron densities, respectively, with Z the atomic number. Throughout this Section, the ions are assumed to be immobile, and $Z = 1$ is assumed because Hydrogen gas is used in experiments to realize fully ionized plasma (to reduce ionization diffraction [132]). The ion response time $[\sim \omega_{pi}^{-1} = (4\pi e^2 n_i/M_i)^{-1/2}$, where M_i is the mass of the ions] is typically much greater than the time scale of the laser-plasma interaction considered here (a few tens of femtoseconds). For a proton plasma with $n_i \sim 10^{18}$ cm^{-3}, $\omega_{pi}^{-1} \sim 1$ ps, and so the ions are largely immobile. With the ion density given by the equilibrium plasma density $n_i = n_0$, and assuming immobile ions $\boldsymbol{v_i} = 0$, Eqs. (2.1) and (2.4) become:

$$\nabla \cdot \boldsymbol{E} = 4\pi e(n_0 - n) , \tag{2.5}$$

$$\nabla \times \boldsymbol{B} = \frac{\partial \boldsymbol{E}}{c\partial t} - \frac{4\pi en\boldsymbol{v}}{c} , \tag{2.6}$$

where $n_e = n$ and $\boldsymbol{v}_e = \boldsymbol{v}$ are used for simplicity. The electric (E) and magnetic (B) fields can be described with the vector $\boldsymbol{A}$ and scalar Φ potentials:

$$\boldsymbol{E} = -\nabla\Phi - \frac{\partial \boldsymbol{A}}{c\partial t} , \tag{2.7}$$

$$\boldsymbol{B} = \nabla \times \boldsymbol{A} . \tag{2.8}$$

Equations (2.5) and (2.6) can be rewritten in terms of the potentials:

$$\nabla \cdot \left(\nabla\phi + \frac{\partial \boldsymbol{a}}{c\partial t}\right) = \frac{4\pi e^2(n - n_0)}{m_e c^2} , \tag{2.9}$$

$$\nabla \times \nabla \times \boldsymbol{a} + \frac{\partial}{c\partial t}\left(\nabla\phi + \frac{\partial \boldsymbol{a}}{c\partial t}\right) = -\frac{4\pi e^2 n\boldsymbol{u}}{\gamma m_e c^2} , \tag{2.10}$$

where $\boldsymbol{a}$ is the normalized vector potential as defined by:

$$\boldsymbol{a} = \frac{e\boldsymbol{A}}{m_e c^2} \ , \tag{2.11}$$

ϕ is the normalized scalar potential:

$$\phi = \frac{e\Phi}{m_e c^2} \ , \tag{2.12}$$

and $\boldsymbol{u}$ is the normalized electron momentum:

$$\boldsymbol{u} = \frac{\boldsymbol{p}}{m_e c} = \frac{\gamma \boldsymbol{v}}{c} = \gamma\boldsymbol{\beta} \ . \tag{2.13}$$

Here, $\boldsymbol{p}$ is the momentum of electron fluid, $\boldsymbol{\beta} = \boldsymbol{v}/c$ is the normalized velocity of the electron fluid, and γ is the relativistic factor, which can be written as:

$$\gamma = \sqrt{1 + u^2} \ . \tag{2.14}$$

In the Coulomb gauge, $\nabla \cdot \boldsymbol{A} = 0$, Eqs. (2.9) and (2.10) yield the normalized Poisson equation and normalized wave equation:

$$\nabla^2 \phi = k_p^2 \frac{n - n_0}{n_0} \ , \tag{2.15}$$

$$\left(\nabla^2 - \frac{\partial^2}{c^2 \partial t^2} \right) \boldsymbol{a} = k_p^2 \frac{n}{n_0} \frac{\boldsymbol{u}}{\gamma} + \frac{\partial}{c \partial t} \nabla\phi \ , \tag{2.16}$$

where the vector identity $\nabla \times \nabla \times \boldsymbol{a} = \nabla(\nabla \cdot \boldsymbol{a}) - \nabla^2 \boldsymbol{a}$ was used, and k_p is the plasma wave number:

$$k_p = \frac{\omega_p}{c} = \sqrt{\frac{4\pi e^2 n_0}{m_e c^2}} \ . \tag{2.17}$$

Since a cold fluid is considered here, neglecting the pressure tensor and the collision term, the equation of motion and the continuity equation for the electron fluid can be

written as:

$$\left(\frac{\partial}{\partial t} + \boldsymbol{v} \cdot \nabla\right) \boldsymbol{p} \;=\; -e\left(\boldsymbol{E} + \frac{1}{c}\boldsymbol{v} \times \boldsymbol{B}\right) , \qquad (2.18)$$

$$\frac{\partial n}{\partial t} + \nabla \cdot (n\boldsymbol{v}) \;=\; 0 . \qquad (2.19)$$

In terms of the normalized potentials and momentum, Eqs. (2.18) and (2.19) can be rewritten as:

$$\left(\frac{\partial}{c\partial t} + \frac{\boldsymbol{u}}{\gamma} \cdot \nabla\right) \boldsymbol{u} \;=\; \nabla\phi + \frac{\partial \boldsymbol{a}}{c\partial t} - \frac{\boldsymbol{u}}{\gamma} \times (\nabla \times \boldsymbol{a}) , \qquad (2.20)$$

$$\frac{\partial n}{c\partial t} + \nabla \cdot \left(n\frac{\boldsymbol{u}}{\gamma}\right) \;=\; 0 . \qquad (2.21)$$

The equation of motion can be simplified further. By using the vector identity $\nabla(u^2/2) = (\boldsymbol{u} \cdot \nabla)\boldsymbol{u} + \boldsymbol{u} \times (\nabla \times \boldsymbol{u})$, and Eq. (2.14), Eq. (2.20) becomes:

$$\left(\frac{\partial}{c\partial t} - \frac{\boldsymbol{u}}{\gamma} \times \nabla\times\right)(\boldsymbol{u} - \boldsymbol{a}) = \nabla(\phi - \gamma) . \qquad (2.22)$$

Introducing the generalized vorticity [133]:

$$\boldsymbol{\Omega} = c\nabla \times (\boldsymbol{u} - \boldsymbol{a}) , \qquad (2.23)$$

and taking the curl of Eq. (2.22), we obtain:

$$\frac{\partial \boldsymbol{\Omega}}{c\partial t} - \nabla \times \frac{\boldsymbol{u}}{\gamma} \times \boldsymbol{\Omega} = 0 . \qquad (2.24)$$

Equation (2.24) indicates that the flux of the generalized vorticity through an arbitrary surface bounded by a contour moving together with the fluid is constant [133]. Therefore, the quantity $\boldsymbol{\Omega}$ at a given point vanishes provided that it vanished at the same point before the laser pulse arrives. In other words, since Eq. (2.24) has no source term, $\boldsymbol{\Omega} = 0$ for $t > 0$ if $\Omega|_{t=0} = 0$. The simplified equation of motion is obtained by using $\boldsymbol{\Omega} = c\nabla\times(\boldsymbol{u}-\boldsymbol{a}) = 0$:

$$\frac{\partial}{c\partial t}(\boldsymbol{u} - \boldsymbol{a}) = \nabla(\phi - \gamma) . \qquad (2.25)$$

Here, $\nabla\phi$ represents the space-charge force $\boldsymbol{F}_s = m_e c^2 \nabla\phi$, and $\nabla\gamma$ represents the gener-

alized nonlinear ponderomotive force, $\boldsymbol{F}_{pm}^{nl} = -m_e c^2 \nabla \gamma$.

For a drive laser pulse propagating in an initially homogeneous plasma $\nabla n_0 = 0$, Eqs. (2.15), (2.16), (2.21), and (2.25) can be solved in the linear regime $a^2 \ll 1$ by a perturbation expansion of the fluid quantities in powers of the normalized vector potential of the laser field:

$$f = \sum f_n a^n \ , \tag{2.26}$$

where f_n is a coefficient for the n-th order. For example, the normalized scalar potential can be written as $\phi = \phi_0 + \phi_1 + \phi_2 + \cdots = f_0 + f_1 a + f_2 a^2 + \cdots$.

The zeroth order equations describe the equilibrium state. Therefore, the electron density is given by the equilibrium density n_0, no electron velocity, and no charge separation: $n_e = n_0$, $\boldsymbol{u_0} = 0$, and $\phi_0 = 0$. From Eq. (2.14), the relativistic factor γ can be expanded in terms of the normalized momentum $\boldsymbol{u}$, $\gamma = \gamma_0 + \gamma_1 + \cdots = 1 + u^2/2 - u^4/8 + \cdots$, which gives $\gamma_0 = 1$ and $\gamma_1 = 0$.

To study the first order response of the plasma, Eqs. (2.15), (2.16), (2.21), and (2.25) can be rewritten in terms of the first order plasma parameters:

$$\nabla^2 \phi_1 = k_p^2 \frac{n_1}{n_0} \ , \tag{2.27}$$

$$\left(\nabla^2 - \frac{\partial^2}{c^2 \partial t^2} \right) \boldsymbol{a} = k_p^2 \boldsymbol{u}_1 + \frac{\partial}{c \partial t} \nabla \phi_1 \ , \tag{2.28}$$

$$\frac{\partial n_1}{c \partial t} + n_0 \nabla \boldsymbol{u}_1 = 0 \ , \tag{2.29}$$

$$\frac{\partial}{c \partial t} (\boldsymbol{u}_1 - \boldsymbol{a}) = \nabla \phi_1 \ . \tag{2.30}$$

Equations (2.29), (2.30), and (2.27) can be combined to yield the equation for the first order plasma density:

$$\left(\frac{\partial^2}{c^2 \partial t^2} + k_p^2 \right) \frac{n_1}{n_0} = 0 \ . \tag{2.31}$$

Since there is no source term in Eq. (2.31), by having $n_1|_{t=0} = 0$, we obtain $n_1 = 0$, and with no charge separation, $\phi_1 = 0$. Therefore, from Eq. (2.30), we obtain $\boldsymbol{u}_1 = \boldsymbol{a}$, which describes the electron quiver motion in the laser field. The first order wave equation (2.28) describes the linear dispersion relation for electromagnetic wave inside the plasma $\omega^2 =$

$\omega_p^2 + c^2 k^2$, which can be seen by taking a Fourier transform of Eq. (2.28):

$$\left(\omega^2 - c^2 k^2 - \omega_p^2\right) \tilde{\boldsymbol{a}} = 0 \ , \tag{2.32}$$

where $\tilde{\boldsymbol{a}}$ indicates a Fourier transform of $\boldsymbol{a}$, k and ω are laser wave number and frequency, respectively, and the normalized vector potential is assumed to take a form of $\boldsymbol{a} = a_0 \exp i(\boldsymbol{k} \cdot z - \omega t)\boldsymbol{e}_\perp$. Note that 1D is considered here.

To second order, Eqs. (2.15), (2.16), (2.21), and (2.25) can be rewritten in terms of the second order plasma parameters as follows:

$$\nabla^2 \phi_2 = k_p^2 \frac{n_2}{n_0} \ , \tag{2.33}$$

$$\frac{\partial}{c\partial t} \nabla \phi_2 = -k_p^2 \boldsymbol{u}_2 \ , \tag{2.34}$$

$$\frac{\partial n_2}{c\partial t} + n_0 \nabla \boldsymbol{u}_2 = 0 \ , \tag{2.35}$$

$$\frac{\partial \boldsymbol{u}_2}{c\partial t} = \nabla \left(\phi_2 - \frac{a^2}{2} \right) \ , \tag{2.36}$$

with $\gamma_2 = u_1^2/2 = a^2/2$. The above equations can be combined to yield:

$$\left(\frac{\partial^2}{c^2 \partial t^2} + k_p^2 \right) \frac{n_2}{n_0} = \nabla^2 \frac{a^2}{2} \ , \tag{2.37}$$

$$\left(\frac{\partial^2}{c^2 \partial t^2} + k_p^2 \right) \phi_2 = k_p^2 \frac{a^2}{2} \ . \tag{2.38}$$

The right-hand side of Eq. (2.37) represents the second-order ponderomotive force of the laser pulse $F_{pm}^{2nd} \simeq -m_e c^2 \nabla a^2/2$, and this drives the second-order plasma density perturbation (wakefield). The solutions for the second-order density perturbation ($n_2/n_0 \ll 1$) and the electric field of the wake ($\boldsymbol{E_2} = -\nabla \Phi_2$) are given by:

$$\frac{n_2}{n_0} = \frac{c^2}{\omega_p} \int_0^t \sin\left[\omega_p(t - t')\right] \nabla^2 \frac{a^2(\boldsymbol{r}, t')}{2} dt' \ , \tag{2.39}$$

$$\frac{\boldsymbol{E_2}}{E_0} = -c \int_0^t \sin\left[\omega_p(t - t')\right] \nabla \frac{a^2(\boldsymbol{r}, t')}{2} dt' \ , \tag{2.40}$$

where $E_0 = m_e c \omega_p / e$ is the cold nonrelativistic wavebreaking field Eq. (1.3). Equations (2.39) and (2.40) are valid for $n_2 < n_0$, and $E_2 < E_0$, respectively, and implies that

the plasma waves are generated at the frequency ω_p, and the radial extent of the plasma wave is of order the transverse spot size of the laser. The electric field of the wake consists of the longitudinal field E_z and radial field $E_r - B_\theta$. The radial wakefields are related to the longitudinal wakefield by the Panofsky-Wenzel theorem [134, 135]:

$$\frac{\partial E_z}{\partial r} = \frac{\partial (E_r - B_\theta)}{\partial (z - ct)} \; . \tag{2.41}$$

For simplicity, assuming that the phase velocity of the longitudinal wakefield is $v_{pp} \simeq c$, and using a sinusoidal wakefield, the longitudinal wakefield and radial wakefields are:

$$E_z = E \exp\left(-\frac{2r^2}{r_s^2}\right) \cos\left[k_p(z - ct)\right] , \tag{2.42}$$

$$E_r - B_\theta = E \frac{4r}{k_p r_s^2} \exp\left(-\frac{2r^2}{r_s^2}\right) \sin\left[k_p(z - ct)\right] , \tag{2.43}$$

where E is the amplitude of the wake. The Eqs. (2.42) and (2.43) imply that the radial force is zero on axis, and that there is a $\pi/4$ of phase region of the wake where an electron is longitudinally accelerated ($E_z < 0$) and radially focused ($E_r - B > 0$). Here, $\Psi = k_p(z - ct) \simeq k_p \zeta$ is the wake phase. This relation is illustrated in Fig. 2.1, where a linearly-polarized half-sine envelope laser pulse with length L [$a = a_0 \sin(\pi\zeta/L)$ for $-L < \zeta < 0$, and $a_0 = 0.5$], and resonant condition $L = \lambda_p$ were assumed. Shown by a white area is the region where the electron experiences a focusing radial electric field, and the solid line shows the normalized second-order accelerating field E_{2z}/E_0, while the dashed curve shows the normalized density perturbation n_2/n_0. One can see that the radial focusing regime ($E_r - B_\theta > 0$) is synchronized with $n_2/n_0 < 0$ for $k_p \zeta < -2\pi$. Since the carrier frequency of the laser ω is much higher than the typical plasma frequency ω_p because of the need for high v_g, the ponderomotive force associated with the laser pulse envelope (time-averaged intensity profile) is considered here (the plasma response time $\sim 1/\omega_p \gg 1/\omega$). With its carrier frequency, the vector potential is assumed to take a form of $\boldsymbol{a} = a_0 \sin(\pi\zeta/L) \cos(kz - \omega t)\boldsymbol{e}_x$ with $\boldsymbol{e}_x$ the unit vector for the x plane (plane of polarization). In the following part of this Chapter, it is assumed that the laser pulse is linearly polarized, and that $a^2 = \langle a^2 \rangle = (1/2) a_0^2 \sin^2(\pi\zeta/L)$ for the time-averaged envelope, unless otherwise specified. Here, $\langle \rangle$ indicates time-averaging over a laser cycle. The more general case, including a circularly-polarized laser pulse is discussed later in
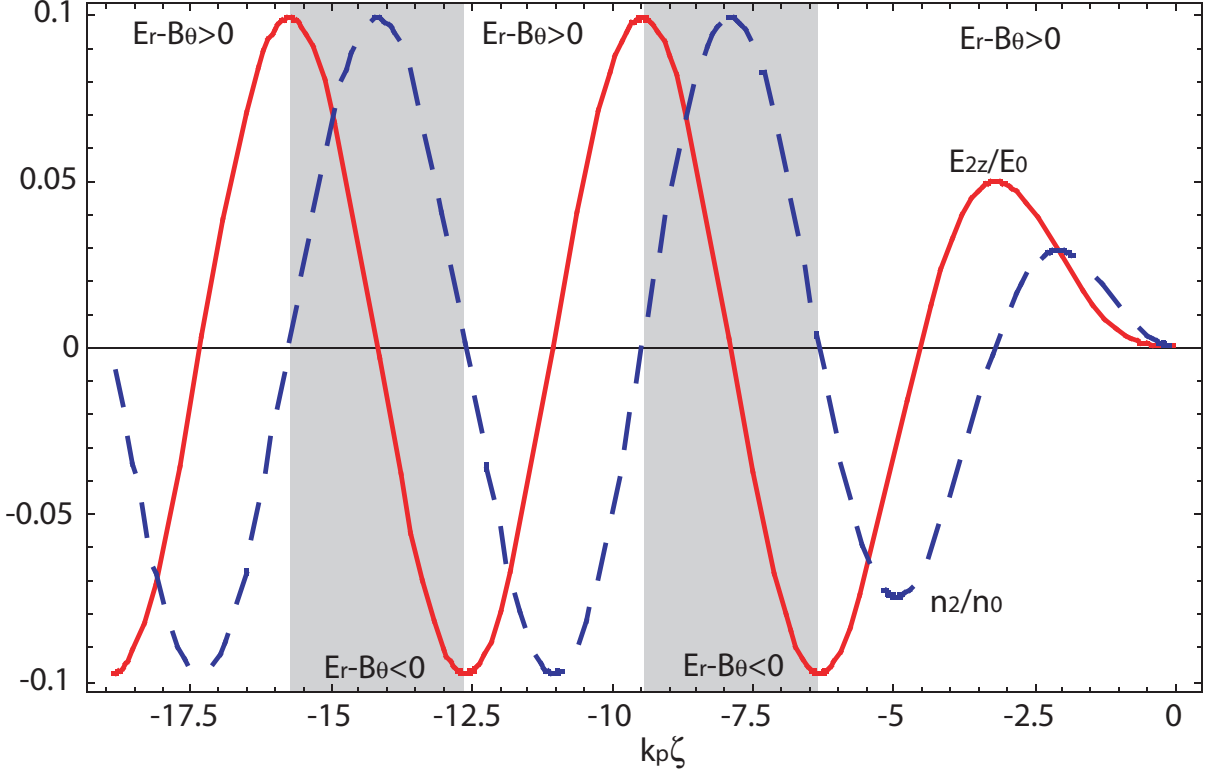
Figure 2.1: Normalized density variation n_2/n_0 (dashed curve) and longitudinal electric field E_{2z}/E_0 (solid curve) versus phase $\Psi = k_p\zeta$. Shown by a white areas are the regions where the electron experiences a focusing radial electric field. A half-sine envelope laser pulse $a = a_0 \sin\left(\pi\zeta/L\right)$ with $a_0 = 0.5$ propagates to the right, and the resonant condition $\lambda_p = L$ were assumed.

this Section.

In the nonlinear regime $E \gtrsim E_0$, wakefield generation can be examined in the 1D limit by applying the quasi-static approximation [136, 137], where the plasma fluid quantities are assumed to be functions only of the coordinate $\zeta = z - v_{pp}t$. In the 1D limit ($\nabla_\perp = 0$, plane wave), the Coulomb gauge implies $a_z = 0$. Therefore, the equation of motion Eq. (2.25) can be separated into transverse and longitudinal components:

$$a_\perp = u_\perp \,, \tag{2.44}$$

$$\frac{\partial}{c\partial t}u_z = \frac{\partial}{\partial z}(\phi - \gamma) \,. \tag{2.45}$$

A variable transform $\zeta = z - v_{pp}t$, $t = \tau$ can be applied, which yields the operators:

$$\frac{\partial}{\partial t} = \frac{\partial}{\partial \zeta}\frac{\partial \zeta}{\partial t} + \frac{\partial}{\partial \tau}\frac{\partial \tau}{\partial t} = -v_{pp}\frac{\partial}{\partial \zeta} + \frac{\partial}{\partial \tau} \ , \tag{2.46}$$

$$\frac{\partial}{\partial z} = \frac{\partial}{\partial \zeta}\frac{\partial \zeta}{\partial z} + \frac{\partial}{\partial \tau}\frac{\partial \tau}{\partial z} = \frac{\partial}{\partial \zeta} \ . \tag{2.47}$$

By using these transformations and neglecting $\partial/\partial\tau$ terms in the plasma fluid equations, Eq. (2.45) and the continuity equation Eq. (2.21) can be integrated to give:

$$\gamma - \phi - \beta_{pp}u_z = 1 \ , \tag{2.48}$$

$$n(\beta_{pp} - \beta_z) = \beta_p n_0 \ , \tag{2.49}$$

where $\beta_{pp} = v_{pp}/c$ is the normalized phase velocity of the wake, and the integral constants were obtained from the equilibrium state. Using Eqs. (2.48) and (2.49) together with the assumption of $\beta_{pp} = 1$, the Poisson equation Eq. (2.15) and plasma electron density can be described in terms of the normalized potentials as follows:

$$\frac{\partial^2 \phi}{\partial \zeta^2} = \frac{k_p^2}{2}\left[\frac{1+a^2}{(a+\phi)^2} - 1\right] \ , \tag{2.50}$$

$$\frac{n}{n_0} = 1 + \frac{1}{2}\left[\frac{1+a^2}{(1+\phi)^2} - 1\right] \ . \tag{2.51}$$

In the nonlinear regime, the electric field exhibits a "sawtooth" profile with a highly peeked density profile as shown in Fig. 2.2, where a half-sine envelope laser pulse with length $a = a_0 \sin(\pi\zeta/L)$ for $-L < \zeta < 0$, and $a_0 = 2.0$, and at the resonant condition for the linear plasma wavelength $L = \lambda_p$ were used. The nonlinear regime may have some advantages against the linear regime in addition to the higher electric field of the wake. As can be seen from Fig. 2.2, the period of the nonlinear plasma wave increases, which extends the dephasing length leading to higher net energy gain as discussed in Chapter 1. The nonlinear plasma wavelength in the $v_{pp} \sim c$ limit is given as:

$$\lambda_p^{nl} = \lambda_p \times \begin{cases} 1 & \text{for } E_{\max}/E_0 \ll 1, \\ 2E_{\max}/(\pi E_0) & \text{for } E_{\max}/E_0 \gg 1, \end{cases} \tag{2.52}$$
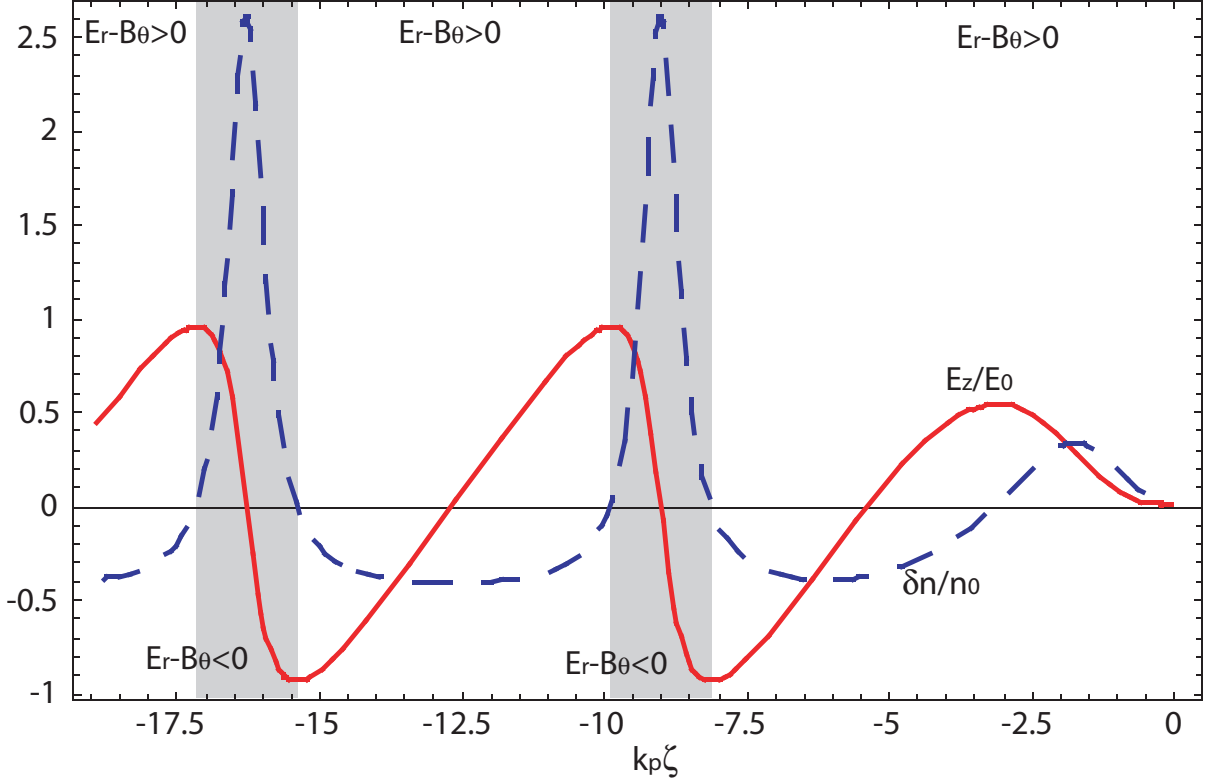
Figure 2.2:   Normalized nonlinear density variation $(n - n_0)/n_0 = \delta n/n_0$ (dashed curve) and longitudinal electric field E_z/E_0 (solid curve) versus the wake phase $\Psi = k_p\zeta$. Shown by a white areas are the regions where the electron may experience a focusing radial electric field. A half-sine envelope laser pulse $a = a_0 \sin(\pi\zeta/L)$ with $a_0 = 2.0$ propagates to the right, and the resonant condition for the linear plasma wavelength $\lambda_p = L$ were used.

where E_{max} is the peak electric field of the plasma wave. Although a complete discussion of the transverse fields can not be provided in the 1D analysis above, the region where the radial electric field provides focusing force may be extended in the nonlinear regime, as shown in Fig. 2.2 by the darkened area. The nonlinear wakefield may provide advantage for e-beam collimation.

In the 2D nonlinear regime, the laser intensity dependence of the plasma wavelength [Eq. (2.52) via E_{max}] suggests that the plasma wavelength varies as a function of radius in the case of a non-uniform laser radial profile (e.g., a Gaussian profile). The longer plasma wavelength near the axis causes wavefront of the wake to curve, resulting in a "horseshoe" shape of the wake, as illustrated in Fig. 2.3. In Fig. 2.3, the laser radial profile was assumed to be $a = a_0 \exp(-r^2/r_0^2)$ with spot size $r_0 = 25$ μm, $P = 300$ TW
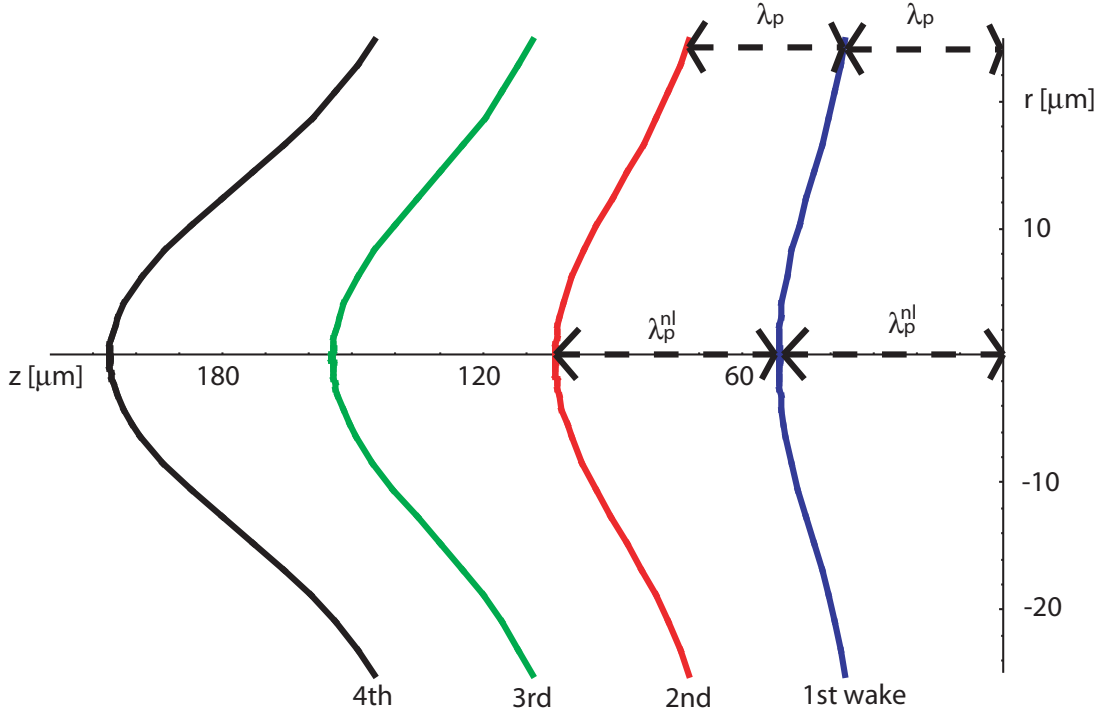
Figure 2.3: Radial profile of the nonlinear wakefield due to the intensity dependence of the plasma wavelength. The horizontal axis is the laser propagation axis z, and vertical axis is radial axis r. Shown by the solid lines are plasma wavelength $N \times \lambda_p(a(r))$ with integer N. For calculation, laser radial profile is assumed to be $a = a_0 \exp{(-r^2/r_0^2)}$ with spot size $r_0 = 25$ μm, $P = 300$ TW ($a_0 \sim 3.8$), and plasma density $n_0 \sim 4.8 \times 10^{18}$ cm^{-3}.

($a_0 \sim 3.8$), and plasma density $n_0 \sim 4.8 \times 10^{18}$ cm^{-3}. This curved wakefield implies an enhanced radial component of the wake electric field E_r, which may affect the resultant e-beam divergence.

A capillary discharge guided laser wakefield accelerator (CDG-LWFA) provides a plasma radial profile with a density minimum on axis for guiding. A plasma channel produces a similar effect on the radial dependence of the plasma wavelength, resulting in curved wakefields. The structure of the wakefield in a plasma channel was studied numerically and analytically by Andreev et al., [138], where an extended plasma wave period in which simultaneous acceleration and focusing of electrons was found. The curved wakefield may provide advantages: a) increases useful phase region, b) increases focusing leading to smaller e-beam size.

In the highly nonlinear 3D regime, a laser pulse can expel all of the plasma electrons

from the vicinity of the propagation axis [56–58, 139–142]. This regime has been referred
to as the blow-out, bubble, or cavitation regime. The required laser plasma parameters
for complete blow-out (no electron) may be obtained as follows. The ponderomotive
force $\boldsymbol{F}_{pm} = -mc^2 \nabla \gamma$ to expel electrons has to be matched to the space charge force
$\boldsymbol{F}_s = mc^2 \nabla \phi$ under the condition of the blow-out, namely electron density $n = 0$ with
$\boldsymbol{F}_s = \boldsymbol{F}_{pm}$. From the Piosson equation Eq. (2.15), we obtain:

$$\nabla^2 \phi = -k_p^2 = \nabla^2 \gamma \ . \tag{2.53}$$

Assuming a transverse laser profile $a = a_0 \exp\left(-r^2/r_0^2\right)$, $\gamma_\perp = \sqrt{1 + a^2}$ can be written as:

$$\gamma_\perp = \begin{cases} 1 + \frac{1}{4}a_0^2 \exp\left(-\frac{2r^2}{r_0^2}\right) & \text{for } a_0 \ll 1 \ , \\[2mm] \frac{1}{\sqrt{2}}a_0 \exp\left(-\frac{r^2}{r_0^2}\right) & \text{for } a_0 \gg 1 \ . \end{cases} \tag{2.54}$$

Substituting Eq. (2.54) into Eq. (2.53), and considering transverse motion ($\nabla^2 = \nabla_\perp^2$) the
condition for the complete blow-out at $r = 0$ becomes:

$$k_p^2 r_0^2 = \begin{cases} 2a_0^2 & \text{for } a_0 \ll 1 \ , \\[2mm] 2\sqrt{2}a_0 & \text{for } a_0 \gg 1 \ . \end{cases} \tag{2.55}$$

For example, for a 1600 mJ Ti:Sapphire laser ($\lambda = 0.8 \ \mu$m) to meet the blow-out condition
for $n_0 = 1 \times 10^{18}$cm^{-3}, the laser pulse has to be focused to $r_0 \sim 15.5 \ \mu$m for a laser pulse
length of $\tau_L \sim 20$ fs ($a_0 \sim 3.0$). Equation (2.55) suggests that a tightly focused laser pulse
with low density can realize the blow-out condition even in the linear regime ($a_0 < 1$). For
the highly nonlinear regime ($a \gg 1$), similar results were obtained using 3D particle-in-cell
(PIC) simulations (e.g., $k_p r_0 = \sqrt{a_0}$ from Ref. [140], and $k_p r_0 = 2\sqrt{a_0}$ from Ref. [142]).
Note that only the transverse component was considered above, and the longitudinal
component could be comparable when the resonant condition ($L = \lambda_p$) is provided. This
contribution may affect a coefficient in Eq. (2.55), but not change the a_0 dependence.
Typically, the longitudinal length of the laser pulse L is much shorter than λ_p in blow
out regime, and the transverse size of the cavitated region (bubble) is on the order of
the laser spot size r_0 [142]. In the linear regime ($a < 1$), the blow-out condition can be

derived for the resonant condition ($L = \lambda_p$) from the 3D density perturbation (resonant for a half-sine envelope laser pulse):

$$\frac{n_2}{n_0} = \frac{\pi}{8}a_0^2 \left[1 + \frac{8}{k_p^2 r_0^2} \left(1 - \frac{2r^2}{r_0^2} \right) \right] \exp \left(-\frac{2r^2}{r_0^2} \right) \sin(k_p \zeta). \tag{2.56}$$

The requirement to realize a complete blow-out on axis ($r = 0$) is:

$$k_p^2 r_0^2 = \pi a_0^2 \quad \text{for } a_0 \ll 1, \text{ and } L = \lambda_p . \tag{2.57}$$

In the blow-out regime, radial force is always positive inside of the cavitated region (ion channel), which can be depicted as a reduced darkened phase area of Fig. 2.2. During the acceleration and even in the deceleration phase, injected electrons experience a radial focusing field. This ion channel can also guide an intense laser pulse (blow-out guiding). Laser self guiding in such highly nonlinear regime with an initially uniform plasma was observed from 3D PIC simulations [142]. The simulations suggest that a preformed channel may not be needed for such ultra-intense laser pulses to propagate a distances greater than the Rayleigh length.

As has been shown, the laser strength parameter (normalized vector potential a_0 for the laser pulse) is one of the key parameters for the discussion of the physics of laser driven wakefields. The laser strength parameter is related to the experimental parameters as follows. The parameters measured in experiments are the energy of the laser pulse U_L, and the pulse length τ_L, which is defined as a full width half maximum (FWHM) of a Gaussian temporal laser intensity profile. From these measurements, one can then obtain the peak power of the laser pulse:

$$P = \frac{U_L}{\int_{-\infty}^{\infty} \exp\left(-4\log 2\, t^2/\tau_L^2\right)dt} = \sqrt{\frac{\log 2}{\pi}} \frac{2U_L}{\tau_L}. \tag{2.58}$$

In practical units, P [TW] $\simeq U_L$ [mJ] $/\tau_L$ [fs]. One has to measure the laser spot waist r_0, which is defined assuming a Gaussian transverse transverse profile as $I = I_0 \exp\left(-2r^2/r_0^2\right)$, to evaluate the laser peak intensity I_0:

$$I_0 = \frac{P}{4[\int_0^{\infty} \exp\left(-2r^2/r_0^2\right)dr]^2} = \frac{2P}{\pi r_0^2}. \tag{2.59}$$

Consider a normalized vector potential of the form:

$$\boldsymbol{a} = a_0[\cos{(kz - \omega t)}\boldsymbol{e}_x + \alpha \sin{(kz - \omega t)}\boldsymbol{e}_y], \qquad (2.60)$$

where the parameter α characterizes the polarization of the radiation ($\alpha = 0$ for linear, and $\alpha = \pm 1$ for circular polarization, respectively). By using Eqs. (2.7) and (2.11), the laser peak intensity I_0 can be related to a_0 through the laser cycle time averaged field strength as:

$$I = \frac{c}{4\pi}\langle E^2 \rangle = \frac{(1 + \alpha^2)}{8\pi c}\left(\frac{\omega m_e c^2 a_0}{e}\right)^2 = \frac{(1 + \alpha^2)\pi c}{2}\left(\frac{m_e c^2 a_0}{e\lambda}\right)^2. \qquad (2.61)$$

In practical units, for a linearly-polarized laser pulse, $a_0 \simeq 8.55{\times}10^{-10}\lambda\,[\mu\mathrm{m}]\,\sqrt{I_0[\mathrm{W\ cm^{-2}}]}$, or:

$$a_0 \simeq 6.61 \times \frac{\lambda\,[\mu\mathrm{m}]}{r_0\,[\mu\mathrm{m}]}\sqrt{\frac{U_L\,[\mathrm{mJ}]}{\tau_L\,[\mathrm{fs}]}}. \qquad (2.62)$$

2.3   Electron Injection and Acceleration

Injection of electrons into the wakefield and acceleration may be discussed via a phase space analysis. In the 1D limit with the quasi-static approximation, it can be shown that the Lorenz force is integrable, and the integral provides a constant of the motion, namely the Hamiltonian H:

$$H(u_z, \Psi) = \gamma - \phi(\Psi) - \beta_{pp}u_z \qquad (2.63)$$

The Hamiltonian specifies the orbit of an electron in (Ψ, u_z) phase space. For example, the Hamiltonian describing the background electrons, $H_0 = 1$, is obtained by considering the equilibrium state in front of the laser pulse ($u_z = \phi = a_0 = 0$, and $\gamma = \gamma_0 = 1$). With a specified Hamiltonian H_c and the relation $\gamma = \sqrt{1 + u_z^2 + a^2}$ in the 1D limit, the normalized axial momentum of an electron in the plasma wave may be written as:

$$u_z(\Psi, a) = \gamma_{pp}^2\beta_{pp}(H_c + \phi) \pm \gamma_{pp}\sqrt{\gamma_{pp}^2(H_c + \phi)^2 - 1 - a^2}\,, \qquad (2.64)$$

where $\gamma_{pp} = 1/\sqrt{1 - \beta_{pp}^2}$, and $\phi(\Psi, a)$ can be obtained by soluving Eq. (2.50). Note that u_z depends on plasma density through β_{pp}, which limits the maximum energy gain via

dephasing as discussed in Chapter 1.

The Hamiltonian that gives the separatrix $H_s(u_{zs}, \Psi_s)$, which describes the boundary orbit between the trapped and untrapped regimes, can be obtained by considering the unstable fixed points ("X points"), where $du_z/d\Psi = \infty$ and the phase that gives local minimum for $\phi(\Psi)$. In the linear regime ($a_0 \ll 1$), X points lie at $u_{zs} = \gamma_{pp}\beta_{pp}$ and $\Psi_s = -5\pi/2 - 2N\pi$ for a half-sine envelope drive laser pulse with length L [$a = a_0 \sin(\pi\zeta/L)$ for $-L < \zeta < 0$], leading to $H_s = H(u_{zs}, \Psi_s) = 1/\gamma_{pp} + \phi(-5\pi/2)$. Here, N is an integers. The Hamiltonian describing the orbit in which electrons do not experience the radial defocusing field H_f may be given by the conditions $du_z/d\Psi = \infty$ and $\Psi_s = -2N\pi$ in the linear regime.

Figure 2.4 shows a cold fluid orbit (blue dashed line), trapping threshold (separatrix, red solid line), and trapped and focused orbit (green dash-dotted line) for a half-sine envelope laser pulse with $a_0 = 0.2$ and the resonant condition for linear plasma wavelength $\lambda_p = L$, $n_0 = 5 \times 10^{18}$ cm^{-3}. The phase velocity of the wake is assumed to be the group velocity of the laser pulse ($v_{pp} = v_{lg}$). Trapping of dark current (background plasma electrons) into the trapped orbit may occur when electrons somehow gain enough momentum to reach the trapped orbit [illustrated as (1) in Fig. 2.4]. This could be realized via high temperature plasma [143], wavebraking, or interaction with other waves such as the Raman backscattered light [144] or additional laser pulses [75–79, 145]. One could also externally inject an electron beam, the momentum of which satisfies trapping condition. From the 1D point of view, self-trapping may occur about the region where the distance between the cold orbit and trapped orbit [$\delta u_z(\Psi) = u_z(H_s) - u_z(H_0)$] is the smallest, which is $\Psi \sim -3\pi/2$ for the case shown in Fig. 2.4. Once electrons in the wake gain the momentum enough to reach inside of the separatrix, they will be trapped and accelerated. First, the trapped electrons move toward the back of the wakefield in the case that electrons are slower than the phase velocity of the wakefield v_{pp} [(2) in Fig. 2.4] (typically true for self-trapping case). At some point, the electrons gain enough momentum such that they move faster than v_{pp}, and move toward the front of the wake [(3) in Fig. 2.4]. As has been discussed, this phase space analysis is based on a 1D analysis. If the initial momentum of the electrons are high enough to be inside of the trapped and focused orbit, then the electrons do not experience a radial defocusing force in multi-D. In multi-D, electrons that experience the radial defocusing force may go off-axis, resulting in
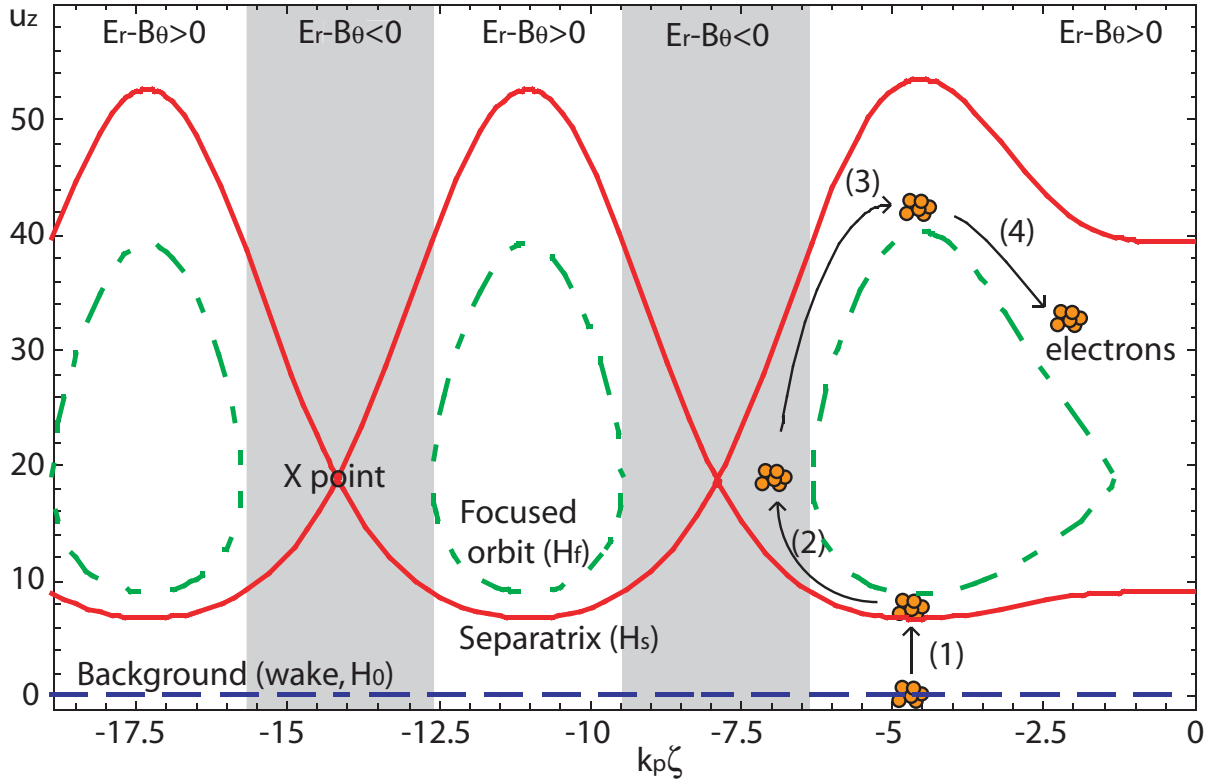
Figure 2.4:　Orbits in phase space (linear regime). Background plasma cold fluid orbit [wakefield, dashed line, $H_0 = 1$], trapping threshold [separatrix, solid line, $H_s = H(u_{zs}, -5\pi/2)$], and trapped and focused orbit [dash-dotted line, $H_f = H(u_{zs}, -2\pi)$] for a half-sine envelope laser pulse with $a_0 = 0.2$ and the resonant condition for linear plasma wavelength $\lambda_p = L$, $n_0 = 5 \times 10^{18}$ /cm^{-3}. The phase velocity of the wake is assumed to be the group velocity of the laser pulse ($v_{pp} = v_{lg}$). Shown by a white areas are the regions where the electron experiences a focusing radial electric field (see Fig. 2.1). Trapping and acceleration of electrons are also illustrated.

seeing a reduced accelerating field E_z. Note that the orbits for those off-axis electrons can not be described by the 1D phase space shown in Fig. 2.4. Eventually, the electrons reach the top of the closed orbit, and then experience a decelerating force [dephasing, (4) in Fig. 2.4]. The performance may be optimized in terms of the energy gain by terminating interaction just before reaching dephasing. The maximum energy gain obtainable in the linear regime was shown in Eq. (1.8). During acceleration, the energy spread is given by the projection of the bunch onto the vertical (u_z) axis, showing the phase dependence and preserving the area in the phase space. This rotation in phase space affects energy spread, and the impact depends on the significance of the other effects that induce energy

spread. The plasma temperature also can affect energy spread, as it can determine the initial electron orbits.

Orbits in phase space for the nonlinear regime ($a_0 = 2.0$) are shown in Fig. 2.5. In this regime, the oscillation amplitude of the wake is much stronger than the linear regime ($-1 \lesssim u_z \lesssim 1$), and the separatrix approaches the background orbit. Therefore, the separatrix-background distance δu_z is much smaller than the linear regime, suggesting that electron trapping may occur more readily. In other words, the linear regime may be suitable for providing a dark current free accelerating structure, without self trapping. For LWFA systems with an external electron beam source, or triggered injection scheme,
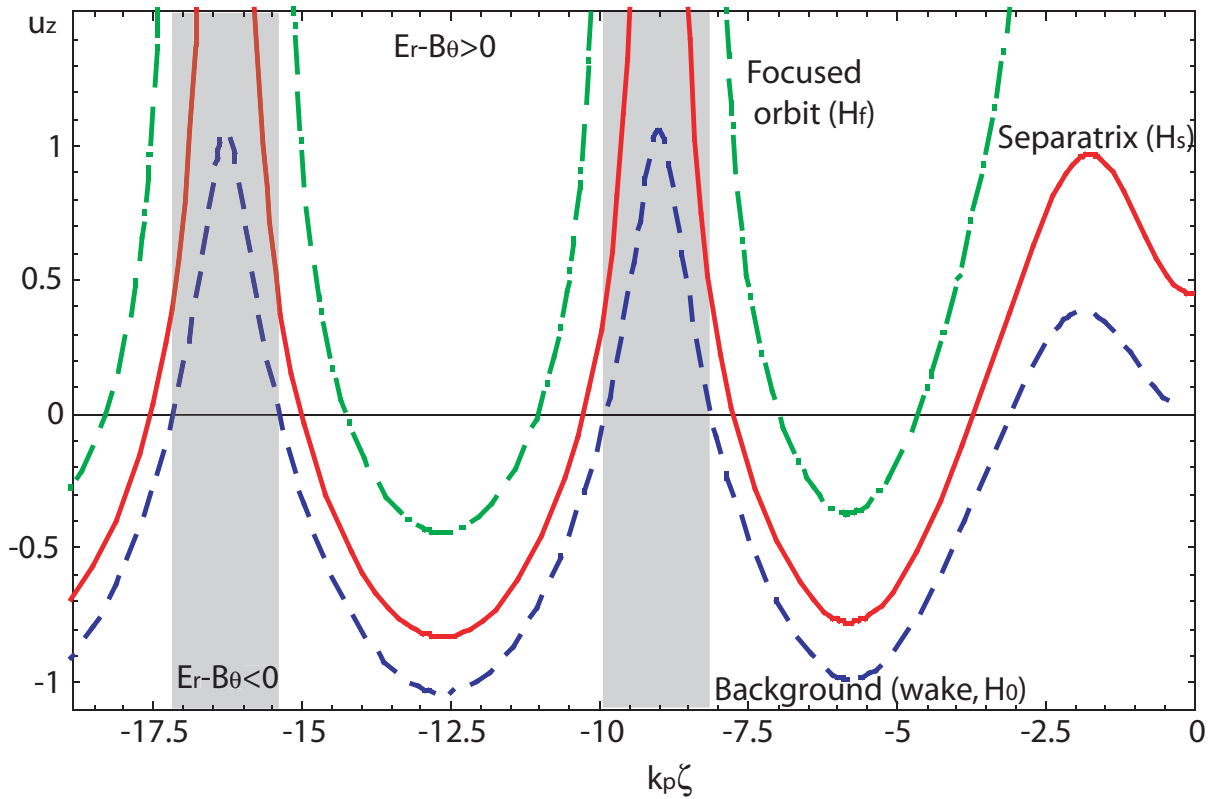
Figure 2.5: Orbits in phase space (nonlinear regime). Plasma background cold fluid orbit (wakefield, dashed line, $H_0 = 1$), trapping threshold (separatrix, solid line, H_s), and trapped and focused orbit (dash-dotted line, H_f) for a half-sine envelope laser pulse with $a_0 = 2.0$ and the resonant condition for linear plasma wavelength $\lambda_p = L, n_0 = 5 \times 10^{18}$ /cm^{-3}. The phase velocity of the wake is assumed to be the group velocity of the laser pulse ($v_{pp} = v_{lg}$). Shown by white areas are the regions where the electron probably experiences a focusing radial electric field (see Fig. 2.2). Maximum u_z of the separatrix reaches $u_z \sim 1500$ (not shown).

such as optical injection [74–81, 145], the linear regime would be preferred to suppress self injection. The distance δu_z also depends on the plasma density through the wake phase velocity β_{pp} in Eq. (2.64); higher density leads to smaller δu_z. If the LWFA system relies on self-trapping for electron injection, it will require a sufficiently high plasma density and laser intensity a_0 to realize small δu_z. As discussed in Section 2.2, a high laser intensity results in a stronger wakefield together with a stretched plasma wavelength in the nonlinear regime leads to higher energy gain. The maximum u_z for the separatrix of Fig. 2.5 reaches $u_z \simeq 1500$ (not shown). The maximum energy gain obtainable in the nonlinear regime was shown in Eq. (1.8). Also illustrated in Fig. 2.5 is the reduced radial defocusing regimes, and widened trapped and focused regions.

A laser pulse may evolve during interaction with plasma, such as depletion, steepening, and etc. The longitudinal and transverse modulation of the laser pulse during the interaction may be described as the interaction of the plasma wave ($\propto a^2$) and laser ($\propto a$). These third-order effects are called Raman scattering [146–148] for the longitudinal modulation, and self modulation for the transverse modulation, and are beyond the scope of this dissertation. Although a theoretical discussion of Raman scattering [149] and self modulation [150–152] will not be discussed here, the evolution of the laser pulse, namely evolution of a_0 could be deduced by the experimentally observed maximum electron energy. The phase space analysis gives the maximum energy obtainable for given plasma density and laser intensity. By using the Eq. (1.8), one can roughly estimate the evolution of a_0 in the cases where dephasing is observed experimentally.

The discussion of electron injection presented above is limited to 1D. As discussed in Section 2.2, the wavefront of the plasma wave may be curved in the 2D nonlinear regime, which can lead transverse wavebreaking [153]. One can see from Fig. 2.3 that the curvature of the wake is enhanced more in the tail of the wakefield due to the pile up of the difference $\lambda_p^{nl} - \lambda_p$. Sufficiently far behind the 1st period of the wake, the regular structure of the wake can be destroyed and electron injection may occur (i.e., transverse wavebreaking). The significance of this injection mechanism may depend on the strength of the wake. If electrons are injected via other mechanisms at an earlier period of the wake, a interfering wakefield from the injected electrons (beam-driven wakefield) will tend to cancel the laser-driven wake, which weakens the later periods of the laser-driven wakefield (beam loading, discussed later in this Section). And hence, the wakefield sufficiently far

from the drive laser pulse may not be strong enough to self-trap plasma electrons.

PIC simulations have suggested that in the blow-out regime, particle trapping occurs transversely in the vicinity of the downstream tail of the bubbles [56–58, 139–142]. The e-beam divergence is determined by the point of injection. If injection occurs close to the axis, it may result in production of the small beam divergence beam. If it occurs far from the axis, the electrons exhibit betatron oscillations with large amplitude, resulting in large e-beam divergence (and significant x-ray generation [94]). The key physics describing the area of injection remains an area of active research.

To produce high quality (small energy spread) electron beams, the trapping of electrons has to be instantaneous (short on the scale of a plasma period). If trapping of background electrons keeps occurring during the interaction, it may result in production of a broadband electron beam. External injection or optical injection can be designed to provide such instantaneous injection [75–79, 145]. For self-trapping to be instantaneous, it may have to rely on the beam loading effect to terminate trapping.

An injected and accelerated e-beam can excite a wake as in a plasma wakefield acceleration (PWFA, see Section 1.1 for reference). In a plasma-based accelerator, the wake from the accelerating bunch will be out of phase with, and thus reduce the wake generated by the drive laser pulse for trailing bukcets. The process by which the wake produced by the accelerated bunch significantly modifies the fields of the accelerating plasma wave is referred to as beam loading [154, 155]. The reduction in the wake leads to a greater distance δu_z in phase space, and may stop self-trapping of electrons into the wake.

The beam loading effect may be necessary to produce high quality e-beam where self-trapping is used for beam generation because it can stop self-trapping. It, however, introduces energy spreads into the e-beam during the acceleration process via the modified wakefield. Analytically, the maximum number of bunch electrons that can be loaded into a small ($\ll \lambda_p$) axial segment of a linear wakefield for acceleration (i.e., the number of electrons required to produce a wakefield that will cancel the accelerating field, i.e., fully beam loads) is [154]:

$$N_{\max} = \frac{n_0 A_b}{k_p} \frac{E_z}{E_0} \simeq 5 \times 10^5 \left(\frac{E_z}{E_0} \right) A_b[\text{cm}^2] \sqrt{n_0[\text{cm}^{-3}]}, \tag{2.65}$$

assuming a normalized axial electric field $E_z/E_0 < 1$, where $A_b \gg \pi/k_p^2$ is the cross-

sectional area of the bunch. As the number of bunch electrons N_e approaches $N_{\max}$, the energy spread $\hat{T} = \delta T / T_0$ scales as:

$$\hat{T} \propto \frac{N_e}{N_{\max}}. \tag{2.66}$$

The efficiency of converging wake energy to electron energy η_{WB} scales as:

$$\eta_{WB} \propto \hat{T}(2 - \hat{T}). \tag{2.67}$$

In the case that the trapping of electrons is instantaneous, the beam loading effect is a mechanism that introduces energy spread. If the electrons are fully loaded to cancel out the laser driven wakefield, the tail part of the beam will not be accelerated, leading to 100% energy spread. Trapping could occur at the second or later buckets, or multiple times in the same bucket. In those cases, the energy spectrum of e-beam may exhibit muti-bunch structure in time and energy space, which complicates the analysis. Although it requires numerical codes, such as a PIC, to study the nonlinear 3D regime and include other effects such as multiple injection, this analytical study provides a tool to discuss the e-beam energy spread and energy in the wakefield. A discussion of energy spread induced by beam loading, and the energy in the wake are presented in Section 4.6.

Regarding the production of small angular divergence e-beams, the nonlinear regime has the advantage of an increased focusing region, as has been discussed and showed in Figs. 2.1, 2.2, 2.4, and 2.5, especially when electron injection relies on self-trapping of the back ground electrons. In the case of transverse injection, namely transverse wave-breaking and injection in the blow-out regime, the beam divergence may be determined by the transverse location of injection. Although the key physics governing the location of injection is an area of research, the transversely larger bubble may more readily inject away from the propagation axis ($r = 0$). Overall, the blow-out regime has an advantage for the production of collimated e-beams due to the creation of an ion channel, compared to the other regimes.

2.4   Summary

Although it requires numerical simulation with PIC or fluid codes to rigorously describe 3D nonlinear phenomena in laser plasma interactions, the analytic study presented in this Chapter provides a qualitative picture of the interactions. The electron properties measurable through the electron magnetic spectrometer which is described Chapter 3 are electron beam charge, divergence, and energy spectrum. From discussions of this Chapter, those measured e-beam properties can be related to the laser-plasma physics as follows:

- **Electron energy**

  1. Laser pulse evolution

     From the experimentally observed maximum electron energy and Eq. (1.8), one may estimate the a_0 obtained during the interaction.

  2. Point of injection

     From the experimentally observed maximum electron energy and the dephasing length given by Eq. (1.4), one may deduce the point where self-injection occurred.

- **Angular divergence**

  1. Regime of interaction

     In a self-trapping based LWFA, nonlinear and blow-out regime may be preferred to linear regime, since the radially defocusing region is decreased by higher a_0.

  2. Transverse particle injection

     If injection occurred via transverse wavebreaking, including trapping in the blow-out regime, the location of injection may decide the beam divergence. In the blow-out regime, it may be related to the size of the bubble, which is given by the laser spot size. The larger spot size may lead to the larger beam divergence.

- **Energy spread**

  1. Injection process

     Duration of injection broadens the energy spread. Higher plasma density and

laser intensity give the smaller δu_z for trapping as discussed in the phase space analysis.

2. Beam loading effect

   Beam loading effect induces the energy spread during the acceleration. Higher charge leads to the larger energy spread.

3. Off-axis propagation

   Electrons that experience radial defocusing force can go to off-axis, and hence experiences lower accelerating field E_z. This effect may introduce beam spread.

4. Phase dependence

   The projection onto the u_z axis in the phase space has phase dependence, meaning that the energy spread has phase dependence.

5. Plasma temperature

   The plasma temperature affects the energy spread.

Chapter 3

Broadband Electron Spectrometer

3.1 Introduction

A charged particle spectrometer [156] is one of the critical diagnostics for any particle accelerator. For the present generation laser wakefield accelerator (LWFA), requirements placed on the electron spectrometer (ESM) are somewhat different from those for conventional accelerators. As discussed in Chapter 1, LWFAs can operate in a regime where beams with large relative momentum spread $\hat{p} = \delta p / p_0$ are generated, or produce narrow spread ($\hat{p} < 10\%$) beams, where p is the electron momentum, and p_0 is the central momentum of the e-beam. To elucidate the mechanisms behinds those regimes, an ESM has to cover a wide range of energy in a single shot. Therefore, a broad momentum acceptance with high resolution is critical for an LWFA ESM.

An ESM used for the gas-jet based LWFA experiments at Lawrence Berkeley National Laboratory (LBNL) utilized an electromagnet and a scintillating screen [157]. Single-shot information of the e-beam energy spectrum was measured for a $\pm 17\%$ range around a central momentum p_0 (factor 1.4), with $< 1\%$ momentum resolution, depending on the slit width [56]. Since it utilized an electromagnet, the observable momentum could be tuned by controlling the applied current. The central momentum was variable from 0.4 to 88.7 MeV/c. Therefore, an averaged e-beam momentum spectrum from 0.3 to 104 MeV/c was obtainable by scanning the applied current. Note that in principle, ultrahigh energy can be measured by observing the near forward window but, with poor resolution. Although it was sufficient for this LWFA system (lower energy, ~ 100 MeV/c), scanning

momentums from 1 MeV/c to 1 GeV/c with $p_0 \pm 17\%$ momentum acceptance/shot would be unpractical. For GeV class LWFAs, a major design change was needed for a ESM. Note that the electron kinetic energy $T \sim p$ for a relativistic electron, as can be seen in:

$$p \text{ [MeV/c]} = \sqrt{T \text{ [MeV]}(T \text{ [MeV]} + 2E_{rest}\text{[MeV]})} \, , \qquad (3.1)$$

where $E_{rest} \simeq 0.511$ MeV is the rest mass energy of an electron. In the following, the term "electron energy" means the kinetic energy of the electron, unless otherwise specified.

When the capillary discharge guided (CDG) LWFA apparatus was designed at the LOASIS Program, the decision was made to develop an ESM with as large a momentum acceptance as possible, and capable of measuring e-beams up to 1 GeV. Furthermore, in the CDG-LWFA accelerator concept, guiding of an intense laser was critical for operation, and simultaneous measurement of laser output mode and e-beam properties was essential. In order to realize the simultaneous measurement of laser and e-beam properties, the laser beam had to be separated from the e-beam without significant distortion. To accommodate the requirements for a single shot broad energy spectrum within a compact system that fits in the experimental cave of the LOASIS Facility, the ESM magnetic field had to be reasonably strong (≥ 1 T) with pole gap commensurate with the F-number of the laser focusing optics because the laser was measured after passing through the ESM. In addition, the design needed to provide sufficient angular acceptance (> 5 mrad, as large as possible) to measure the e-beam angular properties, as well as single-shot evaluation capability with high repetition rate to keep up with the high repetition rate laser system.

In this Chapter, an ESM design that satisfies all those requirements is presented. The requirements are summarized as follows:

- **Momentum acceptance**
  Up to more than 1 GeV e-beam had to be resolved. The single-shot acceptance had to be broad to provide sufficient information on the energy spectra without a scan of the magnetic field (single-shot measurement).

- **Momentum resolution**
  Sufficient to measure % level e-beam energy spread.

- **Angular acceptance**

Wide enough to capture the whole e-beam to evaluate its angular properties. To achieve that, large pole gap would be essential, while keeping high magnetic field.

- **Repetition rate**

  The nominal operation of a CDG-LWFA would be 1 Hz (limited by the vacuum system, other diagnostics, and thermal load on optics). Since the laser and capillary discharge waveguides had potential of providing > 1 Hz operation, the potential for higher than 1 Hz operation was desirable.

- **Charge monitor**

  To provide quantitative measurements for the amount of charge, it should be able to function as a calibrated charge monitor as well.

- **Simultaneous diagnosis of guided laser properties**

  This capability has to be provided since measuring the laser guiding performance was critical during operation to understand CDG-LWFA physics.

- **System dimension**

  The system has to be compact enough to fit in the experimental cave of LOASIS Facility (a couple of meters in propagation and transverse axis. The laser beam height was ~ 1 m, and bending electrons downward was preferred for radiation shielding).

Later in this dissertation, an ESM designed and developed is referred as the GeV-ESM to distinguish from other EMSs. Described in Section 3.2 are the concept and hardware, followed by the performance evaluation of the GeV-ESM in Section 3.3. Presented in Section 3.4 is a calibration study to investigate the energy dependence of the scintillating plate used up to the GeV level, and hence to add a function as a charge monitor to the GeV-ESM. Section 3.5 presents experimental results, and a summary is given in Section 3.6.

3.2 Spectrometer Design

Most spectrometer implementations use a dipole magnet as a dispersive element and a collimator to control the instrumental resolution. To detect the relativistic electron, a

variety of detectors have been employed: surface barrier detectors (SBD) [16, 25, 26, 48], scintilators with photomultipliers (scintillator-PMP) [28, 33, 51, 158], cloud chambers [16], Cerenkov radiation imaged by a camera [88], thermoluminescent dosimeters (TLD) [55], scintillating fibers [159, 160], Radiochromic film [161], imaging plates (IP) [57, 60, 64, 65, 162], and scintillating (or phosphor) screens, mostly Gadox ($Gd_2O_2S : Tb$) [163] with films [26] or cameras (scintillator-camera) [16, 28, 39, 53, 56, 63, 72, 164]. Detection by a SBD and scintillator-PMP were popular methods in early LWFA experiments due to their high sensitivity. By using multiple detectors with different sensitivities, the exponential energy spectrum from sm-LWFAs was effectively measured [165]. Scintillating fibers added the capability of imaging. However, this may not be a cost-effective scheme when the field of view is extended to the meter scale. Cerenkov radiation is well suited for high energy e-beams (>10 GeV), while for low energy e-beams it requires a radiator (high refractive index media such as an aerogel or xenon gas), which might disturb angular properties of the e-beams. Imaging plate (IP) and scintillator-camera based system are now widely used for their capability of imaging with reasonable sensitivity and cost performance. They can provide detailed information on e-beam angular properties. Due to the capability for accumulative measurements, IP has an advantage in sensitivity, while scintillator-camera based system can be arranged to have a high repetition-rate.

In order to satisfy all the requirements imposed on the design, an electromagnet-based ESM was designed with a scintillator-camera based detection system. The schematic of the GeV-ESM is shown in Fig. 3.1. A water-cooled round dipole electromagnet Varian 4012A was found with sufficient field strength and effective field area, and with a 65 mm gap. The electromagnet was powered by an 8 kW class power supply, Glassman SH3R2.7. Since the magnet was originally used for magnetic resonance experiments [166], the field homogeneity in the flat region was very high ($< 1\%$ variations). The magnetic field was measured by a Hall probe along the mid-plane [156], and the effective radius, defined by $R_{eff} = [\int_0^\infty B_x(r)dr]/B_x(0)$, was found to be 195 mm with a peak field $B_x(0) = 1.25$ T. The measured profile and effective boundary are shown in Fig. 3.2. The Hall probe was installed permanently to measure the peak magnetic filed strength $B_x(0)$ for each shot directly, rather than deducing the peak field from the applied magnet current, which could lead to incorrect estimates due to the hysteresis of the magnet. The magnet deflected the electrons vertically downward onto two LANEX Fast Back scintillating screens (LANEX-
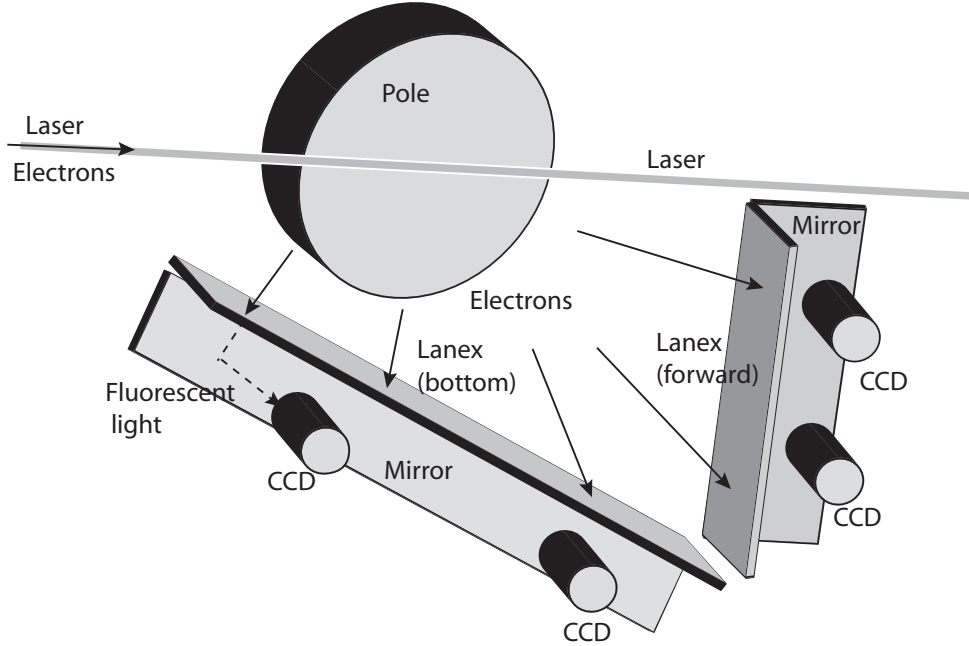
Figure 3.1: Schematic of the electron spectrometer. The magnet deflected the electrons vertically downward onto two LANEX-FBs, which emit fluorescent light. First surface mirrors were installed right after the LANEX screens with 45 degree to separate fluorescent light from e-beam. Four synchronously triggered 12-bit CCD cameras imaged a 75 cm long (bottom) and a 45 cm long (forward) screens, allowing simultaneous single shot measurement of electrons from 0.01 GeV to 0.14 GeV (bottom) and 0.17 GeV to 1.1 GeV (forward) with a peak magnetic field of 1.25 T.

FB), which were mounted on the exit flanges of the vacuum chamber. Four synchronously triggered 12-bit charge-coupled device (CCD) cameras (Pointgrey, Flea high resolution model [167]) imaged a 75 cm long (bottom) and a 45 cm long (forward) screens, allowing simultaneous single shot measurement of electrons from 0.01 GeV to 0.14 GeV (bottom) and 0.17 GeV to 1.1 GeV (forward) with a peak magnetic field of 1.25 T. The spatial resolution of the CCD cameras are shown in Fig. 3.5. Stray laser light was blocked by an aluminum foil of $\simeq 40$ μm thickness on the back of the screens. In addition, bandpass filters (central wavelength 550 nm, width 70 nm full-width half-maximum (FWHM)) were installed in front of each CCD camera to transmit green fluorescent light [168] and block the intense infrared laser light. To avoid electrons from hitting the CCD cameras directly, first-surface mirrors were used at 45° following the exit flanges, which separated fluorescent light from the electrons. The total number of electrons was obtained from the intensity
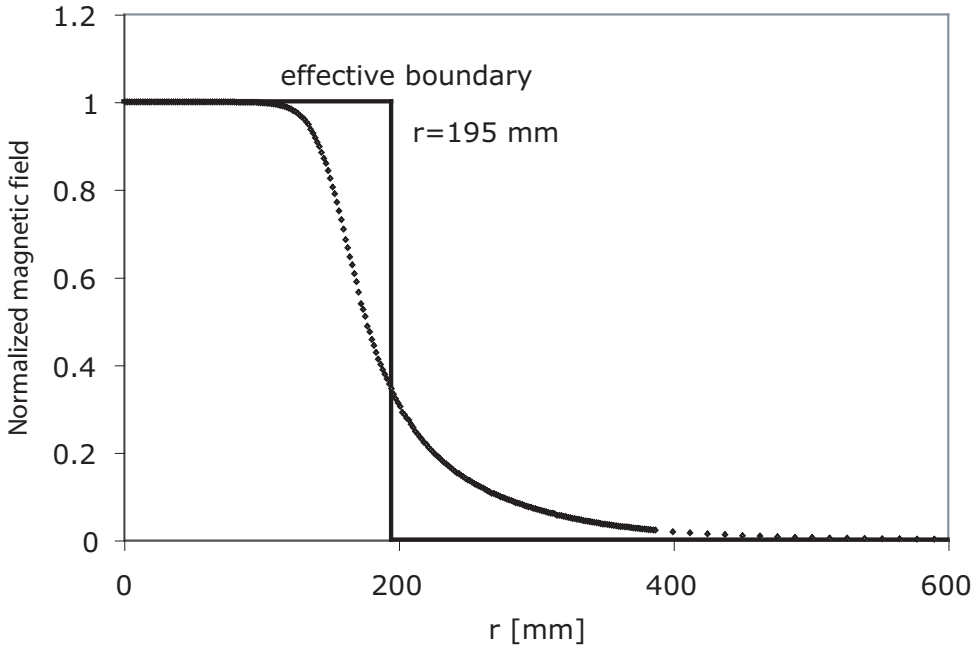
Figure 3.2:   Profile of the magnetic field measured by a Hall probe and the effective boundary of the magnet.

on the scintillating screens, cross-calibrated against an integrating current transformer (ICT) and ALS measurements. The details on the calibration is described in Section 3.5.

The imaging properties of the spectrometer were determined by the edge focusing. The displacement of the dipole magnet center with respect to the laser propagation axis was carefully chosen to provide the necessary edge focusing. Since converging powers in the dispersive (vertical, y) and non-dispersive (horizontal, x) planes needed to be considered [156], a value for the offset had to be determined, which satisfied various requirements such as a momentum resolution, angular acceptance of e-beam and laser beam, and system dimensions. The magnet center was placed such that the focusing strength in the dispersive plane provided sufficient momentum resolution, and that the slight defocusing in the un-dispersive plane kept the e-beam angular acceptance large enough. A vacuum chamber was designed to place the screen on the calculated first-order foci [157] for the bottom view. Shown in Fig. 3.3 is the location of foci for e-beams with various energies. There were trajectories which did not have foci (high energy) and others that had foci inside of the magnetic field. For those trajectories, red dots were located along the effective boundary of the magnetic field. The forward view was designed to
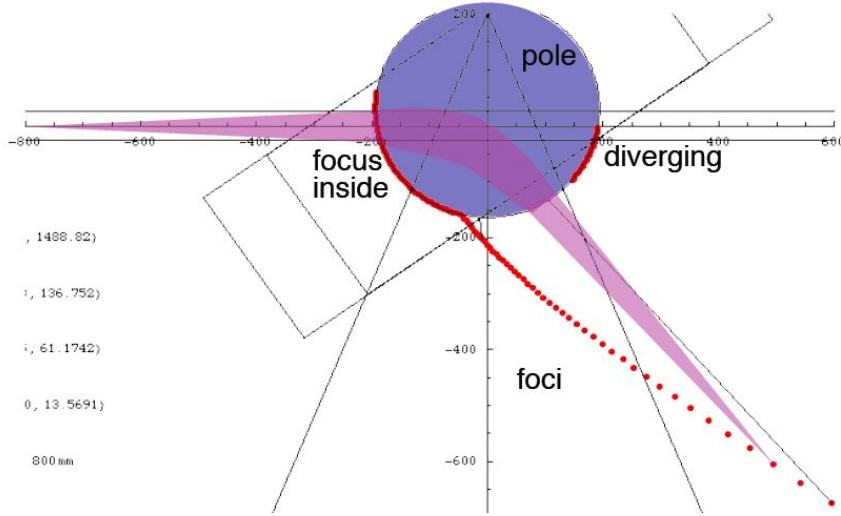
Figure 3.3: Locations of calculated first order foci for bending (vertical) plane are shown by red dots. Blue area shows the effective boundary of the magnetic field. The calculation was done by using sharp edge boundary model [157]. Red dots along the effective boundary indicate either trajectories that does not converge, or trajectories provide focus inside of the effective boundary.

allow viewing of high energy electrons while also providing the maximum possible e-beam angular acceptance and reasonable system dimensions, as well as desired resolution for laser output mode measurements. A detailed evaluation of the resolution and acceptance are presented in the next Section.

3.3 Performance Evaluation

The electron trajectories on the mid-plane (reference trajectories) were computed by calculating the deflection angle based on the Lorentz force. The input midplane field was generated through a 2D interpolation of the measured field profile along the radial axis. The representative trajectories (1.0, 0.5, 0.2, 0.1, 0.05, and 0.01 GeV) under a peak magnetic field $B_x(0) = 1.25$ T are shown in Fig. 3.4. Also shown is the magnetic field profile using a color-map, and the locations of the screens. For each trajectory, the 6-dimensional e-beam properties were calculated by using the arbitrary order beam dynamics code COSY INFINITY (COSY) [169]. To utilize the most accurate fringe field evaluation in COSY, the magnetic field profiles for each trajectory were fitted into a six
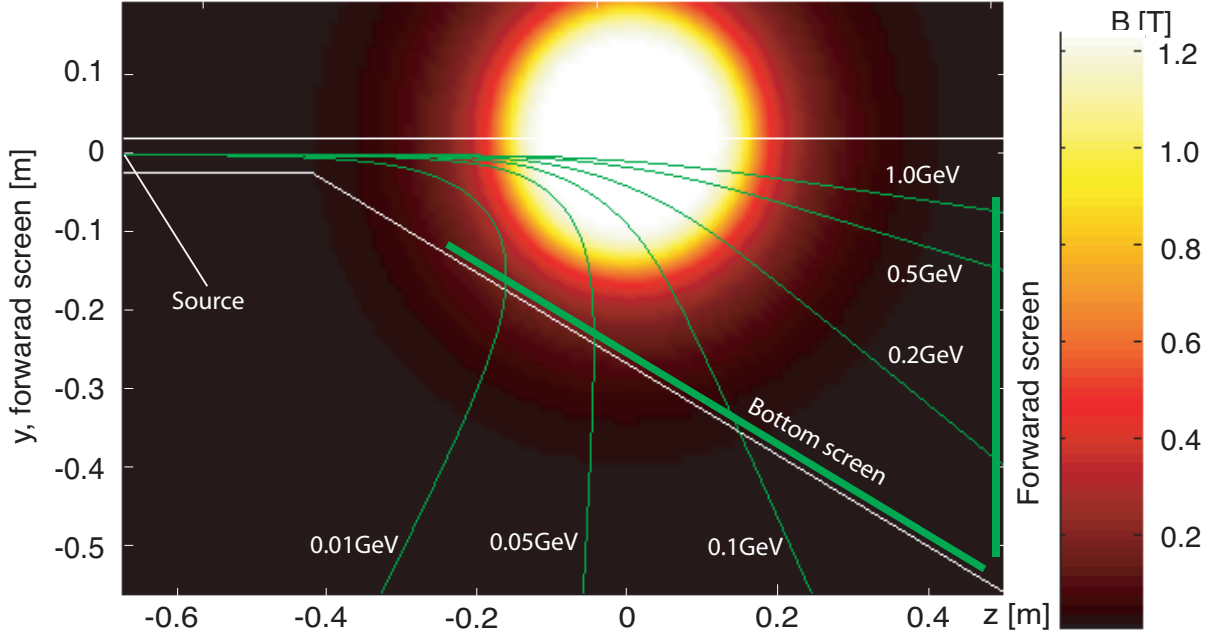
Figure 3.4:   Electron trajectories (1.0, 0.5, 0.2, 0.1, 0.05 and 0.01 GeV) with a peak magnetic field of 1.25 T. The location of the scintillating screens and the vacuum chamber are also illustrated. The center of the magnet is at $z = 0$. Shown by a color-map is the magnetic field profile. The source is the exit of the capillary discharge waveguide.

parameter Enge function $F(s)$ of the form:

$$F(s) = \frac{1}{1 + \exp[a_1 + a_2(s/D) + \cdots + a_6(s/D)^5]}, \tag{3.2}$$

where s is the distance perpendicular to the effective field boundary, D is the gap of the magnet, and $a_1 - a_6$ are the Enge coefficients. In COSY, a particle trajectory $\boldsymbol{X(s)} = (x, x', y, y', \delta l)$ is calculated in the form of a fivefold Taylor expansion, where x (y) indicates horizontal (vertical) plane, $x' = dx/ds$, $y' = dy/ds$, and δl is the path length difference from the reference trajectory. For example, an expansion is written for x:

$$x = \sum (x|x_0^\kappa y_0^\lambda x_0'^\mu y_0'^\nu \hat{p}^\chi) x_0^\kappa y_0^\lambda x_0'^\mu y_0'^\nu \hat{p}^\chi. \tag{3.3}$$

Here, $\hat{p} = \delta p/p$ is the relative momentum spread, subscript 0 indicates that the quantity was evaluated at $s = 0$, namely at beam source, $(x|x_0^\kappa y_0^\lambda x_0'^\mu y_0'^\nu \hat{p}^\chi)$ are the Taylor coefficients, which are a function of s. The order is given by the sum $ord = \kappa + \lambda + \mu + \nu + \chi$.

Shown in Fig. 3.5 are the spatial resolutions of the CCD cameras and each order's contribution to vertical size σ_{y1} versus e-beam energy (assuming a zero energy spread beam), where σ is the root-mean-square (rms) width of the beam distribution, subscript 1 indicates the output (at the screens). The assumed peak magnetic field was 1.25 T, and the input beam profile was a Gaussian distribution with $\sigma_{x0} = \sigma_{y0} = 20$ μm, and $\sigma_{x'0} = \sigma_{y'0} = 2$ mrad (rms). The discontinuity at 160 MeV in Fig. 3.5 comes from the transition between different screens. One can see from Fig. 3.5 that the contribution from 3rd order effects is small. Therefore, calculations up to 3rd order give sufficient accuracy for the evaluation of the spectrometer performance. When the effective spatial resolution of the CCD camera is larger than the beam spot size, as in the low energy case, the momentum resolution would be limited by the CCD camera imaging (not the e-beam
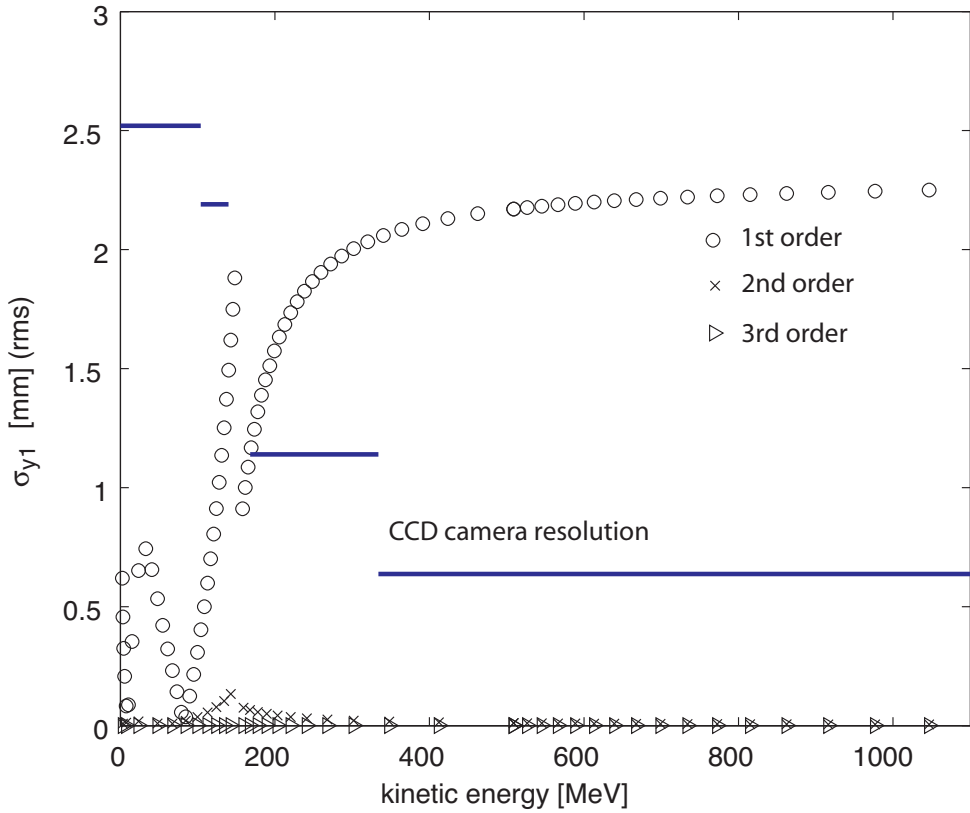
Figure 3.5: Calculated contributions to the vertical beam size of each order. Assumed input beam is a Gaussian distribution with $\sigma_{x0} = \sigma_{y0} = 20$ μm (rms), and $\sigma_{x'0} = \sigma_{y'0} = 2$ mrad (rms). Horizontal axis is the kinetic energy of electron for a peak magnetic field of 1.25 T. Also shown are spatial resolutions of CCD cameras.

optics). Although the momentum resolution could be improved by an imaging system with higher spatial resolution, the scattering effect inside of the screens [163] has to be addressed for a beam size below a few 100 micron.

Due to the collimator-free scheme, the measured momentum resolution contained a contribution from the e-beam divergence, which depended on the accelerator configuration and parameters, such as the laser energy or the capillary length and diameter. As a result, the e-beam divergence had shot-to-shot fluctuations. Therefore, the momentum resolution and the energy spread were evaluated for each shot with the following procedure. From the computed imaging properties, the horizontal beam divergence $\sigma_{x'0}$ was calculated from the measured horizontal beam size σ_{x1} with a given beam size at the source, σ_{x0} and σ_{y0}, which were assumed to be the same size as the laser output mode size. The effect of the source size on the image was almost negligible since the beam size at the source was smaller by more than an order of magnitude than the typical product of beam divergence and propagation distance. By assuming an axisymmetric electron beam profile (i.e., equal horizontal and vertical divergence), the vertical beam divergence $\sigma_{y'0} = \sigma_{x'0}$ was obtained and used to calculate the vertical beam size at the screen with a specific central energy and zero energy spread, σ_{y1mono}. The image size gave the intrinsic resolution of the GeV-ESM, δT_{mono}. The real energy spread of an electron beam δT_{beam} was then calculated by deconvolving the effect of finite divergence from the measured e-beam profile δT_{img} using $\delta T_{img} = \sqrt{\delta T_{beam}^2 + \delta T_{mono}^2}$. A Gaussian e-beam transverse profile was assumed for the calcuration. The momentum resolutions for $\sigma_{x'0} = \sigma_{y'0} = 1$ and 2 mrad electron beams are shown in Fig. 3.6, where the beam profile is assumed to be a Gaussian distribution with $\sigma_{x0} = \sigma_{y0} = 20$ μm. The momentum resolution of the GeV-ESM is below 2% (4%) for a 1 mrad (2 mrad) divergence beam in the energy range of the GeV-ESM. As discussed, and shown in Fig. 3.6, in the case where the beam size is smaller than the spatial resolution of the CCD cameras, the momentum resolution is limited by the CCD camera resolution, which can be seen in the region where the 1 and 2 mrad cases overlap.

The collimator-free scheme also introduced an uncertainty in the determination of the absolute energy [2]. The energy of an electron beam with positive (negative) incident angle in y (see Fig. 3.4 for coordinates) would be measured higher (lower) than the actual energy. The errors in the determination of the energy of electrons with certain incident angle (± 4 and ± 8 mrad) were computed and shown in Fig. 3.7, where the magnetic field
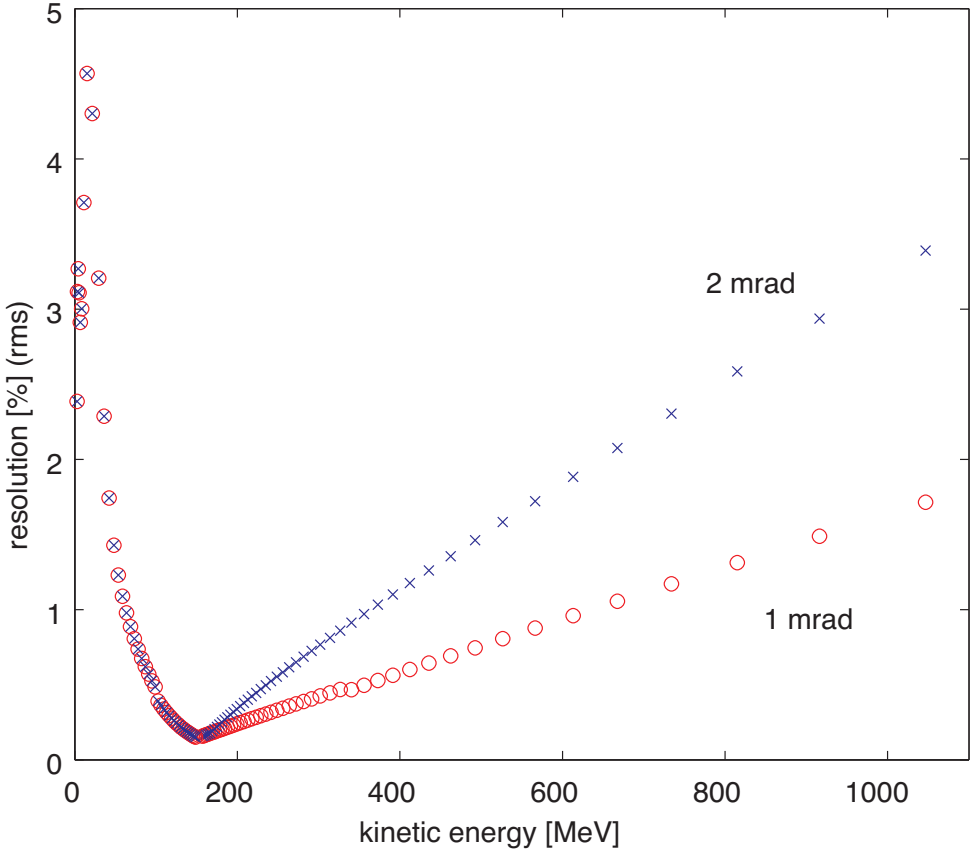
Figure 3.6: Momentum resolutions for $\sigma_{x'0} = \sigma_{y'0} = 1$ and 2 mrad electron beams. Horizontal axis is the kinetic energy of the e-beam for a peak magnetic field of 1.25 T. The input beam size was assumed to be a Gaussian distribution with $\sigma_{x0} = \sigma_{y0} = 20$ μm.

was taken to be 1.25 T. For example, the electron beam measured as 1.0 GeV might have been 0.94 (1.07) GeV with a 0.4 (-0.4) mrad incident angle. The fluctuation level in the incident angle in the vertical plane was evaluated as follows. From the measured beam position in the horizontal plane x_{1peak}, the angular fluctuation in the horizontal plane σ_{x1peak} was statistically evaluated. With the assumption of symmetric behavior in both planes $\sigma_{y1peak} = \sigma_{x1peak}$, the fluctuations in the incident angle in the vertical plane were then determined. The angular fluctuations showed dependence on the accelerator configuration (e.g., the laser energy or the capillary length and diameter), and the typical value was found to be 2 to 6 mrad in rms [170], which gave $\sim \pm 3$ to 11% error at 1.0 GeV, or $\sim \pm 2$ to 5% error at 0.5 GeV. Also shown in Fig. 3.7 is the geometrical acceptance. The acceptance was trajectory dependent due to the differences in the path length and
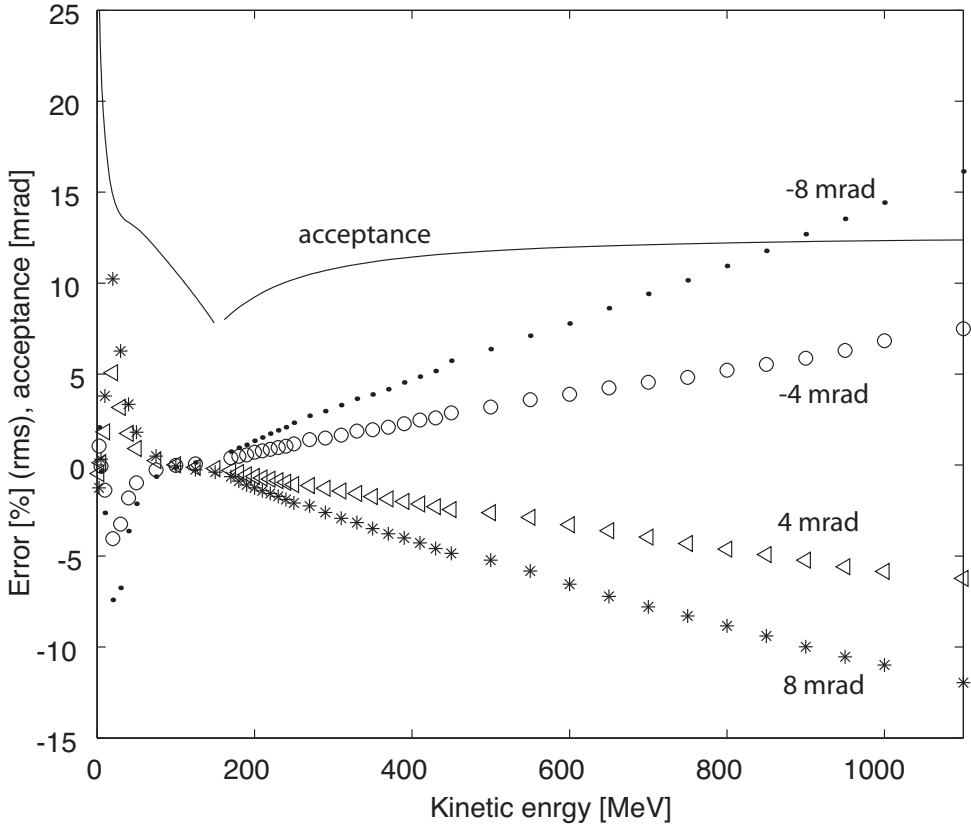
Figure 3.7: Errors in the determination of the absolute energy in cases of ± 4 and ± 8 mrad of the incident angle with the geometrical acceptance. The magnetic field was assumed to be 1.25 T.

the imaging properties. More than ± 10 mrad acceptance was achieved in most of the energy range.

3.4 Scintillating Screen Calibration

3.4.1 Introduction

Scintillating screens are commercially available from various companies such as Kodak, Toshiba, Fuji, or Konica. Those screens have been used mostly for medical application, namely x-ray imaging together with films. Companies have put constant effort into improved sensitivity (ISO speed) and spatial resolution by improving coatings and films [171]. Recently, those scintillating screens have been widely used for relativistic electron beam

detections in the LWFA community for their high electron - fluorescent light efficiencies. For this purpose, fluorescent light was usually observed directly by a digital camera (e.g., a CCD (charge coupled device) or CMOS (complementary metal oxide semiconductor) camera). From the observed intensity, one can deduce the number of electrons incident on the screen provided that a calibration is available. Note that a calibration may not be valid for an identical product from different manufacturing years due to possible improvement of a product.

Most of the screens utilize a compressed monocristalline powder of Gadox as an active material, which sits on a substrate and is covered by a protective coatings. While their properties were well studied for x-rays [172–175] because of the high demand from the medical field and their long history, to the author's knowledge, there was only one publication as of 2007 on the relativistic e-beam detection with such a scintillating screen [164]. Discussed in Ref. [164] was the e-beam energy dependence from 0.1 MeV to 1 GeV with the Monte Carlo simulation, and only from 3 to 8 MeV energy dependence was explored experimentally. In this Section, the e-beam energy dependence of LANEX-FB, which was provided by KODAK and implemented on the GeV-ESM, was measured experimentally from 71.3 to 1230 MeV by using the Booster to storage ring beam line (BTS) of the Advanced Light Source (ALS) at LBNL. The layout of ALS Facility is shown in Fig. 3.8. The calibration work has been carried out with the help of two internship students, Bas Fleskens and Pablo Gallegos, and detailed descriptions can be also found in their reports [176, 177].

3.4.2 Scintillation Process

The general process of scintillation is the absorption of ionizing radiation, such as x-rays or γ-rays, followed by the emission of radiation, usually in the visible range. Relativistic electrons ionize a material as well, consequently leading to the same photon emission process. The scintillating process can be simplified into a three-phase process.

1: **Ionization**

   An ionizing source (electromagnetic radiation or particles) deposits its energy onto an active material via ionization. As in Ref. [164], one may define absorption efficiency $\eta_{dps}(T)$ for this process. In case of an e-beam, there is a direct ionization
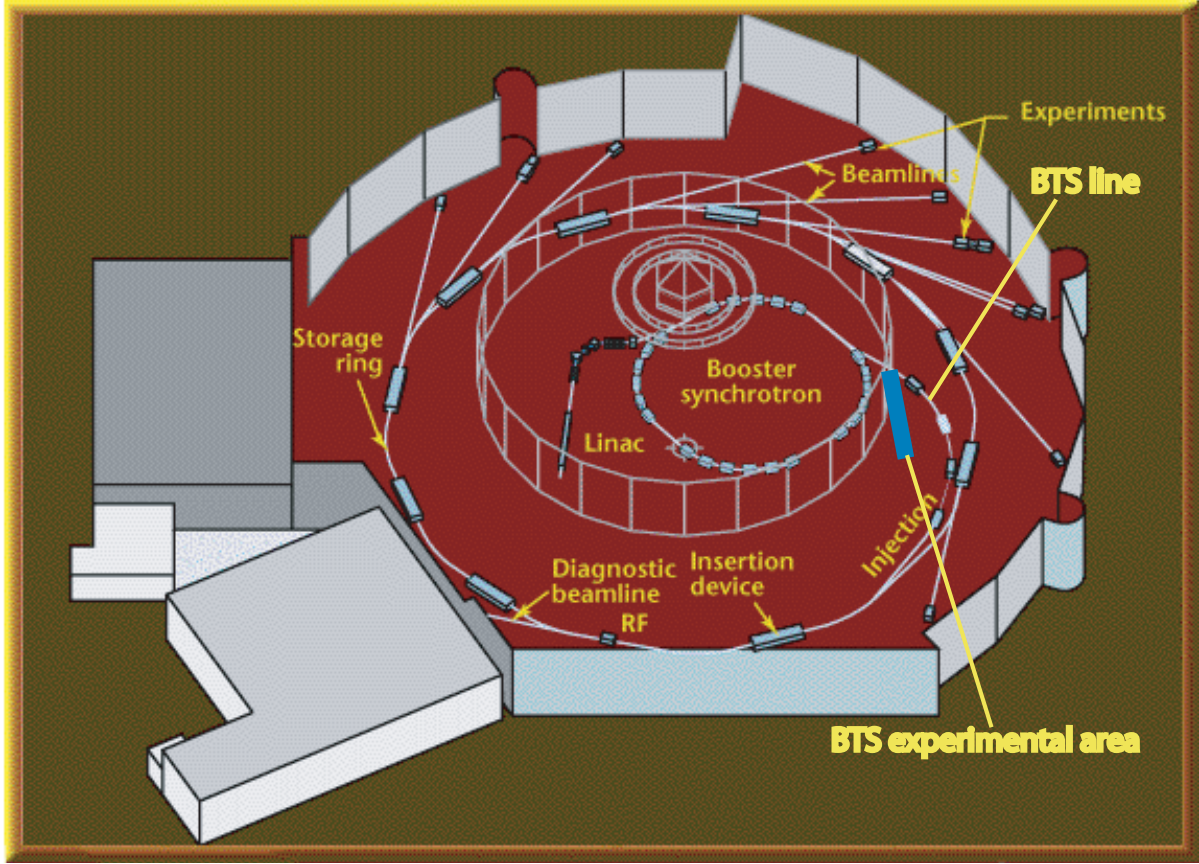
Figure 3.8: Layout of ALS building [105]. The beam line connecting Booster synchrotron and Storage ling is the Booster to Storage (BTS) beam line. BTS experimental are is located at the end of the extra beam line emerging from the middle of the BTS line (illustrated by blue line).

and also absorption of the Bremsstrahlung photons. Both mechanisms may show an energy dependence and could be evaluated via a Monte Carlo simulation.

2: **Non-radiative relaxation**

Excited electron may come back to the ground state, fall into one of the exciton bands, or into one of the metastable excited states without any photon emissions. Each process has a certain probability, which may show a dependence on an initial state of excited electron. Therefore, this process could depend on the input e-beam energy as well, and possibly on the pulse duration of the excitation pulse.

3: **Radiative relaxation**

Scintillating photons may be emitted via the recombination of electrons and holes

from exciton bands, the time scale of which is typically from tens of nanoseconds to several microseconds. Other photons may come from radiative relaxation of metastable states with their characteristic wavelengths, the time scale of which is from microseconds to several hours. The later process of emission is referred as phosphorescence or afterglow. If this emission is dominant, a material may be referred to as a phosphor screen instead of a scintillator. Radiative relaxation may be followed by non-radiative relaxation to a ground state. If one specifies a certain radiation band of interest, efficiency $\eta_{rad}(T)$ can be defined as the ratio of energies of radiative relaxation and non-radiative relaxation.

Shown in Fig. 3.9 is the emission spectrum from Gadox and other compounds from Ref. [168]. One can see that there are multiple emission bands in Gadox, and that the main emission is at $\simeq 545$ nm. The life time of the emitted light from LANEX-FB was measured to find an optimum exposure time for the experiments, as shown in Sectoin 3.4.4. Most of the light ($\simeq 80\%$) was observed earlier than 1 ms. There was, however, a substantial amount of light emitted later than 1 ms, suggesting non-negligible phosphorescent light. Since the time resolution of this experiment was longer than the typical life time of a scintillation, the dominant physics can not be determined from this slow time-resolution measurement. The fact that there are multiple excitation states and levels made rigorous theoretical modeling difficult and unpractical. The discussion of scintillator/phosphor material properties was beyond the scope of this dissertation. Here we focus on the experimental study of the energy dependence of the light yield.

By neglecting any energy dependence in $\eta_{rad}(T)$, one can provide a simple model in which the energy of emitted photons is proportional to the e-beam energy loss (deposition) in the material, as in Ref. [164]. In this model, the energy dependence only exists in the energy deposition process, but not in the relaxation and emission processes. One can numerically obtain the energy loss by using a Monte Carlo simulation [162, 164], or analytically [177] by using the Rorlich and Carlson formula [178], combined with the density correction [179]. The Rorlich and Carlson formula is:

$$-\frac{1}{\rho}\frac{dT}{dx} = \frac{\kappa Z}{2A_w\beta^2}\left\{\ln\left[\frac{(\gamma+1)T^2}{2I_{inz}^2}\right] + (1+\beta^2) - \frac{2\gamma-1}{\gamma^2}\ln(2) + \frac{1}{8}\left(\frac{\gamma-1}{\gamma}\right)^2\right\}, \quad (3.4)$$
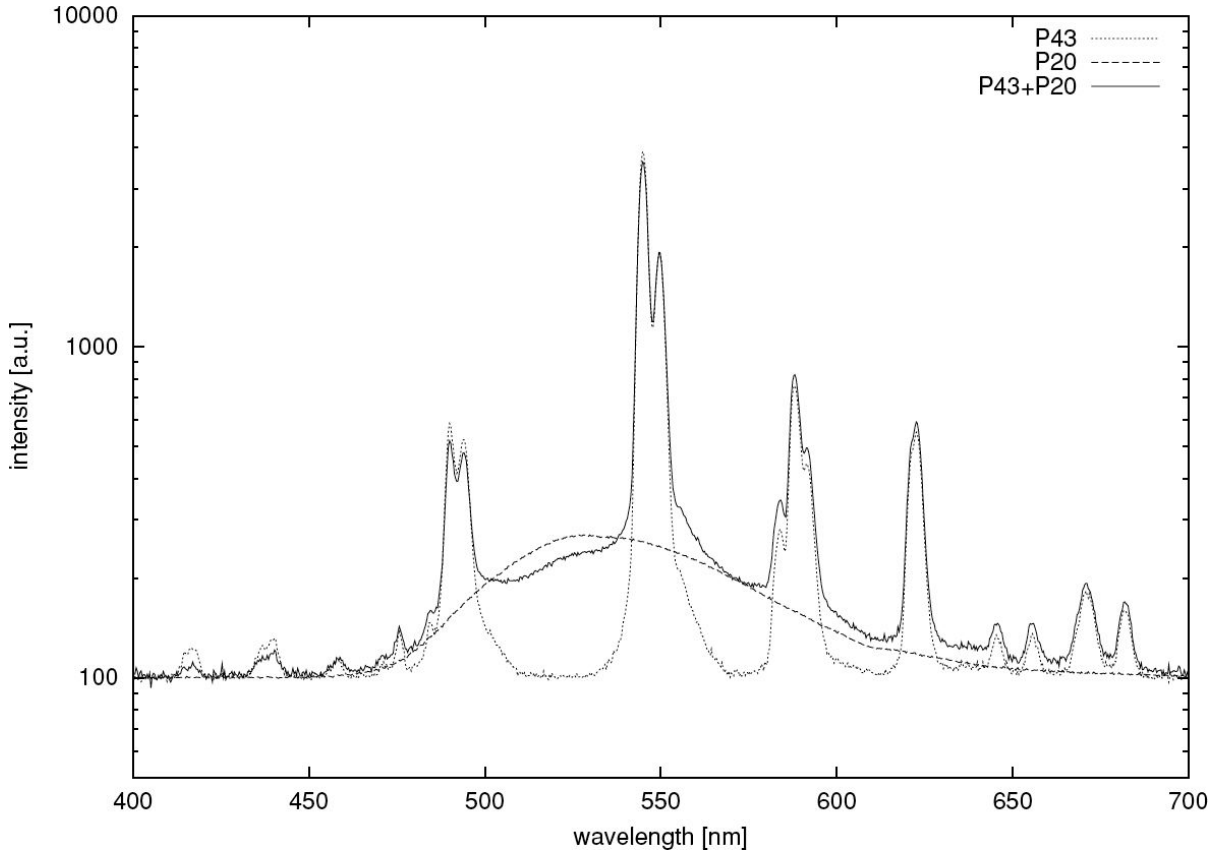
Figure 3.9:   Emission spectrum of the Gadox (dots) from Ref. [168]. Other two spectra (dashed line, straight line) are out of interest here.

where ρ is the density of the medium, $\kappa = 4\pi N_A r_e m_e c^2$ with N_A the Avogadro number, and $r_e = e^2/(m_e c^2)$ the classical electron radius, A_w the atomic weight of the medium, β the normalized electron velocity v_e/c, $\gamma = \sqrt{1 - \beta^2}$ the Lorentz factor, E the kinetic energy of incident electrons, and I_{inz} the mean ionization energy of the medium. This equation suggests that the ionizing energy loss increases in log scale along with an increase of the e-beam energy, while the radiative loss (Bremsstrtahlung) increases linearly. In other words, the analytical study suggests that the higher the e-beam energy, the more the e-beam deposits its energy onto a material.

Possible energy dependent physics and complications further motivated an experimental exploration of the energy dependence of the scintillating screens up to the GeV level. The energy of a bremsstrahlung photon can be high enough to cause electron-positron pair creation, which adds an additional complication in the scintillating processes. High

fluence from high charge e-beams or high instantaneous charge density from ultrafast e-beams could cause saturation effects of the scintillating processes, which cannot be studied by the Monte Carlo simulations.

3.4.3 Experimental Setup

The calibration experiments were carried out at the BTS at ALS. Originating from the ALS Linac (Linear Accelerator), a 50 MeV e-beam was injected into the Booster ring, and was further accelerated up to 1230 MeV. The e-beams were then extracted from the Booster ring by the kicker magnet system, a part of which is shown in Fig. 3.10. The total charge of the e-beams was variable via two methods. One was by changing the number of micro bunches in one macro pulse. The ALS Linac was able to provide a macro pulse containing from 1 to 3 micro bunches with a bunch to bunch separation of 8 ns [180]. The 8 ns separation came from the 125 MHz sub-harmonic buncher. The other method to vary the total charge was to control the charge in one micro bunch. By changing the gun bias voltage of the thermionic electron gun, which was the injector for the ALS Linac, the total charge in one micro bunch was controlled. Each micro bunch contained a total charge of up to 500 pC, and the pulse length at the exit of the Linac was around 8 ps (rms). Note that the lowest gun-bias voltage provided the highest total charge in a bunch. By changing these two parameters, a total charge in one macro bunch was varied from a few pC (limited by the ICT measurement) to 1500 pC. The micro bunch pulse length was stretched to $\gtrsim$ 20 ps at the exit of the Booster ring.

The energy of the e-beam was also variable. In normal operations, the kicker system extracted e-beams at the top of the magnets' current ramp, which gave the highest e-beam energy. By changing the timing and field strength of the kicker system, an e-beam with lower energy was extracted from the Booster ring. A part of the kicker system magnet and some magnets of BTS are shown in Fig 3.10. The detailed procedure to change the e-beam energy was as follows:

1: **Triggers**

The Bump magnet trigger τ_{bm} was scaled down from the nominal value $\tau_{bm1} = \tau_{bm0} \times p_t/p_n$, where p is the electron momentum, subscript n indicates nominal
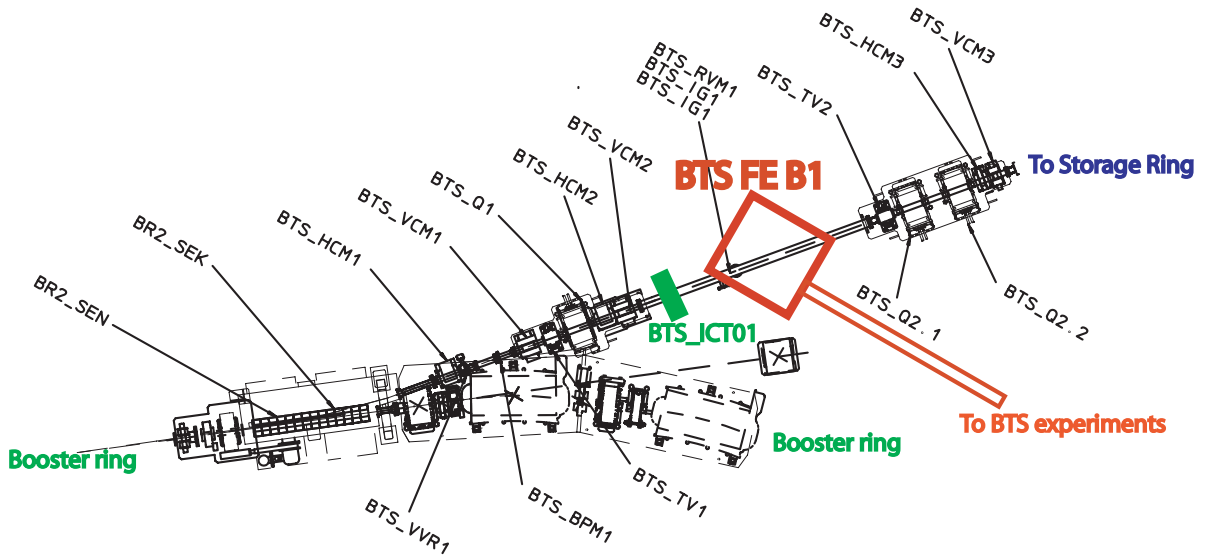
Figure 3.10: A part of the kicker magnet system of the Booster ring and a part of the BTS magnet system. Shown by a red rectangle is the location of the BTS-FE-B1 dipole magnet which was used to send e-beams to BTS experimental area. The other part of the kicker magnet system, namely the BR2- Bump1, Bump2, Bump3, and KE magnets sit further upstream of the Booster ring, and are not shown here. Note that this figure is based on the drawings obtained from the ALS website [105].

value, and subscript t for target value. Then the Extraction field trigger τ_{ext} was set to be $\tau_{ext1} = \tau_{bm1} + 2350$ μs.

2: **Currents for magnets**

The currents for the kicker magnets and a part of BTS magnets (upstream magnets before the BTS-FE-B1 magnet) I_k were scaled down to the target value given by $I_{k1} = I_{k0} \times p_t/p_n$. The kicker system consisted of the magnets BR2- Bump1, Bump2, Bump3, KE (they are not shown in Fig. 3.10), SEN, and SEK. The upstream BTS system consisted of the BTS- HCM2, VCM2, Q1 magnets. The BTS- HCM1 and HVM1 were not used at the experiments.

3: **Alignment of TV1 - TV2**

By fine tuning all the necessary magnets' applied currents, the e-beams were aligned on the middle of phosphor screens, the locations of which are indicated by TV1 and TV2 in Fig. 3.10, respectively. Note that those phosphor screens were not the targets for this calibration work. This alignment etablished the straight line from TV-1 to

TV-2, and hence allowed to evaluation of the e-beam energy via the applied current on the BTS-FE-B1 magnet, which sits in between those phosphor screens.

4: **BTS-FE-B1 magnet**

Set the current for BTS-FE-B1 magnet such that the e-beam can be seen on the middle of the LANEX-FB screen located at the end of the BTS beamline as shonw in Fig. 3.11. Together with Ref. [181], the applied current gave the energy of the e-beam.

The experimental setup for the calibration is shown in Fig. 3.11. E-beams were sent to the middle of the LANEX-FB screen, and the fluorescent light was observed by an identical CCD camera as that used in the GeV-ESM, 12-bit Flea high resolution model from Pointgrey [167]. The elliptical screen (9.5 cm height and 8.0 cm width) was arranged at a 45 degree to the e-beam incident angle, and backed by a $\simeq 40 \mu$m thick Al foil as in the GeV-ESM. In this calibration experiment, an Al foil was not necessary because there was no stray laser lights as in the LOASIS LWFA experiments. In order to realize an identical e-beam - LANEX-FB interaction in this calibration experiments, an Al foil was installed. The angle of screen affects actual e-beam - active-layer interaction length,
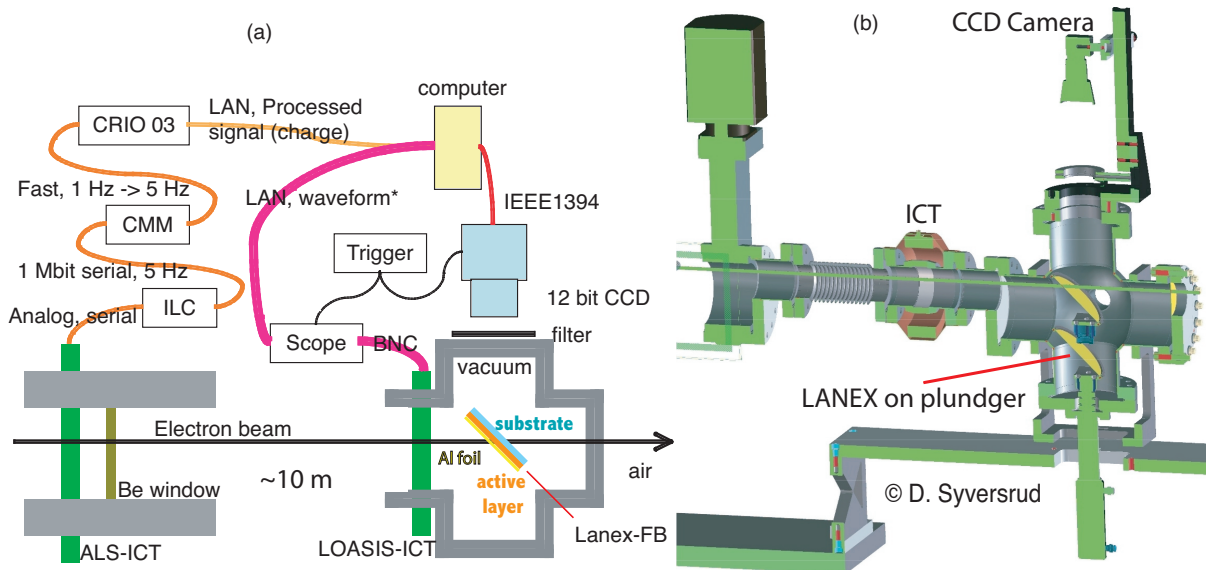
Figure 3.11: Schematic (a) and drawing (b) of the BTS experimental setup. A picture taken by the CCD camera, the raw signal from the LOASIS-ICT, and the processed signal from ALS-ICT, were recorded by a computer.

and the angle of the CCD Camera to the screen also affects collection of light, following the Lambertian law [164, 177]. For data analysis, these effects were taken into account. The beam tube clearance was 5 cm (diameter). As shown in Fig. 3.11(a), the screen was arranged in an irregular way, namely the substrate side was observed by the CCD camera. Since the substrate was not completely opaque, the fluorescent light was still observed. Attenuation of 80% (20% transmission) was observed relative to the measurement done in the regular orientation (see Fig. 3.18(b)). The potential advantage of this arrangement was in the momentum acceptance. Low energy ($<$ 1 MeV) e-beams may be blocked by the substrate in case of the regular orientation. The irregular orientation may allow to measure lower energy e-beams, and heavy particles such as protons. Therefore, the LANEX-FB was installed in an irregular way on the GeV-ESM.

Employed for the calibration reference was an ICT-122-070-05:1 (LOASIS-ICT) [182], from BERGOZ Instrumentation [183]. This low-ratio (high sensitivity) ICT, combined with a regular oscilloscope, allowed detection with a signal to noise ratio (S/N) of $\simeq 2$ for a few pico Coulomb charge (higher S/N ratio for $> \sim$ pC). Raw waveforms were recorded on the computer through LAN-based communication. Also recorded were processed signals from one of the permanently installed ICTs on the ALS, BTS-ICT01 (ALS-ICT), whose location is illustrated in Fig. 3.10(a). The raw signal from this 20:1 ratio ICT was first sent to the beam charge monitor (BCM), then to an EPICS (Experimental Physics and Industrial Control System [184]), and the processed value (charge) was broadcasted through the network at ALS. The background level of the broadcasted values was ($\simeq 10$ pC) because the electronics were optimized for nominal operation, where the total charge was more than 1000 pC. The LOASIS-ICT and ALS-ICT showed good agreement for high energy (small beam size), high charge ($\simeq 500$ pC, one micro bunch) measurements. Since the ALS ICT was located at $\simeq 10$ m away from the screen, any beam loss during beam transport was not detectable from this ICT. Therefore the calibration was performed against the LOASIS-ICT, and in the following part of the dissertation, "the ICT" indicates the LOASIS-ICT and "measured charge" means the charge measured by that ICT unless otherwise specified.

3.4.4 Results and Discussion

The life time of the emitted light from LANEX-FB was measured by changing the trigger delay for the CCD camera in 1 ms steps, with a fixed exposure time $\Delta t_{exp} = 1$ ms. The energy of the e-beams was 1230 MeV in 3-micro bunch mode and with the lowest gun-bias voltage. The number of total counts on the CCD (CCD counts) normalized by the measured charge versus the trigger delay is shown in Fig. 3.12. Here, the trigger delay = 0 was set 1 step (ms) before the CCD camera started to see any signal. One can see that more than 99% of the total counts (emitted light) was within 4 ms, confirming that long-lifetime (> 10 ms) metastable levels did not contribute a substantial portion of the emitted light. All the measurements presented later in this Section were performed with a fixed exposure time $\Delta t_{exp} = 10$ ms starting at 1 ms before the arrival of the beams (0 delay point in Fig. 3.12). The repetition rate of the operation was 0.5 Hz, therefore no interference between shots was expected.

The energy dependence was studied by using 1230, 1000, 712, 497, 377, 261, 143 and 71.3 MeV e-beams. With each energy, a broad range of total charge was scanned
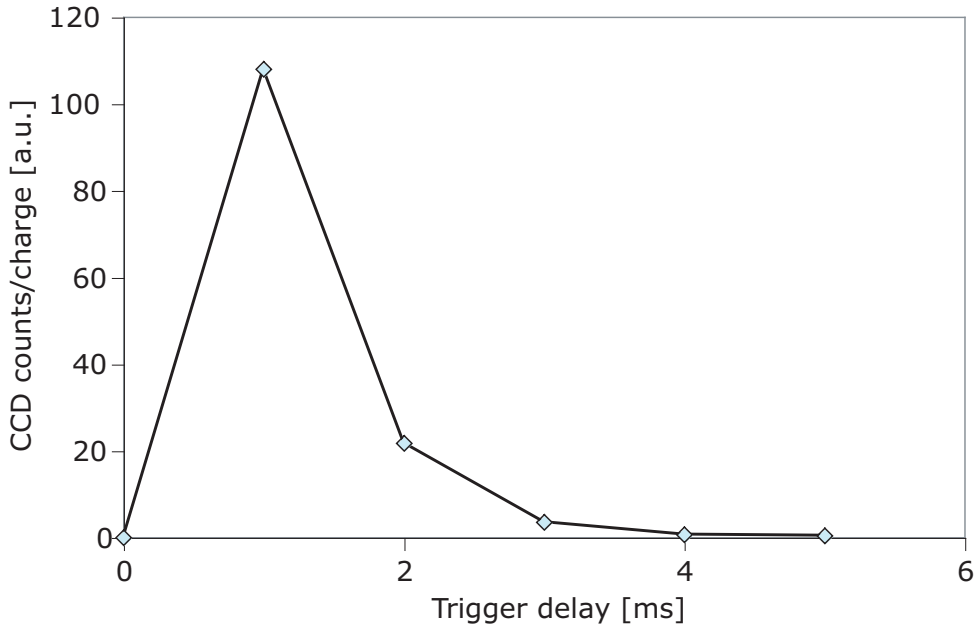
Figure 3.12: Measured life time of the light emitted by the LANEX-FB. About 30 shots were taken for each point. The errorbars (standard deviation σ) were not visible on the plot (fluctuation $= 100 \times \sigma/\text{mean} < 1.5\%$). Note that the measurements did not resolve less than 1 ms.

by varying the gun-bias and using 1- and 3- micro bunch modes. For all the different energies, plots of the CCD counts versus the measured total charge by the ICT are shown in Figs. 3.13–3.16. Also shown as black solid lines in Figs. 3.13–3.16, are the results of linear fitting. The detailed fitting conditions are stated in the captions of figures. The quality of the fit was evaluated by the mean of the normalized deviation $\hat{\epsilon}$:

$$\hat{\epsilon} = \frac{1}{g} \sum^{g} \frac{|\mathrm{CCD}_i - f(\mathrm{ICT}_i)|}{f(\mathrm{ICT}_i)} \ , \tag{3.5}$$

where g is the number of samples, CCD_i is measured CCD counts of the i-th sample, $f(x)$ is a CCD counts predicted by fitting the charge measured by the ICT, and ICT_i is a measured charge by the ICT. One can see that the linear coefficients for the ratio of the CCD counts and the measured charge (counts/charge coefficient, CC-coefficient) showed dependence on the e-beam energy. Non-linearity between the CCD counts and measured charge (counts - charge non-linearity, CC non-linearity) was also observed in 1230, 1000, 712, 143 and 71.3 MeV scans.

A linear relation between the CCD counts and measured charge was observed for the scans with e-beam energies of 497, 377, and 261 MeV. For those scans, the linear fitting
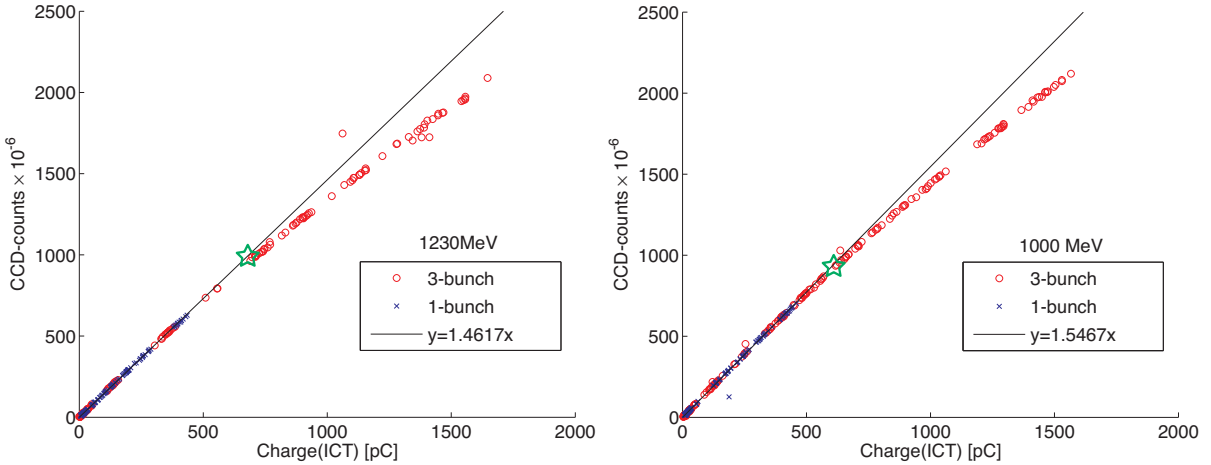
Figure 3.13: The total number of counts on the CCD camera (CCD counts) versus the charge measured by the LOASIS-ICT with beam energy of 1230 MeV (a) and 1000 MeV (b). Shown by the black solid line is the linear fit with acquired data below 500 pC. The quality of the fittings are 4.5% for (a) and 4.6% for (b), respectively. The green star was placed where the measured point started to deviate from fitted line. The charge density where the star is placed is 60 pC/mm² for (a), and 50 pC/mm² for (b).
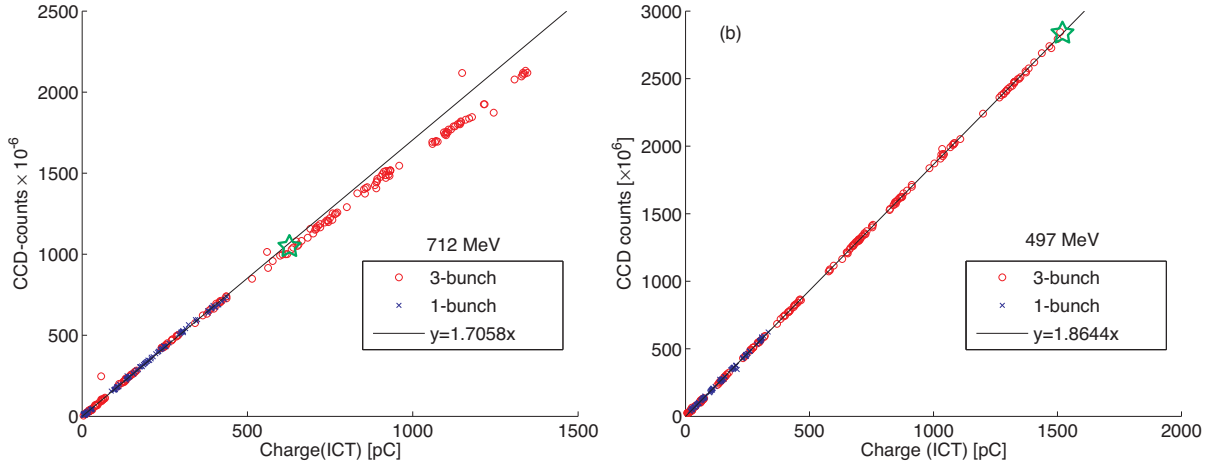
Figure 3.14: The total number of counts on the CCD camera (CCD counts) versus the charge measured by the LOASIS-ICT with beam energy of 710 MeV (a) and 500 MeV (b). Shown by the black solid line is the linear fit with acquired data below 500 pC for (a), and with all the data for (b). The quality of the fittings are 7.3% for (a) and 3.8% for (b), respectively. The green star was placed where the measured point started to deviate from fitted line for (a), and where the maximum charge density was achieved for (b). The charge density where the star is placed is 32 pC/mm^2 for (a), and 27 pC/mm^2 for (b). Due to smaller beam size for lower energy, the maximum charge density was smaller for lower energy beams.

was done by using all the data points acquired.

In the Booster ring, adiabatic cooling and radiation damping occurs along with the acceleration. This results in the higher energy beam having lower emittance (smaller beam size and divergence) than the lower energy beams. For a detailed description of the emittance evolution during the acceleration in the Booster ring, see Ref. [185], Chapter 4. The typical beam size on the screen for each energy is shown in Fig. 3.17(a), with the lowest gun-bias voltage and 1-bunch mode. For the scans with e-beam energy of 143 and 71.3 MeV, beam losses were observed between the ALS-ICT and the LOASIS-ICT, most likely due to the e-beam overfilling of the beam line tube (beam was clipped by the tubes). From Fig. 3.16, one can see that the highest charges measured by the ICT were lower than 1500 pC for those low energy scans. The observed non-linearities for 143 and 71.3 MeV e-beams could be explained by beam loss during the propagation between the ICT and the scintillating screen. The BTS beam line was designed for the transportation of a 1500 MeV e-beam. As shown in Fig. 3.17(b), for a 143 MeV beam, the beam area increased
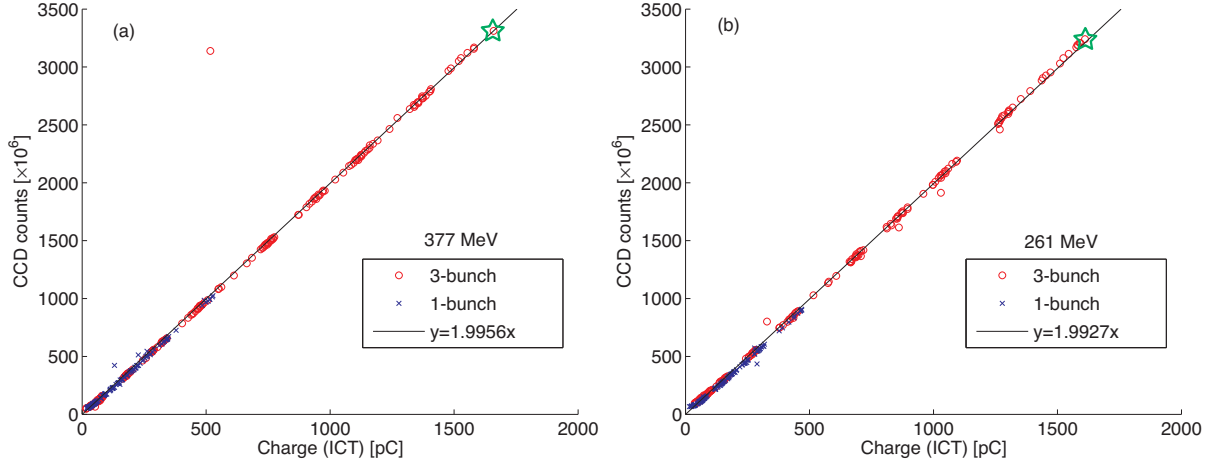
Figure 3.15:   The total number of counts on the CCD camera (CCD counts) versus the charge measured by the LOASIS-ICT with beam energy of 377 MeV (a) and 261 MeV (b). Shown by the black solid line is the linear fit with all the acquired data. The quality of the fittings are 5.4% for (a) and 7.8% for (b), respectively. The green star was placed where the maximum charge density was achieved. The charge density where the star is placed is 14 pC/mm² for (a), and 8 pC/mm² for (b).
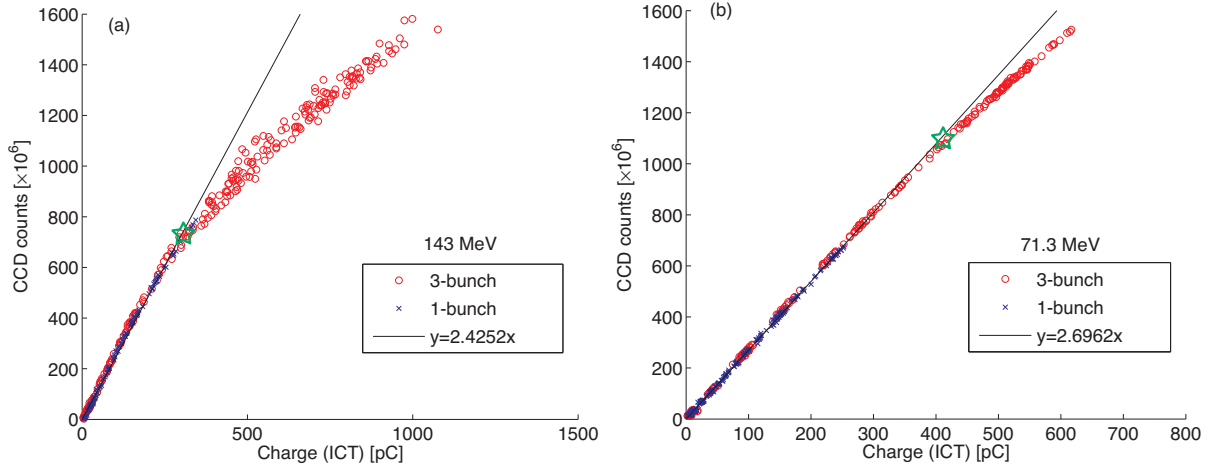
Figure 3.16:   The total number of counts on the CCD camera (CCD counts) versus the charge measured by the LOASIS-ICT with beam energy of 143 MeV (a) and 71.3 MeV (b). Shown by the black solid line is the linear fit with data below 250 pC for (a), and below 400 pC for (b). The quality of the fittings are 15% for (a) and 6.2% for (b), respectively. The green star was placed where the measured point started to deviate from fitted line. The charge density where the star is placed is 0.7 pC/mm² for (a), and 0.5 pC/mm² for (b).
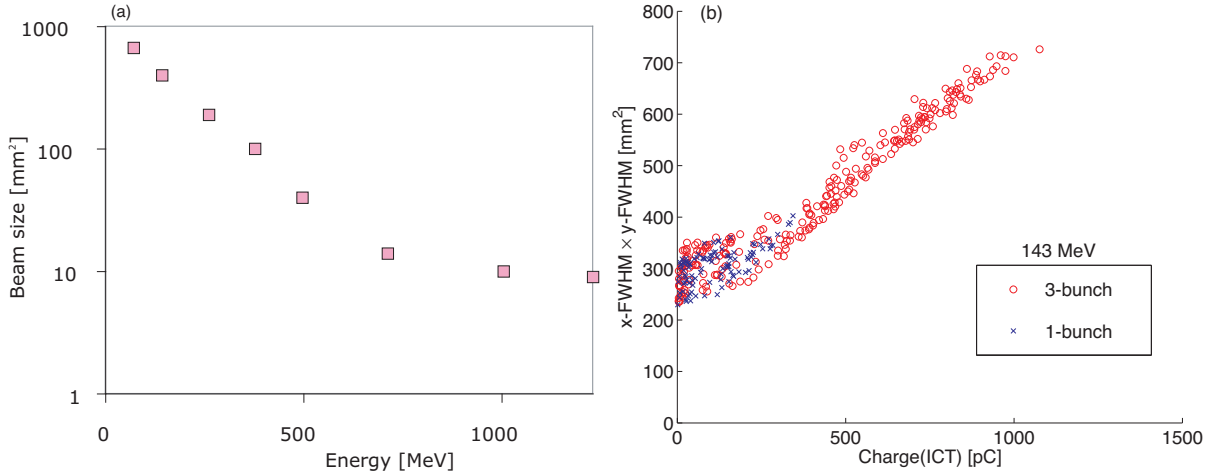
Figure 3.17: (a): the beam size on the scintillator screen versus the energy of the e-beam. The beam size was measured with the lowest gun-bias voltage (highest charge) and 1-bunch mode. (b): the beam area at the scintillating screen versus the charge measured by the ICT with the e-beam energy at 120 MeV. The beam area was defined as the product of the x width and y width in full-width half-maximum (FWHM).

considerably with charge. From 400 pC to 1000 pC, beam area became two times larger. A similar increase in area was observed when scanning the 71.3 MeV e-beam charge from 300 pC (650 mm^2) to 600 pC (850 mm^2). If this is the case, the amount of beam loss is to be proportional to $(r_{beam}^2 - r_{tube}^2)$, where r_{beam} is the FWHM radius of the beam at the screen, and r_{tube} is the inner radius of the beam transporting tube, or ICT. Although whole beam was not measured due to the clipping, evaluation with FWHM would give unclipped beam size. The beam loss in terms of CCD counts was estimated from the deviation from the fitted line [see Fig. 3.16(a)], and plotted versus the measured beam area [see Fig. 3.17(b)] in Fig. 3.18. One can see that the beam loss increased linearly against the measured beam area after the area became bigger than the beam tube area. This is consistent with the model for the beam loss suggested here. For low energy scans, the CCD CC coefficients were deduced from the fitting of the data points below 250 pC.

A non-linearity in CC-coefficient was also observed for the scans of 1023, 1000, and 712 MeV. There was no beam loss between the ICT and scintillating screen as the beam sizes were small enough for the whole beam to be accommodated within the screen. There are two possible scenarios which may introduce this non-linearity. One is a saturation effect of the scintillating material. The excessively high population of the excited level

may have caused these deviations from the linear response against the incident e-beam charge. In this case, this behavior may show a dependence on the peak intensity of the emitted light. The other one is an opacity change of the substrate or coatings due to the high density e-beam load on a material, which caused ionization of the material or thermal loading. If this is the case, this behavior may show a dependence on the peak charge density on the screen and/or the e-beam energy. By carrying out the same measurement with different orientation of LANEX-FB, one can tell whether the non-linearlity was caused in the active layer or substrate. Shown in Fig. 3.18(b) is the CCD counts versus the measured total charge with the regular orientation of the LANEX-FB (active layer surfacing to the CCD camera). A linear relation between the CCD counts and measured charge was obtained. This suggests that the nonlinearity observed with the scans of 1023, 1000, and 712 MeV was not from the saturation of the active material, but was somehow caused by the substrate. As discussed, this may depend on the peak charge density on the screen and/or the e-beam energy. Shown by the green star in Figs. 3.13 – 3.16 is where the measured point started to deviate from fitted line, or where
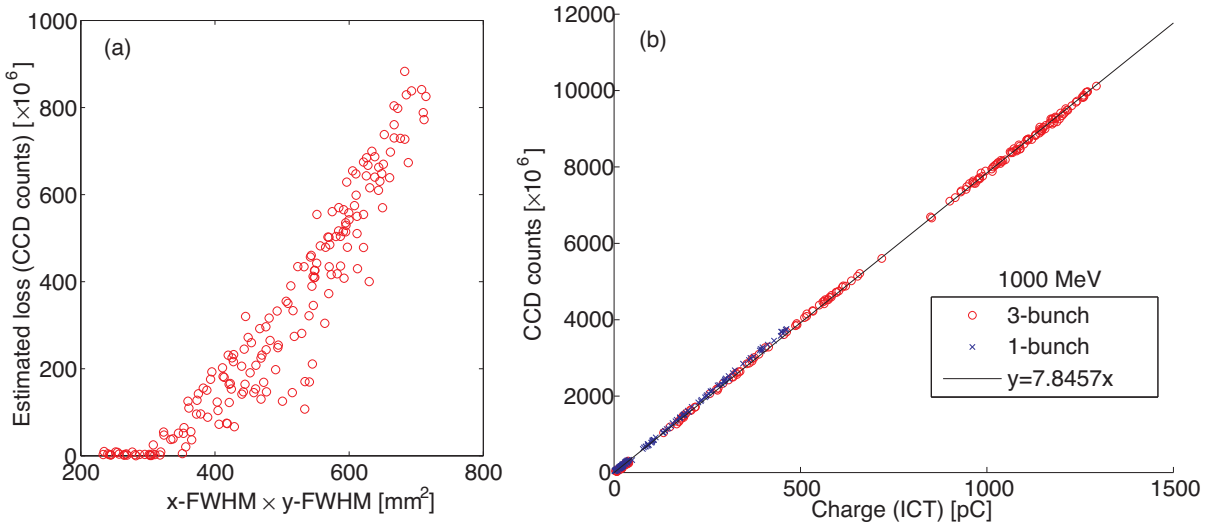
Figure 3.18:   (a): Beam loss size in terms of CCD counts against the beam area. The beam loss was estimated by the difference between the fitted value and measured CCD counts [Fig. 3.16(a)]. The measured beam size is from Fig. 3.17(b). (b): The total number of count on CCD camera (CCD counts) versus the charge measured by the LOASIS-ICT with beam energy of 1000 MeV. For only this plot, the orientation of the LANEX-FB was regular (active layer surfacing to the CCD camera). Shown by the black solid line is the linear fit with all the acquired data.
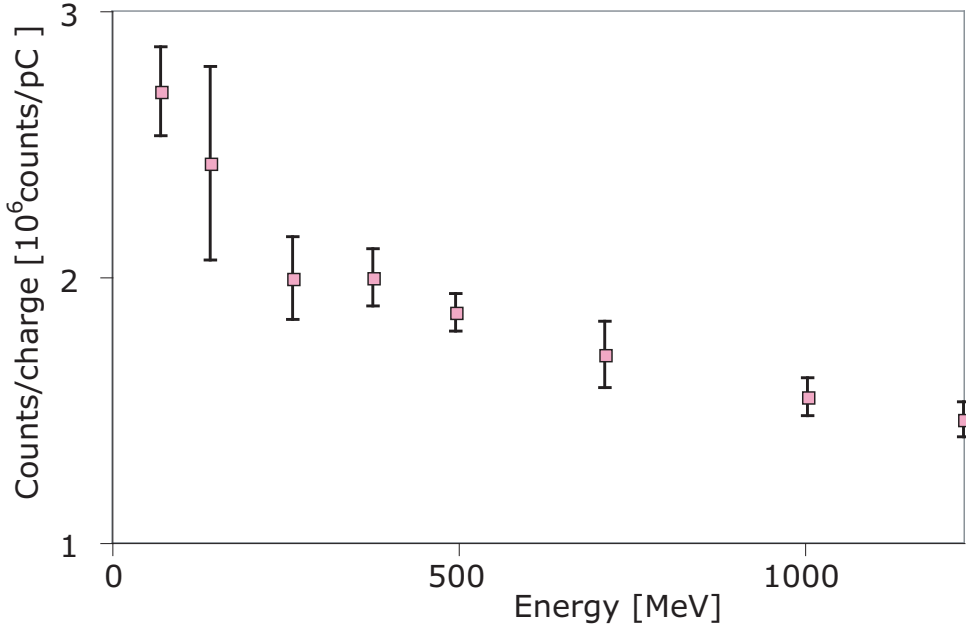
Figure 3.19: The CC-coefficient versus e-beam energy. The errorbar comes from the fitting quality evaluated by Eq. (3.5). Average fitting quality was 6.8%.

the maximum charge density was measured. From the scans of 1023, 1000, and 712 MeV, the charge densities where the measured point started to deviate from fitted line were, 60, 50, and 32 pC/mm², respectively. The threshold of this non-linearlity may depend on both the charge density and e-beam energy. For these three high energy scans, the linear fitting was done by using the data below 500 pC.

The CC-coefficient versus e-beam energy is shown in Fig. 3.19. The trend of lower CC-coefficient for higher energy e-beam is observed. This is counter to what is suggested by Eqn. 3.4 and the assumption of no energy dependence in the relaxation and emission processes. This suggests that there might be an energy dependence in these processes, which is fairly complicated to model theoretically or to study with numerical simulations. Shown by errorbars in Fig. 3.19 is the quality of fittings evaluated by Eq. (3.5). The mean fitting quality for whole scans were 6.8%, and this value is used as the accuracy of this calibration.

Although the CC linearity was verified below a charge density of 50 pC/mm² for 1000 MeV e-beams, there is a critical difference between the e-beams from an LWFA and a RF-accelerator. The longitudinal structure of e-beams used for this calibration was a

macro bunch containing up to three micro bunches with a separation of 8 ns, and a micro bunch duration of $\simeq$ 20 ps (rms). This duration is far longer than the that of e-beams from LWFAs typically $\lesssim$ 50 fs [98]. The question would be whether the response stays linear for femto-second e-beams or not. Considering the saturation effect observed from 1000 MeV e-beam scan (see Fig. 3.13(b)), the CC non-linearity was observed only from 3-bunch mode. The fact that both 1-micro bunch beam and 3-micro bunch beam had the same peak instantaneous charge intensity (pC mm^{-2} s^{-1}) may lead to the conclusion that the non-linearity observed there was not from the instantaneous charge intensity but from the accumulative amount of charge (pC mm^{-2}) on a macro bunch scale ($\sim$ 17 ns). For 1000 MeV e-beams, the linearity up to 50 pC/mm^2 in $\sim$ 17 ns (full width) was confirmed, as well as for an instantaneous charge intensity, up to 2 pC mm^{-2} ps^{-1}. This instantaneous charge intensity is equivalent to an e-beam with charge flux of 20 fC/mm^2 in 10 fs (rms), which gives total a charge of 2 pC with a beam size of 100 mm^2 on a screen.

3.4.5   Calibration Summary

The calibration of the LANEX-FB screen (substrate facing the camera) was performed with e-beams energy ranging from 71.3 to 1230 MeV experimentally at BTS, ALS. The accuracy of the calibration was 6.8%. The CC-coefficient showed energy dependence, with the tendency that higher energy produced lower light yield. The CC-linearity was confirmed below 50 pC/mm^2 in 17 ns with 1000 MeV e-beam. Due to the possible energy dependence of the threshold charge density for non-linear behavior, this threshold charge density is unknown for the e-beams with the energy lower than 712 MeV because high enough beam density was not obtained. The measured threshold charge density for non-linear behavior, and the charge density where linear behavior was confirmed, are plotted in Fig. 3.20 on the left vertical axis. Note that this is for the accumulative charge density saturation effect in $\sim$ 17 ns (full width) range. The linearity against the instantaneous charge intensity was experimentally verified against e-beam with 2 pC mm^{-2} ps^{-1} for 1000 MeV case, where the time ps is the rms width of the e-beam time duration. Shown in Fig. 3.20 on right vertical axis is the instantaneous charge intensity [pC/(ps mm^2)] where the linear response of a LANEX-FB was experimentally verified. Note that instantaneous charge density non-lineariry was not observed from the experiments. The thresholds for
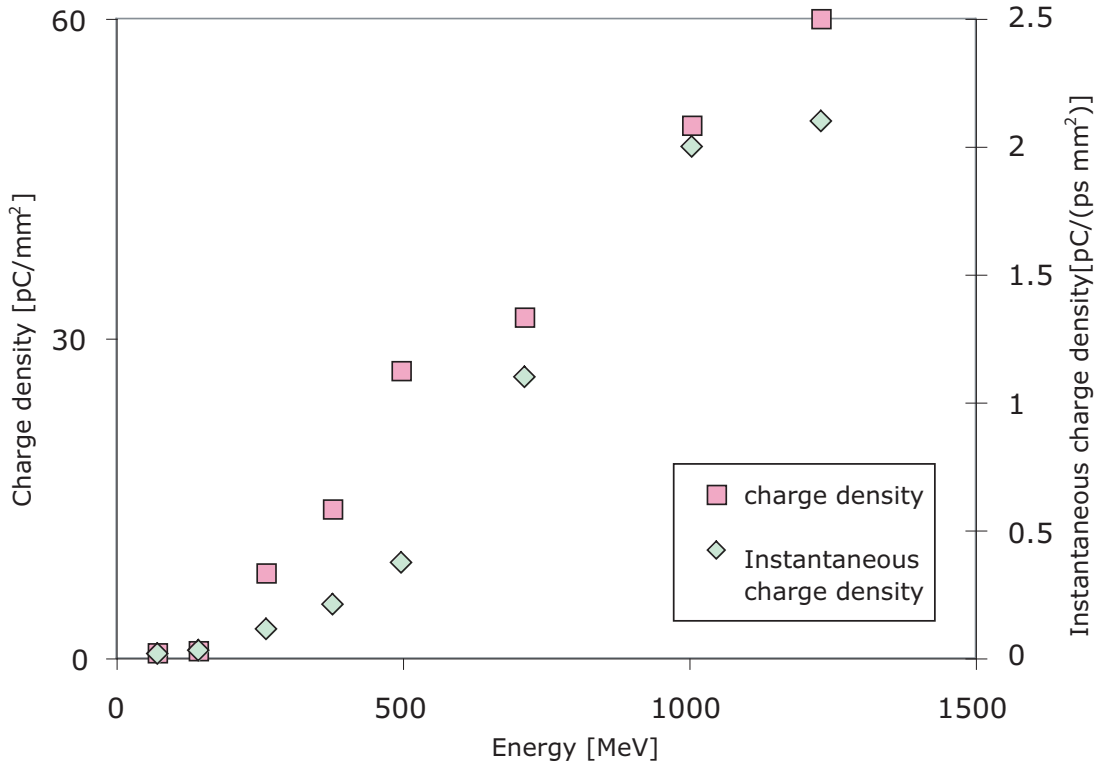
Figure 3.20: Charge density (in ~ 17 ns) for which linear response of LANEX-FB was experimentally verified (left axis), and the instantaneous charge intensity for which linear response of LANEX-FB was experimentally verified.

accumulative non-linearity need to be taken into account in the operation of the GeV-ESM.

The ALS calibration measurements provided more than one order lower light-charge factor than that obtained from the calibration used a LWFA e-beam [186]. Since the results of ALS calibration was used in this dissertation, one may find discrepancy in total charge between the published papers [1, 2] and this desseration. As has been discussed, an instantaneous intensity of the ALS e-beam was not as high as that of LWFA. Therefore, there is a possibility that the ALS calibration underestimated beam charge. In order to provide more accurate calibration, one can arrange activation experiments [42]. The material activation may not depend on an instantaneous intensity of e-beam, it can provide intensity independent result. In this dissertation, the results of ALS calibration was used for evaluations. The calibration results including the thresholds for non-linear behavior, were implemented on the GeV-ESM analysis program, and have enabled the GeV-ESM

to function as a charge monitor.

3.5   Experiments

In this Section, examples of single-shot beam measurements and analysis are presented. Experiments were performed using a high peak power 10Hz Ti:sapphire laser system of the LOASIS Facility at LBNL and a gas-filled capillary discharge waveguide developed at Oxford University [1, 2] as described in Chapter 4.

Shown in Fig. 3.21 (a) is an example of a moderately resolved high energy e-beam. A quasi-monoenergetic beam with the peak energy of 778^{+39}_{-31} MeV, and total charge of 3.3 pC was observed. As stated in Section 3.3, the estimated error range of the absolute energy value was computed from the beam angular fluctuation σ_{x1peak}, and found to be ± 0.38 mrad. The beam divergence was found to be ± 2.5 mrad (rms), which gave a resolution of 2.5% at 778 MeV. The energy spread was measured to be $\pm 4.6\%$ (rms). The maximum charge density on the LANEX-FB was < 0.07 pC/mm^2 at ~ 780 MeV, which was well below the threshold for accumulative saturation effect. With an assumption of a 10 fs e-beam bunch duration, the instantaneous charge intensity is estimated to be 7 pC mm^{-2} ps^{-1}. This is above the value for which the liner response of LANEX-FB was experimentally verified.

Shown in Fig. 3.21 (b) is an example of a finely resolved quasi-monoenergetic e-beam. Applied magnetic field was 1.14 T, which gave momentum acceptances from 0.009 to 1.0 GeV. A quasi-monoenergetic beam with the peak energy of 364^{+9}_{-7} MeV, and total charge of 3.3 pC was observed. The beam divergence was found to be ± 1.3 mrad (rms), which gave a resolution of 0.55% at 364 MeV. The energy spread was measured to be $\pm 5.0\%$ (rms). The maximum charge density on the LANEX-FB was < 0.04 pC/mm^2 at ~ 360 MeV, which was well below the threshold for accumulative saturation effect. With an assumption of 10 fs e-beam bunch duration, the instantaneous charge intensity is estimated to be 4 pC mm^{-2} ps^{-1}. This is above the value for which the liner response of LANEX-FB was experimentally verified.

Shown in Figs. 3.21 (c) is an example of a finely resolved broadband e-beam. Applied magnetic field was 1.14 T, which gave momentum acceptances from 0.009 to 1.0 GeV. A broadband e-beam (from 10 to 450 MeV) with 42 pC total charge was observed. The
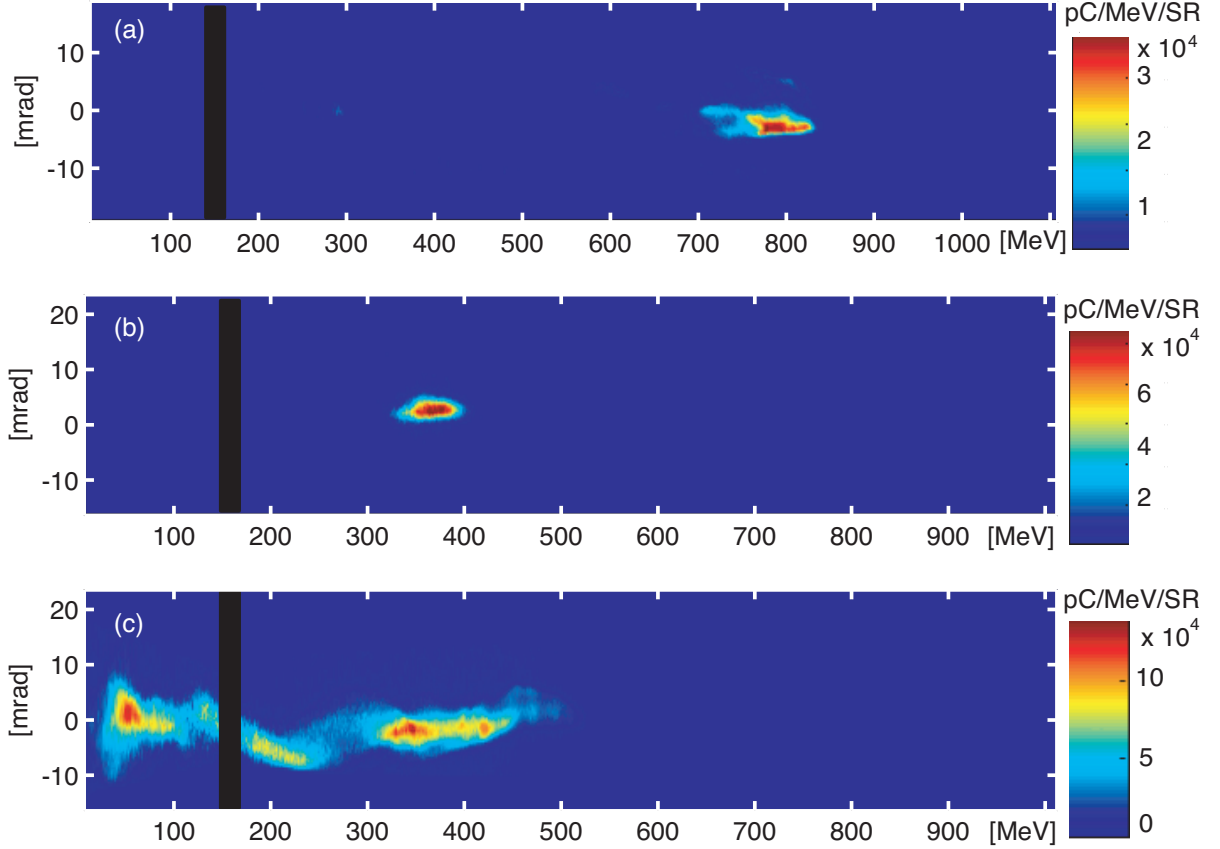
Figure 3.21: Spectra observed by the GeV-ESM. (a): A moderately resolved high energy e-beam. The peak e-beam energy of 778^{+39}_{-31} MeV, the energy spread of 4.6% (2.5% resolution), and total charge of 3.3 pC were observed. The maximum charge density on the LANEX-FB was < 0.07 pC/mm^2. (b): A finely resolved quasi-monoenergetic e-beam. The peak e-beam energy of 364^{+9}_{-7} MeV, the energy spread of 5.0% (0.55% resolution), and total charge of 3.3 pC were observed. The maximum charge density on the LANEX-FB was < 0.04 pC/mm^2. (c): A finely resolved broadband e-beam. A broadband e-beam (from 10 to 450 MeV) with 42 pC total charge was observed. The maximum charge density on the LANEX-FB was < 0.05 pC/mm^2 at the energy of 300 MeV.

maximum charge density on the LANEX-FB was < 0.05 pC/mm^2 at ~ 300 MeV, which was well below the threshold for accumulative saturation effect. With an assumption of 10 fs e-beam bunch duration, the instantaneous charge intensity is estimated to be 5 pC mm^{-2} ps^{-1}. This is above the value for which the liner response of the LANEX-FB was experimentally verified.

As can be seen from examples, the maximum charge density on the LANEX-FB was well below the threshold for accumulative saturation effect in regular operations. But

the instantaneous charge intensity was usually higher than the value for which the linear response of the LANEX-FB was experimentally verified. Although this kind of non-linear behavior was not observed in the experiments, there remains a possibility of underestimation of total charge as discussed in Section 3.4.5. In the following part of the dissertation, it is assumed that no saturation phenomena occurred caused by a high instantaneous charge intensity.

A discussion on the dependence of the CDG-LWFA performance on laser-plasma parameters is presented in the next Chapter. Note that the simultaneous diagnoses of laser output spots were successfully carried out for all measurements [1, 2].

3.6   Summary

A broadband, slitless, single-shot ESM for a GeV-class LWFA beam measurement has been developed. A scintillator-camera based system was employed for relativistic e-beam detection for high repetition rate experiments. The spectrometer covered from 0.01 to 1.1 GeV in a single shot, provided capability for simultaneous measurement of e-beam spectra and output laser properties due to the absence of a slit. The design provided an unprecedentedly large momentum acceptance of a factor 110 with reasonable resolution (below 5%). The design concept and hardware implementation were described, as well as the detailed analysis of the spectrometer performance. The calibration of the scintillating plate, LANEX-FB was performed at BTS of ALS. The e-beam energy dependence of the LANEX-FB at energy ranging from 71.3 to 1230 MeV was experimentally explored. The linearity of the response of the LANEX-FB was discussed. As shown in the Section 3.4, a single shot measurement with sufficient resolution and angular acceptance was demonstrated. The spectrometer design provides a powerful diagnostic tool for the research and development of next generation LWFAs. The followings were the achieved performance characteristics of the GeV-ESM.

- **Momentum acceptance**

  The spectrometer covers from 0.01 to 1.1 GeV in a single shot.

- **Momentum resolution**

  The resolution is below 5% for e-beams with a divergence of 2 mrad over the whole

energy range. Less than 1% resolution is achieved for e-beams with small beam divergence and moderately high energy ($\sim$ 500 MeV). The resolution depends on the beam divergence due to the slitless scheme.

- **Angular acceptance**

  An angular acceptance of more than $\pm$ 10 mrad is achieved over almost the whole range. This is large enough to capture an entire e-beam as shown in Section 3.5.

- **Repetition rate**

  A nominal repetition rate of 1 Hz operation is achieved. In theory, 10 Hz operation is possible by adding computers.

- **Charge monitor**

  Calibration has been performed by using a conventional accelerator. The GeV-ESM provides the function of a charge monitor with an accuracy of 6.8%.

- **Simultaneous diagnosis of guided laser properties**

  The simultaneous observation of guided laser properties was successfully achieved.

- **System dimension**

  The system is compact enough to be implemented in the LOASIS experimental cave.

Chapter 4

Capillary Discharge Guided LWFA

4.1 Introduction

Over the past decade, acceleration gradients in the tens to hundreds of GV/m have been generated in laser wakefield acceleration (LWFA) experiments, which are three orders of magnitude higher than in conventional linear accelerators (linacs, see Chapter 1). Although it was straightforward to achieve such high acceleration gradients in laser wakefield accelerators, the e-beams from such accelerators had 100% energy spread until 2004, when the production and measurements of high quality (i.e., low energy spread) 100 MeV class e-beams were reported [56–58]. To obtain the mono-energetic bunches, two groups used relatively large laser spot sizes [57, 58]. This effectively increased the diffraction (or Rayleigh) range Z_R of the laser beam, permitting propagation over distances on the order of the gas jet length. For example, experiments performed at the Rutherford Appleton Laboratory (RAL) by Mangles *et al.* employed a 16 TW, 40 fs laser pulse focused (25 μm spot size, 2.5×10^{18} W/cm^2) on the plume of a gas jet with a plasma density of 2×10^{19} cm^{-3}. A narrow energy spread bunch was observed at 78 ± 2 MeV with 20 pC of charge [57]. Experiments performed at the Laboratoire d'Optique Appliquée (LOA) by Faure *et al.* used a 30 TW, 33 fs laser pulse focused [21 μm spot size in full-width at half-maximum (FWHM) 3.2×10^{18} W/cm^2] on the plume of a gas jet with a plasma density of 6×10^{18} cm^{-3}. A narrow energy spread bunch was observed at 170 ± 20 MeV with 500 ± 200 pC of charge [58].

The Lawrence Berkeley National Laboratory (LBNL) experiments [56] used a 9 TW,

55 fs laser pulse focused to a relatively tight spot size (8.5 μm FWHM). As discussed in Chapter 1, to mitigate the short Z_R of the beam, a 2 mm long laser produced preformed plasma channel was used to guide the laser beam through the gas jet. The driving laser beam generated 85 MeV e-beams containing 0.3 nC bunch charge, with only 9 TW of laser peak power. Not only those experiments, but also scaling laws and the simulation shown in Chapter 1.2 suggested a higher efficiency in a guided LWFA scheme.

The plasma channels in the LBNL experiments [56] were produced using the ignitor-heater concept [115] and were shown to guide laser pulses with relativistic intensities ($> 10^{18}$ W/cm^2) over $\sim$ 10 Rayleigh lengths. The method relied on rapidly heating a laser-ionized filament using inverse Bremsstrahlung, in which the electrons oscillating in the laser field undergo collisions with ions, transferring part of their oscillation energy into thermal energy [114, 115, 187]. This heating can be expressed as [186]:

$$\frac{3}{2}K_B\frac{\partial T_e}{\partial t} = \frac{1}{2}\nu_{ei}\frac{mv_{os}^2}{2} \ , \tag{4.1}$$

where K_B is Boltzman constant, T is the temperature of the electrons, ν_{ei} is the electron-ion collision rate, and $v_{os} = ca_0$ is the electron quiver velocity. When $v_{os} < v_t$, the thermal velocity in the plasma, the electron-ion collision rate is well described by the thermal collision rate:

$$\nu_{ei} = \frac{8\pi nZe^4\ln(\Lambda)}{6.4m^2v_t^2} \sim \frac{Z\ln\Lambda}{13\Lambda}\omega_p \ , \tag{4.2}$$

where $\Lambda = n\lambda_d^3$ is the plasma parameter with $\lambda_d = \sqrt{T_e/(4\pi ne^2)} \sim 740\sqrt{T_e[\mathrm{eV}]/n[\mathrm{cm}^{-3}]}$ the Debye length. Equations (4.1) and (4.2) suggest that sufficient heating requires high plasma density ($\geq 10^{19}$ cm^{-3}) [186]. This limits the group velocity of the laser pulse and the phase velocity of the plasma wake and hence the maximum achievable electron beam energy.

In order to realize a GeV class LWFA, scaling laws suggested that guiding of a relativistically intense laser pulse over several centimeters with low density plasma ($\simeq 10^{18}$ /cm^3) was essential (see Section 1.2). To circumvent the density limitation imposed by the ignitor-heather method and allow the production of multi-cm scale plasma channels, a gas-filled capillary discharge waveguide [129–131] was employed to develop a new LWFA at the LOASIS Facility. This capillary discharge guided (CDG-) LWFA consists of a 50 TW

class Ti:Sapphire laser, capillary discharge waveguide, laser diagnostics, and e-beam diagnostics. The main e-beam diagnostic, namely the GeV class electron spectrometer (GeV ESM), was developed in this dissertation and described in Chapter 3.

This Chapter describes LOASIS CDG-LWFA experiments and statistical analysis of the performance [1, 2]. The experimental setup is described in Section 4.2, followed by an overview of low power laser guiding in Section 4.3 and e-beam generation with CDG-LWFA in Section 4.4. A statistical analysis is presented in from Section 4.5 to 4.8, leading to a discussion and conclusion in Section 4.9.

4.2 Experimental Setup

The experiments used the short pulse, high peak power and high repetition rate (10 Hz) Ti:Al$_2$O$_3$ laser system of the LOASIS Facility at LBNL, a schematic of which was shown in Fig. 1.5. Low energy laser pulses (of wavelength $\lambda \simeq 0.81$ μm) from a Ti:Al$_2$O$_3$ laser oscillator were first sent to an optical phase controller (Dazzler, Fastlite inc. [188]), which controlled the chirp of the pulses up to 4th order, then temporally stretched. The laser pulse was amplified by multi stage Ti:Sapphire amplifiers up to approximately 3.5 J/pulse, and then compressed using a grating based optical compressor. Following compression, the laser pulse was focused by an F/25 off-axis paraboloid of 200 cm focal length to a spot size $w_0 \simeq 25$ μm at the entrance of a capillary discharge waveguide. The lay-out of the experiment is shown in Fig. 4.1. The peak power P (TW) of the laser was varied by adjusting both the pulse duration and laser energy. At full energy and optimum compression (1.6 J, 37 fs FWHM duration), $P \simeq 44$ TW, resulting in a calculated peak intensity $I = 2P/\pi r_s^2 \simeq 4.5 \times 10^{18}$ W/cm^2 and a normalized vector potential $a_0 \simeq 8.6 \times 10^{-10} \lambda[\mu m] I^{1/2}[$ W/cm$^2] \simeq 1.5$.

The capillaries were laser machined into 33 mm long sapphire blocks with diameters ranging from 190 μm to 310 μm. Hydrogen gas, introduced through holes near the capillary ends, was ionized by striking a discharge between electrodes located at each end of the capillary. Measurements [129] and modeling [189, 190] showed that a fully ionized, approximately parabolic channel was formed. This was also confirmed by the absence of significant ionization induced blueshifting of the laser spectrum when proper guiding conditions were achieved. Previous experiments [130] demonstrated channeling of non-
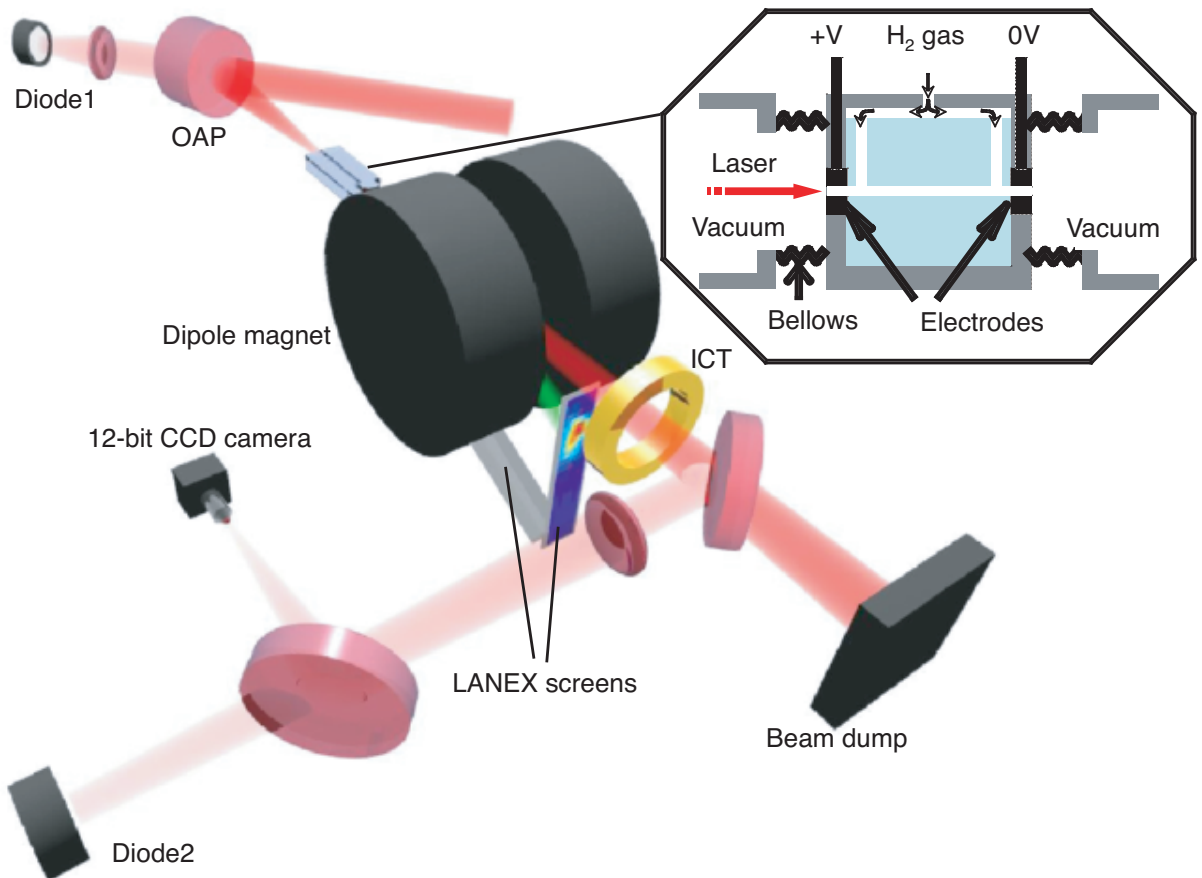
Figure 4.1: Schematic diagram of the capillary-guided laser wakefield accelerator. The plasma channel was formed in a hydrogen-filled capillary discharge waveguide (see inset). Hydrogen gas was introduced into the capillary waveguide using two gas slots in the 190 μm and 225 μm diameter capillary and three in the 310 μm capillary. A discharge was struck between two electrodes located at each end of the waveguide, using a high voltage pulsed power supply that utilized a 2.7 nF capacitor charged to 20 kV. The laser beam was focused onto the entrance of the capillary using an f/25 off-axis parabola (OAP). The guiding efficiency was measured using a pair of optical diodes (Diode 1 and 2) that monitored the amount of laser energy at the entrance and exit of the capillary. The laser beam exiting the capillary was monitored on a 12 bit CCD camera (20 μm resolution), after having been attenuated with a pair of reflective wedges and optical attenuators (not shown). The e-beam energy spectrum was analyzed using a 1.25 T broad-band magnetic spectrometer (see Chapter 3). The e-beam was deflected downward and detected using scintillating screens (LANEX-FB) imaged onto four synchronously triggered 12-bit CCD cameras (not shown).

relativistically intense laser pulses with $I \lesssim 10^{17}$ W/cm^2 in 30–50 mm long capillaries, which did not generate electron beams.

The GeV ESM was placed right after a discharge capillary unit (for distance, see Fig. 3.4). Electron beams were deflected vertically downward onto two scintillating screens LANEX Fast back (LANEX-FB) mounted on the exit flanges of the vacuum chamber. The effective deflection by a strong magnetic field (up to 1.25 T) and the large gap between the poles (65 mm) allowed simultaneous measurements of an e-beam spectrum and laser pulse properties. The spectrometer covered 0.01 to 0.14 GeV (bottom) and 0.17 to 1.1 GeV (forward) in a single shot. Detailed discussions such as the resolution, precision of the absolute energy determination, and charge - light yield calibration were described in Chapter 3. The guiding efficiency was measured using a pair of optical diodes (Diode 1 and 2) that monitored the amount of laser energy at the entrance and exit of the capillary. The laser beam mode profile exiting the capillary was monitored on a 12 bit CCD camera (20 μm resolution). Diagnostics of the transmitted laser beam were installed behind the GeV ESM.

4.3 Low Power Laser Guiding

In the CDG-LWFA experiments, laser pulses were guided by capillary discharge waveguides. In this dissertation, the relativistic electron beam generation via CDG-LWFA was experimentally studied by making use of 33 mm long capillaries with diameters of 190, 225, and 310 μm. Although the development of waveguides and the guiding of a relativistically intense laser pulse are beyond the scope of this dissertation (see A. J. Gonsalves [191] for the development of waveguides), generation of relativistic e-beams via a CDG-LWFA is strongly connected to the guiding performance. This section presents a brief overview of the low power laser guiding results from the experiments presented in this dissertation. Here, "low power" was defined such that the input laser intensity was not high enough to cause self-injection of background electrons into the wakefield. Guiding of high power laser pulses is described with the generation of relativistic e-beams to discuss correlation and laser to e-beam energy efficiency.

The basic mechanism for channel formation is as follows. The discharge current ionizes and heats the plasma, which is cooled at the capillary wall. A temperature profile that is peaked on-axis is formed, and since the pressure gradients are equalized on a timescale much shorter than the period of the discharge, the plasma density increases with distance

from the capillary axis.

At the beginning of experiments, low power laser guiding performance was optimized by adjusting the initial gas density and the delay between the onset of the discharge current and the arrival of the laser beam (discharge delay t_{dsc}). The discharge delay $t_{dsc} = 0$ means that a laser arrives at the entrance of a capillary when the discharge is struck in the capillary (i.e., start of current pulse). In the following part of the dissertation, the term "density" and symbol n_0 indicate the estimated axial electron density $n_e|_{r=0}$ from the measured Hydrogen gas pressure inside the capillary using the scaling law in Ref. [131],

$$n_e|_{r=0}[\text{cm}^{-3}] = 0.87 n_{H_2}|_{r=0}[\text{cm}^{-3}] + 0.11 \times 10^{18}[\text{cm}^{-3}], \tag{4.3}$$

where $r = 0$ indicates parameters on axis, n_e is the electron density, and n_{H_2} is the density of hydrogen gas.

The dependence of the plasma channel profile and on-axis plasma density on the discharge delay was studied at the University of Oxford [191] via transverse interferometry. In Ref. [191], a rectangular shape capillary with 465 μm width was used. The discharge current had a pulse length of 225 ns full width (0 A to 0 A), or $\sim$ 90 ns FWHM, with the peak current of $\sim$ 480 A. It took 80 ns to form the plasma channel and reach stable state with a density minimum on axis. The channel shape did not vary significantly after 80 ns. The stable state lasted till the current fell to almost 0 A. The on-axis plasma density showed a small fluctuation ($\pm \sim$ 3 %) with $75 \lesssim t_{dsc} \lesssim 220$ ns, then dropped. Although similar behavior was expected in the experiments at LBNL, the different high voltage power supply providing different current profile may affect performance.

The following paragraphs describe the dependence of low power guiding performance on the discharge delay from the LBNL experiments. Here, we discuss with the relative transmission loss $\hat{U}_{Lls} = U_{Lls}/U_{Lin}$ and measured output spot size $w_{0Out} = \sqrt{w_{0xOut}w_{0yOut}}$ with different input laser power and different diameters of capillaries, where U_{Lin} is input laser energy [J], U_{Lls} is laser transmission loss [J]. Since transverse interferometry was not implemented at the LBNL facility, plasma density was estimated using Eq. 4.3. The impact of the discharge delay and capillary diameter is shown and discussed.

The discharge delay dependence of low power guiding performance for 225 μm and 190 μm diameter capillaries are shown in Fig. 4.2. For Fig. 4.2(a), the 225 μm diameter
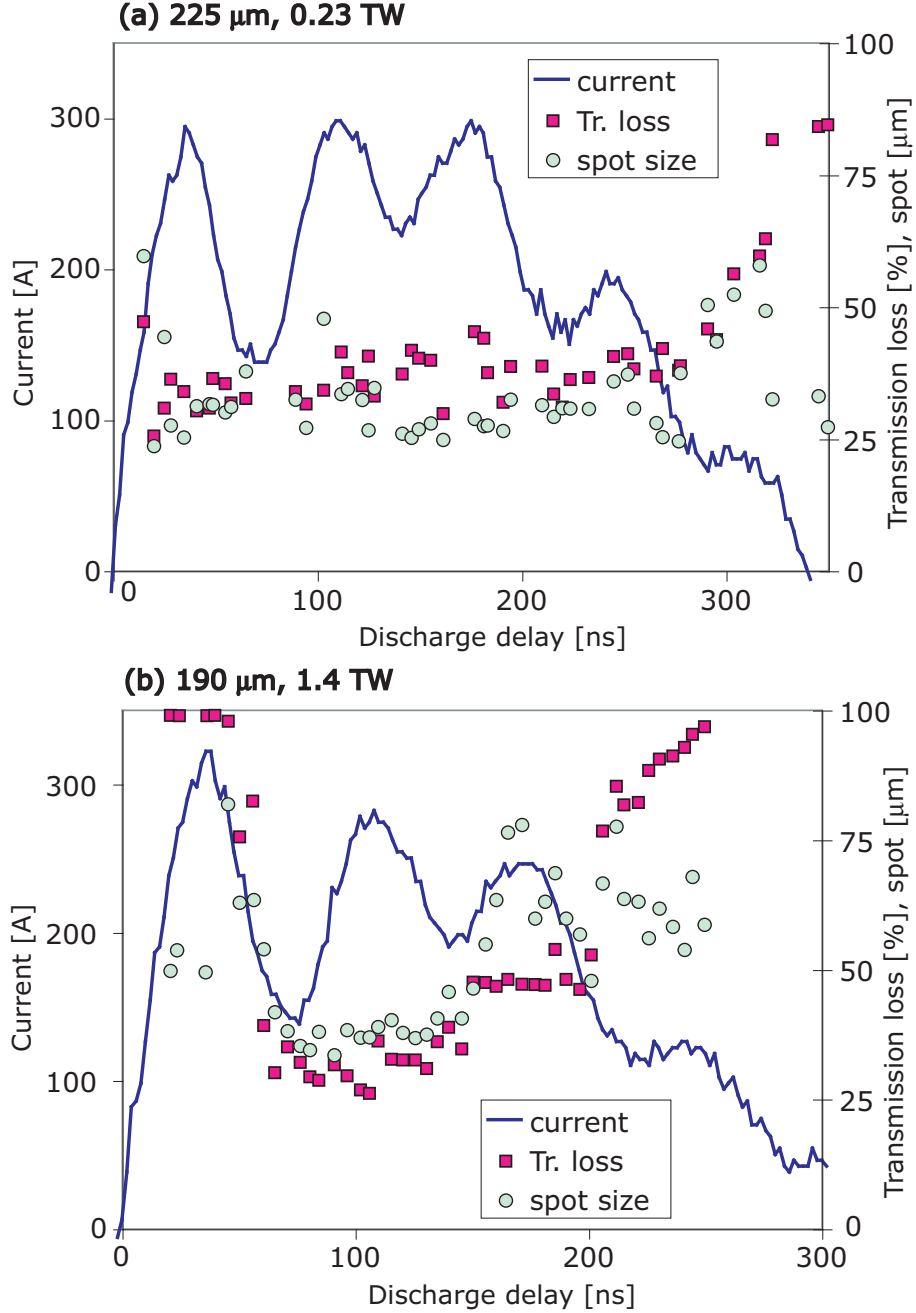
Figure 4.2: Discharge delay dependence of low power guiding performance. Discharge current (solid line, left axis), laser output spot size w_{0Out} (circle, right axis), and transmission loss (square, right axis) against the discharge delay. (a): With the 225 μm diameter capillary, laser plasma parameters were $n_0 \simeq 2.6 \times 10^{18}$ cm^{-3}, $U_{Lin} \sim 9.5$ mJ, and $\tau_L \simeq 42$ fs, which gave $P \sim 0.23$ TW ($a_0 \simeq 0.11$) in average. (b): With the 190 μm diameter capillary, laser plasma parameters were $n_0 \simeq 2.7 \times 10^{18}$ cm^{-3}, $U_{Lin} \sim 57$ mJ, and $\tau_L \simeq 40$ fs, which gave $P \sim 1.4$ TW ($a_0 \simeq 0.26$) in average.

capillary was used, and laser plasma parameters were $n_0 \simeq 2.6 \times 10^{18}$ cm^{-3}, $U_{Lin} \sim 9.5$ mJ, and $\tau_L \simeq 42$ fs, which gave $P \sim 0.23$ TW ($a_0 \simeq 0.11$) in average. For Fig. 4.2(b), the 190 μm diameter capillary was used, and laser plasma parameters were $n_0 \simeq 2.7 \times 10^{18}$ cm^{-3}, $U_{Lin} \sim 57$ mJ, and $\tau_L \simeq 40$ fs, which gave $P \sim 1.4$ TW ($a_0 \simeq 0.26$) in average. The loss observed here may be attributed to the leak from the channel, since almost no wakefield generation was expected with this low laser intensity. Due to this negligible wake generation and low a_0, one can see the quality of the channel (without self focusing and wake-laser interaction).

The measured discharge current was reproducible within shot-to-shot fluctuations of a few percent, and had periodic ripples on its profile as shown in Fig. 4.2. The measured discharge current profile showed small differences between the different capillaries as can be seen in Figs. 4.2(a), (b), and Fig. 4.3. For the 225 μm diameter capillary, an output spot size of $\simeq 30$ μm, almost identical to the input spot size, was observed for discharge delays of $20 \lesssim t_{dsc} \lesssim 230$ ns as shown in Fig. 4.2(a), with $\sim 30\%$ transmission loss. Both the transmission loss and output spot size were somewhat stable and did not show a sharp dependence on the discharge current profile. The 225 μm diameter capillary provided the smallest output spot with the widest range of discharge delay among the three capillaries studied in this work (see also Fig. 4.3).

The 190 μm diameter capillary had a somewhat smaller discharge delay window for guiding [Fig. 4.2(b)]. The transmission loss of $\simeq 25\%$ and output spot size of $\simeq 25$ μm were observed for $50 \lesssim t_{dsc} \lesssim 150$ ns. With this capillary, a bigger spot size was directly correlated to the larger loss. Those observations suggest that the 190 μm diameter capillary was not well matched for the input spot size of $\gtrsim 35$ μm. If a laser spot becomes larger than 35 μm during the propagation, leak from channel becomes substantial. Note that these discharge timing dependences shown in Fig. 4.3 were obtained during the optimization. The lower transmission loss was achieved with different laser and plasma parameters.

The discharge delay dependence for a 310 μm diameter capillary is shown in Fig. 4.3. For the plot shown in Fig. 4.3(a), $n_0 \simeq 2.7 \times 10^{18}$ cm^{-3}, the laser input energy U_{Lin} was 9.5 mJ, and pulse duration τ_L was $\simeq 49$ fs, which gave a laser peak power P of 0.19 TW ($a_0 \simeq 0.097$). Here, the laser pulse duration is defined as the FWHM width of the intensity distribution unless otherwise specified. For Fig. 4.3(b), laser plasma parameters
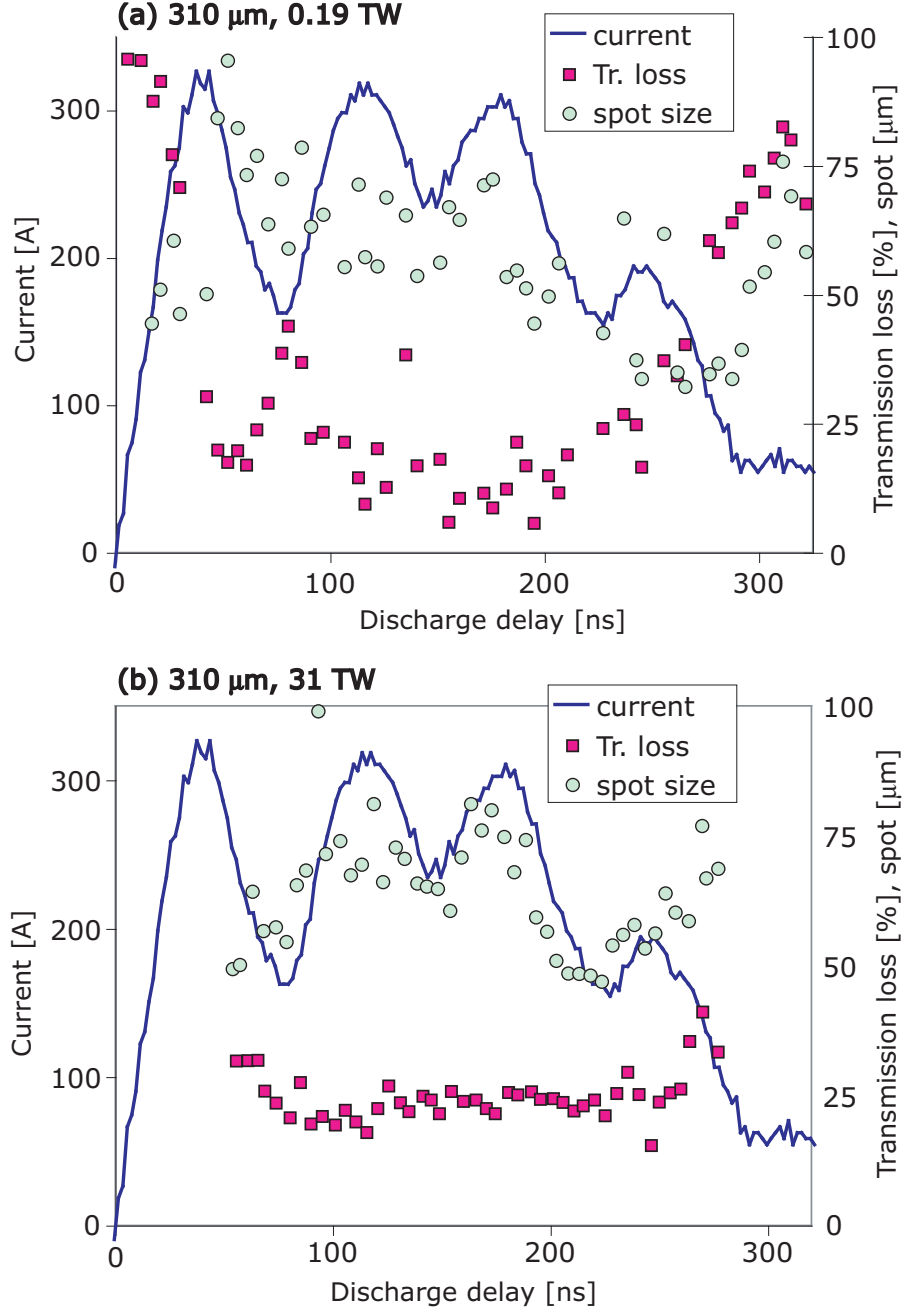
Figure 4.3: Discharge delay dependence of the low power guiding performance with the 310 μm diameter capillary. Discharge current (solid line, left axis), laser output spot size w_{0Out} (circle, right axis), and relative transmission loss $\hat{U}_{Lls}$ (square, right axis) versus the discharge delay. (a): Laser plasma parameters were $n_0 \simeq 2.7 \times 10^{18}$ cm^{-3}, $U_{Lin} \sim 9.5$ mJ, and $\tau_L \simeq 49$ fs, which gave $P \sim 0.19$ TW ($a_0 \simeq 0.097$) in average. (b): Laser plasma parameters were $n_0 \simeq 3.0 \times 10^{18}$ cm^{-3}, $U_{Lin} \sim 1.2$ J, and $\tau_L \simeq 39$ fs, which gave $P \sim 31$ TW ($a_0 \simeq 1.2$) in average.

were $n_0 \simeq 3.0 \times 10^{18}$ cm^{-3}, $U_{Lin} \sim 1.2$ J, and $\tau_L \simeq 39$ fs, which gave $P \sim 31$ TW ($a_0 \simeq 1.2$) in average.

The laser beam transmission loss and resultant output laser spot size correlated with discharge current. As shown in Fig. 4.3(a), with the 310 μm diameter capillary, the relative transmission loss of 0.19 TW laser was $\simeq$ 10 - 20% for $n_0 \simeq 2.7 \times 10^{18}$ cm^{-3} and $110 < t_{dsc} < 210$ ns. Guiding with less than 50% energy loss was achieved for $50 \lesssim t_{dsc} \lesssim 280$ ns. The spot size was somewhat larger than the input spot size $w_{0In} \simeq 25$ μm. The smallest output spot of $\simeq 30$ μm was observed with discharge delay of 280 ns, where the loss was $\simeq 30$%. This low transmission loss with relatively large output spot size (~ 60 μm) suggests that the 310 μm diameter capillary was matched to a large input spot size like $\simeq 60$ μm. For late delay, a plasma channel profile may become suitable for smaller spot size (~ 30 μm) with somewhat higher loss.

Shown in Fig. 4.3(b) is the discharge delay dependence of $P = 31$ TW laser guiding with the 310 μm diameter capillary. Note that no e-beams were observed from this scan of the discharge delay.

One can see that guiding with 25% loss was achieved for $80 < t_{dsc} < 260$ ns, and the fine scale time dependent behavior seen in the transmission loss in Fig. 4.3(a) was gone. This difference could be explained as follows. Even though Hydrogen gas is fully ionized on-axis, it is not fully ionized in the vicinity of cold capillary wall, and therefore, average ionization becomes ~ 70% [191]. A transmission loss of 50% seen in Fig. 4.3(a) for $t_{dsc} \sim 80$ ns may be due to the loss for ionization. With insufficient discharge current, substantial amount of hydrogen existed, and laser pulse lost its energy to ionize them. This was not seen in Fig. 4.3(b) because of much higher input laser energy. The relative loss of laser pulse energy was much smaller for this high input energy case. This loss due to ionization was not seen from Fig. 4.2 because of smaller laser spot size. For the 310 μm diameter capillary, laser spot size was large so that the laser pulse interacts with Hydrogen gas located close to a cold capillary wall.

The output spot size shown in Fig. 4.3(b) clearly showed correlation with discharge current. The minimum spot size achieved with this laser peak power was $\simeq 40$ μm for $t_{dsc} \sim 210$ ns. This strong correlation suggest that a channel profile oscillate with discharge delay. Since it was not seen from neither lower power nor different capillaries, it is probably due to the wakefield modulating laser pulse or relativistic self-focusing. For

such high input power, relativistic self-focusing may have played some role in the onset of guiding. The relativistic self-focusing occurres when the laser peak power P exceeds a critical power $P_c = 2c(e/r_e)^2(\lambda_p/\lambda)^2$ [192, 193], or in practical units for $\lambda = 0.8$ μm case,

$$P_c[\text{TW}] \simeq \frac{30.4}{n_0^{(18)}}, \tag{4.4}$$

where $n_0^{(18)} = n_0 \times 10^{-18}$ cm^{-3}. Therefore, $P/P_c \sim 3 > 1$ for the $P = 31$ TW laser guiding case, and $P/P_c \sim 0.017 \ll 1$ for 0.19 TW laser guiding case.

The input laser power of 31 TW ($a_0 \simeq 1.2$) was intense enough in the 190/225 μm capillaries to observe trapped and accelerated electrons, but not in the 310 μm capillary. This could be explained by the larger spot size due to the mismatch of the channel. With a simple estimate, two times larger spot size w_0 drops the intensity (normalized vector potential) down to a half [$a_0 \simeq 0.6$, see Eq. (2.62)]. Although it is not necessary that the laser pulse had the identical radial profile to the measured output profile during the propagation in the channel, the intensity drop inside the channel seems to explain the results. More loss was observed from input laser power of 31 TW for the 310 μm capillary, while the loss did not show clear correlation with the output spot size.

Guiding performance was critical for e-beam generation for the following reasons. First, without a preformed plasma channel (laser injected ahead of discharge) transmission was below 5% and bulk damage was sustained to the capillary channel walls. Without proper guiding performance, the lifetime of a capillary block might be a few shots. This observation also indicated that self-ionization and relativistic self-focusing could not be relied on for guiding, as expected from short pulse propagation theory [136]. Second, the guiding performance was highly sensitive to input beam alignment as well. For example, for the case of the 310 μm diameter capillary, any displacement > 15 μm away from the optimum location (i.e., defined as the position where a quality-guided beam was produced) resulted in a transmission drop on the order of 20% (see Fig. 4.10). This observation suggests that mis-alignment led to the energy loss not via the wakefield generation but leakage, which can lead to damage of the capillary block as well. Therefore, to avoid damaging the capillary, all the experiments were started using low power lasers ($\lesssim 0.2$ TW) to align and to find the proper discharge delay and plasma density for guiding. The laser energy was then gradually raised while intensity dependent phenomena,

such as relativistic self-focusing, were closely monitored by the laser pulse diagnostics.

4.4   Electron Beam Generation

As discussed in Section 4.3, low power laser pulses (for example, shown in Fig. 4.3(a)) did not deposit significant energy onto a plasma channel, and no generation of relativistic e-beams occurred indicating that no sizable wakefield was generated. The low power guiding performance showed some dependence on the discharge delay. When the laser field gradient was strong enough to expel significant amounts of surrounding electrons, it created a strong wakefield, through which the laser deposited its energy onto the plasma as evidenced by the fact that accelerated electrons were observed. This suggested that background electrons were trapped in the accelerating phase of the wakefield, via wave-breaking or plasma instabilities. This Section gives an overview of e-beam generation from three different capillaries through the representative single shot spectrum for each capillary.

Electron beams with energies of 1 GeV were obtained in a 310 μm diameter channel capillary for $P \sim 42$ TW and $n_0 \simeq 4.3 \times 10^{18}$ cm^{-3}. The single shot e-beam spectrum (a), with the space-integrated energy profile (b), and energy-integrated spatial profile (c), are shown in Fig. 4.4. Using the method described in Section 3.3, the energy spread was found to be 2.6% (with 2.0% resolution) rms. Note that the measurement was resolution limited and as such the energy spread might have been smaller. Total charge of > 2.3 pC is lower than the value in Ref. [1] reflecting the calibration done at the ALS. Although there is a chance that charge was underestimated as discussed in Section 3.4, the results of ALS calibration was used throughout the dissertation. A spatially displaced second beam is visible at $\simeq$0.8 GeV. Multi-bunch features of this type were also observed in experiments with different laser and plasma parameters, and with the other capillaries as well. Possible injection in second or later buckets was discussed in Section 2.3, and numerical simulations also predict this kind of structure, owing to trapping of a second electron bunch in a wake bucket behind the first [68, 155], or multiple injections into one bucket [194]. The operation of this larger diameter capillary was not as stable as that of the others (190 μm and 225 μm capillaries). The detailed performance of this capillary, including stability, is presented in Section 4.6 through a statistical analysis.
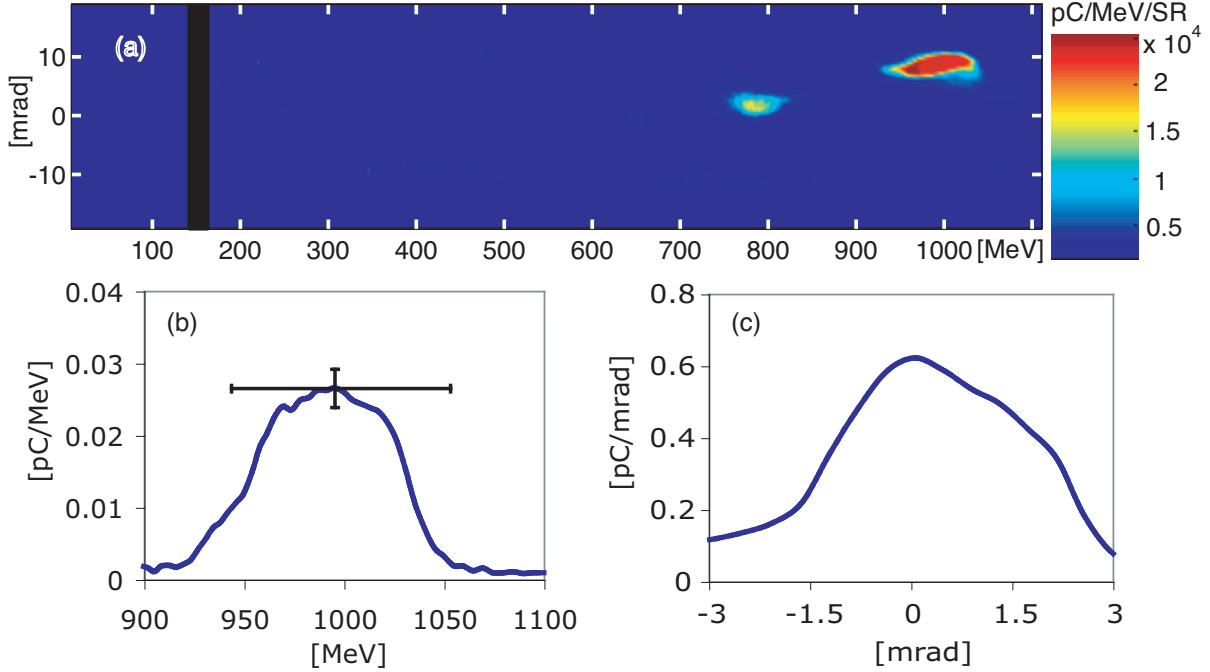
Figure 4.4: Single-shot e-beam spectrum from a 310 μm diameter capillary-guided accelerator with $n_0 \sim 4.3 \times 10^{18}$ cm^{-3} and $P \sim 42$ TW. (a) Image of the electron beam in pC/MeV/SR, with the kinetic energy T (MeV) on the horizontal axis and the divergence (mrad) on the vertical axis. (b) The space-integrated spectrum of the beam in pC/MeV. (c) Energy-integrated spatial profile of the beam in pC/mrad. The peak energy was 1.0 GeV, total charge was > 2.3 pC (lower than Ref. [1], see Section 3.4), and the beam divergence was 1.6 mrad (rms). Using the method discussed in Section 3.3, the energy spread of the beam was estimated to be 2.6% (rms) with resolution of 2.0% (rms). The horizontal error bar in (b) comes from the uncertainty in the energy (+0.058, -0.052, see Fig. 3.7). The vertical error bar in (b) is due to the uncertainty in calibration of the phosphor screen as a charge monitor ($\pm 6.8\%$). A second beam at 0.8 GeV is also visible in (a). The maximum charge density on the LANEX-FB was < 0.08 pC/mm^2.

The stable generation of $\simeq 0.5$ GeV e-beams was found with a 225 μm diameter capillary. High quality (low energy spread) e-beams were generated with high reproducibility from density of $n_0 \sim 3.5 \times 10^{18}$ cm^{-3} and with $P \simeq 11$ TW laser pulses. Detailed statistical analysis of this regime was carried out and is presented in Section 4.7. A typical single-shot e-beam spectrum from this regime is shown in Fig. 4.5. From the energy-integrated vertical profile, which is shown in Fig. 4.5(c), the beam divergence was calculated and used to de-convolve the finite beam effect from space-integrated energy spread, which is shown in Fig. 4.5(b). The beam divergence and energy spread of the beam in Fig. 4.5
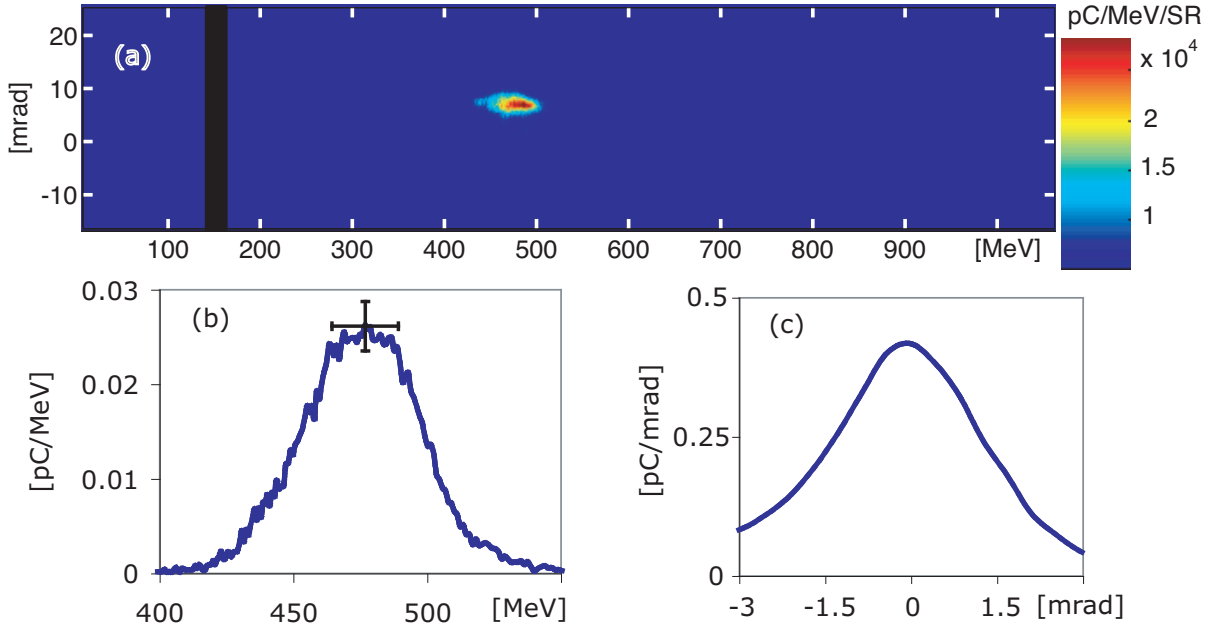
Figure 4.5:   Typical single-shot e-beam spectrum from the stable 0.5 GeV regime of the 225 μm diameter capillary-guided accelerator. (a) Image of the electron beam in pC/MeV/steradian (SR), with the energy on the horizontal axis and on the divergence in vertical axis. (b) The space-integrated spectrum of the beam in pC/MeV. (c) Energy-integrated spatial profile of the beam in pC/mrad. The peak energy was 477 MeV, total charge was $\simeq$1.4 pC, and the beam divergence was 1.5 mrad (rms). The energy spread of the beam was estimated to be 4.2% (rms) with resolution of 0.85% (rms). The horizontal error bar in (b) ($\pm$12) comes from the uncertainty in the energy (+0.026, -0.024, see Fig. 3.7). The vertical error bar in (b) is the uncertainty in calibration of the phosphor screen as a charge monitor ($\pm$6.8%). For this particular shot, laser plasma parameters were $n_0 \simeq 3.5 \times 10^{18}$ cm^{-3}, $U_{Lin} \sim 0.87$ J, and $\tau_L \sim 75$ fs, which gave $P \sim 12$ TW ($a_0 \simeq 0.75$). The maximum charge density on the LANEX-FB was < 0.03 pC/mm^2.

were 1.4 mrad and 4.6% rms, respectively.

The 190 μm capillary provided somewhat "high charge - large divergence" e-beams compared to the 225 μm diameter capillary. Many quasi-monoenergetic e-beams were observed from experiments using the 190 μm diameter capillary, but neither with high stability nor high reproducibility. Shown in Fig. 4.6 is an example of such "high charge and large divergence" e-beam from the 190 μm diameter capillary. The operation of this capillary provided large fluctuations in e-beam quality, such as beam divergence and beam energy spread. The stability and reproducibility were not as good as those of 225 μm capillary. The detailed performance is presented in Section 4.8 through a
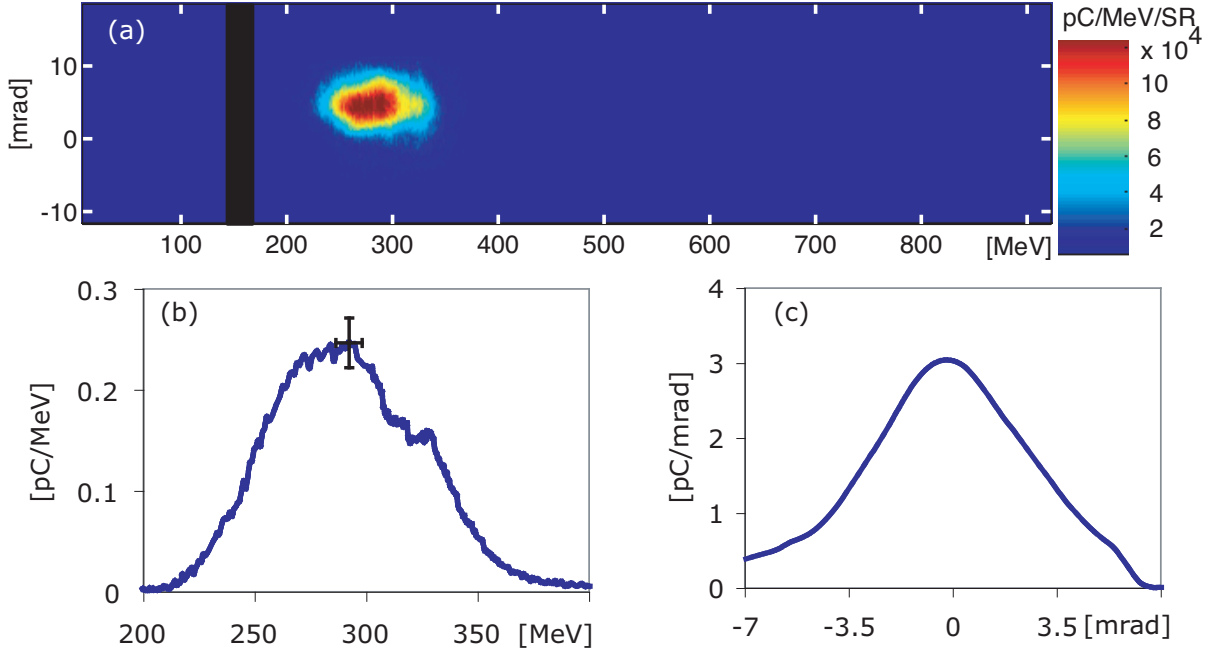
Figure 4.6: A single-shot e-beam spectrum from the 190 μm diameter capillary-guided accelerator with a density of $\simeq 3.2 \times 10^{18}$ cm^{-3}. (a) Image of the electron beam in pC/MeV/steradian (SR), with the energy on the horizontal axis and the divergence on the vertical axis. (b) The space-integrated spectrum of the beam in pC/MeV. (c) Energy-integrated spatial profile of the beam in pC/mrad. The peak energy was 273 MeV, total charge was $\simeq 15$ pC, and the beam divergence was 2.3 mrad (rms). The energy spread of the beam was estimated to be 10% (rms) with resolution of 0.77% (rms). The horizontal error bar in (b) (± 5.9 MeV) comes from the uncertainty in the energy (± 0.022, see Fig. 3.7). The vertical error bar in (b) is from the uncertainty in calibration of the phosphor screen as a charge monitor ($\pm 6.8\%$). For this particular shot, the input laser energy was 1.0 J with pulse duration of 46 fs, which gave the input laser power of 22 TW ($a_0 \simeq 1.1$). The maximum charge density on the LANEX-FB was < 0.04 pC/mm^2.

statistical analysis.

The peak energy of 1 GeV was the highest energy ever achieved from a LWFA. Although the performance of the accelerator at 1 GeV was less stable than $\simeq 0.5$ GeV e-beam generation with the 225 μm capillary, it demonstrated the possibility of compact GeV accelerators based on an LWFA by using a few tens of TW of laser power. Stable generation of the peak energy of 0.5 GeV beam demonstrated that it was possible to stabilize the self-injection process with a CDG-LWFA. Understanding the physics behind the stabilized self-injection would be a key for future stable GeV beam generation. Demand for even higher energy and higher quality, as well as higher stability, motivated a scan

of large parameter fields and their analysis. In the following Sections, statistical analysis on the performance of CDG-LWFAs is presented to elucidate this quite complicated laser plasma interaction for future improvement and optimization of CDG-LWFAs.

4.5   Methods for the Statistical Analysis

The mechanisms of wakefield generation, background electron trapping and their acceleration are fairly complicated, especially when the laser propagates many Z_R, because the laser pulses may undergo severe self-evolution. As the results, the performance of the CDG-LWFAs were found to be sensitive to the laser parameters, such as an energy, intensity, and pulse duration, and plasma parameters such as density, discharge delay, and capillary diameter.

Timing jitter between discharge and laser arrival, pointing fluctuations, and laser power fluctuations were significant for this first generation of experiments. By taking advantage of the high repetition rate experimental system, data sets containing several thousands shots were taken for each capillary and analysis software was developed to find and sort shots with similar parameters, allowing a statistical evaluation of the overall performance. Before showing the results of the statistical analysis, the detailed descriptions of the method and the definitions of the self-injection in this analysis are presented in this section. The results of statistical analysis are presented in Sections 4.6–4.8.

First, the data containing a certain specified parameter, such as the input laser intensity, pulse duration, or plasma density, were selected from a full experimental data group and formed a data set as a function of laser, plasma parameters. Second, the data set was sorted into sub data sets of subsequent, concatenating windows of parameter value ranges ("boxing"). Then the measured values were averaged in each particular "box" and plotted against the "box" parameter, typically the mean value of the box. Shown in Fig. 4.7 are two examples of these analysis plots. In the case of the 1-D plot [see Fig. 4.7(a)], this process was done with one specified parameter, which was the discharge delay in this example. In the case of the 2-D plot [see Fig. 4.7(b)], it was done with two parameters, namely the discharge delay in the horizontal axis, and the plasma density in the vertical axis in this example. The width of the parameter range for sorting was chosen such that each subset contained usually more than 20 shots for statistics, or at least 5
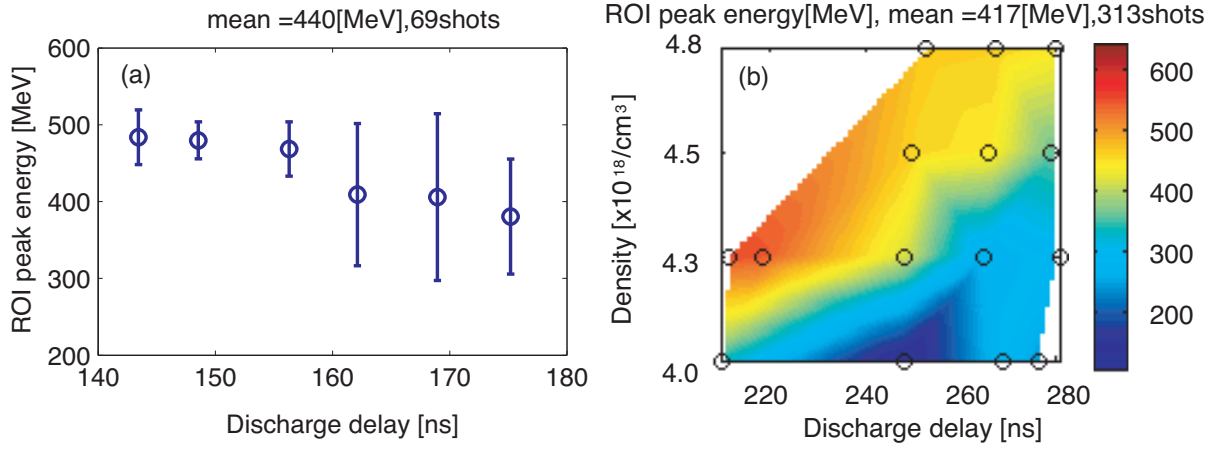
Figure 4.7: Examples of analysis of data set. (a): Example of 1-D plot (ROI peak energy versus discharge delay). (b): Example of 2-D plot (ROI peak energy versus plasma density and discharge delay). See following paragraphs for ROI (region of interest) description.

shots. A data subset that contained less than 5 shots was eliminated, unless otherwise spcified. Third, a mean value and standard deviation σ of x and y (also z for 2-D plot) were calculated for each sub data set. In the case of the 1-D plot, mean values were shown by a solid circle. Errorbars usually show standard deviations ($\pm\sigma$), except when showing the minimum and maximum value is considered to help to depict trends well, in which case this is noted. For the 2-D plot, the circles on the plots in Fig. 4.7(b) show mean values of x (horizontal) and y (vertical) of each sub data set. Those circles show where the data set actually exists, then shown by the color map is the target value (z) of the data set (ROI peak energy in this example). The color map was interpolated in between solid circles to visualize a trend of the target value. The standard deviation was not shown in the 2-D plots. Note that the actual data does not exist where the solid circle is absent on the 2-D plot.

To perform analysis with high accuracy, an automatic region of interest (ROI) was introduced in the Matlab based analysis program. For example, to evaluate total charge observed, an integration of the whole image may introduce enhanced noise, or lead to overestimation. Furthermore, to evaluate energy spread, an angular profile of the beam was obtained by integrating an image over the energy. An e-beam with multiple structures like in Fig. 4.4 may give a larger beam divergence in this case integrated over energy. Defining a ROI for each shot by manual selection became impractical when many thou-

sands of shots were acquired. Those facts motivated introduction an automatic ROI in the analysis.

High energy e-beams were occasionally observed with a low energy tail having larger divergence and higher charge. Since our interest is in the higher energy part of the energy spectrum, ROI was carried out such that higher energy part was prioritized. This prioritization of higher energy was performed by processing on a space linear image, which preserved the image of the beam as observed on the LANEX-FB. For the dispersive plane, 4 times the FWHM width, based on a non-dispersive plane (x) integrated dispersive plane profile in pC/mm, was first taken. Note that here the dispersive axis is not converted to energy yet, resulting in a somewhat compressed higher energy part, and a somewhat stretched lower energy part. Taking ROI based on the space-linear image ensures the peak energy of the spectrum is the high energy part, when substantial amount of high energy electrons was observed. Then second step was to take ROI in the non-dispersive plane (x in Chap. 3). The ROI was taken simply by using 4 times the FWHM width of the energy-integrated spatial e-beam profile. Following conversion into the energy linear profile in pC/MeV, 4 times the FWHM was taken again for the energy dispersive plane. The ROI based processing for the non-dispersive plane was performed in between the two ROI process on the dispersive plane. An example of ROI process for a high energy beam with a low energy tail is shown in Fig. 4.8. One can see that the high charge and divergence of the low energy tail from Fig. 4.8(b), is almost invisible in the space linear image shown in Fig. 4.8(a). In this example, the peak energy was found to be ~ 120 MeV in the full energy spectrum from the energy linear image. But the automatic ROI selected higher energy part based on the space linear image in the first process. Then the high energy component was selected and analyzed by the program.

Although automatic ROI worked perfectly for well-defined e-beams such as one shown in Fig. 4.5, it did not always chose right region for beams with complicated structure. Nevertheless, it significantly reduced noise for well defined beams and made the analysis presented here possible. Non ROI images and values were also used in the analysis depending on the purpose. If ROI-ed image was used for the analysis, it is notified by "ROI" as shown in Fig. 4.7.

Throughout this dissertation, electron injection into a wakefield relied on so called self-injection. There was no external e-beam source. In the following Sections, there are
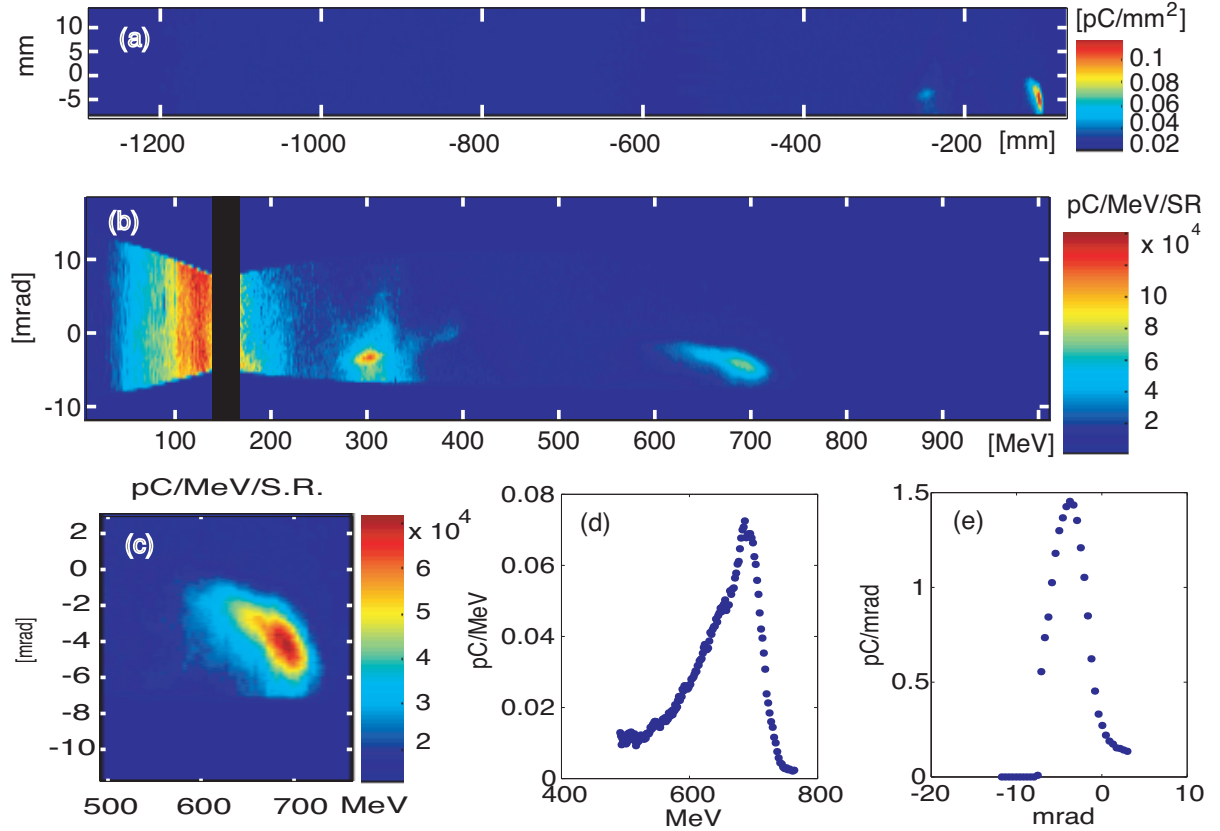
Figure 4.8: Examples of automatic ROI. (a): Space linear full image. (b): Energy linear full image. The vertical axis (non dispersed plane) was converted length [mm] to divergence [mrad], which created waist in the image and outside of the image was filled with 0 value. (c): Automatically ROI-ed part of the image. (d): space-integrated energy profile of the ROI-ed region. (e): Energy-integrated spatial profile of the ROI-ed image.

discussions concerning whether the self-injection occurred or not (injection probability). To make this discussion clear, a criterion for the self-injection was defined as follows.

Applying the maximum current to the electromagnet, the GeV ESM was able to cover the electron energy range and present a spectrum from 10 to 1100 MeV in a single shot. In other words, the e-beam could not be seen if its energy was less than 10 MeV. In this study, self-injection was considered to have occurred in all those cases, when an electron signal was recorded anywhere in the range between 10 and 1100 MeV with a total integrated energy of $U_b = \int T Q(T) dT > 0.01$ mJ within the ROI-ed subregion, $Q(T)$ [pC/MeV] being the observed charge/energy as the function of the kinetic energy, T, of the electrons. A total beam energy of $U_b = 0.01$ mJ corresponded to a total charge

Q_{tot} of 10 fC at 1 GeV, or 1 pC at 10 MeV. The reason for using total beam energy instead of total charge was that the sensitivity of the spectrometer was different for the high and low energy parts. A beam containing 20 fC was clearly visible in the 500 MeV range but not in the 10 MeV range. Note that electrons below 10 MeV might have been present even when no self-injection was considered to have occurred in this analysis. The statistical analysis of e-beam properties was performed on shots where self-injection occurred. The values such as mean and standard deviation of the e-beam properties did not include shots where self-injection was not observed.

The high power guiding performance presented in the following Sections has to be considered preliminary. A laser pulse may lose its energy during the propagation via a leak from channel and via deposition into the plasma through the creation of a wakefield. To discuss the physics of the loss quantitatively, the measurement of the optical spectrum is necessary, because creation of the wakefield causes red shifting of laser wavelength (energy conservation). Throughout the experiments, measurements of optical spectra were unstable, probably due to issues with the radiation collection and quality of the available optical spectrometer. In high power operation, the optical spectra had significant distortion such as blue- or red shift, or modulation. The photo detector used for throughput energy measurement had optical spectral dependence, which was not included in the analysis. Although an achromatic lens was employed for output laser mode imaging, focal position still depended on the central wavelength due to the large increase in spectral bandwidth. Therefore, changes in the mode spot size might also have been caused by the change in optical spectrum. Therefore, the measurement of high power laser guiding performance may include a factor of error. Because the effects from the spectral shifts are not included in this analysis, and results on the high power guiding have to be considered preliminary.

Lastly, the performance showed complicated interdependence on multiple input parameters. The input and output parameters of this analysis are summarized as follows:

- **Laser Input parameters**
  Input laser energy U_{Lin} [J], pulse duration τ_L [fs], input laser intensity in terms of a normalized laser vector potential a_0, and laser pointing (displacement of the input laser focus at the entrance of a capillary).

- **Plasma channel Input parameters**

  On axis plasma density n_0 [cm^{-3}], discharge delay t_{dsc} [ns], and discharge current I_{dsc} [A].

- **Laser output parameters**

  Laser transmission loss U_{Lls} [J], and waist of output laser mode w_{0out} [µm].

- **E-beam output parameters**

  Probability of self-injection occurrence, peak kinetic energy T_{pk} [MeV], rms energy spread [%], total charge Q_{tot} [pC], rms beam divergence σ_{r1} [mrad], beam pointing σ_{rpeak} [mrad], and total beam energy U_b [J].

4.6 Analysis of Experiments using the 310 µm Diameter Capillary

In this Section, the results of statistical analysis of the performance of the CDG-LWFA employing the 310 µm diameter capillary is presented. The explored parameter field is illustrated in Fig. 4.9. Note that green circles show regions where data actually exist, and the color map shows interpolation among them. Blue circles and rectangles show parameter regions where each parameter dependence is discussed in the following Sections. Laser parameter dependences including laser intensity dependence are presented in Section 4.6.1, discharge delay dependence in Section 4.6.2, plasma density dependence in Section 4.6.3, and analysis on high energy electron generation is presented in Section 4.6.4.

4.6.1 Laser Parameter Dependence

This Section discusses the laser parameter dependence, such as laser pointing, intensity, and pulse duration, of a CDG-LWFA using the 310 µm diameter capillary. During operations, the laser pointing stability was monitored with an optical system that used leakage light, at the same location where Diode 1 was implemented (see Fig. 4.1 for the location of Diode 1). By measuring the spot displacement of the focused leakage light, the incident angle of the laser pulse was evaluated. The incident angle was calibrated to the
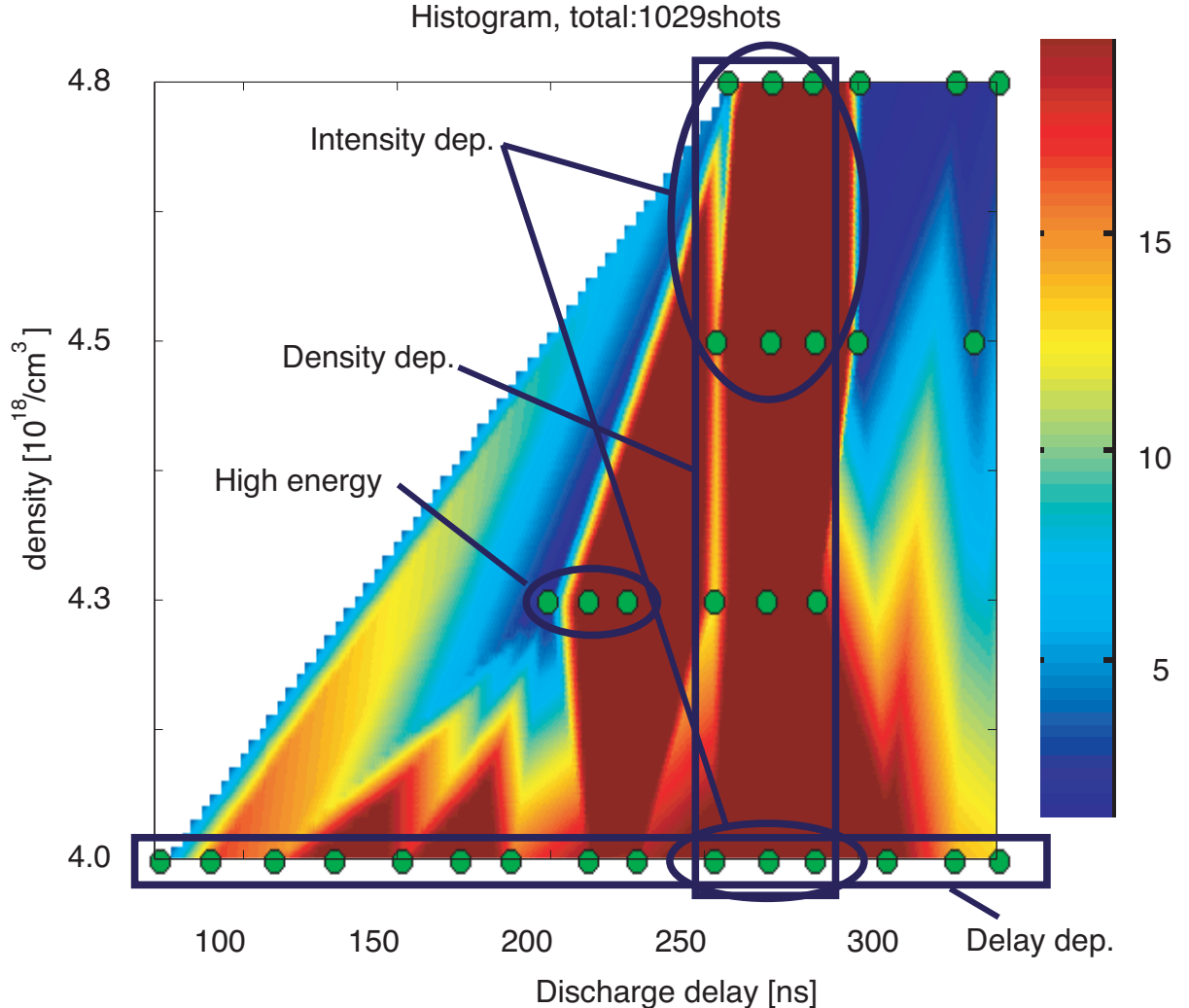
Figure 4.9:   Histogram of number of shots collected (circle, colormap) versus discharge delay (horizontal) and plasma density (vertical). The parameter regimes where each parameter dependence was discussed are illustrated by circles and rectangles. Area filled with dense red is where more than 20 shots were obtained.

displacement at the laser pulse focus on the entrance of a capillary. The laser transmission loss versus calculated focus position on the entrance of the 310 μm diameter capillary is shown in Fig. 4.10. The input laser plasma parameters were $n_0 \simeq 4.0 \times 10^{18}$ cm^{-3}, $250 < t_{dsc} < 300$ ns, $U_{Lin} \sim 1.6$ J with 5.7% fluctuation, and $\tau_L \simeq 38$ fs, which gave $P \sim$ 43 TW ($a_0 \simeq 1.5$) in average. Here, a fluctuation was defined as $fluc(\%) = 100 \times \sigma/\text{mean}$, where σ is the standard deviation of the target parameter. Since it was monitored and constantly corrected during operations, there is only a small amount of statistics on the
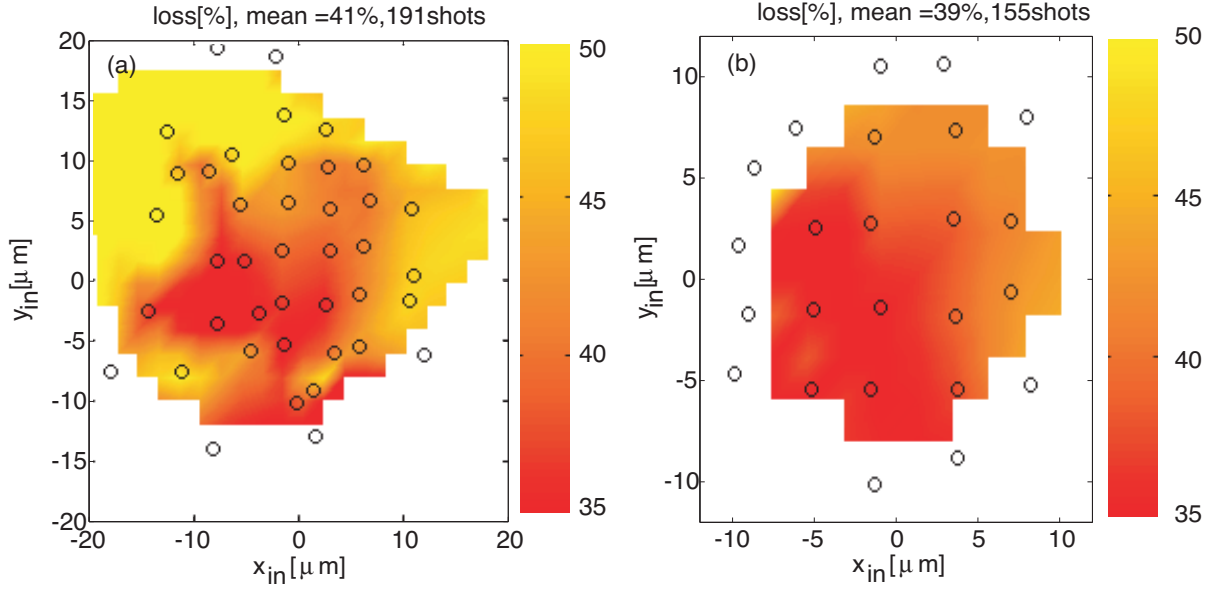
Figure 4.10: Loss of the laser input energy versus laser pointing onto the entrance of the capillary (310 μm). (a): With all shots. (b): Selected only $r_{in} < 11$ μm. The input laser plasma parameters were $n_0 \simeq 4.0 \times 10^{18}$ cm^{-3}, $250 < t_{dsc} < 300$ ns, $U_{Lin} \sim 1.6$ J with 5.7% fluctuation, and $\tau_L \simeq 38$ fs, which gave $P \sim 43$ TW ($a_0 \simeq 1.5$) in average. Data subsets containing less than 5 shots were also shown for (a).

behavior of focus location far from center. To visualize the effect of misalignment, data subsets containing less than 5 shots were shown as well in Fig. 4.10(a). One can see that with a displacement from optimum location $r_{in} = \sqrt{x_{in}^2 + y_{in}^2} \gtrsim 10$ μm, the transmission loss started to increase. For shots $r_{in} \sim 15$ μm, the increase of loss on the order of 15% was observed. To separate the effect of misalignment from the other effects, shots within $r_{in} < 11$ μm were taken into account for the subsequent analyses, unless otherwise notified. The transmission loss versus focal displacement where shots with $r_{in} < 11$ μm were taken [shown in Fig. 4.10(b)] demonstrates almost uniform transmission loss in terms of displacement. Note that the laser was linearly polarized, and the polarization plane was in the horizontal x plane. No clear horizontal-vertical asymmetry was observed in terms of the transmission loss.

The threshold laser intensity for self-trapping of electrons into the wakefield was explored by changing the laser pulse duration via the tuning of the inter-grating distance in the optical compressor, and the laser energy via adjustment of the 532 nm Nd:YAG pumping power of the main amplifier system. Focal position changes when adjusting the

level of pumping power on the cryogenically cooled amplifier crystal were found to be negligible ($< 0.1 \; Z_R$), and consequently no spot size changes were observed.

The 310 μm diameter capillary was found to have a high threshold laser intensity for self-injection. It required high energy operation ($\simeq 1.7$ J/pulse) and well compressed laser pulses (< 50 fs), to generate any energetic electron beams with a plasma density of $\simeq 4.0 \times 10^{18}$ cm^{-3}. Shown in Figs. 4.11(a) and (b) are the injection probability (see Section 4.5 for the definition) versus laser pulse duration and intensity, respectively. Both
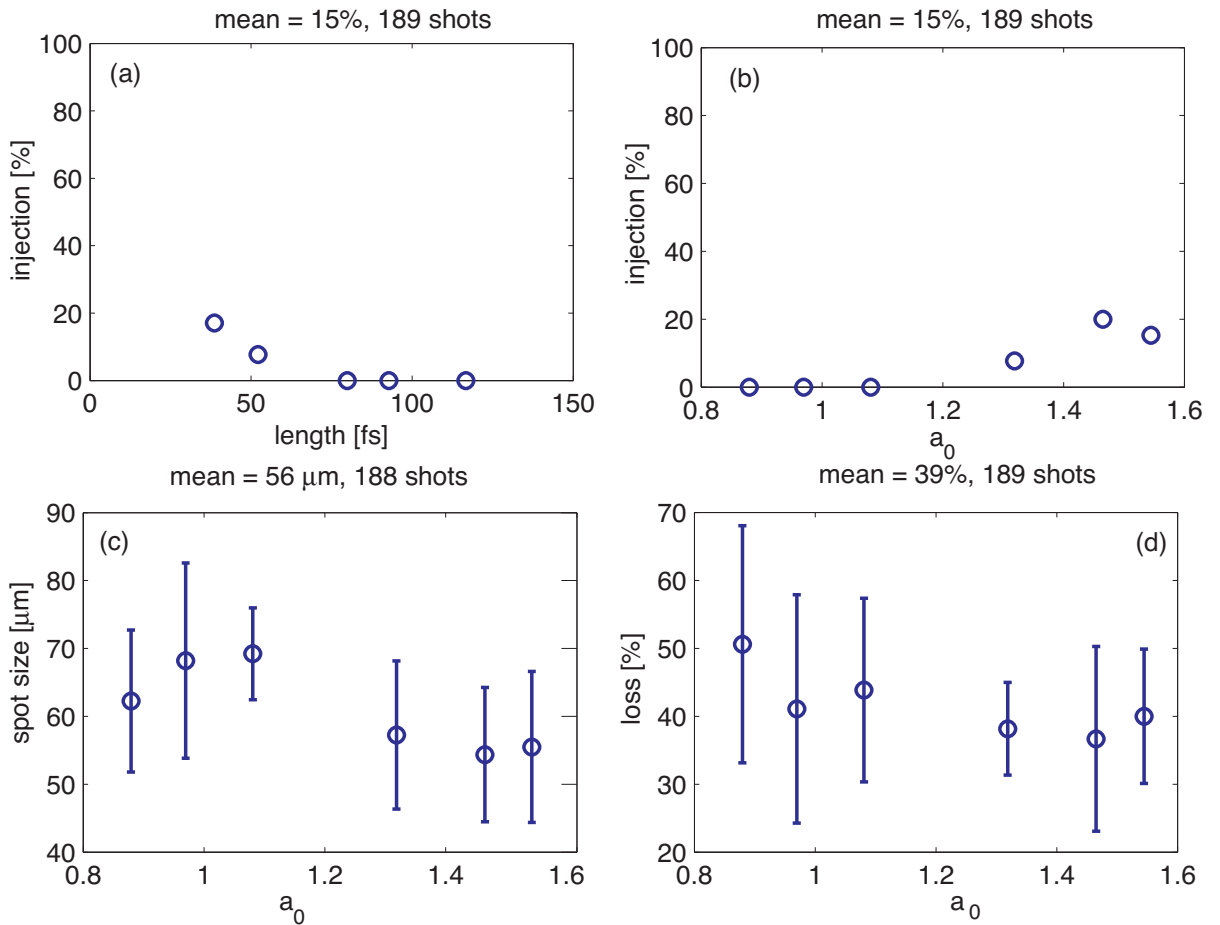
Figure 4.11:   Injection probability as a function of the laser pulse duration (a), and as a function of the input laser intensity (b). The laser guiding performance, namely the output spot size (c) and the transmission loss of the laser energy (d), as a function of the input laser intensity (see Section 4.5 for the definition of the injection). The 310 μm diameter capillary was used. The input laser plasma parameters were $n_0 \simeq 4.0 \times 10^{18}$ cm^{-3}, $260 < t_{dsc} < 290$ ns, and $U_{Lin} \sim 1.6$ J with 5.6% fluctuation. Shots with $r_{in} < 11$ μm were selected to eliminate the effect from misalignment.

plots may be identical if there was infinitesimal fluctuation in the input laser energy. The pulse duration dependence shows purely pulse duration dependence no matter how much the input intensity is, while a_0 dependence shows the input laser intensity dependence including the fluctuation in the input laser energy. To extract only the laser parameter dependence, the discharge delay was limited at $260 < t_{dsc} < 290$ ns, and plasma density was fixed at $\simeq 4.0 \times 10^{18}$ cm^{-3}. The laser energy was 1.6 J/pulse, with 5.6 % fluctuation.

One can see from Fig. 4.11(a) that self-injected electron beams were observed only when the laser pulse was compressed below 50 fs. From Fig. 4.11(b), the injection threshold intensity was found to be $a_0 \simeq 1.3$, which corresponded to 1.5 J, 49 fs (31 TW) laser pulse. This intensity was the highest threshold intensity among the three capillaries discussed in this dissertation. Note that threshold intensity may depend on the plasma density and discharge delay as well. A possible reason for high threshold for self-trapping is the probable larger laser mode size during the interaction as also discussed in Section 4.3. For example, $w_0 = 55$ μm gives a_0 0.56 for 1.5 J, 49 fs (31 TW) laser pulse.

The laser guiding performance with the identical data set is also shown in Fig. 4.11. The tendency of higher intensity laser pulses to provide smaller output spot sizes and lower losses was observed. In theory, higher intensity laser pulses were expected to loose more energy via wakefield generation. A possible explanation for the results is as follows. As shown in Section 4.3, this 310 μm diameter capillary might have been mismatched to the input laser spot. Relativistic self-focusing or blow-out guiding (see Section 2.2) might be responsible for the smaller output spot size from the higher intensity laser pulses, which consequently led to a lower transmission loss due to the low leakage from the channel. For reference, from Eq. 4.4, one obtains $1.7 \lesssim P/P_c \lesssim 5.3$ for $0.84 \lesssim a_0 \lesssim 1.5$ with the laser plasma parameters here. For blow-out guiding, the higher intensity laser is closer to realize blow-out regime. This reduced transmission loss for higher input intensity shots suggests that an important mechanism of transmission loss is the leakage from the channel in addition to the wakefield generation, especially for lower input intensity pulses. With higher input intensity or shorter pulse duration, leakage from channel was reduced by the help of relativistic self-focusing, and energy deposition onto the plasma via wakefield generation may be enhanced. If the leakage improvement was larger than the enhancement of energy deposition due to wake generation, overall transmission loss would be improved with higher input intensity of laser pulse as observed. Note that guiding performance has

to be considered preliminary as discussed in Section 4.3, and errorbars are larger than variations. Furthermore, nonlinear depletion may cause stronger depletion in the vicinity of the propagation axis ($r = 0$) and less depletion on the edge, leading to the transverse laser profile being flattened. This effect was not taken into account on the analysis.

Overall, this operation regime showed large fluctuation $\gtrsim 20\%$ in the output spot size and transmission loss, suggesting unstable operation. Due to the small number of shots with e-beams, the pulse duration or input intensity dependence of the e-beam properties such as e-beam energy or total charge is not discussed with this data set.

Laser intensity dependence was also studied with higher plasma density, $\simeq 4.5 \leqq n_0 \leqq 4.8 \times 10^{18}$ cm^{-3}, where the self-injection process was stabilized. The injection probability and guiding performance versus input laser intensity are shown in Fig. 4.12, and e-beam properties versus input laser intensity are shown in Fig. 4.13. Here, the laser pulse duration was fixed at ~ 37 fs, and, therefore, the change in input laser intensity was only from the fluctuation of the input laser energy. The discharge delay was $260 < t_{dsc} < 290$ ns.

With this higher plasma density, self-injection was stabilized to above $> 90\%$ and did not show strong dependence on the laser input intensity, as shown in Fig. 4.12(a). Since the discussion of the density dependence is presented in Section 4.6.4, here the discussion is focused on the intensity dependence. For laser guiding, one can see from Fig. 4.12(b) that the output spot size was clearly affected by the input laser intensity. There are two possible scenario for this result. One possibility as discussed early in this Section, the relativistic self-focusing of the laser pulse or blow-out guiding played some role with this higher plasma density as well ($6.3 \lesssim P/P_c \lesssim 7.7$ for $1.47 \lesssim a_0 \lesssim 1.61$). The transmission loss also showed similar dependence on the input laser intensity. This is the same trend observed from the lower density case (see Fig. 4.11), and, therefore, an important mechanism for the transmission loss was probably again the leakage from channel. The other scenario is that the lower intensity laser pulses actually generated stronger wakefields. In the nonlinear regime, laser pulse evolution can occur via the interaction between the laser pulse and the wakefield generated by the laser pulse. The larger output spot size may have not from poor guiding quality but from stronger depletion. This scenario is discussed more in the following Sections.

Resultant e-beam properties showed a mild dependence on the input intensity, and fluctuations of all parameters were large, and especially so for the total charge ($\sim 100\%$)
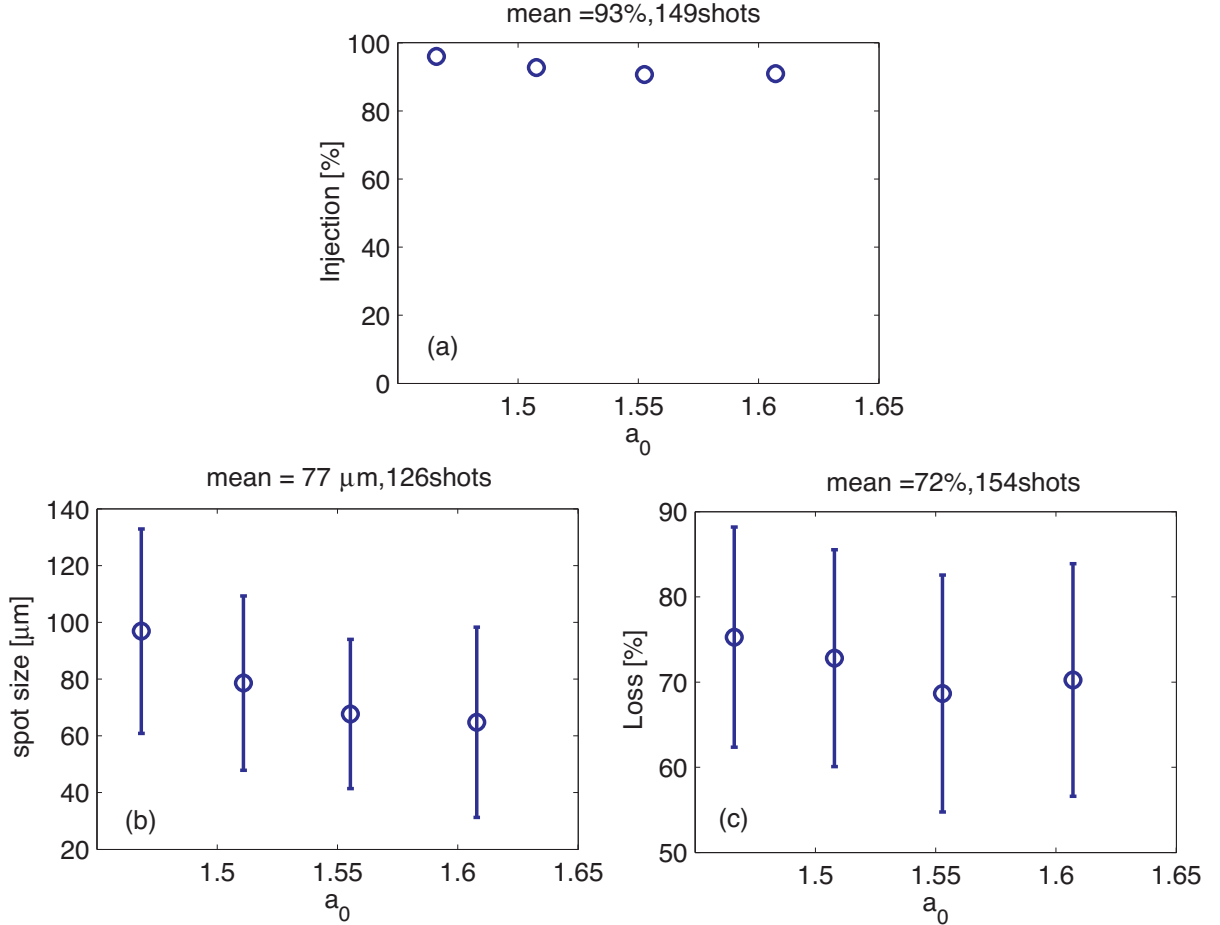
Figure 4.12: Laser input intensity dependence of the injection probability (a), the laser output spot size (b), and the transmission energy loss (c), for 310 μm diameter capillary. The input laser plasma parameters were $\simeq 4.5 \leqq n \leqq 4.8 \times 10^{18}$ cm^{-3}, $260 < t_{dsc} < 290$ ns, $U_{Lin} \sim 1.6$ J with 6.3% fluctuation, and $\tau_L \simeq 37$ fs, which gave $P \sim 43$ TW ($a_0 \simeq 1.5$) on average. Shots with $r_{in} < 11$ μm were selected.

as shown in Fig. 4.13(c). Overall, relatively high charge (~ 15 pC), large divergence (~ 3.5 mrad), high energy e-beams (~ 430 MeV) with large energy spread were observed from this parameter regime. The beam divergence showed an interesting trend, as shown in Fig. 4.13(d). The smaller divergence e-beams were observed at higher input laser intensity. From the discussions presented in Chapter 2, a stronger wakefield generated by higher a_0 may provide smaller beam divergence due to the suppressed phase region of the radial defocusing field.

If operation is in the blow-out regime, the smaller laser spot size may provide smaller
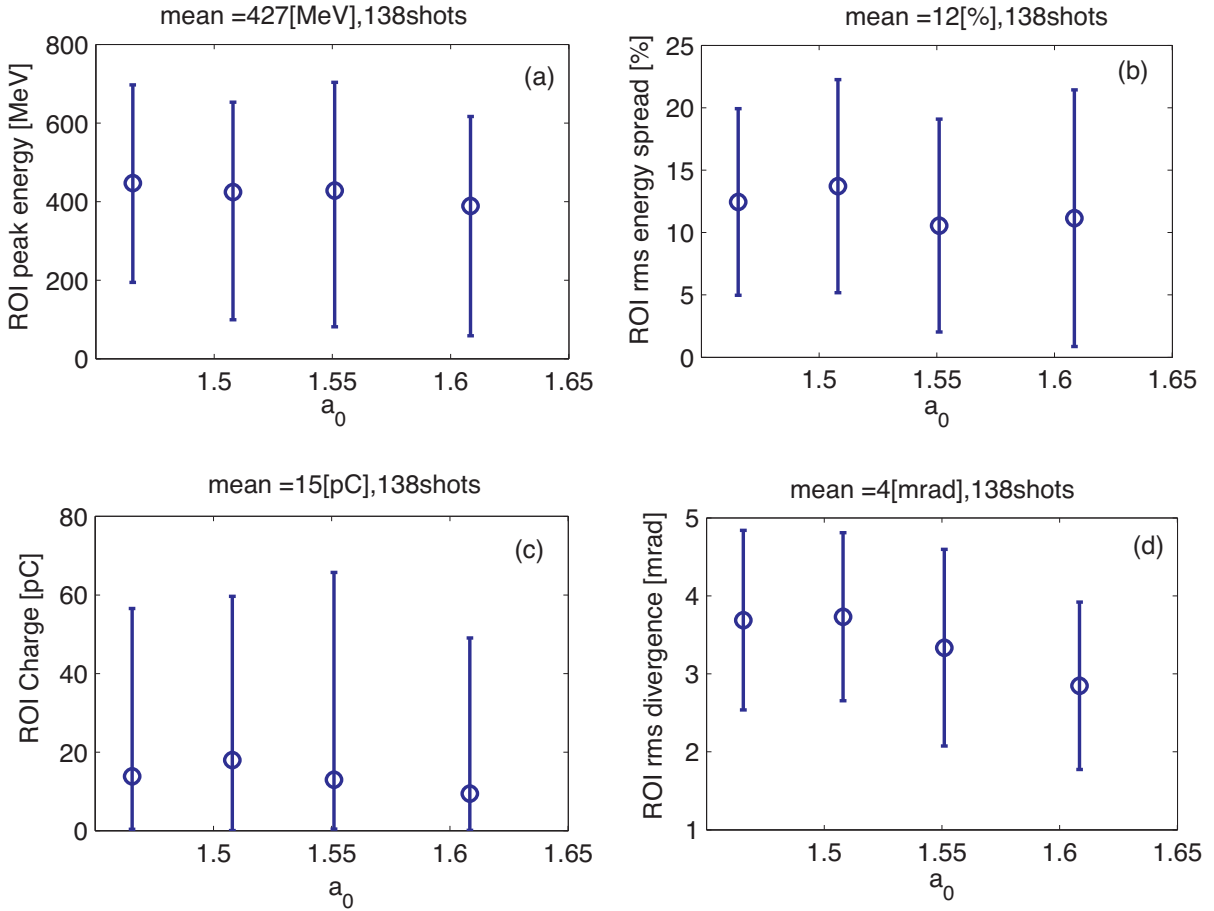
Figure 4.13: E-beam parameters, namely the peak energy (a), energy spread (b), total charge (c), and beam divergence (d) for 310 μm diameter capillary. The input laser plasma parameters were $\simeq 4.5 \leqq n \leqq 4.8 \times 10^{18}$ cm^{-3}, $260 < t_{dsc} < 290$ ns, $U_{Lin} \sim 1.6$ J with 6.3% fluctuation, and $\tau_L \simeq 37$ fs, which gave $P \sim 43$ TW ($a_0 \simeq 1.5$) on average. Shots with $r_{in} < 11$ μm were selected, the ROI image was used for the analysis of e-beam properties, and the maximum and minimum values are shown by errorbars for (a) and (c) instead of the standard deviation.

divergence. This scenario fits the observation of the output spot size shown in Fig. 4.12(b). For 1.6 J laser to satisfy the blow-out condition Eq. (2.55) with $n_0 = 4.6 \times 10^{18}$, the laser pulse has to be focused to $r_0 \sim 10$ μm and $\tau_L = 15$ fs ($a_0 \sim 5.6$). Although such a drastic modulation was observed from PIC simulations [195], no experimental evidence has been observed yet. Another possible explanation for smaller beam divergence with higher input intensity would be space charge effect of the injected electrons [109]. If space charge of the injected electron beam is stronger than the radial focusing force from the wakefield,

e-beam divergence may blow-up. Trends seen from Figs. 4.12(c) and (d) fits this scenario.

Overall, the mean (maximum) output total energy U_b was around 5 mJ (80 mJ), which was $\sim 0.3\%$ (1.2%) of the input laser energy. The operation was not stable, all the e-beam properties were observed to exhibit large fluctuations. The e-beams from this parameter regime was sometimes quasi-monoenergetic, and sometimes broadband. Although there is no "typical" beam in this regime due to the large fluctuation, single shot spectra for 2 representative e-beams are shown in Fig. 4.14. One can see that a quasi-monoenergetic beam with peak energy of 540 MeV in Fig. 4.14(a), and a large beam divergence, broadband e-beam which possibly consisted of more than two separate micro bunches in Fig. 4.14(b).
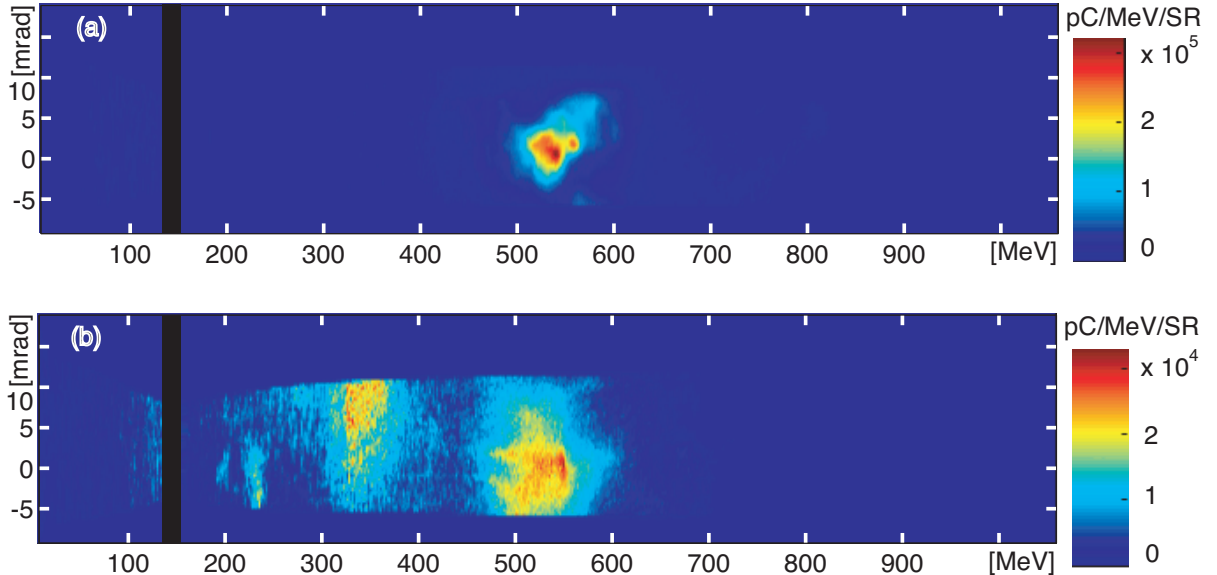
Figure 4.14: Representative single shot e-beam spectra from the regime described in Fig. 4.13. (a): The input laser plasma parameters for this shot were $n_0 \simeq 4.8 \times 10^{18}$ cm^{-3}, $t_{dsc} \sim 274$ ns, $U_{Lin} \sim 1.4$ J, and $\tau_L \simeq 37$ fs, which gave $P \sim 37$ TW ($a_0 \simeq 1.4$). The e-beams contained a total charge of 38 pC, and the beam divergence was 3.6 mrad. The peak energy was 540 MeV, with energy spread of 6.2% (rms) which was resolved with 2.5% resolution. The transmission loss was $\sim 78\%$, and e-beam total energy was 21 mJ, which gives $U_{wake}^{1st} > 180$ mJ. The maximum charge density on the LANEX-FB was < 0.3 pC/mm^2. (b): The input laser plasma parameters for this shot were $n_0 \simeq 4.8 \times 10^{18}$ cm^{-3}, $t_{dsc} \sim 279$ ns, $U_{Lin} \sim 1.6$ J, and $\tau_L \simeq 37$ fs, which gave $P \sim 43$ TW ($a_0 \simeq 1.5$). The e-beams contained a total charge of > 20 pC. The beam divergence was > 6 mrad (overfilled). The maximum charge density on the LANEX-FB was < 0.03 pC/mm^2.

A plasma density of $\simeq 4.8 \times 10^{18}$ cm^{-3} and input laser intensity of $a_0 \sim 1.4$ give non-linear dephasing length of $L_{dph}^{nl} \sim 0.7$ cm (Eq. 1.4), and non-linear dephasing limited total energy gain of $\Delta W_{dph}^{nl} \sim 350$ MeV (Eq. 1.7), which are shorter than the total interaction length, and lower than the measured energy shown in Fig. 4.14(a), respectively. This suggests that the injection occurred close to the end of the capillary, and that the laser pulse underwent severe transverse and longitudinal modulation, leading to an increase in intensity. The large fluctuation in the output spot size could have come from the transverse oscillation of the laser pulse envelope. A longitudinal modulation may also occur on the scale of characteristic wavelength of the plasma. The resonant condition where the laser pulse length L is matched to the plasma wavelength for the Gaussian shape laser pulse is

$$\lambda_p = \pi L, \tag{4.5}$$

where the laser pulse length L is defined as

$$I(z) \propto \exp\left(-\frac{2z^2}{L^2}\right). \tag{4.6}$$

Here, $I(z)$ is the intensity profile of the laser pulse along the propagation axis z. A conversion for the laser pulse duration with a practical unit is give by L [μm] $\simeq 0.255\ \tau_L$ [fs]. A 37 fs pulse duration gives $\pi L \simeq 30\ \mu$m, which is two times longer than the plasma wavelength $\lambda_p(4.8 \times 10^{18}) \simeq 15\ \mu$m. The laser pulse was hence long enough to suffer from longitudinal modulations. Laser pulse compression in plasma waves was reported with similar laser plasma parameters [196]. In Ref. [196], the laser pulse with ~ 38 fs was focused onto a 3 mm length helium gas jet target, producing focused intensity of $I = 3 \times 10^{18}$ W/cm^2 ($a_0 \sim 1.3$). The fully ionized plasma density was $\sim 6-7.5 \times 10^{18}$ cm^{-3}. Laser pulse compression down to $\simeq 14$ fs was observed. Although the experiments did not utilize a capillary discharge waveguide, the parameter regime was close. For the laser pulse described in Fig. 4.14(a), if the laser intensity reaches $a_0 \sim 1.7$, one obtains $\Delta W_{dph}^{nl} > 500$ MeV. This intensity corresponds to a pulse duration of ~ 23 fs.

As discussed in Chapter 2, if trapping of electrons into the wake occurs instantaneously (giving infinitesimal energy spread at the moment of injection), and neglecting the effect from the rotation in phase space and plasma temperature, there are two other mechanisms

to induce energy spread. One is acceleration off-axis, and the other is the beam loading effect. One can estimate an amount of energy in the wakefield, especially in the first bucket, by using Eqs. 2.66 and assuming that electrons are located in the vicinity of the axis ($r \sim 0$). For the e-beam shown in Fig. 4.14(a), the energy spread of 6.2% gives $\eta_{WB} \sim 0.12$. From 21 mJ of beam total energy, the energy in the first bucket of the wakefield $U_{wake}^{1st} > 180$ mJ was estimated, which corresponds to $\sim 13\%$ of the input laser energy. Note that there are other effects may increase energy spread. If this is the case, the energy spread induced by the beam loading effect becomes smaller, consequently leading to higher estimates of the energy in the wakefield. Therefore, the estimate provided here is the minimum limit (could be only larger) for the energy of the wakefield. Energetics can be shown as

$$
\begin{aligned}
U_{Lin} &= U_{Ltr} + U_{Lls} \\
&= U_{Ltr} + U_b + U_{wake}^{1st} + U_{wake}^{>2nd} + U_{Llk} \ ,
\end{aligned}
\tag{4.7}
$$

where U_{Ltr} is the transmitted laser energy, U_b is the energy of the e-beam, $U_{wake}^{>2nd}$ is the energy of the wake of later than 2nd buckets, and U_{Llk} is the energy loss via leakage from the channel. The estimated relative minimum energy in the beam and 1st bucket of the wake $\hat{U}_{b+w} = (U_b + U_{wake}^{1st})/U_{Lin}$ and U_{wake}^{1st} are shown in Fig. 4.15, where errorbar shows minimum and maximum value instead of the standard deviation. The reason is that this estimate of U_{wake}^{1st} becomes accurate when beam loading effect is the dominant mechanism for the energy spread. Instantaneous injection might have not occurred with the stable manner in this regime, and this estimate gives the minimum value. Therefore, a maximum value may provide more accurate picture of the interaction rather than the mean and standard deviation.

One can see from Fig. 4.15(b) that up to 20% of energy went to the wake and e-beam. The fact that this value did not exceed the laser transmission loss of $\sim 70\%$ [Fig. 4.12(c)] supports accuracy of this estimate model, and accuracy of charge measurements of the GeV ESM in order. If the calibration gave one order higher (lower) charge, the energy in the wake and beam would have exceed the loss of the laser energy (would have been 2%, too small energy compared to the loss of 70%). Due to the nature of this estimation, by taking the maximum value as the representative value, the loss from the leakage and
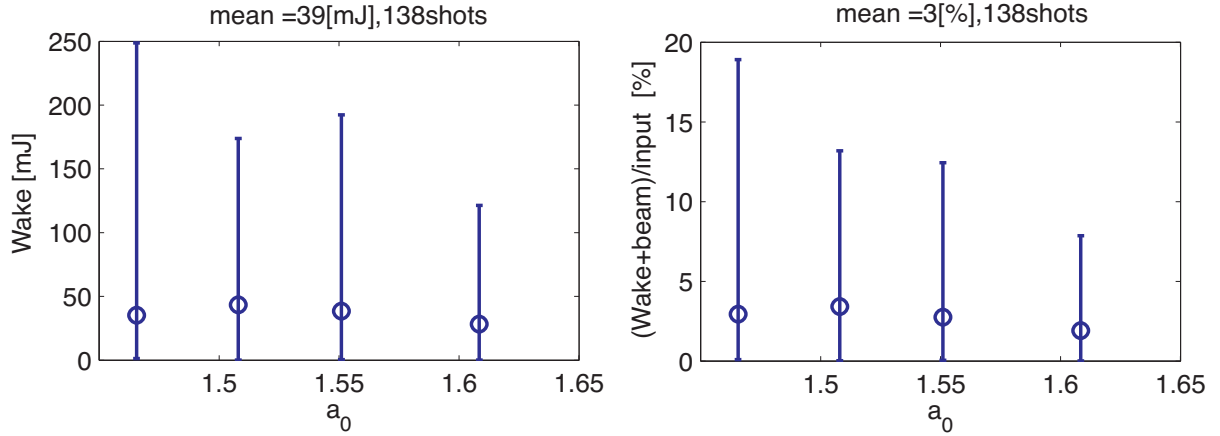
Figure 4.15:   Estimated energy for the 1st bucket of the wake U_{wake}^{1st} (a) and estimated relative energy in the beam and 1st bucket of the wake $\hat{U}_{b+w}$ (b) for 310 μm diameter capillary. The input laser plasma parameters were $\simeq 4.5 \leqq n \leqq 4.8 \times 10^{18}$ cm^{-3}, $260 < t_{dsc} < 290$ ns, $U_{Lin} \sim 1.6$ J with 6.3% fluctuation, and $\tau_L \simeq 37$ fs, which gave $P \sim 43$ TW ($a_0 \simeq 1.5$) in average. Shots with $r_{in} < 11$ μm were selected. Errorbar shows minimum and maximum value instead of the standard deviation.

the tail of the wake was estimated to be $< 50\%$. Note that this could be only smaller. As a summary, considering the precision of the measurements of high power guiding performance, possible existence of the second or more buckets, and the fact that beam loading effect estimates a minimum amount of energy in the first bucket of the wakefield, this estimation of the energetics is reasonable. This simple estimate yields the correct order of magnitude estimates for the energetics, but a more accurate estimation requires more information on laser, plasma, and e-beams.

Back to the discussion of the input intensity dependence, higher wake+beam energy estimates were obtained for lower input intensity in terms of maximum value. For mean value, it did not show strong correlation with input intensity. Instantaneous injection might have occurred more frequently with lower input intensity because it is closer to threshold as discussed in Chapter 2. If injection is instantaneous, the accuracy of this estimates becomes better. It is possible that the wakefield was probed by e-beam in higher accuracy for lower laser input intensity, giving higher amount of estimates. Other possibility is that the lower input laser intensity actually provided stronger wakefield.

Findings from the analysis of the laser parameter dependence are summarized as follows:

- The acceptance of the 310 μm diameter capillary was $r_{in} \sim 11$ μm.

- The 310 μm diameter capillary was probably mismatched to the input laser spot of ~ 25 μm, resulting in substantial loss due to the leakage from channel. Relativistic self-focusing or blow-out guiding of the laser pulse might have helped the guiding performance for higher input intensity.

- Threshold input laser intensity for self-trapping was $a_0 \sim 1.3$ (1.5 J, 49 fs, 31 TW) for $n_0 \simeq 4.0 \times 10^{18}$ cm^{-3}, and $260 < t_{dsc} < 290$ ns. This high threshold is probably due to the larger spot size during the propagation.

- Space charge force of the injected electrons might be the dominant mechanism of induced beam divergence in this parameter regime (requirement for blow-out regime was well above the input laser plasma parameters). Higher amounts of injection led to generation of larger beam divergence.

- The laser pulse evolution during the propagation may be responsible for the generation of high energy e-beams above the analytical limit provided by the initial parameters.

- The estimation of energetics based on the beam loading effect provided reasonable values. Against the laser energy loss of 70%, more than 20% went to the wake and e-beam, and less than 50% went to the leakage and the tail of the wake for the parameter regime shown in Fig. 4.15.

4.6.2 Discharge Delay Dependence

The discharge delay dependence was studied for $n_0 \simeq 4.0 \times 10^{18}$ cm^{-3}. Shown in Fig. 4.16 are the discharge delay dependence of the injection probability (a) and the guiding performance (b) and (c). Electron beam properties, namely the peak energy, energy spread, total charge and beam divergence are shown in Fig. 4.17. The input laser parameters were $U_{Lin} \sim 1.6$ J with 6.2% fluctuation, and $\tau_L \simeq 38$ fs, which gave $P \sim 43$ TW ($a_0 \simeq 1.5$). The ROI image was used for the analysis. Due to the small amount of statistics, sub data sets containing less than 5 shots are also shown on the plots.
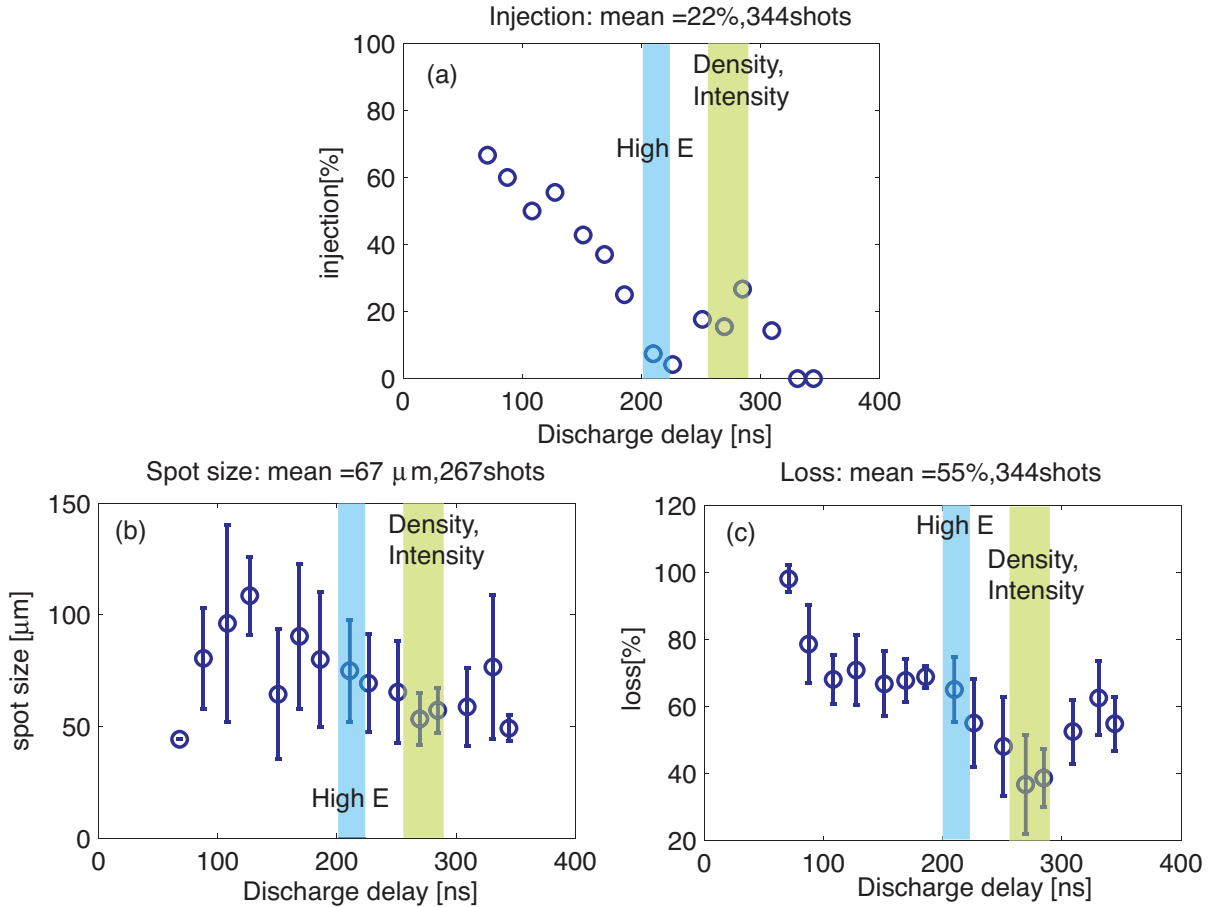
Figure 4.16: Discharge delay dependence of the injection probability (a), the laser output spot size (b), and the transmission energy loss (c), for the 310 μm diameter capillary. The input laser plasma parameters were $n_0 \simeq 4.0 \times 10^{18}$ cm^{-3}, $U_{Lin} \sim 1.6$ J with 6.2% fluctuation, and $\tau_L \simeq 38$ fs, which gave $P \sim 43$ TW ($a_0 \simeq 1.5$). The shots with $r_{in} <$ 11 μm were selected. Due to the small amount of data, subsets of data containing less than 5 shots are also shown on the plots. Shown by green areas are the parameter range discussed in Sections 4.6.1 and 4.6.3, and by blue areas are for Section 4.6.4.

From Figs. 4.16 and 4.17, one can see that the performance showed strong dependence on the discharge delay. The guiding performance was different from lower power operation, shown in Fig. 4.3. The laser transmission loss became substantially high in early discharge delay. The later discharge delay seemed to provide the channel suitable for smaller spot size, as seen in also from low power guiding performance.

For $t_{dsc} < 220$ ns, the earlier the discharge delay, the more frequent self-injection occurred with higher amounts of injected charge. From the discussion presented in Chap-
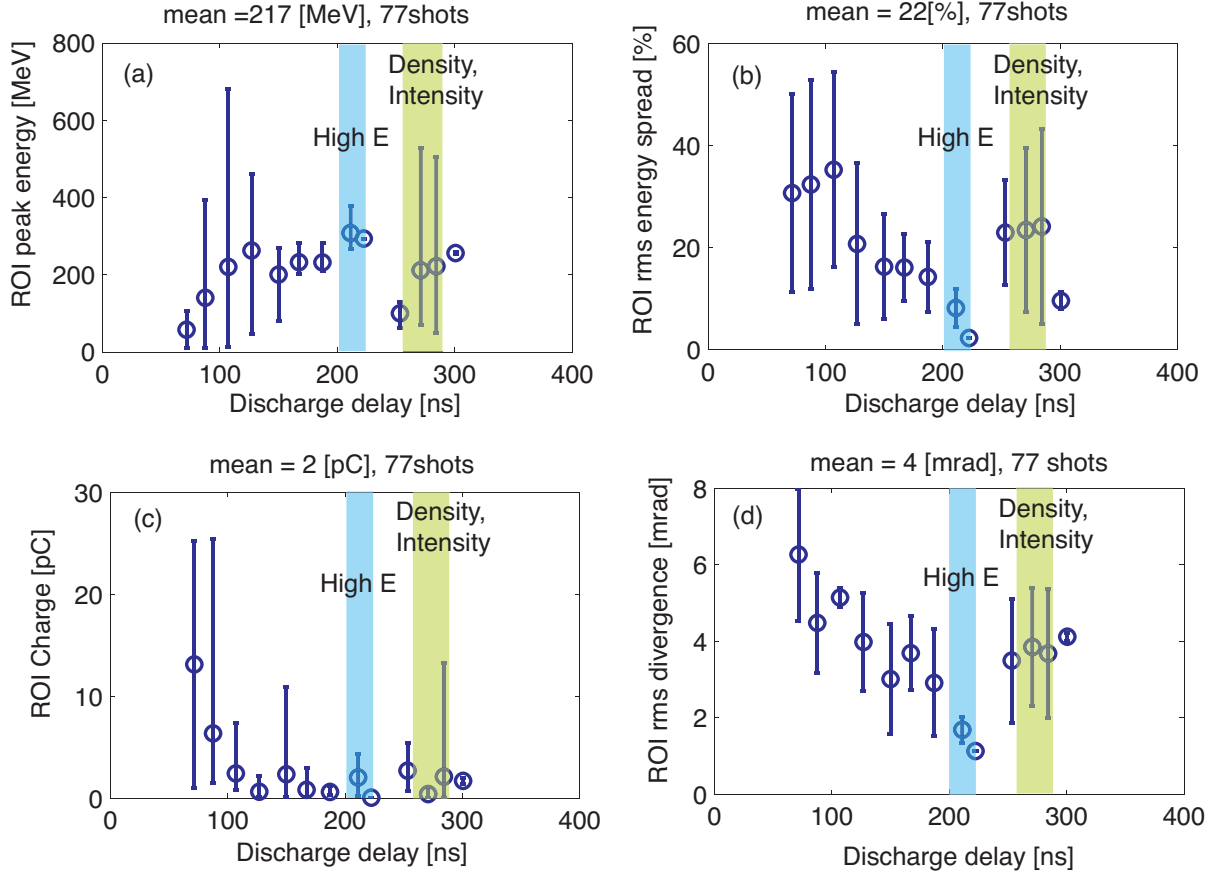
Figure 4.17: Discharge delay dependence of the e-beam properties, namely the peak energy (a), energy spread (b), total charge (c), and beam divergence (d), for 310 µm diameter capillary. The input laser plasma parameters were $n_0 \simeq 4.0 \times 10^{18}$ cm^{-3}, $U_{Lin} \sim$ 1.6 J with 6.2% fluctuation, and $\tau_L \simeq 38$ fs, which gave $P \sim 43$ TW ($a_0 \simeq 1.5$). The shots with $r_{in} < 11$ µm were selected, and the ROI image was used for the analysis. Due to the small amount of data, subsets of data containing less than 5 shots are also shown on the plots. For (a) and (c), errorbars show mininum and maximum value obtained instead of the standard deviation. Shown by green areas are the parameter range discussed in Sections 4.6.1 and 4.6.3, and by blue areas are for Section 4.6.4.

ter 2, the higher injection probability can be explained by the stronger wakefield, or/and higher plasma density. Meanwhile, beam angular divergence was smaller for the later discharge delay. Since the stronger wakefield is expected to provide smaller beam divergence via suppressed defocusing phase region, those trends suggest that plasma density was dropped for later discharge delay.

A typical single shot spectrum for early discharge delay ($t_{dsc} \sim 68$ ns) is shown in Fig. 4.18(a). The actual energy spread of the e-beams from this regime might have been

larger, due to the energies not measured by the GeV-ESM (less than < 10 MeV). Such low peak energy, broadband, and large divergence properties can be explained as follows. The stabilized injection via higher plasma density may have made the point of injection earlier, which led to dephasing. The depasing length of this regime was $L_{dph}^{nl} \sim 0.9$ cm (could have been longer due to the possibly lower plasma density, and higher laser intensity from modulation), which was one third of the whole interaction length. The higher amounts of injection suggests a long lasting injection process. Even if injection occurred instantaneously, the beam loading effect would be significant, resulting in large energy spread e-beam. Since higher charge resulted in larger beam divergence, the space charge effect may be responsible for large beam divergence.

For the later delay, possibly due to the density drop, amounts of trapping become smaller and the point of injection became later. For $t_{dsc} \sim 120$ ns, the plasma density might be optimum such that dephasing length was matched to the acceleration length, resulting in the production of highest energy e-beam. Further later delay, amounts of injection and peak energy became flat ($160 < t_{dsc} < 220$) while injection probability, energy spread and beam divergence kept on decreasing. Drop in the energy spread and injection probability suggests that plasma density still keeps on dropping. Meanwhile, improved guiding performance lead higher a_0 and stronger wakefield, as such electron energy was kept high with shorter acceleration length. A typical single shot spectrum from this regime ($t_{dsc} \sim 200$ ns) is shown in Fig. 4.18(b). Although injection was not stable and charge was somewhat low, moderately high energy beams with smaller divergence and energy spread were obtained from this regime.

With a discharge delay of ~ 200 ns, self-injection almost ceased. Then later timing regime ($t_{dsc} \sim 280$ ns), the self-injection started again with much better guiding performance, smaller output spot size ($\sim 60~\mu$m) and low loss ($\sim 30\%$). This improved guiding performance or/and plasma density back up could be responsible for the self-injection in this regime. A typical single shot spectrum for $t_{dsc} \sim 215$ ns is shown in Fig. 4.18(c). The observation of electron injection with smaller amounts of input laser energy into the plasma, and smaller output spot sizes suggests that leakage from the channel was reduced in this timing, and actual energy deposition into the plasma via wakefield generation may have increased. Although resultant e-beam properties in this regime were comparable to those for $t_{dsc} \sim 140$ ns, guiding performance suggestes that laser to e-beam efficiency
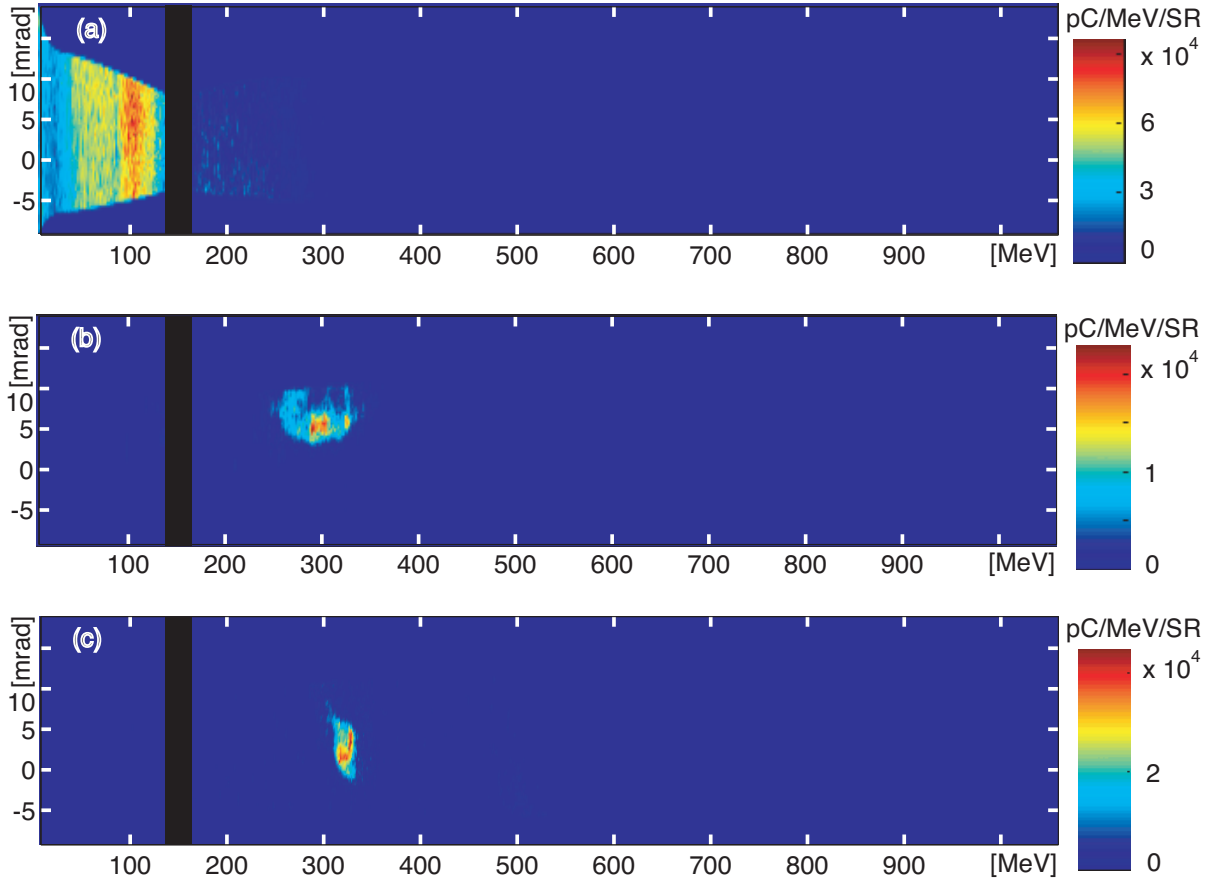
Figure 4.18: Representative single shot e-beam spectra from the regime described in Fig. 4.17. The plasma density was $\simeq 4.0 \times 10^{18}$ cm^{-3}. (a): Shot with the discharge delay of ($t_{dsc} = 68$ ns). The input laser parameters for this shot were $U_{Lin} \sim 1.9$ J, and $\tau_L \simeq 38$ fs, which gave $P \sim 51$ TW ($a_0 \simeq 1.7$). The e-beams contained a total charge of > 29 pC, and the beam divergence was > 5 mrad (overfilled). The peak energy was 107 MeV, with broadband spectrum. The beam total energy was 3 mJ. The maximum charge density on the LANEX-FB was < 0.003 pC/mm^2. (b): Shot with the discharge delay of ($t_{dsc} = 215$ ns). The input laser parameters for this shot were $U_{Lin} \sim 1.8$ J, and $\tau_L \simeq 38$ fs, which gave $P \sim 46$ TW ($a_0 \simeq 1.6$). The e-beams contained a total charge of 1.3 pC, the beam divergence was 2 mrad, and the peak energy was 297 MeV with the energy spread of 12% (rms) which was resolved with 0.6% resolution. The beam total energy was 0.3 mJ, which gives $U_{wake}^{1st} > 1.3$ mJ. The maximum charge density on the LANEX-FB was < 0.005 pC/mm^2. (c): Shot with the discharge delay of ($t_{dsc} = 296$ ns). The input laser parameters for this shot were $U_{Lin} \sim 1.5$ J, and $\tau_L \simeq 38$ fs, which gave $P \sim 41$ TW ($a_0 \simeq 1.5$). The peak energy was 331 MeV with energy spread of 2.6% (rms) which was resolved with 0.9% resolution. The beam total energy was 0.3 mJ, which gives $U_{wake}^{1st} > 5.9$ mJ. The maximum charge density on the LANEX-FB was < 0.015 pC/mm^2. For higher density ($n_0 = \simeq 4.8 \times 10^{18}$ cm^{-3}), typical shots are shown in Fig. 4.14.

was very high because later delay regime provided high energy e-beam with smaller laser transmission loss. On the earlier timing regime, the majority of the loss was probably from the leakage of the plasma channel. The output total energy U_b was around 0.2 mJ, which gives $U_{wake}^{1st} > 10$ mJ for an e-beam with 1% energy spread. The mean energy spread was $\sim 10\%$, as shown in Fig. 4.17(b). Therefore, in this regime, the beam loading effect may have not been a dominant mechanism induced the energy spread, or the energy of the wake was very small ~ 10 mJ.

Findings from the analysis of the discharge delay dependence are summarized as follows:

- The change in the discharge delay, with possible change in plasma density and channel profile, affected both the high power guiding performance and e-beam generation significantly, affecting all the output parameters.

- Injection probability suggests that plasma density was dropping down toward later discharge delay for $80 < t_{dsc} < 200$.

- At early discharge delay, higher plasma density provided stable self-injection, and it probably occurred early in the capillary, leading to the dephasing of e-beams. High charge, large divergence, large energy spread beams observed in this regime are from the convolution of long-lasted injection process, heavy beam loading, and space charge effect.

- Guiding performance was improved toward the later discharge delay, which led far more efficient production of electron beams.

- Although injection process was not stable, high quality e-beams were generated for $t_{dsc} \sim 200$ ns.

4.6.3   Plasma Density Dependence

The plasma density dependence was studied experimentally by changing the backing pressure of the hydrogen feed line. Figure 4.19 shows the plasma density dependence of the injection probability (a), the ouput spot size of the laser pulse (b), the transmission loss of the laser pulse (c), and estimated relative energy in the wake and beam $\hat{U}_{b+w}$
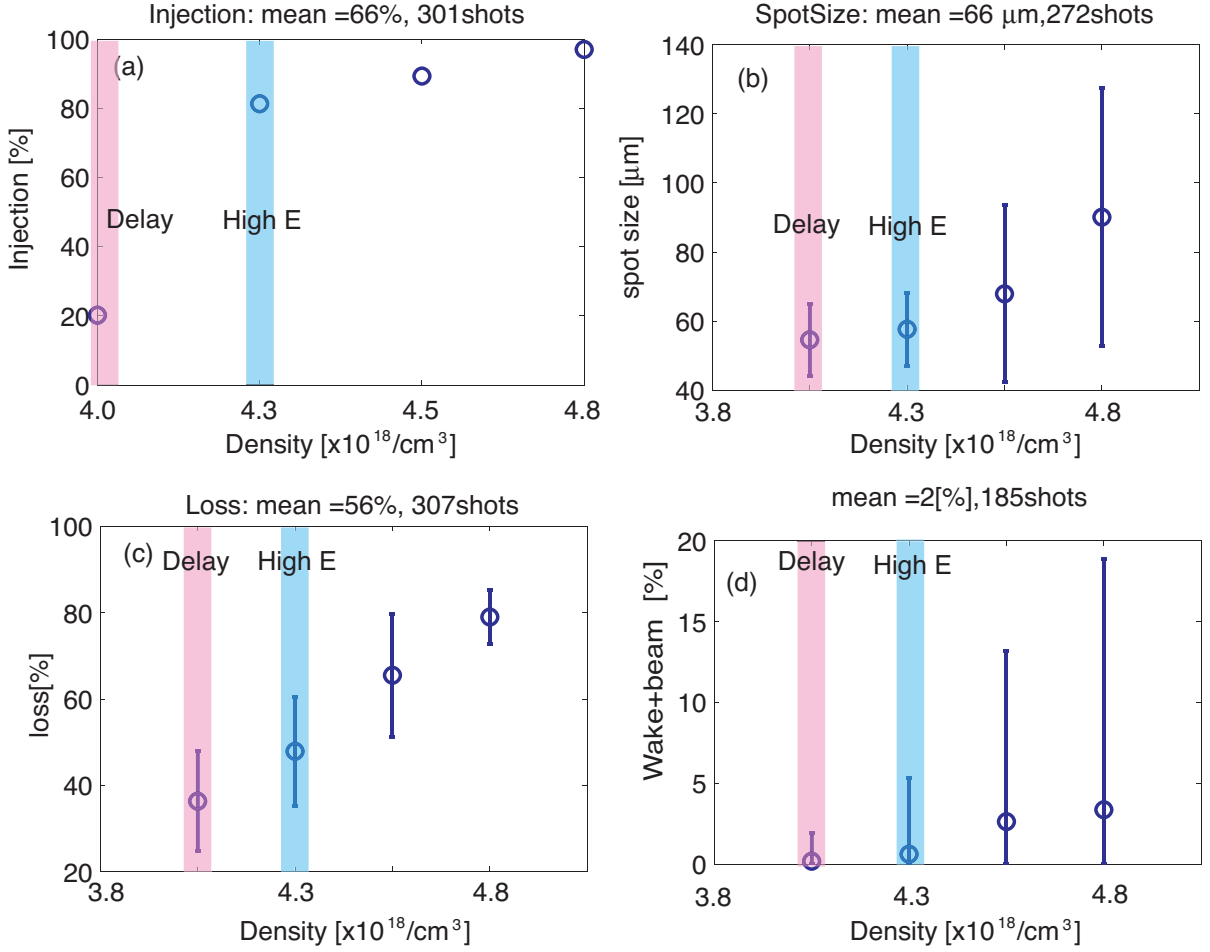
Figure 4.19: Injection probability (a), guiding performance, namely the output spot size (b) and transmission loss (c), and estimated relative energy in the wake and beam $\hat{U}_{b+w}$ (d) as a function of the plasma density for the 310 μm diameter capillary. The input laser plasma parameters were $260 < t_{dsc} < 290$ ns, $U_{Lin} \sim 1.6$ J with 6.3% fluctuation, and $\tau_L \simeq 37$ fs, which gave $P \sim 43$ TW ($a_0 \simeq 1.5$). For (d), errorbars show mininum and maximum value obtained instead of the standard deviation. Shown by red areas are the parameter range discussed in Sections 4.6.2, and by blue areas are for Section 4.6.4.

(d). Electron beam properties, namely the peak energy, energy spread, total charge and beam divergence are shown in Fig. 4.20. The input laser plasma parameters were $260 < t_{dsc} < 290$ ns, $U_{Lin} \sim 1.6$ J with 6.3% fluctuation, and $\tau_L \simeq 37$ fs, which gave $P \sim 43$ TW ($a_0 \simeq 1.5$). Although it is not shown in Fig. 4.19(c) due to a small number of statistics, e-beams were observed at lower plasma densities, down to $\simeq 3.5 \times 10^{18}$ cm^{-3}, where the resultant peak energy and total charge were very low. Representative single shot spectra for $n_0 \simeq 4.0 \times 10^{18}$ cm^{-3} and $n_0 \simeq 4.8 \times 10^{18}$ cm^{-3} are shown in Fig. 4.18(c)
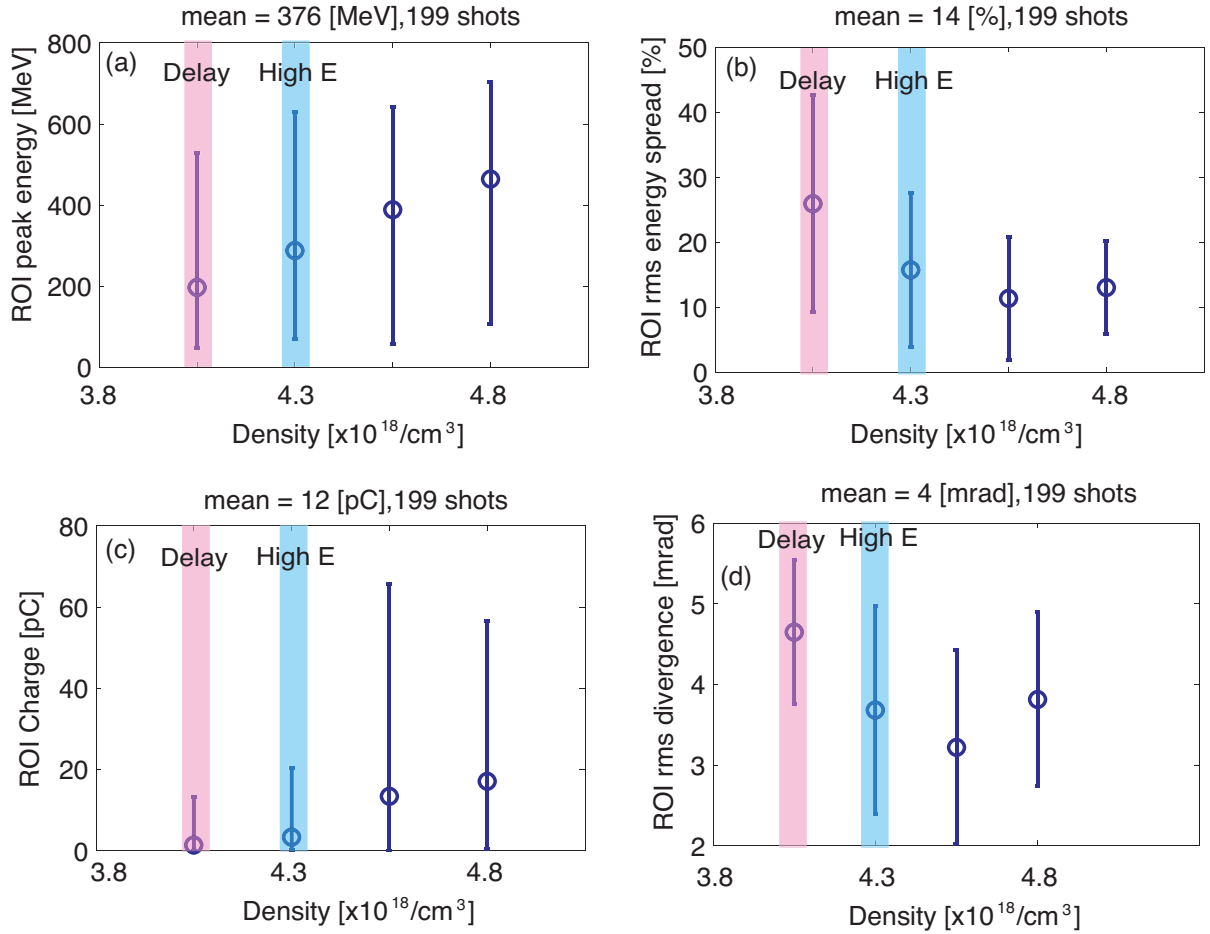
Figure 4.20:   E-beam parameters, namely the peak energy (a), energy spread (b), total charge (c), and beam divergence (d) as a function of the plasma density for the 310 μm diameter capillary. The input laser plasma parameters were $260 < t_{dsc} < 290$ ns, $U_{Lin} \sim 1.6$ J with 6.3% fluctuation, and $\tau_L \simeq 37$ fs, which gave $P \sim 43$ TW ($a_0 \simeq 1.5$). The ROI image was used for the analysis, and shots with $r_{in} < 11$ μm were selected. For (a) and (c), errorbars show mininum and maximum value obtained instead of the standard deviation. Shown by red areas are the parameter range discussed in Sections 4.6.2, and by blue areas are for Section 4.6.4.

and Fig. 4.14, respectively.

One can see that self-injection occurred more frequently with the higher plasma density. With this capillary and the discharge delay, the higher plasma density helped to stabilize self-injection, which follows the results of the phase space analysis presented in Chapter 2.

The output spot size became larger and had larger fluctuation at higher plasma density.

The larger fluctuations of the output spot with the higher plasma density suggests that the laser pulse underwent heavier transverse modulations during the propagation. The transmission loss also increased to almost full depletion for $n_0 \simeq 4.8 \times 10^{18}$ cm^{-3}. The larger spot size for higher density is probably due to the high depletion. Although the guiding performance alone did not elucidate the dominant mechanism for the transmission loss, the resultant e-beam properties shown in Fig. 4.20 imply that a significant amount of laser energy was used for wakefield generation. By the same manner discussed in Section 4.6.1, relative energy in the wake and beam $\hat{U}_{b+w}$ was estimated and shown in Fig. 4.19(d). From the fact that relative loss for the leakage and the tail of the wake $\hat{U}_{lk+t} = \hat{U}_{Ltr} - \hat{U}_{b+w}$ [(c) - (d) for Fig. 4.19] showed slight increase ($40 < \hat{U}_{lk+t} < 60\%$ for $4.0 < n_0^{(18)} < 4.8$), higher density may have not improved guiding performance, but simply led to generation of stronger wakefield.

The higher plasma density led to higher amounts of self-injected charge as shown in Fig. 4.20(c), but did not result in lowering the peak e-beam energy from the shorter dephasing length [see Fig. 4.20(a)] nor enlarge the energy spread [see Fig. 4.20(b)] via the beam loading effect. This suggests generation of stronger wakefields for higher plasma density, probably via the modulation of the laser pulse as discussed in Section 4.6.1. The larger fluctuations observed in the output spot size suggest that the laser pulse underwent significant transverse modulation. Via enhanced longitudinal and transverse modulations, especially longitudinal pulse compression, laser intensity became higher, and stronger wakefield was generated.

The stronger wake generation with $n_0^{(18)} \simeq 4.8$ suggests that higher density enhanced laser pulse evolution or/and this density provided more optimum nonlinear plasma wavelength for wake generation than $n_0^{(18)} \simeq 4.0$. The optimum (probably resonant) condition for nonlinear plasma wave generation (matching of pulse length and plasma wavelength) is not simple when a laser pulse length evolves. The nonlinear plasma wavelength depends on a laser intensity a_0 as discussed in Chapter 2, which keeps on changing due to the pulse compression and energy deposition. The optimum density may depend on the input laser duration, intensity, and interaction length. From the results, plasma length was too short for $n_0^{(18)} \simeq 4.0$ to be resonant. To examine this scenario, here we consider a particular case shown in Fig. 4.14(a). First, the linear plasma wavelength for $4.0 < n_0^{(18)} < 4.8$ is $16.7 < \lambda_p < 15.2$ µm. The input laser pulse was 37 TW, 37 fs ($a_0 \sim 1.4$), which gives non-

linear plasma wavelength $17.8 < \lambda_p^{nl} < 16.2 \ \mu$m, and resonant pulse length $\pi L = 29.6 \ \mu$m. For these initial conditions, $n_0^{(18)} = 4.0$ seems to be better for wake generation. As discussed in Section 4.6.1, here we consider the laser pulse compressed down to 23 fs, giving $a_0 = 1.7$. These parameters give $18.4 < \lambda_p^{nl} < 16.7 \ \mu$m, and $\pi L = 18.4 \ \mu$m. This is exactly the resonant condition for $n_0^{(18)} = 4.0$. If pulse was shorter than 23 fs, the non-linear plasma length would become longer than pulse length πL, then density $n_0^{(18)} > 4.0$ might provide better condition for wake generation. Suggested in Section 4.6.2 was the possible density drop for $t_{dsc} > 150$. Although the absolute value of density drop is hard to evaluate from available information, any drop will result in $\lambda_p^{nl} > \pi L$, favoring higher initial density.

Although the resultant beam divergence was large (> 3 mrad), with large fluctuations, the higher plasma density helped the collimation of the beam somewhat. The stronger wakefield suppresses the defocusing phase region, as discussed in Chapter 2. The stronger field also compensates the space charge effect. Then, collimated of the e-beam reduces the energy spread introduced by the off-axis effect, and the stronger wakefield reduce the beam loading effect. Those are the probable explanations of reduced energy spread shown in Fig. 4.20(b). The optimum density to acquire the highest e-beam quality was $n_0 \simeq 4.5 \times 10^{18} \ \mathrm{cm}^{-3}$, because the beam energy spread and beam divergence started to increase at $n_0 > 4.5 \times 10^{18} \ \mathrm{cm}^{-3}$ probably due to the excessive injection resulting in heavier beam loading and larger space charge effect.

Findings from the analysis of the plasma density dependence are summarized as follows:

- The higher plasma density led to larger output spot sizes and higher transmission loss, probably due to the increase of the energy deposition via wakefield generation. The higher plasma density may have not improved guiding performance in terms of the loss due to the leakage from the channel.

- The higher plasma density stabilized the injection process, with higher amounts of injected electrons as expected from the theory.

- The higher plasma density led to the generation of e-beams with higher total charge, and higher peak energy. The enhanced longitudinal compression of laser pulse during

the propagation with higher plasma density may be responsible for the generation of stronger wakefield.

- In terms of the beam quality, the optimum density was $n_0 \simeq 4.5 \times 10^{18}$ cm^{-3}.

4.6.4   High Energy Beams

The e-beam properties, namely the peak energy and total charge were analyzed in the vicinity of the parameter set where high energy e-beams, such as a GeV beam shown in Fig. 4.4, were generated to understand the underlying mechanisms. A GeV beam shown in Fig. 4.4 was found with parameters $n_0 \simeq 4.3 \times 10^{18}$ cm^{-3}, and $t_{dsc} \sim 216$ ns (high energy regime, blue rectangle). Shown in Fig. 4.21 are the peak energy (a), total charge (b), energy spread (c), and beam divergence (d) in colormap versus the discharge delay (horizontal axis) and plasma density (vertical axis). It basically shows the discharge delay dependence (Section 4.6.2, orange rectangle), plasma density dependence (Section 4.6.3, red rectangle), and high energy regime (blue rectangle) at once. The input laser plasma parameters were $n_0 \simeq 4.0$ to 4.8×10^{18} cm^{-3}, $80 < t_{dsc} < 290$ ns, $U_{Lin} \sim 1.6$ J with 6.3% fluctuation, and $\tau_L \simeq 37$ fs, which gave $P \sim 44$ TW ($a_0 \simeq 1.5$). The ROI image was used for the analysis.

With the 310 μm diameter capillary, most of high energy beams (> 700 MeV) were found with $t_{dsc} \simeq 210$ ns, and $n_0 \simeq 4.3 \times 10^{18}$ cm^{-3}. From the discharge delay dependence discussed in Section 4.6.2, relatively high energy (300 MeV), small energy spread ($< 10\%$), small beam divergence (~ 2 mrad), and small charge (~ 1 pC) beams were obtained with unstable injection ($< 10\%$) for $t_{dsc} \simeq 210$ ns and $n_0 \simeq 4.0 \times 10^{18}$ cm^{-3}. With higher density ($n_0 \simeq 4.3 \times 10^{18}$ cm^{-3}), injection was somewhat stabilized ($\sim 40\%$) and electron energy became higher (~ 500 MeV). This trend was seen from the plasma density dependence for $t_{dsc} \simeq 270$ ns. The different characteristic is the fluctuation in the peak energy. The peak energy for the high energy regime exhibited a large fluctuation (~ 220 MeV, not shown), which is much larger than that for $t_{dsc} \simeq 270$ ns and $n_0 \simeq 4.8 \times 10^{18}$ cm^{-3} (~ 120 MeV, not shown).

Those observations suggest a following scenario for the generation of high energy e-beams. With $n_0 \simeq 4.3 \times 10^{18}$ cm^{-3} and $a_0 \sim 1.5$, the dephasing limited energy is $\Delta W_{dph}^{nl} \sim 440$. (Although decrease in the plasma density was suggested at this discharge
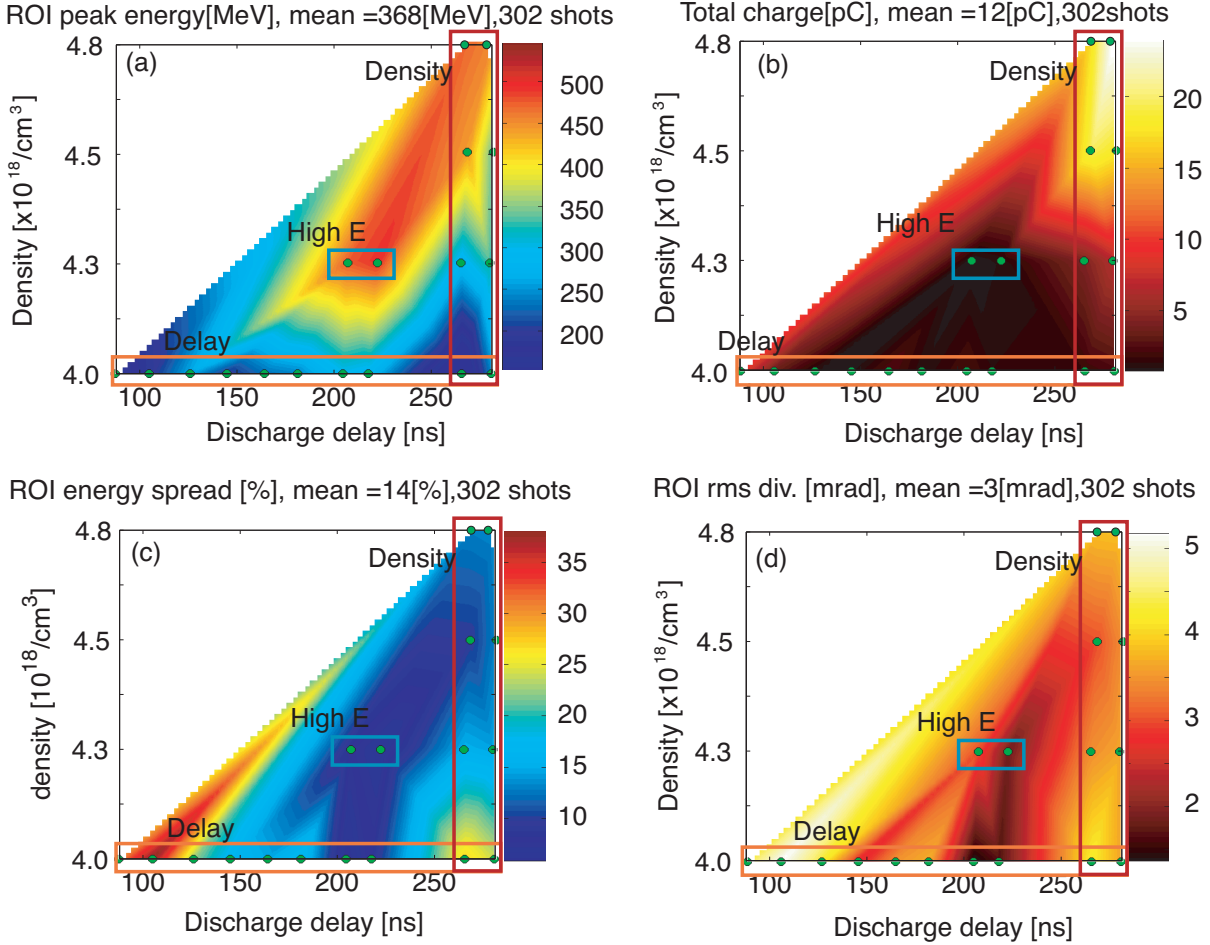
Figure 4.21: Peak energy (a), total charge (b), energy spread (c), and beam rms angular divergence in color map versus the discharge delay (horizontal axis) and plasma density (vertical axis). The input laser plasma parameters were $n_0 \simeq 4.0$ to 4.8×10^{18} cm^{-3}, $80 < t_{dsc} < 290$ ns, $U_{Lin} \sim 1.6$ J with 6.3% fluctuation, and $\tau_L \simeq 37$ fs, which gave $P \sim 44$ TW ($a_0 \simeq 1.5$). The solid circles show where the data actually exists. The ROI image was used for (a), (c), and (d), and shots with $r_{in} < 11$ μm were selected. Shown by the blue rectangle is the parameter range where high energy beams were found, and by the orange and red rectangles are the areas where discussed in Sections 4.6.2 and 4.6.3, respectively.

delay in Section 4.6.2, no change was assumed here due to the limited data for evaluation.) As has been discussed, the modulation of the laser pulse may have been critical for the generation of higher energy ($> \Delta W_{dph}^{nl}$) e-beams. Total gain of > 1000 MeV can be attained with the laser intensity of $a_0 \sim 2.3$, which corresponds to a 16 fs, 1.6 J laser pulse (no transverse modulation or density drop are assumed). By increasing plasma

density from $n_0^{(18)}$ from 4.0 to 4.3, the operation entered a highly nonlinear regime, where the pulse evolution was significant. While it maintained small divergence, small energy spread, and small charge, injection was somewhat stabilized and the peak energy and its fluctuation were increased significantly. The difference from $t_{dsc} \sim 270$ ns regime was probably the guiding performance. Guiding performance was better for $t_{dsc} \sim 270$ ns as discussed in Section 4.6.4 providing better efficiency. With moderate performance of guiding for $t_{dsc} \sim 210$ ns, amounts of injection kept low (~ 1 pC), leading to low beam loading and space charge effects. This de-tuned condition provided unstable (close to threshold of self-trapping), but high energy and high quality e-beams. Unfortunately, $n_0 > 4.3 \times 10^{18}$ cm^{-3} was not explored for $t_{dsc} \sim 210$ ns, it could have provided more stable or/and higher energy electron beams.

For energetics, consider the shot shown in Fig. 4.4. Observed energy spread was small (2.6%) and resolution limited, suggesting there was almost no beam loading. For example, if a 1% energy spread is induced by the beam loading effect for this shot, $U_{wake}^{1st} > 120$ mJ, which is about 10% of the input energy. The transmission loss for this particular shot was $\sim 60\%$, which is larger than the estimated wake energy in 1st bucket. Since the beam loading on the first bucket was low, later buckets could be significant, leading to multiple injections. The energy for (leak + tail) $\hat{U}_{lk+t}$ of $< 50\%$ is comparable with the value from other parameter regime (Section 4.6.3). Figure 4.22 shows relative energy in the wake and e-beam (a), and peak energy (b) versus the normalized vector potential a_0. The wake energy showed strong dependence on the laser input intensity, suggesting that the pulse evolution strongly depends on the initial condition of laser. The efficiency shown in Fig. 4.22 is somewhat smaller than that shown in Fig. 4.19(d), which is consistent to the discussion in the previous paragraph. For the discharge delay of $200 < t_{dsc} < 220$, input laser energy of $1.5 < U_{Lin} < 1.7$, and $n_0 \simeq 4.3 \times 10^{18}$ cm^{-3}, the mean e-beam energy was found to be $\simeq 670$ MeV with a standard deviation of $\simeq 190$ MeV. Statistically, the probability of observing an e-beam above 860 MeV (1σ) was $\simeq 16\%$, and above 1000 MeV (1.7σ) was $\simeq 4.5\%$.

Findings from the analysis of the high energy regime are summarized as follows.

- High energy (700 MeV) beams with small energy spread, small beam divergence, and small charge were found for $n_0 \simeq 4.3 \times 10^{18}$ cm^{-3}, and $t_{dsc} \sim 210$ ns.
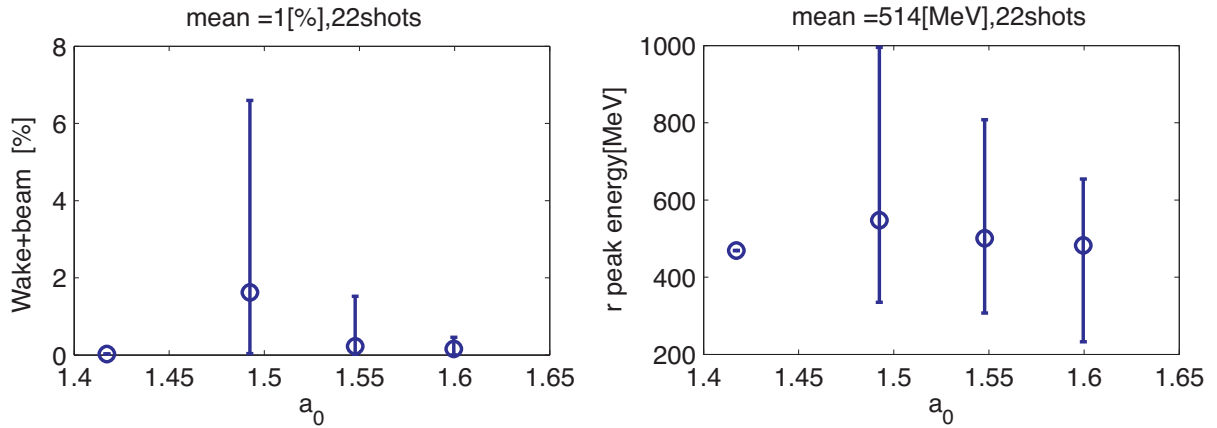
Figure 4.22: Relative energy in the wake (1st period) and e-beam (a), and peak energy (b) versus the normalized vector potential a_0. The input laser plasma parameters were $n_0 \simeq 4.3 \times 10^{18}$ cm^{-3}, $200 < t_{dsc} < 220$ ns, $U_{Lin} \sim 1.6$ J with 6.3% fluctuation, and $\tau_L \simeq 37$ fs, which gave $P \sim 44$ TW ($a_0 \simeq 1.5$). Shots with $r_{in} < 11$ μm were selected.

- Generation of high energy e-beams relied on the pulse evolution, which resulted in the unstable operation.

- In order to generate high energy e-beams with high quality (small energy spread, small beam divergence), optimum guiding performance may not always be best. The high quality beams were obtained where guiding performance was not optimized, led to the smaller amounts of electron injection, and generation of high quality e-beams.

4.7   Analysis of Experiments Using the 225 μm Diameter Capillary

As stated in Section 4.4, stable generation of $\simeq 0.5$ GeV e-beams was observed from a CDG-LWFA with the 225 μm diameter capillary. The probability of the self-injection, and the electron beam properties [beam peak energy T_{pk} (MeV), relative energy spread $\hat{T}$ (%), and total charge Q_{tot} (pC)] were analyzed in the vicinity of the parameter set where the stable generation of half-GeV beams (see Fig. 4.5 for a typical spectrum) was observed. The probability and all the e-beam prameters were found to be sensitive against the discharge delay and input laser intensity. Shown in Fig. 4.23 are the injection probability, total charge, beam peak energy, and energy spread (rms) versus the discharge
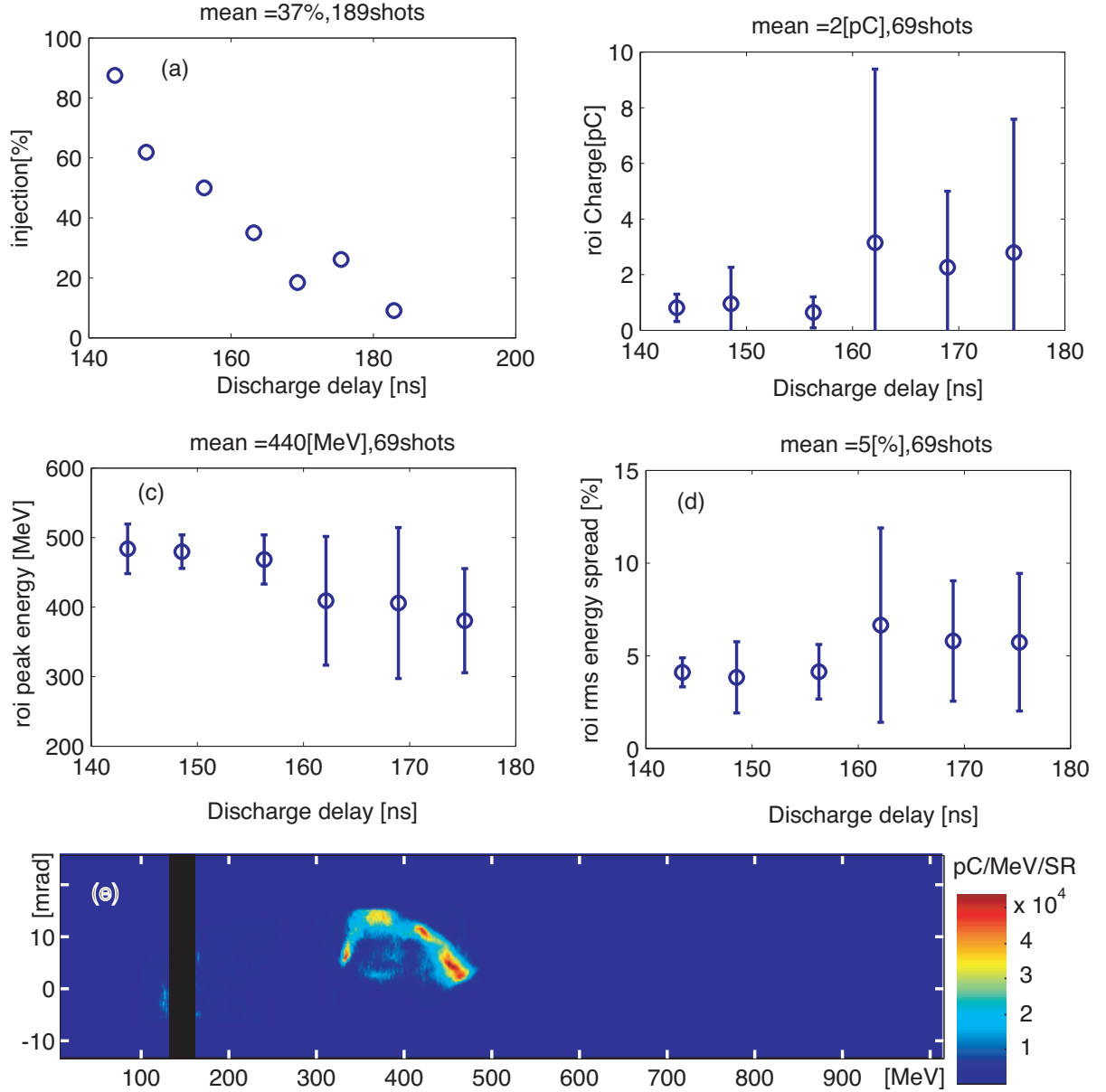
Figure 4.23: Discharge delay dependence of (a) injection probability, (b) total charge, (c) peak energy, and (d) rms energy spread. The plasma density was 3.5×10^{18} cm^{-3}. Laser pulse duration was 81 fs with the input energy of 0.87 J with 3.9% fluctuation, which gave the average input power of 11 TW ($a_0 \simeq 0.73$). Shown in (e) is an example of out-of-phase shot. The input laser plasma parameters for this particular shot were $t_{dsc} \sim 167$ ns, $U_{Lin} \sim 0.95$ J, and $\tau_L \simeq 82$ fs, which gave $P \sim 12$ TW ($a_0 \simeq 0.77$). The peak energy was 453 MeV, and total charge was 8.0 pC. Discharge delay earlier than 140 ns was not explored in the experiments.

delay. The ROI images were used for the analysis. The input laser plasma parameters were $n_0 \simeq 3.5 \times 10^{18}$ cm^{-3}, $U_{Lin} \sim 0.87$ J with 3.9% fluctuation, and $\tau_L \simeq 81$ fs, which gave $P \sim 11$ TW ($a_0 \simeq 0.73$). Here, laser pulses with input energy, U_{Lin} between 0.82 and 0.96 J were selected, to separate the discharge delay dependence from laser parameter dependence.

From Fig. 4.23, one can see that the high energy ($\simeq 0.5$ GeV), low charge ($\simeq 1$ pC), and small energy spread ($\simeq 4$ %) e-beams were observed with high probability ($\simeq 90$ %) when the discharge delay was around 145 ns. If the discharge delay was not in the right regime, the injection probability went down, and resultant electron beams had higher total charge and lower peak energy with larger energy spread. A few ns shift in the discharge delay significantly reduced the probability of the self-injection. For later timing (> 165 ns), both the injection probability and all the e-beam parameters became unstable. The stabilized injection with lower amount of injected charge is an interesting regime. Increasing the plasma density stabilized self-injection with higher amounts of injected electrons in the case of the 310 μm Diameter Capillary (see Fig. 4.21). This suggests that the changing discharge delay is physically different from changing only plasma density. As discussed in Section 4.3, a small change in the channel profile may be critical for injection process. Shown in Fig. 4.23(e) is a typical broad band shot from later discharge delay. The input laser plasma parameters for this particular shot were $t_{dsc} \sim 167$ ns, $U_{Lin} \sim 0.95$ J, and $\tau_L \simeq 82$ fs, which gave $P \sim 12$ TW ($a_0 \simeq 0.77$). The peak energy was 453 MeV, and total charge was 8.0 pC. For the shot shown in Fig. 4.5, the input laser plasma parameters were $t_{dsc} \sim 144$ ns, $U_{Lin} \sim 0.87$ J, and $\tau_L \simeq 75$ fs, which gave $P \sim 12$ TW ($a_0 \simeq 0.76$).

The laser intensity dependence from fluctuations in the vicinity of stable half-GeV regime was analyzed in a similar manner as the discharge delay dependence, and is shown in Fig. 4.24. The input laser energy was 0.90 J with 14% fluctuation, and the discharge delay was selected at $142 < t_{dsc} < 162$ ns to extract only laser intensity dependence. Other parameters were $n_0 \simeq 3.5 \times 10^{18}$ cm^{-3}, and $\tau_L \simeq 38$ fs. The ROI images were used for the analysis.

The input laser intensity dependence shows that $\simeq 0.5$ GeV electron beams containing $\simeq 1$ pC were generated with laser power below $a_0 \simeq 0.78$. Above that laser intensity, electron beam energy started to decrease with broader spread while total charge of the beam increases, consistent with the higher amount of charge resulting in beam loading,
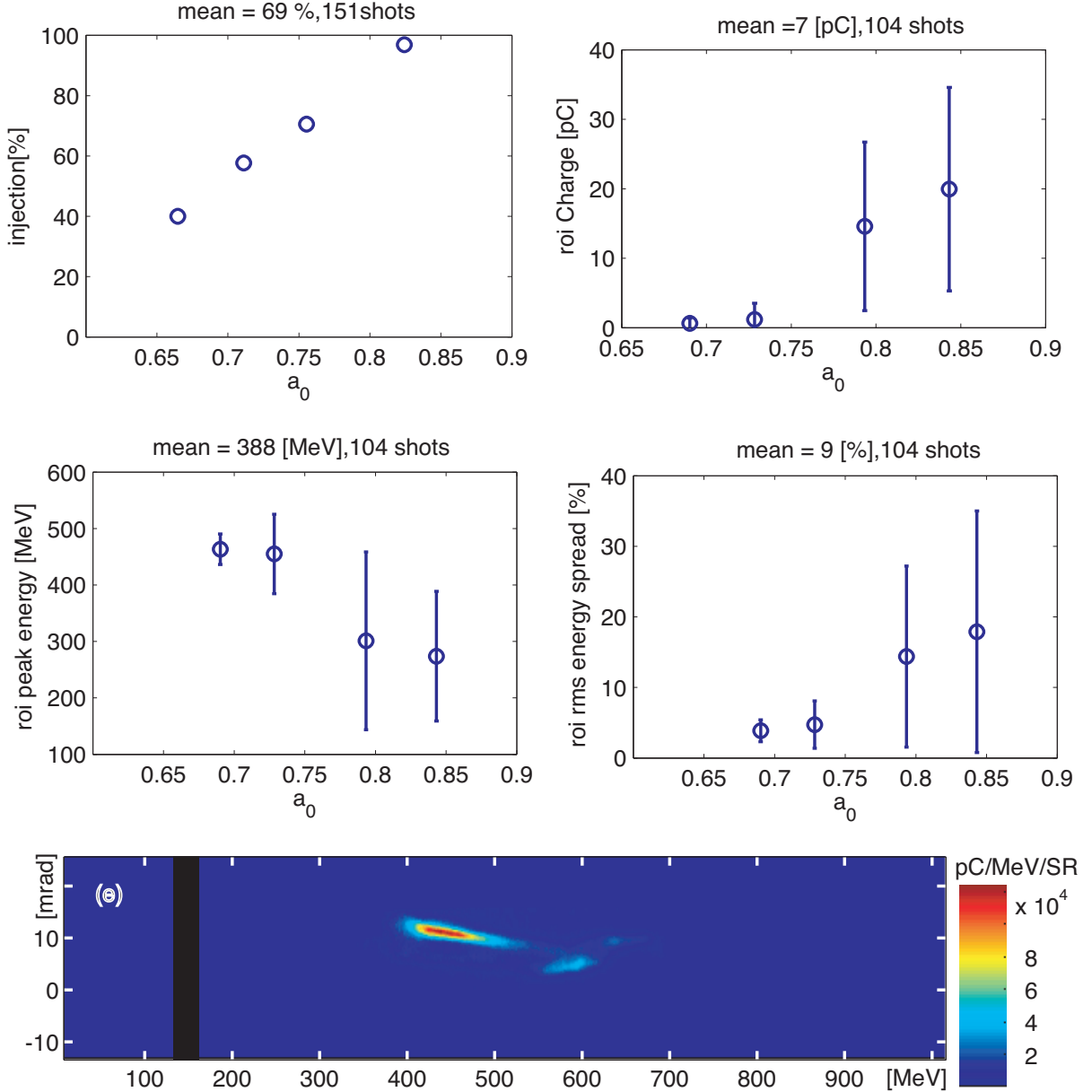
Figure 4.24: Laser intensity dependence of (a) injection probability, (b) total charge, (c) peak energy, and (d) rms energy spread. The input laser plasma parameters were $n_0 \simeq 3.5 \times 10^{18}$ cm^{-3}, $142 < t_{dsc} < 162$ ns, $U_{Lin} \sim 0.9$ J with 14% fluctuation, and $\tau_L \simeq 82$ fs. The ROI images were used for the analysis. Shown in (e) is an example of excessive input intensity shot. The input laser plasma parameters for this particular shot were $t_{dsc} \sim 144$ ns, $U_{Lin} \sim 1.1$ J, and $\tau_L \simeq 82$ fs, which gave $P \sim 13$ TW ($a_0 \simeq 0.82$). The peak energy was 441 MeV, and total charge was 12 pC.

and earlier injection resulting in the dephasing. The higher input intensity clearly helped to stabilize injection with increased amount of injected charge, which was a similar effect

as with the increase in a plasma density. Shown in Fig. 4.24(e) is a typical broad band shot with excessive input laser intensity. The input laser plasma parameters for this particular shot were $t_{dsc} \sim 144$ ns, $U_{Lin} \sim 1.1$ J, and $\tau_L \simeq 82$ fs, which gave $P \sim 13$ TW ($a_0 \simeq 0.82$). The peak energy was 441 MeV, and total charge was 12 pC. Although the peak energy was 441 MeV, it contained a high energy tail which contained 3 pC at 600 MeV.

From the discharge delay dependence shown in Fig. 4.23 and the input intensity dependence shown in Fig. 4.24, it is clear that the control of the discharge delay and input laser intensity (energy) are critical for the stable generation of high quality e-beam from self-injection CDG-LWFA. If a certain range of the discharge delay $142 < t_{dsc} < 152$ ns and the input energy $0.82 < U_{Lin} < 0.9$ J is taken, resultant self-injection probability is 77%, the peak energy is 481 MeV with 5.8% fluctuation, a total charge is 0.9 pC with 100% fluctuation, the energy spread is 3.9% (rms) with 40% fluctuation, and the beam divergence is 1.5 mrad with 31% fluctuation. Note that 40% fluctuation in an energy spread of 3.9% means only $\pm1.6\%$ of total energy, and 31% fluctuation in the beam divergence of 1.5 mrad is ±0.45 mrad. A total of 26 shots were taken within this parameter range, 20 shots resulted generating e-beam. Stable generation of high quality e-beam via self-injection required the control of the discharge delay with less than 10 ns accuracy and the input laser energy less than 10% accuracy. Note that by narrowing the range of discharge delay and input energy, 100% injection could be shown, but with smaller number of statistics. This result demonstrated that self-injection based LWFA can provide high quality e-beams with stabilized electron energy and high reproducibility, which has never been achieved before [1, 2]. This could be unique property of a CDG-LWFA. By understanding the physics behind with further experiments and simulations, a next generation CDG-LWFA may be designed to provide stable operation without further complication of a setup.

4.8 Analysis of Experiments Using the 190 μm Diameter Capillary

4.8.1 Laser Parameter Dependence

The 190 μm diameter capillary was found to have the lowest threshold laser energy for the self-injection among the three capillaries analyzed in this work. By using laser pluses with energy of 0.6 J with 2.7% fluctuation, electron self-injection occurred 2%. Although this is very low probability, no e-beams were observed with an energy 0.6 J from the other two capillaries. The other input laser plasma parameters were $n_0 \simeq 2.5$ to 3.2×10^{18} cm^{-3}, $t_{dsc} < 100$ ns with 11% fluctuation, and $\tau_L \simeq 65$ fs, which gave $P \sim 9.5$ TW ($a_0 \simeq 0.72$). The peak energy was found to be from 100 to 300 MeV with up to 1 pC of total charge.

In the same manner as the other capillaries, the threshold laser intensity for self-electron injection into a plasma wakefield was experimentally explored with higher input energy than that of the previous paragraph. Shown in Fig. 4.25(a) is the probability of self-injection versus laser pulse length, and in Fig. 4.25(b) is the probability versus normalized vector potential a_0. To extract only a laser parameter dependence, the discharge delay and plasma density were fixed at 110 ns with 5.4% fluctuation and $\simeq 3.0 \times 10^{18}$ cm^{-3},
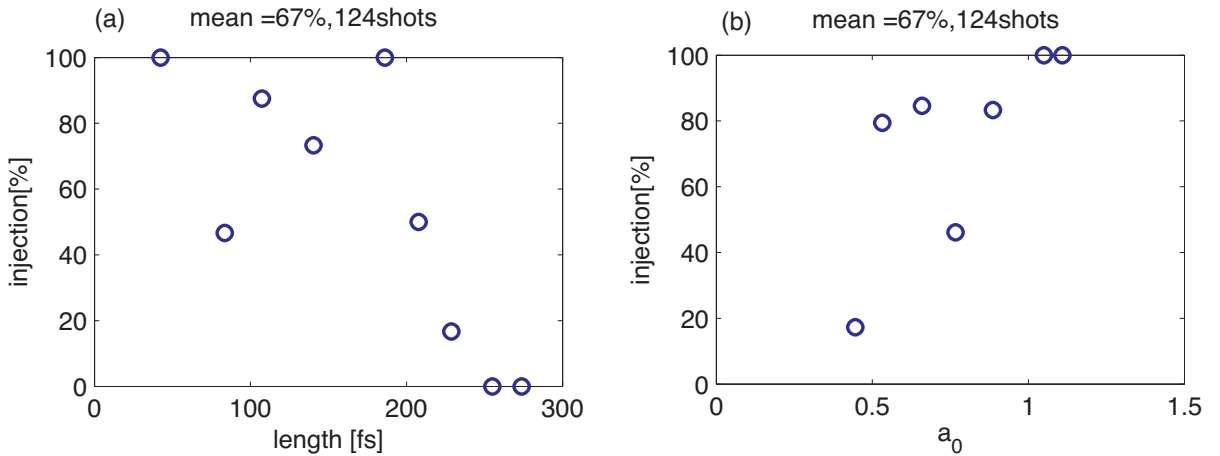
Figure 4.25: Injection probability as a function of the laser pulse duration (a), and as a function of the normalized vector potential a_0 (b), for a 190 μm diameter capillary (See Subsection 4.5 for the definition of the injection probability). The input laser plasma parameters were $n_0 \simeq 3.0 \times 10^{18}$ cm^{-3}, $t_{dsc} \sim 100$ ns with 5.4% fluctuation, $U_{Lin} \sim 0.91$ J with 5.7% fluctuation.

respectively. The laser energy was 0.91 J/pulse with 5.7 % fluctuation.

First, even lower threshold intensity for the self-injection was observed. The injection threshold intensity was found to be $a_0 \simeq 0.45$, which corresponded to 3.7 TW, 240 fs (0.87 J) laser pulse. It is clear that both the input laser intensity and the total energy in the laser pulse affects injection process. For the total energy to play a critical role in the injection, the evolution of laser during the propagation in the plasma channel, especially pulse compression seems to be critical [196]. This input intensity $a_0 \simeq 0.45$ had been believed to give no self-injection in sm-LWFA. This may be a unique property in the CDG-LWFA due to the exceptionally long propagation length in contrast to other LWFAs, allowing self modulation for longer period of the plasma wave.

Second, the injection probability exhibits a somewhat complicated dependence on the laser pulse length or/and intensity. From Fig. 4.25, one can see two peaks in the probability. In terms of the laser pulse length τ_L (laser intensity a_0), one was found at $\tau_L \simeq 42$ fs ($a_0 \simeq 1.1$) and the other was found at $\tau_L \simeq 160$ fs ($a_0 \simeq 0.55$). Surprisingly, e-beams with similar properties were found from those two regimes. E-beams from those two regimes were somewhat collimated, and had large energy spreads that looked like snakes. Typical snake-like beam from each regime together with typical beam, found in between are shown in Fig. 4.26. In between these two regimes, e-beams were found to have larger divergence. The laser pulse length seemed to be more crucial for the generation of snakes rather than the input laser intensity. In the first "snake regime" (shorter pulse length), the snake-like beams were found for $\tau_L < 42$ fs. The mean total charge (no ROI) was 26 pC with 64% fluctuation, and the mean beam divergence (no ROI) was 3.6 mrad with 18% fluctuation. Shown in Fig.4.26(a) is a typical shot from this regime. The laser pulse for this particular shot was 21 TW, 42 fs (0.88 J), which gave a_0 of 1.1. The discharge delay was 103 ns. The e-beams contained a total charge of 37 pC, and the beam divergence was 2.9 mrad. In the second "snake regime" (longer pulse length), the snake-like beams were found for $150 \lesssim \tau_L \lesssim 180$ fs. The mean total charge (no ROI) was 14 pC with 91% fluctuation, and the mean beam divergence (no ROI) was 2.5 mrad with 27% fluctuation. Shown in Fig. 4.26(c) is a typical shot from this regime. The laser pulse for this particular shot was 5.5 TW, 180 fs (0.98 J), which gave a_0 of 0.54. The discharge delay was 111 ns. The e-beams contained a total charge of 42 pC, and the beam divergence was 2.9 mrad. Here, full images (no ROI) were analyzed due to the broadband
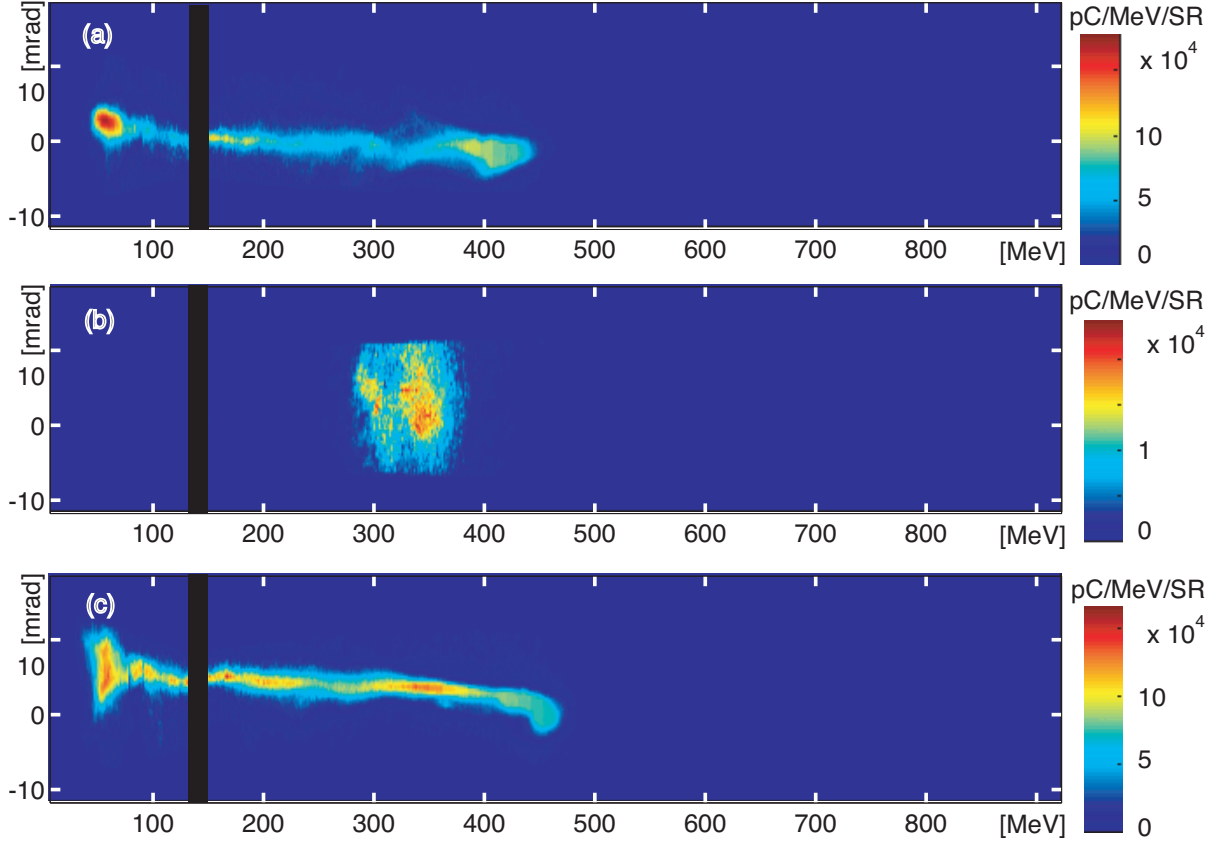
Figure 4.26: (a): Typical single shot e-beam spectra in the first "snake regime" (shorter laser pulse). The laser pulse for this example shot was 21 TW, 42 fs (0.88 J), which gave a_0 of 1.1. The discharge delay was 103 ns. The e-beams contained a total charge of 37 pC, and the beam divergence was 2.9 mrad. (b): Typical large beam divergence shot from between two regimes. The laser pulse for this example shot was 13 TW, 79 fs (0.99 J), which gave a_0 of 0.82. The discharge delay was 122 ns. The e-beams contained a total charge of 5.2 pC, and the beam divergence was more than 4.7 mrad (overfilled). (c): Typical single shot e-beam spectra in the second "snake regime" (longer laser pulse). The laser pulse for this example shot was 5.5 TW, 180 fs (0.98 J), which gave a_0 of 0.54. The discharge delay was 111 ns. The e-beams contained a total charge of 42 pC, and the beam divergence was 2.9 mrad.

property. Since the beam divergence was evaluated from the energy-integrated profile, it could be overestimated if the incident angle of the e-beam has energy dependence. Shown in Fig. 4.26(b) is a typical large beam divergence shot from between two regimes. The laser pulse for this particular shot was 13 TW, 79 fs (0.99 J), which gave a_0 of 0.82. The discharge delay was 122 ns. The e-beams contained a total charge of 5.2 pC, and the beam divergence was more than 4.7 mrad (overfilled).

As can be seen from Fig. 4.26, despite a 4 times difference in pulse length and two times difference in input laser intensity, resultant e-beams were quite similar. In both regimes, self-injection occurred in the accelerating and converging phase, which is 1/4 of the total phase of the wakefield if operation was in the linear regime (see Section 2). The broadband property suggests either heavy beam loading or that the self-injection lasted quite long. The possible mechanism for the different laser pulses resulting in the generation of quite similar e-beam is unknown.

The threshold laser parameters for self-injection were also studied for different discharge delays and plasma densities. Shown in Fig. 4.27(a) is the probability of self-injection versus laser pulse length, and in Fig. 4.27(b) is the probability versus normalized vector potential a_0. The discharge delay and plasma density were fixed at 80 ns with 3.3% fluctuation and $\simeq 2.7 \times 10^{18}$ cm^{-3}, respectively. The laser energy was 0.89 J/pulse with 6.0 % fluctuation.

With those discharge delays and plasma densities, the injection probability did not show the structure exhibited in the previous discussion shown in Fig. 4.25. The injection probability did not reach 100 % with the shortest pulse duration or the highest input intensity. Observed e-beams did not show a clear dependence on laser parameters. The
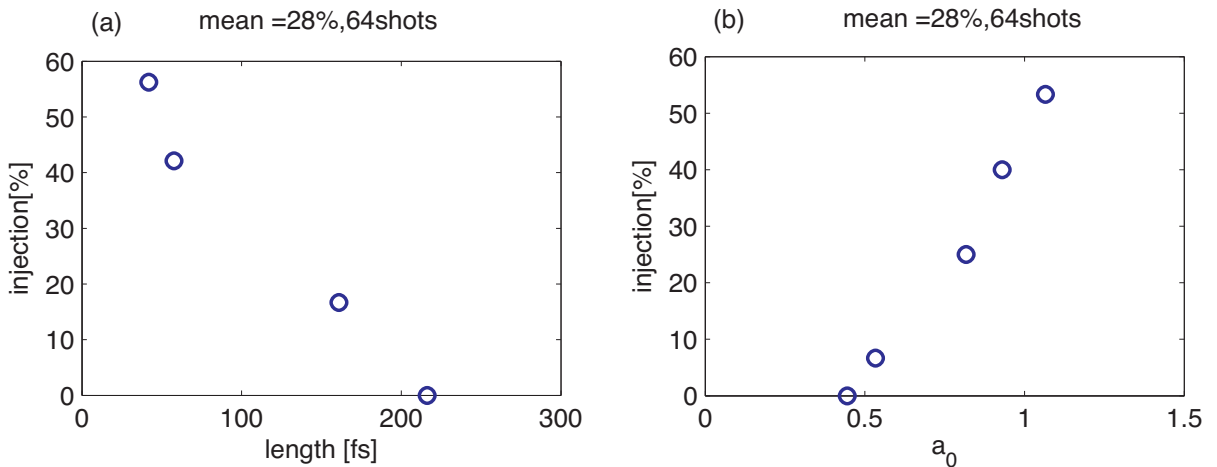

Figure 4.27: Injection probability as a function of the laser pulse duration (a), and as a function of the normalized vector potential a_0 (b), for a 190 μm diameter capillary (See Subsection 4.5 for the definition of the injection probability). The laser energy was 0.89 J/pulse with 6.0 % fluctuation, and the discharge delay and plasma density were fixed at 80 ns with 3.3% fluctuation and $\simeq 2.7 \times 10^{18}$ cm^{-3}, respectively.

mean peak energy (ROI) was 280 MeV with 35% fluctuation, and mean total charge (ROI) was 0.69 pC with 100% fluctuation. It suggest that all of the parameters: laser pulse length, plasma density, and discharge delay (channel profile) played some role in the generation of snake-like beams.

4.8.2 Plasma Density Dependence

The dependence of the injection probability on the plasma density was experimentally studied by changing the backing pressure of the hydrogen feed line. Figure 4.28 shows the probability of self-injection versus plasma density. The input laser plasma parameters were $t_{dsc} \sim 109$ ns with 5.3% fluctuation, $U_{Lin} \sim 0.95$ J with 5.9% fluctuation, and $\tau_L \simeq 45$ fs, which gave $P \sim 21$ TW ($a_0 \simeq 1.1$). The statistics were on more than 100 shots for $n_0 \simeq 3.0$ and 3.2×10^{18} cm^{-3}, while less than 20 shots were taken for the other densities. With this laser intensity, almost 100% injection was achieved for $n_0 \simeq 2.5$ to 4.0×10^{18} cm^{-3}. Drop of the injection probability for higher plasma density ($n_0 > 4.0 \times 10^{18}$ cm^{-3}) contradicts to the physics of the self-trapping discussed in Chapter 2. A possible explanation is that the shorter plasma wavelength from higher plasma density resulted in splitting the laser pulse into more than 2 parts due to the shorter period modulation. This could
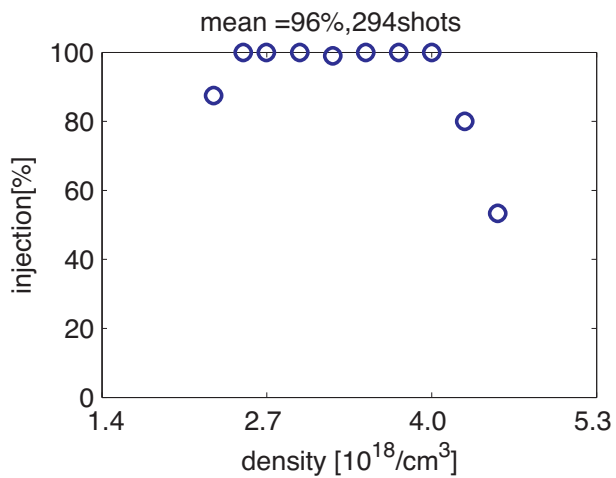
Figure 4.28: Injection probability as a function of a plasma density, for a 190 µm diameter capillary. The input laser plasma parameters were $t_{dsc} \sim 109$ ns with 5.3% fluctuation, $U_{Lin} \sim 0.95$ J with 5.9% fluctuation, and $\tau_L \simeq 45$ fs, which gave $P \sim 21$ TW ($a_0 \simeq 1.1$). The statistics were more than 100 shots for $n_0 \simeq 3.0$ and 3.2×10^{18} cm^{-3}, while less than 20 shots were taken for the other densities.

lead to the waker wakefield (but more buckets). Introducing the linear modulation factor $M_L = \pi L/\lambda_p$, which is the ratio of the laser pulse length and the linear plasma wavelength ($M_L = 1$ is the resonant condition), for $2.5 < n_0^{18} < 4.3$, we obtain $1.7 < M_L < 2.2$. In other words, laser pulse modulation was not optimized for high plasma density.

The e-beam properties showed clear density dependence, while the injection probability was simply always high. The e-beam properties, namely the peak energy, energy spread (rms), total charge, and beam divergence (rms) as a function of the plasma density are shown in Fig. 4.29(a) - (d). The ROI images were used for the analysis. The
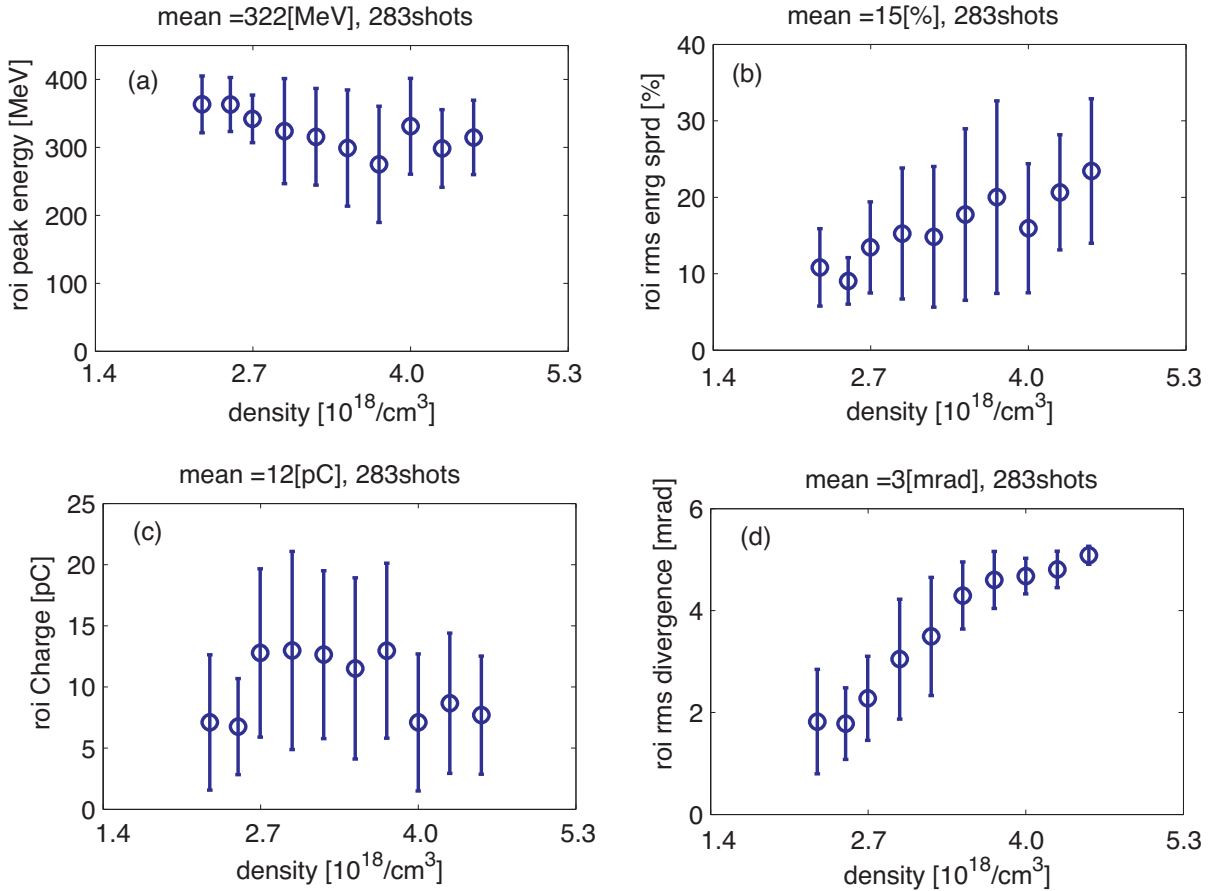
Figure 4.29: E-beam properties as a function of plasma density for the 190 μm diameter capillary. (a): Peak energy. (b): Energy spread (rms). (c): Total charge. (d): Beam divergence (rms). ROI-ed images were used for the analysis. The input laser plasma parameters were $t_{dsc} \sim 109$ ns with 5.3% fluctuation, $U_{Lin} \sim 0.95$ J with 5.9% fluctuation, and $\tau_L \simeq 45$ fs, which gave $P \sim 21$ TW ($a_0 \simeq 1.1$). The statistics were more than 100 shots for $n_0 \simeq 3.0$ and 3.2×10^{18} cm^{-3}, while less than 20 shots were taken for the other densities.

beam divergence exhibited clear dependence on the plasma density as can be seen from Fig. 4.29(d). For higher plasma density, the beam lost its collimation, and overfilled the screen of the GeV-ESM. This may have contributed to the drop in a total charge observed in Fig. 4.29(c). Actual total charge might have looked different on the higher density side. This could be explained by following three mechanisms. One is the weaker wakefield for higher density, which could also explain the drop seen in the injection probability (see Fig. 4.28). As discussed in Chapter 2, the weaker wakefield has narrower phase range in which simultaneous acceleration and radial focusing of electrons is found. Second mechanism is blow-out regime. If operation is close to be in the blow-out regime, higher plasma density requires stronger laser to expel all the surrounding electrons as in Eq. (2.54). The closer to the blow-out condition, the smaller the beam divergence could be due to an ion channel. Last mechanism is the increased space charge force by the increased injection. Either one or more mechanisms may be responsible for the divergence dependence on plasma density.

For lower density, e-beams were sometimes mono-energetic, sometimes broadband. One can see from Fig. 4.29(b) that statistically, lower plasma density provided lower energy spread e-beams. Together with increased total charge, this could be explained by the beam loading effect.

The peak energy did not show clear or simple dependence on plasma density as seen in Fig. 4.29(a). The fluctuation of the peak energy was somewhat smaller for lower density, suggesting weaker modulation on the laser pulse. As discussed in Section 4.6, the stronger modulation may lead to stronger wakefield and larger fluctuation. For higher density, laser pulse modulation might have been stronger, but the peak energy did not increased due to the dephasing, resulting in introducing only larger fluctuation. Stabilized injection for higher density could also lead dephasing due to the earlier injection, giving lower energy. All those mechanisms can provide such complicated peak energy dependence on plasma density.

4.8.3 Discharge Delay Dependence

The injection dependence on the discharge delay was studied as well. Shown in Fig. 4.30 is the probability of self-injection versus the discharge delay. The input laser plasma
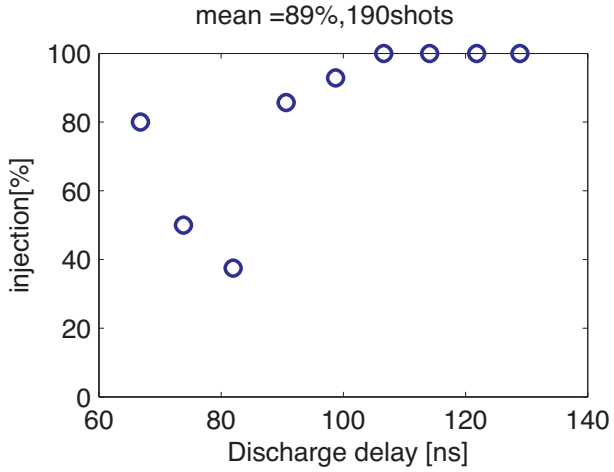
Figure 4.30:   Injection probability as a function of the discharge delay, for a 190 μm diameter capillary. The input laser plasma parameters were $n_0 \simeq 3.2 \times 10^{18}$ cm^{-3}, $U_{Lin} \sim$ 0.95 J with 6.9% fluctuation, and $\tau_L \simeq 45$ fs, which gave $P \sim 21$ TW ($a_0 \simeq 1.1$).

parameters were $n_0 \simeq 3.2 \times 10^{18}$ cm^{-3}, $U_{Lin} \sim 0.95$ J with 6.9% fluctuation, and $\tau_L \simeq 45$ fs, which gave $P \sim 21$ TW ($a_0 \simeq 1.1$).   One can see that the injection process strongly depends on discharge delay, with a big drop in injection probability for $t_{dsc} \sim 80$ ns. This drop in injection probability could be explained by a drop of plasma density.   Probable density drop associated with a drop of a discharge current was suggested in Section 4.6 for the 310 μm diameter capillary. A large drop of a discharge current at $t_{dsc} \sim 80$ ns can be seen from Fig. 4.2(b).

The discharge delay dependence of the e-beam properties is shown in Fig. 4.31, in which ROI images were used for the evaluation.   One can see from Fig. 4.31(d) that the beam divergence followed the trend of the injection probability shown in Fig. 4.30. The observed total charge also roughly followed the same trend, except for shots in the early timing (< 80 ns). The relatively higher injection probability with lower amount of injected charge observed with the early delay is somewhat similar to the stable 0.5 GeV regime from the 225 μm capillary. On the other side (later delay), stabilization of self-injection seems to be tied to excessive injection suggesting the space charge force affecting the beam divergence. The larger e-beam energy spread caused by the excessive injection [Fig. 4.31(b)] is consistent with beam loading effect.

With the discharge delay of 100 ns, the high peak energy (400 MeV), low energy spread
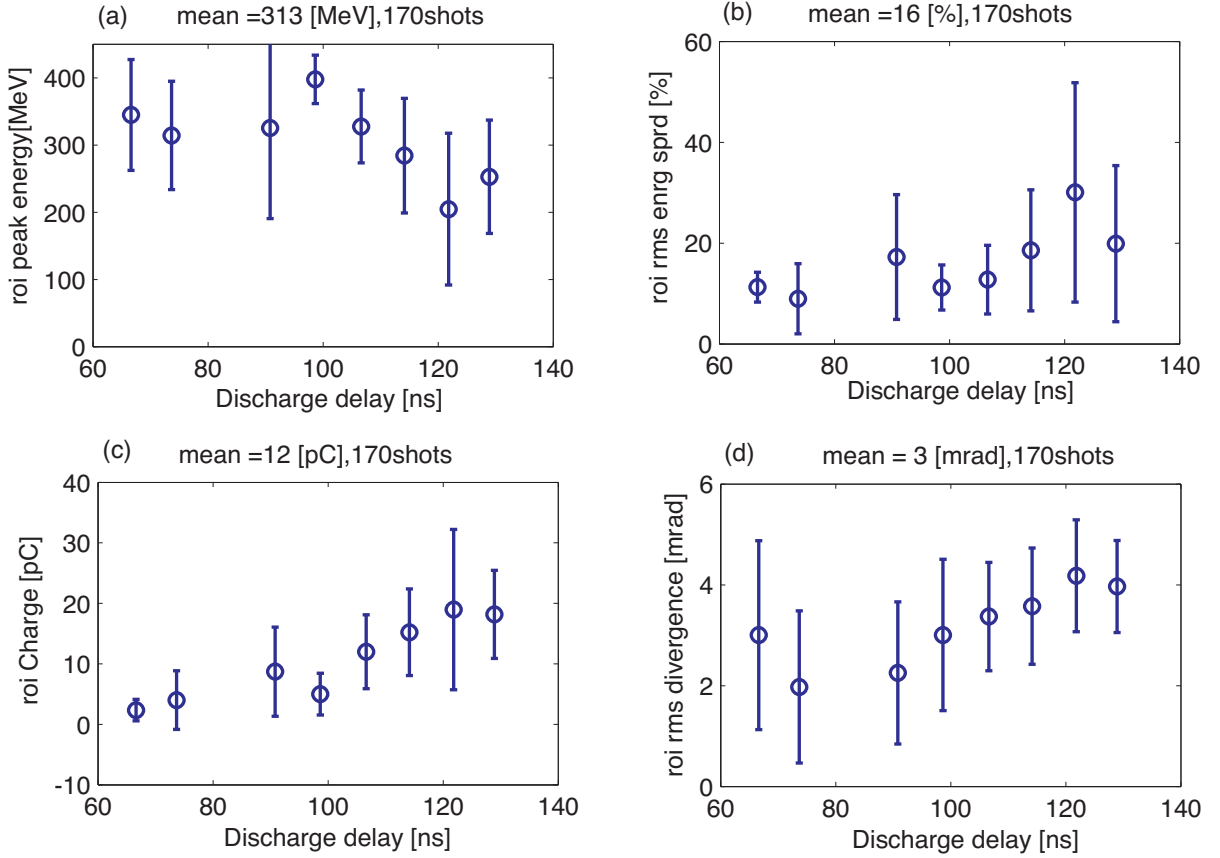
Figure 4.31: E-beam properties as a function of the discharge delay for 190 µm diameter capillary. (a): Peak energy. (b): Energy spread (rms). (c): Total charge. (d): Beam divergence (rms). ROI-ed images were used for the analysis. The input laser plasma parameters were $n_0 \simeq 3.2 \times 10^{18}$ cm^{-3}, $U_{Lin} \sim 0.95$ J with 6.9% fluctuation, and $\tau_L \simeq 45$ fs, which gave $P \sim 21$ TW ($a_0 \simeq 1.1$).

(11%), and low charge ($\simeq 5$ pC) beams with moderate beam divergence were observed. In this 100 ns regime, e-beams were found with big fluctuation in the beam divergence as can be seen in Fig. 4.31(d). The collimated e-beams were obtained about one shot in three shots. Shown in Fig. 4.32 are typical small divergence and large divergence shots. Throughout this parameter field, the beam divergence was unstable. By shortening the laser pulse length, it could reach "snake regime" where the beams were collimated but broadband.
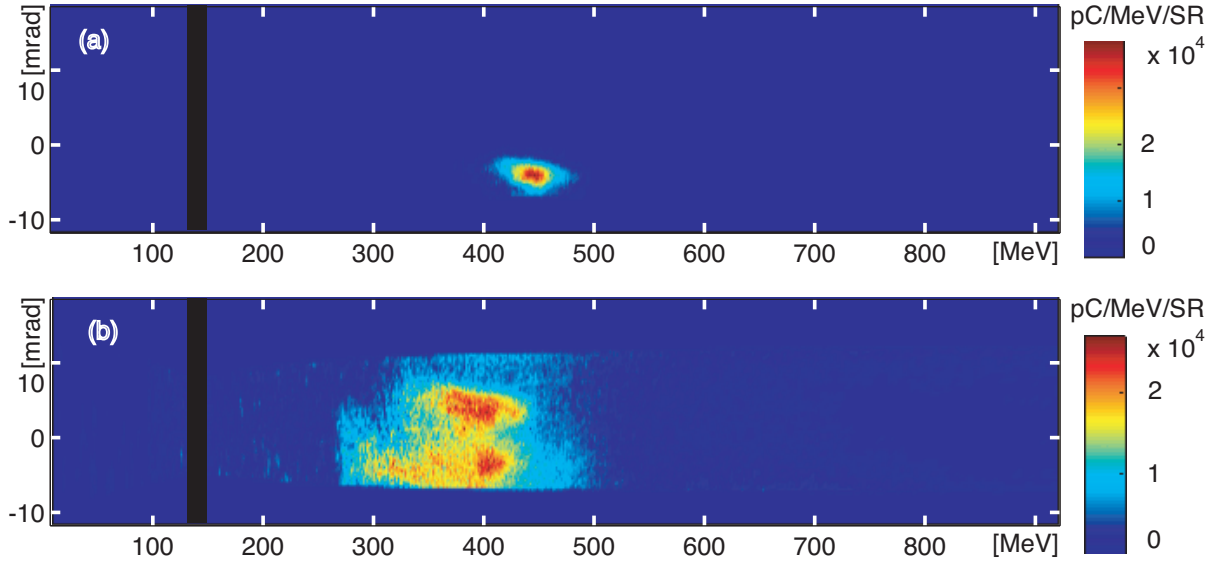
Figure 4.32: (a): Typical small divergence e-beam single shot spectra from the regime described in the paragraph. The input laser plasma parameters for this particular shot were $n_0 \simeq 3.2 \times 10^{18}$ cm^{-3}, $t_{dsc} \sim 98$ ns, $U_{Lin} \sim 1.0$ J, and $\tau_L \simeq 46$ fs, which gave $P \sim 22$ TW ($a_0 \simeq 1.1$). The e-beams contained a total charge of 1.4 pC, and the beam divergence was 1.3 mrad. (b): Typical small divergence e-beam single shot spectra from the same regime as (a). The input laser plasma parameters for this particular shot were $n_0 \simeq 3.2 \times 10^{18}$ cm^{-3}, $t_{dsc} \sim 98$ ns, $U_{Lin} \sim 1.0$ J, and $\tau_L \simeq 46$ fs, which gave $P \sim 22$ TW ($a_0 \simeq 1.1$). The discharge delay was 98 ns. The e-beams contained a total charge of 12 pC, and the beam divergence was more than 4.8 mrad (overfilled). ROI images were used for the evaluation.

4.9 Discussion and Conclusion

The performance of the capillary discharge channel guided accelerator was found to depend on capillary diameter, plasma density, discharge delay, and laser pulse pointing, energy, duration and peak power. By using a 310 μm diameter capillary, an e-beam with peak energy of 1 GeV was observed. This is the highest energy ever achieved from LWFAs. Full analysis including the guiding performance was carried out on the operation of the 310 μm diameter capillary. The statistical analysis suggested that the generation of GeV beams came from a highly unstable regime. Having plasma density at close to the threshold for the self-injection led to a small amount of injection and the longest dephasing length possible. This arrangement allowed the generation of a high energy e-beam, and also resulted in large fluctuations in the peak energy due to unstable self-injection and

significant modulation of the laser pulse. Higher plasma density stabilized the injection process and lowered the fluctuations in the peak energy. The down side was the shorter dephasing length, which led to the lower peak energy of e-beams. Also excessive injection resulted in heavy beam loading, leading to large energy spread. The unstable performance of this capillary might have come from (a) a greater difference between the spot size of the input laser pulse and the matched spot size of the plasma channel, (b) weaker transverse variation of the plasma density leading to a reduction in transverse injection, and (c) the significance of small variations in the laser plasma parameters for this high power (highly nonlinear) regime [68].

The analysis also suggested that by stabilizing the injection process other than by using higher plasma density, stable generation of GeV e-beam may be possible. There are many possible way to stabilize injection process, roughly categorized into two kinds. One is to stabilize self-injection, the other is not to use self-injection. Stabilized self-injection was shown to be possible in Section 4.7 by finding the proper parameter regime [plasma density, laser energy and duration, and discharge delay(channel profile)] and improving the jitter in the discharge delay and laser energy. The other way to stabilize the self-injection may be realized by using a tailored longitudinal plasma profile, for example the density ramp [197]. Using external magnetic fields [82] may be another way to obtain the condition for stable self-injection. Apart from self-injection, laser triggered injection is another promising injection scheme [74–79, 145, 198]. It is clear that stabilizing injection is the key technology for stable > GeV e-beams.

Regimes in parameter space were found where reproducible self-trapped electron beams were generated with energy around 0.5 GeV by using 225 μm diameter capillary. It was demonstrated that self-injection can be stabilized with a CDG-LWFA and electrons can be accelerated up to 0.5 GeV. In this regime, self-injection was stabilized with small amount of trapping, led to stable high quality (a few percent energy spread and $\simeq$1.5 mrad beam divergence) e-beams generation. Shown through a statistical analysis was that the control of the discharge delay and input energy were critical for stable operation. A change of < 10 ns in the discharge delay, and of < 10% in the input energy significantly affected performance. Especially, the discharge delay may be responsible for stabilized low amount injection. A change in discharge delay may introduce a small change in the channel profile. To elucidate the physical effect introduced by the change in a discharge delay requires an

extra diagnostic, such as transverse interferometry, and further studies via modeling and simulations. Then, a capillary discharge system specialized for stable self-injection could be designed.

The 190 μm diameter capillary operation provided the lowest threshold laser energy for self-injection among the three capillaries and the generation of higher charge beam, but with unstable beam divergence. Another interesting regime was found where snake-like beams were generated. The "snake regime" had a strong dependence on the pulse length, with similar snake-like beams found for $\tau_L \simeq 40$ fs and $\tau_L \simeq 160$ fs laser pulses. The possible mechanism by which different laser pulses result in the generation of quite similar e-beams is not understood.

The threshold intensities for injection should be regarded as tentative since experiments were not performed with identical parameters (for density and discharge delay) for different capillaries. Nevertheless, a comparison of the threshold intensities from available data suggests that the threshold laser intensity is lower for capillaries with smaller diameters. The electron beam divergence seemed to be larger for capillaries with smaller diameter. From those observations, a possible scenario may be either or both of the following: (a) the fact that the plasma channel has a smaller matched spot for smaller diameter [131] influences the propagation of the laser pulse, which affects injection, and (b) transverse wakefields play a key role in self-injection and e-beam properties in the capillary-guided LWFA (narrower channels result in larger transverse density gradients and larger transverse wakefields).

From simple scaling laws discussed in Section 1.2, one can estimate the dephasing limited energy gain with parameters where GeV energy gain was observed. With the laser power of 42 TW and spot size of 25 μm, $I \simeq 4.3 \times 10^{18}$ W/cm^2. The dephasing limited energy gain shown in Eq. 1.7 gives $W_{dph} \simeq 400$ MeV. Also for 0.5 GeV beam generation case, it gives $W_{dph} \simeq 220$ MeV. These are a factor 2 lower than observed, and possible reasons are following. Although this simple dimensional analysis yields the correct order of magnitude estimates for the accelerator length and energy gain, a more accurate estimation of the energy gain would require the full plasma channel properties, the effects of laser pulse evolution, instabilities, self-focusing, and e-beam loading on the plasma wake. For example, simulations indicate that pulse evolution is essential to the trapping and acceleration process [199, 200]. As the pulse propagates, it self-modulates

and steepens such that the plasma electrons are completely blown out from the region of the axis (cavitation or bubble regime [139]), at which point electrons are self-trapped and accelerated from the background plasma, in a manner similar to that described in previous experiments on high quality beam production at the 100 MeV level [56, 68].

Chapter 5

Conclusions

5.1 Summary

The first objective of this dissertation work was to develop an electron spectrometer for a GeV class laser wakefield accelerator. As detailed in Chapter 3, a slitless, broadband electron magnetic spectrometer has been developed [3]. Simultaneous measurement of e-beam spectra and output laser properties was realized by a slitless scheme. A scintillator - CCD camera system allowed faster than 1 Hz operation and evaluation of the spatial property of e-beams. Measurement of beam divergence was essential for this slitless spectrometer to evaluate the momentum resolution. With measured divergence and calculation of third order magnet optics, the momentum resolution was evaluated. The spectrometer covered unprecedentedly wide range, from 0.01 to 1.1 GeV (factor 110) in a single shot, with sufficient resolution (below 5% for beams with 2 mrad divergence). The light yield to total charge calibration and study on the energy dependence (0.071 to 1.23 GeV) of the scintillating plate were performed by using e-beams from a conventional accelerator (ALS). This allowed the function as a charge monitor to be implemented successfully on the spectrometer.

The spectrometer was installed on a laser wakefield accelerator system using a 50 TW class Ti:Sapphire laser amplifier in the LOASIS Facility. It has been serving as the main diagnostic for the system. The production of high quality electron beams up to 1 GeV from a centimeter-scale accelerator was demonstrated [1]. This is the highest beam energy yet reported for a laser-driven accelerator, and the shortest accelerator of

any type to accelerate electrons from rest to GeV energies. This was enabled by the use of gas-filled capillary discharge waveguides that channeled relativistically-intense laser pulses over several centimeters of sufficiently low density plasma. Also demonstrated was the stable self injection and acceleration to $\simeq 0.5$ GeV. This further motivated statistical analysis on CDG-LWFA operations.

The other objective of this dissertation was to understand how to control a GeV class LWFA. Thousands of shots with a broad range of laser and plasma parameters have been taken in the experiments. Using statistical analysis, to find key technology and physics for control of GeV class LWFA was the goal. As detailed in Chapter 4, a program for such statistical analysis was developed, and a statistical analysis to study the laser and plasma parameter dependence of CDG-LWFAs was carried out [2].

The statistical analysis suggested that the generation of GeV beams came from a highly unstable regime. Having the plasma density at a value close to the threshold for the self injection led to a small amount of injection and the longest dephasing length possible. The capillary diameter of 310 μm raised the threshold intensity for self injection high, probably due to the relatively low contributions of transverse wakefield and larger matched spot size. This way have allowed to the higher intensity laser to provide higher gradient wakefield without self injection. This arrangement allowed the generation of high energy e-beams, and also resulted in large fluctuation in the peak energy due to the unstable self injection. Higher plasma density stabilized the injection process and lowered the fluctuations in the peak energy. The down side of having higher plasma density was the shorter dephasing length, which led to the lower peak energy of e-beams.

The analysis showed requirements on stable self injection and acceleration for the CDG-LWFA which employed the 225 μm diameter capillary. The control of the discharge delay and input energy was critical for the stable operation. A change of < 10 ns in the discharge delay, and of $< 10\%$ in the input energy significantly affected performance. Combined with the analysis performed on the 310 μm capillary, possible schemes to stabilize injection process for $>$ GeV e-beams were discussed in Section 4.6.

Although more experiments and modeling with particle-in-cell simulations are required to understand the detailed physics of injection and acceleration of a CDG-LWFA, such as the role of transverse wakefields, the statistical analysis provided information for future optimization.

5.2 Prospects and Future Work

There are several diagnostics that could be employed in the future to gain a better understanding of the CDG-LWFA, and perhaps improve performance. The analysis suggested that the longitudinal laser pulse modulation during propagation may be critical for the generation of high energy e-beam. A technique that provides information on the temporal profile of the laser pulse, such as an auto-correlator [201], FROG (frequency-resolved optical gating) [202], or SPIDER (spectral phase interferometry for direct electric-field reconstruction) [203], could give a better understanding of the importance of the longitudinal laser evolution. These techniques, however, show only the integrated effect along the propagation axis, such as a transverse and longitudinal modulation, effect from injected electrons, or pump depletion via wake field generation. In comparison, a transverse diagnostic could provide spatially resolved information. Furthermore, the change in the discharge delay induces small amounts of fluctuation in the plasma density, and a change in the channel profile. Therefore, transverse interferometry [131] of the plasma density should be investigated. Ultimately, a snap-shot of the wakefield [204] would provide full information on the wakefield. Laser pulse spot size during propagation may hard to measure. Observation of nonlinear Thomson scattering could provide some information of spot size.

The analysis suggested that control of the electron injection into the wakefield would be a key technology for a generation of higher quality e-beams with higher stability. Although stabilized self injection was shown to be possible in this work, by the help of extra diagnostics suggested above and further theoretical and numerical study, the required physical conditions for stabled self injection can be determined. With better understanding of the injection process, a capillary with longitudinal or transverse structure [191] could be designed to improve a CDG-LWFA. For example, a plasma density ramp may provide stabilized injection, and could be used as an injector for CDG-LWFA. Apart from the self injection, laser triggered injection [74–79, 145, 198] is another promising injection scheme, albeit more complex and challenging. Better understanding through extra diagnostics and stabilizing the electron injection into the wakefield would lead a CDG-LWFA to the next level in terms of beam quality and stability.

The short wavelength of the plasma accelerating structure results in femtosecond du-

ration bunches (> 10 kA peak current), that are well suited for driving pulsed radiation sources. This offers the prospect of novel, compact, and intrinsically-synchronized sources of femtosecond electron pulses and radiation tunable from x-ray [93–95] to THz frequencies [44, 98, 205], as needed for pump-probe measurements in the basic and applied sciences. The GeV beams pave the way for compact femtosecond free electron lasers producing keV x-rays using existing cm-scale period undulators, which was not possible with 100 MeV-class beams. Furthermore, it is anticipated that longer accelerating structures can be made by staging capillary discharge waveguides, thereby opening a path to compact accelerators beyond the multi-GeV level for applications in high energy physics.

Appendix A

Symbols

A.1 Symbols

Summarized here are symbols used in this dissertation and a brief description of the symbol. The nominal value and unit are also shown, unless otherwise specified in the main Chapters.

Symbol	Description	Value	Unit
$\boldsymbol{A}$	vector potential		
$\boldsymbol{a}$	normalized vector potential		
A_b	cross sectional area of the electron bunch		
A_w	atomic weight		
$\boldsymbol{B}$	magnetic field		
$\boldsymbol{\beta}$	normalized electron velocity		
c	speed of light in vacuum	3×10^{10}	cm/s
e	charge of an electron	4.8×10^{-10}	esu
$\boldsymbol{e}$	unit vector to indicate laser polarization		
$\boldsymbol{E}$	electric field		
E_0	cold nonrelativistic wavebreaking field		esu/cm
E_r	transverse electric field of the wake		esu/cm
E_z	longitudinal electric field of the wake		esu/cm

E_{rest}	rest mass energy of an electron	0.511	MeV
$\hat{\epsilon}$	mean normalized deviation		
F_{pm}	ponderomotive force		
γ	Lorentz factor		
H	Hamiltonian		W/cm^2
I	radiation intensity		W/cm^2
I_{inz}	the mean ionization energy of the medium		
I_k	current for kicker magnets		A
I_{dsc}	discharge current		A
k	wave number of radiation		cm^{-1}
k_p	plasma wave number		cm^{-1}
L_{acc}	acceleration length		cm
L_{dph}	dephasing length		cm
L_{pd}	depletion length		cm
L	laser pulse length		cm
λ_p	plasma wavelength		cm
λ	laser wavelength	0.8×10^{-4}	cm
m_e	rest mass of electron	0.91×10^{-27}	g
N	number of plasma periods that the bunch is located		
N_e	number of bunch electrons		
N_A	the Avogadro number		
n, n_e	electron density		cm^{-3}
n_0	0th order, or equilibrium plasma density		cm^{-3}
n_i	ion density		cm^{-3}
$\boldsymbol{p}$	momentum of electron (particle or fluid)		MeV/c
$\hat{p}$	relative momentum spread of e-beam		%

δp	momentum spread of e-beam		MeV/c
p_0	central momentum of e-beam		MeV/c
P	laser peak power		TW
P_c	critical power for self focusing		TW
Ψ	phase of the wake		
Φ	scaler potential		
ϕ	normalized scaler potential		
Q_{tot}	total charge in a beam		pC
Q_{tot}^{ROI}	ROI total charge in a beam		pC
R_{eff}	effective radius of a magnetic field		mm
r_e	classical electron radius	2.82×10^{-13}	cm
ρ	medium density		g/cm^3
s	electron curve linear coordinate		m
T	kinetic energy of an electron		MeV
$\hat{T}$	relative energy spread of e-beam		%
δT	energy spread of e-beam		MeV
T_0	central kinetic energy of e-beam		MeV
T_{pk}	peak kinetic energy of e-beam		MeV
t_{dsc}	the delay between the onset of the discharge current and the arrival of the laser beam (discharge delay)		ns
Δt_{exp}	exposure time		ms
τ_{bm}	bump magnet trigger		
τ_L	laser pulse length		fs
$\boldsymbol{u}$	normalized momentum of electron (particle or fluid)		
U_b	total energy of an e-beam		J
U_{Lin}	input laser energy		J

U_{Llk}	laser energy loss via leakage from the channel		J
$\hat{U}_{Llk}$	relative laser energy loss via leakage from the channel		%
U_{Lls}	laser transmission loss		J
$\hat{U}_{Lls}$	relative laser transmission loss		%
U_{wake}	wakefield energy		J
$\hat{U}_{wake}$	relative wakefield energy		%
v_{beam}	velocity of electron beam		cm/s
$\boldsymbol{v}, \boldsymbol{v_e}$	electron velocity		cm/s
v_g	laser group velocity		cm/s
$\boldsymbol{v_i}$	ion velocity		cm/s
v_{pp}	phase velocity of the plasma wave		cm/s
ΔW	energy gain		MeV
ΔW_{dph}	dephasing limited energy gain		MeV
ΔW_{pd}	pump depletion limited energy gain		MeV
w_0	spot size		μm
w_{0out}	output spot size		μm
$\boldsymbol{\Omega}$	generalized vorticity		
ω_0	laser frequency		s^{-1}
ω_p	plasma frequency		s^{-1}
η_{dps}	deposition efficiency of LANEX		
η_{rad}	Radiation efficiency of LANEX		
η_{WB}	wake to beam efficiency		
Z	atomic number		
z_R	Rayleigh length		cm
ζ	laser co-moving frame		cm

A.2 Abbreviations

Abbreviation	Description
ALS	Advanced Light Source
AFRD	Acceleration and Fusion Research Division
BCM	Beam Charge Monitor
BTS	Booster To Storage section
CBP	Center of Beam Physics
CC-coefficient	Counts/Charge coefficient
CC-nonlinearity	Counts - Charge nonlinearity
CCD	Charge-Coupled device
CDG	Capillary Discharge Guided
CMOS	Complementary Metal Oxide Semiconductor
CPA	Chirped Pulse Amplification
e-beam	Electron Beam
EPICS	Experimental Physics and Industrial Control System
ESM	Electron SpectroMeter
FEL	Free Electron Laser
FROG	Frequency-Resolved Optical Gating
FWHM	Full-Width Half-Maximum
Gadox	terbium activated GADolinium OXysulphide, $Gd_2O_2S{:}Tb$
ICT	Integrate Current Transformer
IP	Imaging Plate
LANEX-FB	Lanex Fast Back
LBNL	Lawrence Berkeley National Laboratory
LOA	Laboratoire d'Optique Appliquée
LOASIS	Lasers, Optical Accelerator Systems Integrated Studies
LWFA	Laser WakeField Acceleration
OAP	Off-Axis Parabola
PBWA	Plasma Beat Wave Acceleration

PIC	Perticle In Cell
PMP	PhotoMultiPlier
PWFA	Plasma WakeField Acceleration
RAL	Rutherford Appleton Laboratory
RF	Radio Frequency
ROI	Region Of Interest
SBD	Surface Barrier Detector
sm-LWFA	self modulated Laser WakeField Acceleration
SLAC	Stanford Linear Accelerator Center
SPIDER	Spectral Phase Interferometry for Direct Electric-field Reconstruction
TLD	ThermoLuminescent Dosimeter
UCLA	University of California Los Angels
USC	University of Southern California
U-Tokyo	University of Tokyo
WFA	WakeField Acceleration

Bibliography

[1] W. P. Leemans, B. Nagler, A. J. Gonsalves, Cs. Tóth, K. Nakamura, C. G. R. Geddes, E. Esarey, C. B. Schroeder, and S. M. Hooker. Gev electron beams from a centimetre-scale accelerator. *Nature Physics*, 2:696–699, 2006.

[2] K. Nakamura, B. Nagler, Cs. Tóth, C. G. R. Geddes, C. B. Schroeder, E. Esarey, W. P. Leemans, A. J. Gonsalves, and S. M. Hooker. Gev electron beams from a centimeter-scale channel guided laser wakefield accelerator. *Physics of Plasmas*, 14(5):056708, 2007.

[3] K. Nakamura, W. Wang, N. Ybarrolaza, D. Syversrud, J. Wallig, and W.P. Leemans. Broadband single-shot electron spectrometer for GeV-class laser-plasma-based accelerators. *Rev. Sci. Instrum.*, 79:053301, 2008.

[4] T. Tajima and J. M. Dawson. Laser electron accelerator. *Phys. Rev. Lett.*, 43(4):267–70, 1979.

[5] Pisin Chen, J. M. Dawson, Robert W. Huff, and T. Katsouleas. Acceleration of electrons by the interaction of a bunched electron beam with a plasma. *Phys. Rev. Lett.*, 54(7):693–696, Feb 1985.

[6] E. Esarey, P. Sprangle, J. Krall, and A. Ting. Overview of plasma-based accelerator concepts. *IEEE Trans. Plasma Sci.*, 24(2):252–288, 1996.

[7] C. Joshi. The development of laser- and beam-driven plasma accelerators as an experimental field. *Phys. Plasmas*, 14:055501, 2007.

[8] G. Malka, E. Lefebvre, and J. L. Miquel. Experimental observation of electrons accelerated in vacuum to relativistic energies by a high-intensity laser. *Phys. Rev. Lett.*, 78(17):3314–3317, Apr 1997.

[9] M. H. Key, M. D. Cable, T. E. Cowan, K. G. Estabrook, B. A. Hammel, S. P. Hatchett, E. A. Henry, D. E. Hinkel, J. D. Kilkenny, J. A. Koch, W. L. Kruer, A. B. Langdon, B. F. Lasinski, R. W. Lee, B. J. MacGowan, A. MacKinnon, J. D. Moody, M. J. Moran, A. A. Offenberger, D. M. Pennington, M. D. Perry, T. J. Phillips, T. C. Sangster, M. S. Singh, M. A. Stoyer, M. Tabak, G. L. Tietbohl, M. Tsukamoto, K. Wharton, and S. C. Wilks. Hot electron production and heating by hot electrons in fast ignitor research. *Phys. plasmas*, 5(5):1966–1972, 1998.

[10] T. E. Cowan, A. W. Hunt, T. W. Phillips, S. C. Wilks, M. D. Perry, C. Brown, W. Fountain, S. Hatchett, J. Johnson, M. H. Key, T. Parnell, D. M. Pennington, R. A. Snavely, and Y. Takahashi. Photonuclear fission from high energy electrons

from ultraintense laser-solid interactions. *Phys. Rev. Lett.*, 84(5):903–906, Jan 2000.

[**11**] C. Rousseaux, M. Rabec le Gloahec, S. D. Baton, F. Amiranoff, J. Fuchs, L. Gremillet, J. C. Adam, A. Héron, and P. Mora. Strong absorption, intense forward-raman scattering and relativistic electrons driven by a short, high intensity laser pulse through moderately underdense plasmas. *Physics of Plasmas*, 9(10):4261–4269, 2002.

[**12**] X. Wang, K. Nishikawa, and K. Nemoto. Observation of a quasimonoenergetic electron beam from a femtosecond prepulse-exploded foil. *Physics of Plasmas*, 13(8):080702, 2006.

[**13**] C. Joshi, T. Tajima, J. M. Dawson, H. A. Baldis, and N. A. Ebrahim. Forward raman instability and electron acceleration. *Phys. Rev. Lett.*, 47(18):1285–1288, Nov 1981.

[**14**] Y. Kitagawa, T. Matsumoto, T. Minamihata, K. Sawai, K. Matsuo, K. Mima, K. Nishihara, H. Azechi, K. A. Tanaka, H. Takabe, and S. Nakai. Beat-wave excitation of plasma wave and observation of accelerated electrons. *Phys. Rev. Lett.*, 68(1):48–51, Jan 1992.

[**15**] C. E. Clayton, K. A. Marsh, A. Dyson, M. Everett, A. Lal, W. P. Leemans, R. Williams, and C. Joshi. Ultrahigh-gradient acceleration of injected electrons by laser-excited relativistic electron plasma waves. *Phys. Rev. Lett.*, 70(1):37–40, Jan 1993.

[**16**] C. E. Clayton, M. J. Everett, A. Lal, D. Gordon, K. A. Marsh, and C. Joshi. Acceleration and scattering of injected electrons in plasma beat wave accelerator experiments. *Physics of Plasmas*, 1(5):1753–1760, 1994.

[**17**] N. A. Ebrahim. Optical mixing of laser light in a plasma and electron acceleration by relativistic electron plasma waves. *Journal of Applied Physics*, 76(11):7645–7647, 1994.

[**18**] M. Everett, A. Lal, D. Gordon, C. E. Clayton, K. A. Marsh, and C. Joshi. Trapped electron acceleration by a laser-driven relativistic plasma wave. *Nature*, 368:527–529, 1994.

[**19**] F. Amiranoff, D. Bernard, B. Cros, F. Jacquet, G. Matthieussent, P. Miné, P. Mora, J. Morillo, F. Moulin, A. E. Specka, and C. Stenz. Electron acceleration in nd-laser plasma beat-wave experiments. *Phys. Rev. Lett.*, 74(26):5220–5223, Jun 1995.

[**20**] S. Ya. Tochitsky, R. Narang, C. V. Filip, P. Musumeci, C. E. Clayton, R. B. Yoder, K. A. Marsh, J. B. Rosenzweig, C. Pellegrini, and C. Joshi. Enhanced acceleration of injected electrons in a laser-beat-wave-induced plasma channel. *Physical Review Letters*, 92(9):095004, 2004.

[**21**] P. Maine, D. Strickland P. Bado, M. Pessot, and G. Mourou. Generation of ultrahigh peak power pulses by chirped-pulse amplification. *IEEE J. Quantum Electron.*, QE-24:398–403, 1988.

[22] K. Nakajima, D. Fisher, T. Kawakubo, H. Nakanishi, A. Ogata, Y. Kato, Y. Kitagawa, R. Kodama, K. Mima, H. Shiraga, K. Suzuki, K. Yamakawa, T. Zhang, Y. Sakawa, T. Shoji, Y. Nishida, N. Yugami, M. Downer, and T. Tajima. Observation of ultrahigh gradient electron acceleration by a self-modulated intense short laser pulse. *Phys. Rev. Lett.*, 74(22):4428–4431, May 1995.

[23] F. Amiranoff, S. Baton, D. Bernard, B. Cros, D. Descamps, F. Dorchies, F. Jacquet, V. Malka, J. R. Marquès, G. Matthieussent, P. Miné, A. Modena, P. Mora, J. Morillo, and Z. Najmudin. Observation of laser wakefield acceleration of electrons. *Phys. Rev. Lett.*, 81(5):995–998, Aug 1998.

[24] F. Dorchies, F. Amiranoff, V. Malka, J. R. Marquès, A. Modena, D. Bernard, F. Jacquet, Ph. Miné, B. Cros, G. Matthieussent, P. Mora, A. Solodov, J. Morillo, and Z. Najmudin. Acceleration of injected electrons in a laser wakefield experiment. *Physics of Plasmas*, 6(7):2903–2913, 1999.

[25] C. A. Coverdale, C. B. Darrow, C. D. Decker, W. B. Mori, K-C. Tzeng, K. A. Marsh, C. E. Clayton, and C. Joshi. Propagation of intense subpicosecond laser pulses through underdense plasmas. *Phys. Rev. Lett.*, 74(23):4659–4662, Jun 1995.

[26] A. Modena, Z. Najmudin, A. E. Dangor, C. E. Clayton, K. A. Marsh, C. Joshi, V. Malka, C. B. Darrow, C. Danson, D. Neely, and F. N. Walsh. Electron acceleration from the breaking of relativistic plasma waves. *Nature*, 377:606–608, 1995.

[27] S. P. D. Mangles, B. R. Walton, M. Tzoufras, Z. Najmudin, R. J. Clarke, A. E. Dangor, R. G. Evans, S. Fritzler, A. Gopal, C. Hernandez-Gomez, W. B. Mori, W. Rozmus, M. Tatarakis, A. G. R. Thomas, F. S. Tsung, M. S. Wei, and K. Krushelnick. Electron acceleration in cavitated channels formed by a petawatt laser in low-density plasma. *Physical Review Letters*, 94(24):245001, 2005.

[28] D. Umstadter, S.-Y. Chen, A. Maksimchuk, G. Mourou, and R. Wagner. Nonlinear optics in relativistic plasmas and laser wake field acceleration of electrons. *Science*, 273(5274):472–5, 1996.

[29] R. Wagner, S.-Y. Chen, A. Maksimchuk, and D. Umstadter. Electron acceleration by a laser wakefield in a relativistically self-guided channel. *Phys. Rev. Lett.*, 78(16):3125–3128, Apr 1997.

[30] Ping Zhang, Ned Saleh, Shouyuan Chen, Zhengming Sheng, and Donald Umstadter. An optical trap for relativistic plasma. *Physics of Plasmas*, 10(5):2093–2099, 2003.

[31] D. Gordon, K. C. Tzeng, C. E. Clayton, A. E. Dangor, V. Malka, K. A. Marsh, A. Modena, W. B. Mori, P. Muggli, Z. Najmudin, D. Neely, C. Danson, and C. Joshi. Observation of electron energies beyond the linear dephasing limit from a laser-excited relativistic plasma wave. *Phys. Rev. Lett.*, 80(10):2133–2136, Mar 1998.

[32] M. I. K. Santala, Z. Najmudin, E. L. Clark, M. Tatarakis, K. Krushelnick, A. E. Dangor, V. Malka, J. Faure, R. Allott, and R. J. Clarke. Observation of a hot high-current electron beam from a self-modulated laser wakefield accelerator. *Phys. Rev. Lett.*, 86(7):1227–1230, Feb 2001.

[33] C. I. Moore, A. Ting, K. Krushelnick, E. Esarey, R. F. Hubbard, B. Hafizi, H. R. Burris, C. Manka, and P. Sprangle. Electron trapping in self-modulated laser wakefields by raman backscatter. *Phys. Rev. Lett.*, 79(20):3909–3912, Nov 1997.

[34] A. Ting, C. I. Moore, K. Krushelnick, C. Manka, E. Esarey, P. Sprangle, R. Hubbard, H. R. Burris, R. Fischer, and M. Baine. Plasma wakefield generation and electron acceleration in a self-modulated laser wakefield accelerator experiment. *Phys. Plasmas*, 4(5):1889–1899, 1997.

[35] C. I. Moore, A. Ting, S. J. McNaught, J. Qiu, H. R. Burris, and P. Sprangle. A laser-accelerator injector based on laser ionization and ponderomotive acceleration of electrons. *Phys. Rev. Lett.*, 82(8):1688–1691, Feb 1999.

[36] C. I. Moore, A. Ting, T. Jones, E. Briscoe, B. Hafizi, R. F. Hubbard, and P. Sprangle. Measurements of energetic electrons from the high-intensity laser ionization of gases. *Phys. Plasmass*, 8(5):2481–2487, 2001.

[37] A. Ting, D. Kaganovich, D. F. Gordon, R. F. Hubbard, and P. Sprangle. Generation and measurements of high energy injection electrons from the high density laser ionization and ponderomotive acceleration. *Physics of Plasmas*, 12(1):010701, 2005.

[38] Yoneyoshi Kitagawa, Yasuhiko Sentoku, Shin Akamatsu, Wataru Sakamoto, Ryosuke Kodama, Kazuo A. Tanaka, Ken Azumi, Takayoshi Norimatsu, Takeshi Matsuoka, Hisanori Fujita, and Hidetsugu Yoshida. Electron acceleration in an ultraintense-laser-illuminated capillary. *Physical Review Letters*, 92(20):205002, 2004.

[39] N. Hafz, M. S. Hur, G. H. Kim, C. Kim, I. S. Ko, and H. Suk. Quasimonoenergetic electron beam generation by using a pinholelike collimator in a self-modulated laser wakefield acceleration. *Physical Review E (Statistical, Nonlinear, and Soft Matter Physics)*, 73(1):016405, 2006.

[40] C. Gahn, G. D. Tsakiris, A. Pukhov, J. Meyer-ter Vehn, G. Pretzler, P. Thirolf, D. Habs, and K. J. Witte. Multi-mev electron beam generation by direct laser acceleration in high-density plasma channels. *Phys. Rev. Lett.*, 83(23):4772–4775, Dec 1999.

[41] C. Gahn, G. D. Tsakiris, G. Pretzler, K. J. Witte, P. Thirolf, D. Habs, C. Delfin, and C.-G. Wahlström. Generation of mev electrons and positrons with femtosecond pulses from a table-top laser system. *Physics of Plasmas*, 9(3):987–999, 2002.

[42] W. P. Leemans, D. Rodgers, P. E. Catravas, C. G. R. Geddes, G. Fubiani, E. Esarey, B. A. Shadwick, R. Donahue, and A. Smith. Gamma-neutron activation experiments using laser wakefield accelerators. *Phys. Plasmas*, 8(5):2510–2516, 2001.

[43] W. P. Leemans, P. Catravas, E. Esarey, C. G. R. Geddes, C. Toth, R. Trines, C. B. Schroeder, B. A. Shadwick, J. van Tilborg, and J. Faure. Electron-yield enhancement in a laser-wakefield accelerator driven by asymmetric laser pulses. *Phys. Rev. Lett.*, 89(17):174802, Oct 2002.

[44] W. P. Leemans, C. G. R. Geddes, J. Faure, Cs. Tóth, J. van Tilborg, C. B. Schroeder, E. Esarey, G. Fubiani, D. Auerbach, B. Marcelis, M. A. Carnahan, R. A. Kaindl, J. Byrd, and M. C. Martin. Observation of terahertz emission from a laser-plasma

accelerated electron bunch crossing a plasma-vacuum boundary. *Phys. Rev. Lett.*, 91(7):074802, Aug 2003.

[45] W. P. Leemans, J. van Tilborg, J. Faure, C. G. R. Geddes, Cs. Tóth, C. B. Schroeder, E. Esarey, G. Fubiani, and G. Dugan. Terahertz radiation from laser accelerated electron bunches. *Phys. Plasmas*, 11(5):2899–2906, 2004.

[46] Tomonao Hosokai, Kenichi Kinoshita, Alexei Zhidkov, Kei Nakamura, Takahiro Watanabe, Toru Ueda, Hideyuki Kotaki, Masaki Kando, Kazuhisa Nakajima, and Mitsuru Uesaka. Effect of a laser prepulse on a narrow-cone ejection of mev electrons from a gas jet irradiated by an ultrashort laser pulse. *Phys. Rev. E*, 67(3):036407, Mar 2003.

[47] Tomonao Hosokai, Kenichi Kinoshita, Alexei Zhidkov, Kei Nakamura, Hideyuki Kotaki, Masaki Kando, Kazuhisa Nakajima, and Mitsuru Uesaka. Refraction effects on the cavity formation and interaction of an intense ultra-short laser pulse with a gas jet. *Physics of Plasmas*, 11(10):L57–L60, 2004.

[48] V. Malka, J. Faure, J. R. Marquès, F. Amiranoff, J. P. Rousseau, S. Ranc, J. P. Chambaret, Z. Najmudin, B. Walton, P. Mora, and A. Solodov. Characterization of electron beams produced by ultrashort (30 fs) laser pulses. *Physics of Plasmas*, 8(6):2605–2608, 2001.

[49] S. Fritzler, E. Lefebvre, V. Malka, F. Burgy, A. E. Dangor, K. Krushelnick, S. P. D. Mangles, Z. Najmudin, J.-P. Rousseau, and B. Walton. Emittance measurements of a laser-wakefield-accelerated electron beam. *Physical Review Letters*, 92(16):165006, 2004.

[50] Y. Glinec, J. Faure, L. Le Dain, S. Darbon, T. Hosokai, J. J. Santos, E. Lefebvre, J. P. Rousseau, F. Burgy, B. Mercier, and V. Malka. High-resolution gamma-ray radiography produced by a laser-plasma driven electron source. *Physical Review Letters*, 94(2):025003, 2005.

[51] M. Kando, S. Masuda, A. Zhidkov, A. Yamazaki, H. Kotaki, S. Kondo, T. Homma, S. Kanazawa, K. Nakajima, Y. Hayashi, M. Mori, H. Kiriyama, Y. Akahane, N. Inoue, H. Ueda, Y. Nakai, K. Tsuji, Y. Yamamoto, K. Yamakawa, J. Koga, T. Hosokai, M. Uesaka, and T. Tajima. Electron acceleration by a nonlinear wakefield generated by ultrashort (23-fs) high-peak-power laser pulses in plasma. *Physical Review E (Statistical, Nonlinear, and Soft Matter Physics)*, 71(1):015403, 2005.

[52] W.-T. Chen, T.-Y. Chien, C.-H. Lee, J.-Y. Lin, J. Wang, and S.-Y. Chen. Optically controlled seeding of raman forward scattering and injection of electrons in a self-modulated laser-wakefield accelerator. *Physical Review Letters*, 92(7):075003, 2004.

[53] T.-Y. Chien, C.-L. Chang, C.-H. Lee, J.-Y. Lin, J. Wang, and S.-Y. Chen. Spatially localized self-injection of electrons in a self-modulated laser-wakefield accelerator by using a laser-induced transient density ramp. *Physical Review Letters*, 94(11):115003, 2005.

[54] Xiaofang Wang, Mohan Krishnan, Ned Saleh, Haiwen Wang, and Donald Umstadter. Electron acceleration and the propagation of ultrashort high-intensity laser pulses in plasmas. *Phys. Rev. Lett.*, 84(23):5324–5327, Jun 2000.

[55] L. M. Chen, J. J. Park, K.-H. Hong, J. L. Kim, J. Zhang, and C. H. Nam. Emission of a hot electron jet from intense femtosecond-laser˘cluster interactions. *Phys. Rev. E*, 66(2):025402, Aug 2002.

[56] C. G. R. Geddes, Cs. Tóth, J. van Tilborg, E. Esarey, C. B. Schroeder, D. Bruhwiler, C. Nieter, J. Cary, and W. P. Leemans. High quality electron beams from a plasma channel guided laser wakefield accelerator. *Nature*, 431:538–541, 2004.

[57] S.P.D. Mangles, C.D. Murphy, Z. Najmudin, A.G.R. Thomas, J.L. Collier, A.E. Dangor, E.J. Divali, P.S. Foster, J.G. Gallacher, C.J. Hooker, D.A. Jaroszynski, A.J. Langley, W.B. Mori, P.A. Norreys, F.S. Tsung, R. Viskup, B.R. Walton, and K. Krushelnick. Monoenergetic beams of relativistic electrons from intense laser-plasma interactions. *Nature*, 431:535–538, 2004.

[58] J. Faure, Y. Glinec, A. Pukhov, S. Kiselev, S. Gordienko, E. Lefebvre, J.-P. Rousseau, F. Burgy, and V. Malka. A laser-plasma accelerator producing monoenergetic electron beams. *Nature*, 431:541–544, 2004.

[59] E. Esarey, C. B. Schroeder, and W. P. Leemans. Physics of laser-driven plasma-based electron accelerators. *Review of Modern Physics*, 2007. in press.

[60] Eisuke Miura, Kazuyoshi Koyama, Susumu Kato, Naoki Saito, Masahiro Adachi, Yoichi Kawada, Tatsufumi Nakamura, and Mitumori Tanimoto. Demonstration of quasi-monoenergetic electron-beam generation is laser-driven plasma acceleration. *Appl. Phys. Lett.*, 86:251501, 2005.

[61] M. Adachi, E. Miura, S. Kato, K. Koyama, T. Watanabe, A. Ogata, H. Okamoto, and M. Tanimoto. Monoenergetic electron beam generation in a laser-driven plasma acceleration. *Laser Phys. Lett.*, 3(2):79, 2006.

[62] S. Masuda, E. Miura, K. Koyama, S. Kato, M. Adachi, T. Watanabe, K. Torii, and M. Tanimoto. Energy scaling of monoenergetic electron beams generated by the laser-driven plasma based accelerator. *Physics of Plasmas*, 14(2):023103, 2007.

[63] Tomonao Hosokai, Kenichi Kinoshita, Takeru Ohkubo, Akira Maekawa, Mitsuru Uesaka, Alexei Zhidkov, Atsushi Yamazaki, Hideyuki Kotaki, Masaki Kando, Kazuhisa Nakajima, Sergei V. Bulanov, Paolo Tomassini, Antonio Giulietti, and Danilo Giulietti. Observation of strong correlation between quasimonoenergetic electron beam generation by laser wakefield and laser guiding inside a preplasma cavity. *Physical Review E (Statistical, Nonlinear, and Soft Matter Physics)*, 73(3):036407, 2006.

[64] A. Yamazaki, H. Kotaki, I. Daito, M. Kando, S. V. Bulanov, T. Zh. Esirkepov, S. Kondo, S. Kanazawa, T. Homma, K. Nakajima, Y. Oishi, T. Nayuki, T. Fujii, and K. Nemoto. Quasi-monoenergetic electron beam generation during laser pulse interaction with very low density plasmas. *Physics of Plasmas*, 12(9):093101, 2005.

[65] B. Hidding, K.-U. Amthor, B. Liesfeld, H. Schwoerer, S. Karsch, M. Geissler, L. Veisz, K. Schmid, J. G. Gallacher, S. P. Jamison, D. Jaroszynski, G. Pretzler, and R. Sauerbrey. Generation of quasimonoenergetic electron bunches with 80-fs laser pulses. *Physical Review Letters*, 96(10):105004, 2006.

[66] C.-T. Hsieh, C.-M. Huang, C.-L. Chang, Y.-C. Ho, Y.-S. Chen, J.-Y. Lin, J. Wang, and S.-Y. Chen. Tomography of injection and acceleration of monoenergetic electrons in a laser-wakefield accelerator. *Physical Review Letters*, 96(9):095001, 2006.

[67] C.-L. Chang, C.-T. Hsieh, Y.-C. Ho, Y.-S. Chen, J.-Y. Lin, J. Wang, and S.-Y. Chen. Production of a monoenergetic electron bunch in a self-injected laser-wakefield accelerator. *Physical Review E (Statistical, Nonlinear, and Soft Matter Physics)*, 75(3):036402, 2007.

[68] C. G. R. Geddes, Cs. Tóth, J. van Tilborg, E. Esarey, C. B. Schroeder, D. Bruhwiler, C. Nieter, J. Cary, and W. P. Leemans. Production of high-quality electron bunches by dephasing and beam loading in channeled and unchanneled laser plasma accelerators. *Physics of Plasmas*, 12(5):056709, 2005.

[69] V. Malka, J. Faure, Y. Glinec, A. Pukhov, and J.-P. Rousseau. Monoenergetic electron beam optimization in the bubble regime. *Physics of Plasmas*, 12(5):056702, 2005.

[70] K. Krushelnick, Z. Najmudin, S. P. D. Mangles, A. G. R. Thomas, M. S. Wei, B. Walton, A. Gopal, E. L. Clark, A. E. Dangor, S. Fritzler, C. D. Murphy, P. A. Norreys, W. B. Mori, J. Gallacher, D. Jaroszynski, and R. Viskup. Laser plasma acceleration of electrons: Towards the production of monoenergetic beams. *Physics of Plasmas*, 12(5):056711, 2005.

[71] S. P. D. Mangles, A. G. R. Thomas, M. C. Kaluza, O. Lundh, F. Lindau, A. Persson, F. S. Tsung, Z. Najmudin, W. B. Mori, C.-G. Wahlström, and K. Krushelnick. Laser-wakefield acceleration of monoenergetic electron beams in the first plasma-wave period. *Physical Review Letters*, 96(21):215001, 2006.

[72] S. P. D. Mangles, A. G. R. Thomas, O. Lundh, F. Lindau, M. C. Kaluza, A. Persson, C.-G. Wahlström, K. Krushelnick, and Z. Najmudin. On the stability of laser wakefield electron accelerators in the monoenergetic regime. *Physics of Plasmas*, 14(5):056702, 2007.

[73] A. G. R. Thomas, Z. Najmudin, S. P. D. Mangles, C. D. Murphy, A. E. Dangor, C. Kamperidis, K. L. Lancaster, W. B. Mori, P. A. Norreys, W. Rozmus, and K. Krushelnick. Effect of laser-focusing conditions on propagation and monoenergetic electron production in laser-wakefield accelerators. *Physical Review Letters*, 98(9):095004, 2007.

[74] J. Faure, C. Rechatin, A. Norlin, A. Lifschitz, Y. Glinec, and V. Malka. Controlled injection and acceleration of electrons in plasma wakefields by colliding laser pulses. *Nature*, 444:737 – 739, 2006.

[75] E. Esarey, R. F. Hubbard, W. P. Leemans, A. Ting, and P. Sprangle. Electron injection into plasma wakefields by colliding laser pulses. *Phys. Rev. Lett.*, 79(14):2682–2685, Oct 1997.

[76] E. Esarey, C. B. Schroeder, W. P. Leemans, and B. Hafizi. Laser-induced electron trapping in plasma-based accelerators. *Phys. Plasmas*, 6(5):2262–2268, 1999.

[77] C. B. Schroeder, P. B. Lee, J. S. Wurtele, E. Esarey, and W. P. Leemans. Generation of ultrashort electron bunches by colliding laser pulses. *Phys. Rev. E*, 59(5):6037–6047, May 1999.

[78] G. Fubiani, E. Esarey, C. B. Schroeder, and W. P. Leemans. Beat wave injection of electrons into plasma waves using two interfering laser pulses. *Physical Review E (Statistical, Nonlinear, and Soft Matter Physics)*, 70(1):016402, 2004.

[79] G. Fubiani, E. Esarey, C. B. Schroeder, and W. P. Leemans. Improvement of electron beam quality in optical injection schemes using negative plasma density gradients. *Physical Review E (Statistical, Nonlinear, and Soft Matter Physics)*, 73(2):026402, 2006.

[80] K. Nakamura, G. Fubiani, C. G. R. Geddes, P. Michel, J. van Tilborg, C. Tóth, E. Esarey, C. B. Schroeder, and W. P. Leemans. Laser triggered injection of electrons in a laser wakefield accelerator with the colliding pulse method. In V. Yakimenko, editor, *Advanced Accelerator Concepts. Eleventh Workshop*, AIP Conf. Proc., New York, 2005. Amer. Inst. Phys.

[81] Csaba Toth. Colliding pulse injection experiments in non-collinear geometry for controlled laser plasma wakefield acceleration of electrons. In *Proceedings of the 2007 Particle Accelerator Conference*, page 2975, Piscataway, NJ, 2007. IEEE.

[82] Tomonao Hosokai, Kenichi Kinoshita, Alexei Zhidkov, Akira Maekawa, Atsushi Yamazaki, and Mitsuru Uesaka. Effect of external static magnetic field on the emittance and total charge of electron beams generated by laser-wakefield acceleration. *Physical Review Letters*, 97(7):075004, 2006.

[83] N. Barov, J. B. Rosenzweig, M. E. Conde, W. Gai, and J. G. Power. Observation of plasma wakefield acceleration in the underdense regime. *Phys. Rev. ST Accel. Beams*, 3(1):011301, Jan 2000.

[84] M. J. Hogan, R. Assmann, F.-J. Decker, R. Iverson, P. Raimondi, S. Rokni, R. H. Siemann, D. Walz, D. Whittum, B. Blue, C. E. Clayton, E. Dodd, R. Hemker, C. Joshi, K. A. Marsh, W. B. Mori, S. Wang, T. Katsouleas, S. Lee, P. Muggli, P. Catravas, S. Chattopadhyay, E. Esarey, and W. P. Leemans. E-157: A 1.4-m-long plasma wake field acceleration experiment using a 30 gev electron beam from the stanford linear accelerator center linac. *Physics of Plasmas*, 7(5):2241–2248, 2000.

[85] P. Muggli, B. E. Blue, C. E. Clayton, S. Deng, F.-J. Decker, M. J. Hogan, C. Huang, R. Iverson, C. Joshi, T. C. Katsouleas, S. Lee, W. Lu, K. A. Marsh, W. B. Mori, C. L. O'Connell, P. Raimondi, R. Siemann, and D. Walz. Meter-scale plasma-wakefield accelerator driven by a matched electron beam. *Physical Review Letters*, 93(1):014802, 2004.

[86] M. J. Hogan, C. D. Barnes, C. E. Clayton, F. J. Decker, S. Deng, P. Emma, C. Huang, R. H. Iverson, D. K. Johnson, C. Joshi, T. Katsouleas, P. Krejcik, W. Lu, K. A. Marsh, W. B. Mori, P. Muggli, C. L. O'Connell, E. Oz, R. H. Siemann, and D. Walz. Multi-gev energy gain in a plasma-wakefield accelerator. *Physical Review Letters*, 95(5):054802, 2005.

[87] E. Oz, S. Deng, T. Katsouleas, P. Muggli, C. D. Barnes, I. Blumenfeld, F. J. Decker, P. Emma, M. J. Hogan, R. Ischebeck, R. H. Iverson, N. Kirby, P. Krejcik, C. O'Connell, R. H. Siemann, D. Walz, D. Auerbach, C. E. Clayton, C. Huang, D. K. Johnson, C. Joshi, W. Lu, K. A. Marsh, W. B. Mori, and M. Zhou. Ionization-induced electron trapping in ultrarelativistic plasma wakes. *Physical Review Letters*, 98(8):084801, 2007.

[88] Ian Blumenfeld, Christopher E. Clayton, Franz-Josef Decker, Mark J. Hogan, Chengkun Huang, Rasmus Ischebeck, Richard Iverson, Chandrashekhar Joshi, Thomas Katsouleas, Neil Kirby, Wei Lu, Kenneth A. Marsh, Warren B. Mori, Patric Muggli, Erdem Oz, Robert H. Siemann, Dieter Walz, and Miaomiao Zhou. Energy doubling of 42 gev electrons in a metre-scale plasma wakefield accelerator. *Nature*, 445:741–744, 2007.

[89] M. I. K. Santala, M. Zepf, F. N. Beg, E. L. Clark, A. E. Dangor, K. Krushelnick, M. Tatarakis, I. Watts, K. W. D. Ledingham, T. McCanny, I. Spencer, A. C. Machacek, R. Allott, R. J. Clarke, and P. A. Norreys. Production of radioactive nuclides by energetic protons generated from intense laser-plasma interactions. *Applied Physics Letters*, 78(1):19–21, 2001.

[90] K. W. D. Ledingham, P. McKenna, and R. P. Singhal. Applications for nuclear phenomena generated by ultra-intense lasers. *Science*, 300:1107, 2003.

[91] C. B. Schroeder, E. Esarey, J. van Tilborg, and W. P. Leemans. Theory of coherent transition radiation generated at a plasma-vacuum interface. *Physical Review E (Statistical, Nonlinear, and Soft Matter Physics)*, 69(1):016501, 2004.

[92] W. Leemans, S. Chattopadhyay, E.Esarey, A. Zholents, M. Zolotorev, A. Chin, R. Schoenlein, and C.V. Shank. Femtosecond x-ray generation through relativistic electron beam-laser interaction. *Comptes Rendus de l'Academie des Sciences Serie IV Physique Astrophysique*, 1:279–296, 2000.

[93] P. Catravas, E. Esarey, and W. P. Leemans. Femtosecond x-rays from thomson scattering using laser wakefield accelerators. *Meas. Sci. Technol.*, 12:1828–1834, 2001.

[94] E. Esarey, B. A. Shadwick, P. Catravas, and W. P. Leemans. Synchrotron radiation from electron beams in plasma-focusing channels. *Phys. Rev. E*, 65(5):056505, May 2002.

[95] Antoine Rousse, Kim Ta Phuoc, Rahul Shah, Alexander Pukhov, Eric Lefebvre, Victor Malka, Sergey Kiselev, Fréderic Burgy, Jean-Philippe Rousseau, Donald Umstadter, and Daniéle Hulin. Production of a kev x-ray beam from synchrotron radiation in relativistic laser-plasma interaction. *Physical Review Letters*, 93(13):135005, 2004.

[96] Ned Saleh, Kirk Flippo, Koshichi Nemoto, Donald Umstadter, Robert A. Crowell, Charles D. Jonah, and Alexander D. Trifunac. Pulse radiolysis of liquid water using picosecond electron pulses produced by a table-top terawatt laser system. *Review of Scientific Instruments*, 71(6):2305–2308, 2000.

[**97**] J. van Tilborg, C. B. Schroeder, E. Esarey, and W. P. Leemans. Pulse shape and spectrum of coherent diffraction-limited transition radiation from electron beams. *Laser and Particle Beams*, 22(4):415, 2004.

[**98**] J. van Tilborg, C. B. Schroeder, C. V. Filip, Cs. Tóth, C. G. R. Geddes, G. Fubiani, R. Huber, R. A. Kaindl, E. Esarey, and W. P. Leemans. Temporal characterization of femtosecond laser-plasma-accelerated electron bunches using terahertz radiation. *Phys. Rev. Lett.*, 96:014801, January 2006.

[**99**] J. van Tilborg, C. B. Schroeder, C. V. Filip, Cs. Tóth, C. G. R. Geddes, G. Fubiani, E. Esarey, and W. P. Leemans. Terahertz radiation as a bunch diagnostic for laser-wakefield-accelerated electron bunches. *Physics of Plasmas*, 13(5):056704, 2006.

[**100**] J. van Tilborg, C. B. Schroeder, Cs. Tóth, C. G. R. Geddes, E. Esarey, and W. P. Leemans. Single-shot spatiotemporal measurements of high-field terahertz pulses. *Opt. Lett.*, 32(3):313–315, 2007.

[**101**] Kim Ta Phuoc, Fréderic Burgy, Jean-Philippe Rousseau, Victor Malka, Antoine Rousse, Rahul Shah, Donald Umstadter, Alexander Pukhov, and Sergei Kiselev. Laser based synchrotron radiation. *Physics of Plasmas*, 12(2):023101, 2005.

[**102**] R. C. Shah, F. Albert, K. Ta Phuoc, O. Shevchenko, D. Boschetto, A. Pukhov, S. Kiselev, F. Burgy, J.-P. Rousseau, and A. Rousse. Coherence-based transverse measurement of synchrotron x-ray radiation from relativistic laser-plasma interaction and laser-accelerated electrons. *Physical Review E (Statistical, Nonlinear, and Soft Matter Physics)*, 74(4):045401, 2006.

[**103**] Kim Ta Phuoc, Sebastien Corde, Rahul Shah, Felicie Albert, Romuald Fitour, Jean-Philippe Rousseau, Fréderic Burgy, Brigitte Mercier, and Antoine Rousse. Imaging electron trajectories in a laser-wakefield cavity using betatron x-ray radiation. *Physical Review Letters*, 97(22):225002, 2006.

[**104**] K. Ta Phuoc, R. Fitour, A. Tafzi, T. Garl, N. Artemiev, R. Shah, F. Albert, D. Boschetto, A. Rousse, D-E. Kim, A. Pukhov, V. Seredov, and I. Kostyukov. Demonstration of the ultrafast nature of laser produced betatron radiation. *Physics of Plasmas*, 14(8):080701, 2007.

[**105**] www-als.lbl.gov.

[**106**] www.aps.anl.gov.

[**107**] www.spring8.or.jp.

[**108**] C. B. Schroeder, W. M. Fawley, E. Esarey, and W. P. Leemans. Design of an xuv fel driven by the laser-plasma accelerator at the lbnl loasis facility. In *Proceedings of the 28th International Free Electron Laser Conference*, Berlin, 2006. BESSY.

[**109**] G. Fubiani, J. Qiang, E. Esarey, W. P. Leemans, and G. Dugan. Space charge modeling of dense electron beams with large energy spreads. *Physical Review Special Topics-Accelerators and Beams*, 9(6):064402, 2006.

[110] Y. Muroya, M. Lin, T. Watanabe, G. Wu, T. Kobayashi, K. Yoshii, T. Ueda, M. Uesaka, and Y. Katsumura. Ultra-fast pulse radiolysis system combined with a laser photocathode rf gun and a femtosecond laser. *Nuclear Instruments and Methods in Physics Research Section A*, 489:554–562, 2002.

[111] Y. Muroya, M. Lin, H.Iijima, T. Ueda, and Y. Katsumura. Current status of the ultra-fast pule radiolysis system at nerl, the university of tokyo. *Res. Chem. Intermed.*, 31:261 – 272, 2005.

[112] Mitsuru Uesaka, Akira Sakumi, Tomonao Hosokai, Kenichi Kinoshita, Nobuaki Yamaoka, Alexei Zhidkov, Takeru Ohkubo, Toru Ueda, Yusa Muroya, Yosuke Katsumura, Hokuto Iijima, Hiromitsu Tomizawa, and Noritaka Kumagai. New accelerators for femtosecond beam pump-and-probe analysis. *Nucl. Instrum. Meth. B*, 241:880, 2005.

[113] T. Ohkubo, A. Maekawa, R. Tsujii, T. Hosokai, K. Kinoshita, K. Kobayashi, M. Uesaka, A. Zhidkov, K. Nemoto, Y. Kondo, and Y. Shibata. Temporal characteristics of monoenergetic electron beams generated by the laser wakefield acceleration. *Phys. Rev. ST Accel. Beams*, 10(3):031301, Mar 2007.

[114] C. G. Durfee and H. M. Milchberg. Light pipe for high intensity laser pulses. *Phys. Rev. Lett.*, 71(15):2409–2412, Oct 1993.

[115] P. Volfbeyn, E. Esarey, and W. P. Leemans. Guiding of laser pulses in plasma channels created by the ignitor-heater technique. *Phys. Plasmas*, 6(5):2269–2277, 1999.

[116] C. G. R. Geddes, Cs. Toth, J. van Tilborg, E. Esarey, C. B. Schroeder, J. Cary, and W. P. Leemans. Guiding of relativistic laser pulses by preformed plasma channels. *Physical Review Letters*, 95(14):145002, 2005.

[117] G. Dugan. Advanced accelerator system requirements for synchrotron radiation facility linacs. In Vitaly Yakimenko, editor, *ADVANCED ACCELERATOR CONCEPTS: Eleventh Advanced Accelerator Concepts Workshop*, volume 737, pages 245–250. AIP, 2004.

[118] G. Dugan. Advanced accelerator system requirements for future linear colliders. In Vitaly Yakimenko, editor, *ADVANCED ACCELERATOR CONCEPTS: Eleventh Advanced Accelerator Concepts Workshop*, volume 737, pages 29–60. AIP, 2004.

[119] W. P. Leemans, C. W. Siders, E. Esarey, N. E. Andreev, G. Shvets, and W. B. Mori. Plasma guiding and wakefield generation for second-generation experiments. *IEEE Trans. Plasma Sci.*, 24:331–342, 1996.

[120] E. Esarey, C. B. Schroeder, B. A. Shadwick, and W. P. Leemans. Non-linear pump depletion and electron dephasing in laser wakefield accelerators. In Vitaly Yakimenko, editor, *ADVANCED ACCELERATOR CONCEPTS: Eleventh Advanced Accelerator Concepts Workshop*, volume 737, pages 245–250. AIP, 2004.

[121] W. P. Leemans, E. Esarey, C. Geddes, C. Schroeder, and Cs. Tóth. Laser guiding for gev laser-plasma accelerators. *Philos. Trans. R. Soc. London, Ser. A*, 364:585–600, 2006.

[**122**] A. F. Lifschitz, J. Faure, V. Malka, and P. Mora. Gev wakefield acceleration of low energy electron bunches using petawatt lasers. *Physics of Plasmas*, 12(9):093104, 2005.

[**123**] Y.-F. Xiao, H.-H. Chu, H.-E. Tsai, C.-H. Lee, J.-Y. Lin, J. Wang, and S.-Y. Chen. Efficient generation of extended plasma waveguides with the axicon ignitor-heater scheme. *Physics of Plasmas*, 11(5):L21–L24, 2004.

[**124**] A. Zigler, Y. Ehrlich, C. Cohen, J. Krall, and P. Sprangle. Optical guiding of high intensity laser pulses in a long plasma channel formed by a slow capillary discharge. *J. Opt. Soc. Am. B.*, 13:68–71, 1996.

[**125**] D. Kaganovich, A. Ting, C. I. Moore, A. Zigler, H. R. Burris, Y. Ehrlich, R. Hubbard, and P. Sprangle. High efficiency guiding of terawatt subpicosecond laser pulses in a capillary discharge plasma channel. *Phys. Rev. E*, 59(5):R4769–R4772, May 1999.

[**126**] T. Hosokai, M. Kando, H. Dewa, H. Kotaki, S. Kondo, K. Nakajima, and K. Horioka. Optical guidance of terawatt laser pulses by the implosion phase of a fast z-pinch discharge in a gas-filled capillary. *Optics Letters*, 25:10–12, 2000.

[**127**] M. C. Downer, C. Chiu, M. Fomyts'kyi, E. W. Gaul, F. Grigsby, N. H. Matlis, B. Shim, P. J. Smith, and R. Zgadzaj. Plasma channels and laser pulse tailoring for gev laser-plasma accelerators. In *ADVANCED ACCELERATOR CONCEPTS: Tenth Workshop*, volume 647, pages 654–663. AIP, 2002.

[**128**] N. C. Lopes, G. Figueira, L. O. Silva, J. M. Dias, R. Fonseca, L. Cardoso, C. Russo, C. Carias, G. Mendes, J. Vieira, and J. T. Mendonça. Plasma channels produced by a laser-triggered high-voltage discharge. *Phys. Rev. E*, 68(3):035402, Sep 2003.

[**129**] D. J. Spence and S. M. Hooker. Investigation of a hydrogen plasma waveguide. *Phys. Rev. E*, 63(1):015401, Dec 2000.

[**130**] A. Butler, D. J. Spence, and S. M. Hooker. Guiding of high-intensity laser pulses with a hydrogen-filled capillary discharge waveguide. *Phys. Rev. Lett.*, 89(18):185003, Oct 2002.

[**131**] A. J. Gonsalves, T. P. Rowlands-Rees, B. H. P. Broks, J. J. A. M. van der Mullen, and S. M. Hooker. Transverse interferometry of a hydrogen-filled capillary discharge waveguide. *Phys. Rev. Lett.*, 98:025002, 2007.

[**132**] W. P. Leemans, C. E. Clayton, W. B. Mori, K. A. Marsh, A. Dyson, and C. Joshi. Plasma physics aspects of tunnel-ionized gases. *Phys. Rev. Lett.*, 68:321–324, 1992.

[**133**] Leonid M. Gorbunov, Patrick Mora, and Jr. Thomas M. Antonsen. Quasistatic magnetic field generated by a short laser pulse in an underdense plasma. *Physics of Plasmas*, 4(12):4358–4368, 1997.

[**134**] Rhon Keinigs and Michael E. Jones. Two-dimensional dynamics of the plasma wakefield accelerator. *Physics of Fluids*, 30(1):252–263, 1987.

[135] W. K. H. Panofsky and W. A. Wenzel. Some considerations concerning the transverse deflection of charged particles in radio-frequency fields. *Review of Scientific Instruments*, 27(11):967–967, 1956.

[136] P. Sprangle, E. Esarey, and A. Ting. Nonlinear theory of intense laser-plasma interactions. *Phys. Rev. Lett.*, 64:2011–2014, 1990.

[137] P. Sprangle, E. Esarey, and A. Ting. Nonlinear interaction of intense laser pulses in plasmas. *Phys. Rev. A*, 41:4463–4469, 1990.

[138] N. E. Andreev, L. M. Gorbunov, V. I. Kirsanov, K. Nakajima, and A. Ogata. Structure of the wake field in plasma channels. *Physics of Plasmas*, 4(4):1145–1153, 1997.

[139] A. Pukhov and J. Meyer-ter-Vehn. Laser wake field acceleration: the highly nonlinear broken-wave regime. *Appl. Phys. B*, 74:355–361, 2002.

[140] S. Gordienko and A. Pukhov. Scalings for ultrarelativistic laser plasmas and quasimonoenergetic electrons. *Phys. Plasmas*, 12:043109, April 2005.

[141] F. S. Tsung, W. Lu, M. Tzoufras, W. B. Mori, C. Joshi, J. M. Vieira, L. O. Silva, and R. A. Fonseca. Simulation of monoenergetic electron generation via laser wakefield accelerators for 5–25 tw lasers. *Physics of Plasmas*, 13(5):056708, 2006.

[142] W. Lu, C. Huang, M. Zhou, M. Tzoufras, F. S. Tsung, W. B. Mori, and T. Katsouleas. A nonlinear theory for multidimensional relativistic plasma wave wakefields. *Physics of Plasmas*, 13(5):056709, 2006.

[143] C. B. Schroeder, E. Esarey, B. A. Shadwick, and W. P. Leemans. Trapping, dark current, and wave breaking in nonlinear plasma waves. *Physics of Plasmas*, 13(3):033103, 2006.

[144] E. Esarey, B. Hafizi, R. Hubbard, and A. Ting. Trapping and acceleration in self-modulated laser wakefields. *Phys. Rev. Lett.*, 80(25):5552–5, 1998.

[145] D. Umstadter, J. K. Kim, and E. Dodd. Laser injection of ultrashort electron pulses into wakefield plasma waves. *Phys. Rev. Lett.*, 76(12):2073–6, 1996.

[146] T. M. Antonsen, Jr. and P. Mora. Self-focusing and raman scattering of laser pulses in tenuous plasmas. *Phys. Rev. Lett.*, 69:2204–2207, 1992.

[147] C. D. Decker, W. B. Mori, T. Katsouleas, and D. E. Hinkel. Spatial temporal theory of raman forward scattering. *Phys. Plasmas*, 3:1360–72, 1996.

[148] C. B. Schroeder, E. Esarey, B. A. Shadwick, and W. P. Leemans. Raman forward scattering of chirped laser pulses. *Phys. Plasmas*, 10(1):285–295, January 2003.

[149] William L. Kruer. *The Physics of Laser Plasma Interactions*. Addison-Wesley, Redwood City, CA, 1988.

[150] P. Sprangle, J. Krall, and E. Esarey. Hose-modulation instability of intense laser pulses in plasmas. *Phys. Rev. Lett.*, 73:3544–3547, 1994.

[151] E. Esarey, J. Krall, and P. Sprangle.   Envelope analysis of intense laser pulse self-modulation in plasmas. *Phys. Rev. Lett.*, 72:2887–2890, 1994.

[152] E. Esarey, C. B. Schroeder, B. A. Shadwick, J. S. Wurtele, and W. P. Leemans. Nonlinear theory of nonparaxial laser pulse propagation in plasma channels. *Phys. Rev. Lett.*, 84(14):3081–4, 2000.

[153] S. V. Bulanov, F. Pegoraro, A. M. Pukhov, and A. S. Sakharov. Transverse-wake wave breaking. *Phys. Rev. Lett.*, 78(22):4205–4208, 1997.

[154] T. Katsouleas, S. Wilks, P. Chen, J. M. Dawson, and J. J. Su. Beam loading in plasma accelerators. *Part. Accel.*, 22(1):81–99, 1987.

[155] F. S. Tsung, Ritesh Narang, W. B. Mori, C. Joshi, R. A. Fonseca, and L. O. Silva. Near-GeV-energy laser-wakefield acceleration of self-injected electrons in a centimeter-scale plasma channel. *Phys. Rev. Lett.*, 93(18):185002, October 2004.

[156] K. L. Brown.   A first- and second-order matrix theory for the design of beam transport systems and charged prticle spectrometers. *Tech. Rep. SLAC*, 75, 1975.

[157] G. Dugan, A. Misuri, and W. Leemans.   Design and performance estimates for the l'oasis experiment magnetic spectrometers.   Technical Report LBNL-49394, Lawrence Berkeley National Laboratory, University of California, Berkeley, CA 94720, November 2001.

[158] F. Amiranoff, J. Ardonceau, M. Bercher, D. Bernard, B. Cros, A. Debraine, J. M. Dieulot, J. Fusellier, F. Jacquet, J. M. Joly, M. Juillard, G. Matthieussent, and P. Matricon. The plasma beat-wave acceleration experiment at ecole polytechnique. *Nuclear Instruments and Methods in Physics Research A*, 363:497–510, 1995.

[159] C. Gahn, G. D. Tsakiris, K. J. Witte, P. Thirolf, and D. Habs. A novel 45-channel electron spectrometer for high intensity laser-plasma interaction studies. *Review of Scientific Instruments*, 71(4):1642–1645, January 2000.

[160] H. Chen, P. K. Patel, D. F. Price, B. K. Young, P. T. Springer, R. Berry, R. Booth, C. Bruns, and D. Nelson. A compact electron spectrometer for hot electron measurement in pulsed laser solid interaction. *Review of Scientific Instruments*, 74(3):1551–1553, 2003.

[161] Marco Galimberti, Antonio Giulietti, Danilo Giulietti, and Leonida A. Gizzi. Sheeba: A spatial high energy electron beam analyzer. *Review of Scientific Instruments*, 76(5):053303, 2005.

[162] Kazuo A. Tanaka, Toshinori Yabuuchi, Takeshi Sato, Ryosuke Kodama, Yoneyoshi Kitagawa, Teruyoshi Takahashi, Toshiji Ikeda, Yoshihide Honda, and Shuuichi Okuda. Caliration of imaging plate for high energy electron spectrometer. *Rev. Sci. Instrum.*, 76:013507, 2005.

[163] Rad-Icon Imaging Corp.   Scintillator options for shad-o-box cameras.   Technical Report AN-07, Rad-Icon Imaging Corp., www.rad-icon.com, Santa Clara, CA 95054, 2002.

[164] Y. Glinec, J. Faure, A. Guemnie-Tafo, V. Malka, H. Monard, J. P. Larbre, V. De Waele, J. L. Marignier, and M. Mostafavi. Absolute calibration for a broad range single shot electron spectrometer. *Rev. Sci. Instrum.*, 77:103301, 2006.

[165] C. E. Clayton, K. A. Marsh, C. Joshi, C. B. Darrow, A. E. Dangor, A. Modena, Z. Najmudin, and V. Malka. A broadband electron spectrometer and electron detectors for laser accelerator experiments. In *Proceedings of the 1995 Particle Accelerator Conference*, volume 1, page 637, Piscataway, NJ, 1996. IEEE.

[166] Richard G. Schlecht and Dauglas W. McColm. Hyperfine structure of the stable lithium isotopes. *Phys. Rev.*, 142(1):11, 1966.

[167] http://www.ptgrey.com/.

[168] Sairos Safai, Shixiong Lin, and Eros Pedroni. Development of an inorganic scintillating mixture for proton beam verification dosimetry. *Phys. Med. Biol.*, 49:4637–4655, 2004.

[169] K. Makino and M. Berz. Cosy infinity version 8. *Nucl. Instrum. Methods Phys. Res. A*, 427:338, 1999.

[170] K. Nakamura, E. Esarey, C. G. R. Geddes, A. J. Gonsalves, W. P. Leemans, D. Panasenko, C. B. Schroeder, C. Toth, and S. M. Hooker. Performance of capillary discharge guided laser plasma wakefield accelerator. In *Proceedings of the 2007 Particle Accelerator Conference*, page 2978, Piscataway, NJ, 2007. IEEE.

[171] A. Yoshida, M. Asahara, M. Ohtsuka, H. Sumida, Y. Higasida, Y. Murakami, J. Morisita, K. Yoshida, Y. Kodera, and A. Ohtsuka. *Japanese Journal of Radiological Technology*, 58:322, 2002. In Japanese.

[172] G.E. Giakoumakis and D. M. Miliotis. Light angular distribution of fluorescent screens excited by x-rays. *Phys. Med. Biol.*, 30:21, 1985.

[173] G.E. Giakoumakis, C.D. Nomicos, and P.X. Sandillos. Absolute efficiency of $gd_2 0_2$s:tb screens under fluoroscopic conditions. *Phys. Med. Biol.*, 34:673–678, 1989.

[174] T. Radcliffe, G. Barnea, B. Wowk, R. Rajapakshe, and S. Shalev. Monte carlo optimization of metal/phosphor screens at megavoltage energies. *Medical Physics*, 20(4):1161–1169, 1993.

[175] A. E. Schach von Wittenau, C. M. Logan, M. B. Aufderheide III, and D. M. Slone. Blurring artifacts in megavoltage radiography with a flat-panel imaging system: Comparison of monte carlo simulations with measurements. *Medical Physics*, 29(11):2559–2570, 2002.

[176] B. Fleskens, Calibration of the Detection Efficiency of a Lanex Fast Phosphor Scren using the 1.5 GeV Synchrotron Booster at ALS, Internship thesis, 2007, LBNL, unpublished.

[177] P. Gallegos, Lanex scintillating phospor screns sttudies for laser-wakefield-accelerated electrons characterrization, Internship thesis, 2007, LBNL, unpublished.

[**178**] H. A. Bethe. Molière's theory of multiple scattering. *Phys. Rev.*, 89(6):1256–1266, Mar 1953.

[**179**] R. M. Sternheimer, S. M. Seltzer, and M. J. Berger. Density effect for the ionization loss of charged particles in various substances. *Phys. Rev. B*, 26(11):6067–6076, Dec 1982.

[**180**] Charles H Kim. Modeling of the als linac. In *Proceedings of the 18th International Linac Conference*, 1996.
http://linac96.web.cern.ch/linac96/proceedings/Thursday/THP39/Paper.html.

[**181**] Roderich Keller. Excitation characteristics of the booster-synchrotron lattice-magnets. Technical Report ESG-Tech-Note 175, Lawrence Berkeley National Laboratory, University of California, Berkeley, CA 94720, August 1991.

[**182**] K. B. Unser. Design and preliminary tests of a beam intensity monitor for lep. In *Proceedings of the 1989 Particle Accelerator Conference*, volume 1, page 71, Piscataway, NJ, 1989. IEEE.

[**183**] http://www.bergoz.com.

[**184**] http://www.aps.anl.gov/epics/index.php.

[**185**] 1-2 GeV synchrotron radiation source. Technical Report PUB-5172 Rev., Lawrence Berkeley National Laboratory, University of California, Berkeley, CA 94720, July 1986.

[**186**] C. G. R. Geddes. *Plasma Channel Guided Laser Wakefield Accelerator.* PhD thesis, University of California, Berkeley, 2005.

[**187**] H. M. Milchberg, T. R. Clark, C. G. Durfee III, and T. M. Antonsen, Jr. Development and applications of a plasma waveguide for intense laser pulses. *Phys. Plasmas*, 3(5):2149–2155, 1996.

[**188**] http://www.fastlite.com/en/.

[**189**] N. A. Bobrova, A. A. Esaulov, J.-I. Sakai, P. V. Sasorov, D. J. Spence, A. Butler, S. M. Hooker, and S. V. Bulanov. Simulations of a hydrogen-filled capillary discharge waveguide. *Phys. Rev. E*, 65(1):016407, January 2002.

[**190**] B. H. P. Broks, K. Garloff, and J. J. A. M. van der Mullen. Nonlocal-thermal-equilibrium model of a pulsed capillary discharge waveguide. *Phys. Rev. E*, 71(1):016401, January 2005.

[**191**] A. J. Gonsalves. *Investigation of a Hydrogen-filled Capillary Discharge Waveguide for Laser-Driven Plasma Accelerators.* PhD thesis, University of Oxford, 2006.

[**192**] C. Max, J. Arons, and A. B. Langdon. Self-modulation and self-focusing of electromagnetic waves in plasmas. *Phys. Rev. Lett.*, 33:209–212, 1974.

[**193**] P. Sprangle, C. M. Tang, and E. Esarey. Relativistic self-focusing of short-pulse radiation beams in plasmas. *IEEE Trans. Plasma Sci.*, PS-15:145–153, 1987.

[194] A. Zhidkov, 2007. private communication.

[195] C. G. R. Geddes and Estelle Michel, 2008. private communication.

[196] J. Faure, Y. Glinec, G. Gallot, and V. Malka. Ultrashort laser pulses and ultrashort electron bunches generated in relativistic laser-plasma interaction. *Physics of Plasmas*, 13(5):056706, 2006.

[197] S. Bulanov, N. Naumova, F. Pegoraro, and J. Sakai. Particle injection into the wave acceleration phase due to nonlinear wake wave breaking. *Phys. Rev. E*, 58(5):R5257–R5260, Nov 1998.

[198] D. Kaganovich, A. Ting, D. F. Gordon, R. F. Hubbard, T. G. Jones, A. Zigler, and P. Sprangle. First demonstration of a staged all-optical laser wakefield acceleration. *Physics of Plasmas*, 12(10):100702, 2005.

[199] A. J. Gonsalves, K. Nakamura, E. Esarey, C. G. R. Geddes, W. P. Leemans, D. Panasenko, C. B. Schroeder, C. Toth, E. Cormier-Michel, D. Bruhwiler, J. R. Cary, and S. M. Hooker. Experimental demonstration of 1 gev energy gain in a laser wakefield accelerator. In *Proceedings of the 2007 Particle Accelerator Conference*, page 2978, Piscataway, NJ, 2007. IEEE.

[200] C.G.R. Geddes, D. Bruhwiler, J.R. Cary, E. Cormier-Michel, E. Esarey, C.B. Schroeder, W.A. Isaacs, N. Stinus, P. Messmer, A. Hakim, K. Nakamura, A.J. Gonsalves, D. Panasenko, G.R. Plateau, Cs. Toth, B. Nagler, J. van Tilborg, T. Cowan, S.M. Hooker, and W.P. Leemans. Laser wakefield simulations towards development of compact particle accelerators. *Journal of Physics, Conference Series*, 78:12021, 2007.

[201] F. Salin, P. Georges, G. Roger, and A. Brun. Single-shot measurement of a 52-fs pulse. *Applied Optics*, 26(21):4528, 1987.

[202] Rick Trebino, Kenneth W. Delong, David N. Fittinghoff, John N. Sweetser, and Marco A. Krumbugel adn Bruce A. Richman. Measuring ultrashort laser pulses in the time-frequency domain using frequency-resolved optical gating. *Review of Scientific Instruments*, 68(9):3277, 1997.

[203] Chris Iaconis and Ian A. Walmsley. Self-referencing spectral interferometry for measuring ultrashort optical pulses. *IEEE J. Quantum Electron.*, 35(4):501, 1999.

[204] N. H. Matlis, S. Reed, S. S. Bulanov, V. Chvykov, G. Kalintchnko, T. Matsuoka, P. Rousseau, V. Yanovsky, A. Maksimchuk, S. Kalmykov, G. Shvets, and M. C. Downer. Snapshots of laser wakefields. *Nature Physics*, 2:749, 2006.

[205] W. P. Leemans, E. Esarey, J. van Tilborg, P. A. Michel, C. B. Schroeder, Cs. Tóth, C. G. R. Geddes, and B. A. Shadwick. Radiation from laser accelerated electron bunches: coherent terahertz and femtosecond x-rays. *IEEE Trans. Plasma Sci.*, 33:8–22, 2005.